

THREE DIMENSIONAL NUMERICAL MODELLING OF DISCONTINUOUS
ROCKS BY USING DISTINCT ELEMENT METHOD

A THESIS SUBMITTED TO
THE GRADUATE SCHOOL OF NATURAL AND APPLIED SCIENCES
OF
MIDDLE EAST TECHNICAL UNIVERSITY

BY

ARMAN KOÇAL

IN PARTIAL FULFILLMENT OF THE REQUIREMENTS
FOR
THE DEGREE OF DOCTOR OF PHILOSOPHY
IN
MINING ENGINEERING

SEPTEMBER 2008

Approval of the thesis:

**THREE DIMENSIONAL NUMERICAL MODELLING OF
DISCONTINUOUS ROCKS BY USING DISTINCT ELEMENT METHOD**

submitted by **ARMAN KOÇAL** in partial fulfillment of the requirements for
the degree of **Doctor of Philosophy in Mining Engineering Department,**
Middle East Technical University by;

Prof. Dr. Canan Özgen
Dean, Graduate School of **Natural and Applied Sciences** _____

Prof Dr. Celal Karpuz
Head of Department, **Mining Engineering** _____

Prof Dr. Celal Karpuz
Supervisor, **Mining Engineering Dept., METU** _____

Assoc. Prof. Dr. H.Şebnem Düzgün
Co-supervisor, **Mining Engineering Dept., METU** _____

Examining Committee Members:

Prof. Dr. Seyfi Kulaksız
Mining Engineering Dept., Hacettepe University _____

Prof. Dr. Celal Karpuz
Mining Engineering Dept., METU _____

Assoc. Prof. Dr. H. Şebnem Düzgün
Mining Engineering Dept., METU _____

Assoc. Prof. Dr. Levent Tutluoğlu
Mining Engineering Dept., METU _____

Assoc. Prof. Dr. Sadık Bakır
Civil Engineering Dept., METU _____

Date: 05/09/2008

I hereby declare that all information in this document has been obtained and presented in accordance with academic rules and ethical conduct. I also declare that, as required by these rules and conduct, I have fully cited and referenced all material and results that are not original to this work.

Name, Last name : Arman Koçal

Signature :

ABSTRACT

THREE DIMENSIONAL NUMERICAL MODELLING OF DISCONTINUOUS ROCKS BY USING DISTINCT ELEMENT METHOD

Koçal, Arman

Ph.D., Department of Mining Engineering

Supervisor : Prof. Dr. Celal Karpuz

Co-supervisor : Assoc. Prof. Dr. H. Şebnem Düzgün

September 2008, 198 pages

Shear strength characterization of discontinuities is an important concept for slope design in discontinuous rocks. This study presents the development of a methodology for implementing Barton-Bandis empirical shear strength failure criterion in three dimensional distinct element code, 3DEC, and verification of this methodology.

Normal and shear deformation characteristics of discontinuities and their relations to the discontinuity surface characteristics have been reviewed in detail.

First, a C++ dynamic link library (DLL) file was coded and embedded into 3DEC for modelling the Barton-Bandis shear strength criterion. Then, a numerically developed direct shear test model was used to verify the normal and shear deformation behaviour with respect to empirical results of the Barton-Bandis shear strength criterion.

A three dimensional simple discontinuous rock slope was modelled in 3DEC based on Barton-Bandis shear strength criterion. The slope model was first utilized by Mohr-Coulomb failure criterion. Then, with the use of the new model developed here, the effects of the discontinuity surface properties on shear strength were introduced to the slope problem.

Applicability of the developed model was verified by three large scale real case studies from different open pit lignite mines of Turkish Coal Enterprises (TKİ), namely Bursa Lignites Establishment (BLİ) – 2 cases and Çan Lignite Establishment (ÇLİ). The results with the new model option, which allows users to use important discontinuity surface properties like joint roughness coefficient and joint wall compressive strength, compared well with results of previous studies using Mohr-Coulomb failure criterion.

Keywords: Barton-Bandis Shear Strength Criterion, Numerical Modelling, Distinct Element Method, Slope Stability

ÖZ

AYRIK ELEMAN METODU KULLANILARAK SÜREKSİZLİK İÇEREN KAYALARIN ÜÇ BOYUTLU SAYISAL MODELLENMESİ

Koçal, Arman

Doktora, Maden Mühendisliği Bölümü

Tez Yöneticisi : Prof. Dr. Celal Karpuz

Ortak Tez Yöneticisi : Doç. Dr. H. Şebnem Düzgün

Eylül 2008, 198 sayfa

Süreksizlik içeren kaya kütlelerinde şev tasarımında kesme dayanımı tanımlaması önemli bir kavramdır. Bu çalışma; üç boyutlu ayrik elemanlar programı 3DEC'e Barton-Bandis süreksizlik modelinin uygulanmasına yönelik bir yöntemilimi geliştirilmesini ve bu çalışmanın doğrulamasını sunmaktadır.

Süreksizliklerin dikey ve kesme deformasyon özellikleri ve bunların süreksizlik yüzeyleri ile ilgisi ayrıntılı olarak gözden geçirilmiştir.

Önce, Barton-Bandis kesme kriterinin modellenmesi için C++ programında bir DLL dosyası yazılıp 3DEC programına yerleştirilmiştir. Daha sonra, süreksizliklerin dikey ve kesme deformasyon davranışları, sayısal olarak oluşturulan bir direk kesme modeli kullanılarak Barton-Bandis makaslama dayanım kriterinin ampirik sonuçları ile doğrulanmıştır.

Barton-Bandis kesme dayanımı kriterini esas alan üç boyutlu basit bir kaya şevi 3DEC'de modellenmiştir. Şev modelinde ilk olarak Mohr-Coulomb

yenilme kriteri kullanılmıştır. Ardından, yeni geliştirilen model kullanılarak, süreksizlik yüzey özelliklerinin kesme dayanımı üzerinde etkisi şev sorununa tanıtılmıştır.

Geliştirilen modelin uygulanabilirliği, Türkiye Kömür İşletmeleri (TKİ) nin üç deüişik açık ocağında gerçek heyelan verileri ile doğrulanmıştır. Bunlar, Orhaneli Linyitleri İşletmesi (BLİ) – iki heyelan ve Çan Linyitleri İşletmesi (ÇLİ) açık linyit ocaklarından değışik üç tane büyük ölçekli gerçek modellerle doğrulanmıştır. Kullanıcıya pürüzlülük katsayısı ve yüzey basınç dayanımı gibi önemli süreksizlik yüzey özelliklerini kullanma imkanı veren yeni geliştirilen model seçeneğı ile alınan sonuçlar, Mohr-Coulomb yenilme kriteri kullanılarak elde edilen önceki sonuçlar ile uyumlu bulunmuştur.

Anahtar kelimeler: Barton-Bandis Makaslama Dayanım Kriteri, Sayısal Modelleme, Ayrık Elemanlar Yöntemi, Şev Stabilitesi

To my wife:

Pelin Koçal

ACKNOWLEDGEMENTS

I wish to express my sincerest gratitude to Prof. Dr. Celal Karpuz for his kind supervision, invaluable support, friendship and help during my study.

Moreover, I would like to express my appreciation to Assoc. Prof. Dr. H. Şebnem Düzgün for her supervision, valuable comments and suggestions throughout the study.

I also would like to express my sincere appreciation to Assoc. Prof. Dr. Levent Tutluoğlu for his steady helps, remarks, suggestions and sincere friendship during my study.

Furthermore, I have to express my appreciation to Prof. Dr. Seyfi Kulaksız and Assoc. Prof. Dr. Sadık Bakır for their valuable comments and serving on the PhD committee.

I also express my gratitude to Perit Çakır for his valuable comments in writing the C++ code.

My thanks also go to Reza R. Osgoui for his invaluable encouragement and friendship.

A special gratitude goes to my real mentor Baran Koçal who has always found in assistance to me.

I want to thank İ. Ferid Öge for his kind and steady helps in every stage of this study.

My special thanks also go to Hakan Uysal, Tahsin Işıksal and İsmail Kaya for their continual friendship and encouragement throughout the study.

I am grateful to all members of my great family: my mother Nursel Koçal, my father Cevat Koçal, my brother Baran Koçal; my mother in-law Nedret

Alpaslan, my father in-law Ahmet Alpaslan; Aylin, Böke, Beril and Selin Şahin for their continual encouragement and support in every stage of the entire study.

Finally, I am deeply thankful to my beloved wife Pelin Koçal for her continual love and support. It would not be possible for me to achieve this goal without her patience, understanding and unconditional support. To whom I dedicate this thesis.

TABLE OF CONTENTS

ABSTRACT	iv
ÖZ.....	vi
ACKNOWLEDGEMENTS	ix
TABLE OF CONTENTS	xi
LIST OF TABLES.....	xiv
LIST OF FIGURES.....	xvii
LIST OF SYMBOLS	xxv
CHAPTERS	
1. INTRODUCTION.....	1
1.1 General Description	1
1.2 Statement of the Problem	2
1.3 Objective of the Thesis	3
1.4 Methodology of the Thesis.....	4
1.5 Organization of the Thesis	5
2. BASIC MECHANICS OF DISCONTINUITIES.....	7
2.1 Introduction	7
2.2 Slope Failure Mechanisms.....	7
2.2.1 Plane failure	7
2.2.2 Wedge failure	9
2.2.3 Circular failure	10
2.2.4 Toppling failure.....	11
2.3 Shear Strength of Discontinuities.....	13
2.3.1 Joint wall compressive strength (JCS)	15
2.3.2 Basic friction angle (ϕ_b) and residual friction angle (ϕ_r).....	16
2.3.3 Joint Roughness Coefficient (JRC)	19

2.3.4 Dilation	24
2.3.5 Scale effects	24
2.3.6 Empirical equations for the scale effects on the shear behaviour of rock discontinuities	27
2.3.7 Mobilization of roughness during shear	29
2.3.8 Rock discontinuity deformation	32
Normal deformation	33
Maximum closure	34
Shear deformation	37
2.4 Distinct Element Modelling	39
3. DEVELOPMENT OF THE NUMERICAL MODEL	48
3.1 Introduction	48
3.2 Basic Structure of the Program	48
3.3.1 Input data of the Barton-Bandis criterion	50
3.3.2 Execution stage	51
4. EMPIRICAL VERIFICATION OF THE NUMERICAL MODEL	56
4.1 Introduction	56
4.2 Direct-shear Test Model	57
4.3 Normal Deformation of the Discontinuity Model	58
4.3.1 Normal stress – normal closure	58
Effect of joint roughness coefficient (JRC) on discontinuity normal closure	60
Effect of joint wall compressive strength (JCS) on discontinuity normal closure	62
Effect of uniaxial compressive strength (σ_c) on discontinuity normal closure	64
4.3.2 Discontinuity normal stiffness	65
4.4 Shear Behaviour of the Discontinuity Model	68
4.4.1 Shear strength behaviour of the model	69
Effect of normal stress on shear strength	69
Effect of joint roughness coefficient (JRC) on shear strength	73
Effect of joint wall compressive strength (JCS) on shear strength	79
Effect of residual friction angle on shear strength	82
4.4.2 Dilation	85
4.4.3 Discontinuity shear stiffness	88

4.5 Results and Discussion.....	89
5. APPLICATION OF THE PROPOSED NUMERICAL MODEL FOR FIELD SCALE SLOPE PROBLEMS	91
5.1 Introduction	91
5.2 Basic Slope Model	92
5.2.1 2-D verification of parameter determination	97
5.2.2 3-D verification of parameter determination	98
5.3 Effect of discontinuity surface properties on slope stability.....	102
5.4 Example for large scale slope deformation behaviour – Sliding block.....	103
5.5 Orhaneli Gümüşpınar (A-6 panel) Slope Failure.....	105
5.6 Orhaneli Dikmentepe (A-5 panel) Slope Failure	118
5.7 Çan Open Pit Mine Western Panel Slopes	128
5.8 Results and Discussion.....	139
6. CONCLUSIONS AND RECOMMENDATIONS	141
REFERENCES.....	143
APPENDICES	
A. STRUCTURE OF THE PROGRAM	149
B. NORMAL DEFORMATION BEHAVIOUR	158
C. SHEAR DEFORMATION BEHAVIOUR.....	177
D. DILATATIONAL BEHAVIOUR	195
CURRICULUM VITAE.....	197

LIST OF TABLES

TABLES

Table 2.1 Summary of results of work of Bandis et al. (1981) for scale effects	26
Table 2.2 Values used for calculation of JRC_{mob} (Anon, 2005)	31
Table 4.1 Material and discontinuity properties of the direct shear test model	60
Table 4.2 Results of maximum closure (V_m) analyses with varying joint roughness coefficient (JRC_o) ($\emptyset_r = 20^\circ$, $JCS_o=100\text{MPa}$ and $\sigma_c=150\text{MPa}$)	61
Table 4.3 Results of maximum closure (V_m) analyses with varying joint wall compressive strength (JCS_o) values ($\emptyset_r = 20^\circ$, $JRC_o=8$ and $\sigma_c=150\text{MPa}$)	63
Table 4.4 Results of maximum closure (V_m) analyses with varying uniaxial compressive strength (σ_c) values ($JRC_o=8$ and $JCS_o=50\text{MPa}$)	65
Table 4.5 Empirical and numerical results of normal stiffness (K_n).....	67
Table 4.6 Results of peak shear strength analyses under different normal stresses (σ_n) values ($\emptyset_r = 20^\circ$, $\sigma_c = 150\text{MPa}$, $JRC_o=8$ and $JCS_o=100\text{MPa}$)	71
Table 4.7 Results of peak shear strength (τ_{peak}) analyses under different joint roughness coefficients (JRC) values ($\emptyset_r = 20^\circ$, $\sigma_c = 150\text{MPa}$, $\sigma_n = 5\text{MPa}$ and $JCS_o=100\text{MPa}$).....	75
Table 4.7 Results of residual shear strength analyses ($\emptyset_r = 10^\circ$, $\sigma_c = 150\text{MPa}$, $\sigma_n=5\text{MPa}$ and $JCS_o=100\text{MPa}$).....	78
Table 4.9 Results of peak shear strength (τ_{peak}) analyses under different joint wall compressive strength (JCS_o) values ($\emptyset_r = 20^\circ$, $\sigma_c = 150\text{MPa}$, $JRC_o=8$ and $\sigma_n=5\text{MPa}$).....	80
Table 4.10 Results of peak shear strength (τ_{peak}) analyses under different residual friction angle (\emptyset_r) values ($\sigma_c = 150\text{MPa}$, $JRC_o=8$ and $JCS_o=100\text{MPa}$)	83

Table 4.11 Empirical and numerical results of shear stiffness (K_s).....	89
Table 5.1 Material and discontinuity parameters of the basic slope model with Mohr-Coulomb slip criterion.....	93
Table 5.2 Discontinuity parameters of the basic slope model for Barton-Bandis criterion.....	100
Table 5.3 Material properties of Gümüşpınar landslide obtained from back analyses.....	110
Table 5.4 Discontinuity properties of Gümüşpınar landslide obtained from back analyses.....	111
Table 5.5 Barton-Bandis discontinuity geotechnical properties of the Gümüşpınar landslide.....	116
Table 5.6 Discontinuity properties of Dikmentepe landslide obtained from back analyses.....	122
Table 5.7 Barton-Bandis discontinuity properties of the Dikmentepe landslide.....	126
Table 5.8 Material properties of Çan open pit coal basin from back analyses.....	132
Table 5.9 Discontinuity properties of Çan open pit coal basin from back analyses.....	132
Table 5.10 Barton-Bandis discontinuity properties of the Çan western panel slopes.....	137
Table A.1 Partial class definition for base class, ConstitutiveModel.....	149
Table A.2 Model constructor.....	150
Table A.3 Summary of members of structure State.....	150
Table A.4 Scale correction step.....	151
Table A.5 Normal stiffness calculation step.....	151
Table A.6 Calculation steps for shear stiffness of the joint.....	152
Table A.7 Calculation steps for mobilization of roughness coefficient during shear.....	153
Table A.8 Normal force calculation.....	155

Table A.9 Tensile failure decision step and shear force calculation steps
..... 155

Table A.10 Calculation steps for dilatational component of normal force 157

LIST OF FIGURES

FIGURES

Figure 1.1 Flowchart representing the methodology of the thesis	5
Figure 2.1 Geometry of plane failure (Hoek and Bray, 1981)	8
Figure 2.2 Geometry of wedge failure (Hoek and Bray, 1981)	9
Figure 2.3 Section view of wedge failure (Hoek and Bray, 1981)	9
Figure 2.4 General circular slope failure (Hoek and Bray, 1981)	10
Figure 2.5 Circular slope failure surface, section view (Hoek and Bray, 1981)	11
Figure 2.6 Primary toppling	12
Figure 2.7 Secondary toppling	12
Figure 2.8 Relation between residual friction angle with Schmidt rebound value (Richards, 1975, in Barton and Choubey, 1977)	17
Figure 2.9 Mechanism of residual tilt test (Bandis et al., 1985)	18
Figure 2.10 Laboratory scaled joint roughness profiles (Barton and Choubey, 1977)	20
Figure 2.11 Measurement of asperity amplitude for determining joint roughness (Barton and Bandis (1982), in Hoek (2007))	22
Figure 2.12 Chart for determining joint roughness coefficient from asperity amplitude and profile length (Barton and Bandis (1982), in Hoek (2007))	23
Figure 2.13 Groups of discontinuity types according to their roughness (Bandis et al., 1981)	25
Figure 2.14 Graphs of mean peak shear stress vs. average joint area (Bandis et al., 1981)	26
Figure 2.15 Graphs of peak shear displacement vs discontinuity length (Bandis et al., 1981)	27

Figure 2.16 Sensitivity of scale correction for joint roughness coefficient with a lab scale sample of 0.1 meters	29
Figure 2.17 Typical graphs of normal stress-normal closure and shear stress-shear displacement (Choi and Chung (2004))	32
Figure 2.18 Effects of the joint wall compressive strength (JCS) and mechanical aperture (a_j) on maximum closure (V_m) (Bandis et al., 1983)	34
Figure 2.19 Relation between maximum closure (V_m) and joint roughness coefficient (JRC) (Bandis et al., 1983)	36
Figure 2.20 Summary of experimental joint shear stiffness parameters (Bandis et al. (1983))	39
Figure 2.21 The calculation cycle of 3DEC program (Anon, 2007)	42
Figure 4.1 Direct shear test model used in the verification of the numerical model	58
Figure 4.2 Graph of maximum normal closure (V_m) vs lab scale joint roughness coefficient (JRC_o)	61
Figure 4.3 Graph of maximum normal closure (V_m) vs lab scale joint compressive strength (JCS_o)	63
Figure 4.4 Graph of maximum normal closure (V_m) vs uniaxial compressive strength σ_c	64
Figure 4.5 Graph of normal stress vs normal closure with $\emptyset_r = 20^\circ$, $JRC_o = 8$, $JCS_o = 100$ MPa, $\sigma_c = 150$ MPa	66
Figure 4.6 Graph of normal stiffness (K_n) vs normal closure ΔV ($\emptyset_r = 20^\circ$, $JRC_o = 8$, $JCS_o = 100$ MPa, $\sigma_c = 150$ MPa)	67
Figure 4.7 Graph of peak shear strength of empiric results vs numerical results under different normal stress levels	70
Figure 4.8 Graph of normal stress vs peak shear strength	71
Figure 4.9 Graph of shear stress – shear displacement ($\emptyset_r = 20^\circ$, $\sigma_n = 2$ MPa, $JRC_o=8$ and $JCS_o=100$ MPa)	72
Figure 4.10 Graph of peak shear strength (τ_{peak}) of empirical results vs numerical results with different joint roughness coefficients (JRC_o) ..	74

Figure 4.11 Graph of lab scale joint roughness coefficient vs peak shear strength.....	74
Figure 4.12 Graph of shear stress – shear displacement ($\emptyset_r = 20^\circ$, $\sigma_c = 150$ MPa, $\sigma_n = 5$ MPa and $JCS_o=100$ MPa)	76
Figure 4.13 Graph of shear stress – shear displacement (\emptyset_r , $\sigma_c = 150$ MPa, $JRC_o=8$ and $JCS_o=100$ MPa, $\sigma_n = 5$ MPa).....	78
Figure 4.14 Graph of peak shear strength of empiric results vs numerical results with different joint compressive strengths (JCS_o)	79
Figure 4.15 Graph of lab scale joint wall compressive strength vs peak shear strength.....	80
Figure 4.16 Graph of shear stress – shear displacement.....	81
Figure 4.17 Graph of maximum shear stress of empiric results vs numerical results with different discontinuity residual friction angles (\emptyset_r).....	82
Figure 4.18 Graph of residual friction angle vs peak shear strength	83
Figure 4.19 Graph of shear stress – shear displacement ($\emptyset_r = 25^\circ$, $\sigma_c = 150$ MPa, $JRC_o=8$ and $JCS_o=100$ MPa)	84
Figure 4.20 Graph of shear displacement vs dilation and shear stress vs shear displacement ($\emptyset_r = 20^\circ$, $\sigma_c = 150$ MPa, $JRC_o=12$, $JCS_o=100$ MPa and $\sigma_n = 5$ MPa)	86
Figure 4.21 Graph of shear stiffness (K_s) vs shear displacement.....	88
Figure 5.1 Geometry of basic slope model.....	93
Figure 5.2 Sectional view of the basic slope geometry.....	95
Figure 5.3 2-D Limit equilibrium factor of safety analyses with Mohr-Coulomb parameters	97
Figure 5.4 2-D Limit equilibrium factor of safety analyses with Barton-Bandis parameters.....	98
Figure 5.5 Shear displacement of point A with Mohr-Coulomb criterion ($c=0$, $\emptyset = 25^\circ$)	99
Figure 5.6 Shear displacement of Point A with Barton-Bandis criterion ($\emptyset_r = 22^\circ$, $JRC = 2$, $JCS = 12.97$ MPa).....	101
Figure 5.7 Shear displacement of Point A with Barton-Bandis criterion ..	103

Figure 5.8 Shear displacement of the sliding block under different joint roughness coefficients	104
Figure 5.9 Location and geological map of Orhaneli district (Karpuz et al.(2006)).....	106
Figure 5.10 Orhaneli A-6 panel slope failure	107
Figure 5.11 Lithological section of Orhaneli miocene basin	108
Figure 5.12 Cross section (S-S') of the A-6 panel landslide	108
Figure 5.13 Gümüşpınar 3DEC model geometry	109
Figure 5.14 Gümüşpınar model displacement monitoring points	110
Figure 5.15 Horizontal displacement plots of monitoring points with Mohr-Coulomb model.....	111
Figure 5.16 Vertical displacement plots of monitoring points with Mohr-Coulomb model.....	112
Figure 5.17 Gümüşpınar landslide cross sectional model geometry	113
Figure 5.18 Horizontal displacement plots of monitoring points with Barton-Bandis model	116
Figure 5.19 Vertical displacement plots of monitoring points with Barton-Bandis model	117
Figure 5.20 Geological map of Orhaneli coal basin (Karpuz et al.,2007)	119
Figure 5.21 Cross section of the Dikmentepe (A-5 panel) landslide (T-T')	120
Figure 5.22 Dikmentepe 3DEC model geometry.....	120
Figure5.23 Dikmentepe displacement monitoring points (Top view)	121
Figure 5.24 Horizontal displacement plots of monitoring points with Mohr-Coulomb model.....	122
Figure 5.25 Vertical displacement plots of monitoring points with Mohr-Coulomb model.....	123
Figure 5.26 Simplified cross sectional model geometry of Dikmentepe model.....	124

Figure 5.27 Horizontal displacement plots of monitoring points with Barton-Bandis model	126
Figure 5.28 Horizontal displacement plots of monitoring points with Barton-Bandis model	127
Figure 5.29 Location map of Çan district.....	128
Figure 5.30 Lithological section of Çan miocene basin	129
Figure 5.31 Cross section of Çan western panel slopes (U-U').....	130
Figure 5.32 Çan western panel slopes 3DEC model.....	130
Figure 5.33 Çan western panel slopes model with displacement monitoring points (top view).....	131
Figure 5.34 Horizontal displacement plots of monitoring points with Mohr-Coulomb model.....	133
Figure 5.35 Vertical displacement plots of monitoring points with Mohr-Coulomb model.....	133
Figure 5.36 Simplified cross sectional model geometry of Çan western panel slope	135
Figure 5.37 Horizontal displacement plots of Çan open pit mine western panel slope monitoring points with Barton-Bandis model.....	138
Figure 5.38 Vertical displacement plots of Çan open pit mine western panel slope monitoring points with Barton-Bandis model	138
Figure B.1 Normal stress – normal closure plot with JRC = 2	161
Figure B.2 Normal stress – normal closure plot with JRC = 4	161
Figure B.3 Normal stress – normal closure plot with JRC = 6	162
Figure B.4 Normal stress – normal closure plot with JRC = 8	162
Figure B.5 Normal stress – normal closure plot with JRC = 10	163
Figure B.6 Normal stress – normal closure plot with JRC = 12	163
Figure B.7 Normal stress – normal closure plot with JRC = 14	164
Figure B.8 Normal stress – normal closure plot with JRC = 16	164
Figure B.9 Normal stress – normal closure plot with JRC = 18	165

Figure B.10 Normal stress – normal closure plot with JRC = 20	165
Figure B.11 Normal stress – normal closure plot with JCS = 40 MPa	166
Figure B.12 Normal stress – normal closure plot with JCS = 50 MPa	166
Figure B.13 Normal stress – normal closure plot with JCS = 60 MPa	167
Figure B.14 Normal stress – normal closure plot with JCS = 70 MPa	167
Figure B.15 Normal stress – normal closure plot with JCS = 80 MPa	168
Figure B.16 Normal stress – normal closure plot with JCS = 90 MPa	168
Figure B.17 Normal stress – normal closure plot with JCS = 100 MPa ...	169
Figure B.18 Normal stress – normal closure plot with JCS = 110 MPa ...	169
Figure B.19 Normal stress – normal closure plot with JCS = 120 MPa ...	170
Figure B.20 Normal stress – normal closure plot with JCS = 130 MPa ...	170
Figure B.21 Normal stress – normal closure plot with JCS = 140 MPa ...	171
Figure B.22 Normal stress – normal closure plot with $\sigma_c = 60$ MPa	171
Figure B.23 Normal stress – normal closure plot with $\sigma_c = 70$ MPa	172
Figure B.24 Normal stress – normal closure plot with $\sigma_c = 80$ MPa	172
Figure B.25 Normal stress – normal closure plot with $\sigma_c = 90$ MPa	173
Figure B.26 Normal stress – normal closure plot with $\sigma_c = 100$ MPa	173
Figure B.27 Normal stress – normal closure plot with $\sigma_c = 110$ MPa	174
Figure B.28 Normal stress – normal closure plot with $\sigma_c = 120$ MPa	174
Figure B.29 Normal stress – normal closure plot with $\sigma_c = 130$ MPa	175
Figure B.30 Normal stress – normal closure plot with $\sigma_c = 140$ MPa	175
Figure B.31 Normal stress – normal closure plot with $\sigma_c = 150$ MPa	176
Figure B.32 Normal stress – normal closure plot with $\sigma_c = 160$ MPa	176
Figure C.1 Shear stress –shear displacement plot with $\varnothing_r = 10^\circ$	177
Figure C.2 Shear stress –shear displacement plot with $\varnothing_r = 15^\circ$	178
Figure C.3 Shear stress –shear displacement plot with $\varnothing_r = 20^\circ$	178

Figure C.4 Shear stress –shear displacement plot with $\varnothing_r = 30^\circ$	179
Figure C.5 Shear stress –shear displacement plot with $\varnothing_r = 35^\circ$	179
Figure C.6 Shear stress –shear displacement plot with $\varnothing_r = 40^\circ$	180
Figure C.7 Shear stress –shear displacement plot with JRC = 2	180
Figure C.8 Shear stress –shear displacement plot with JRC = 4	181
Figure C.9 Shear stress –shear displacement plot with JRC = 6	181
Figure C.10 Shear stress –shear displacement plot with JRC = 10	182
Figure C.11 Shear stress –shear displacement plot with JRC = 12	182
Figure C.12 Shear stress –shear displacement plot with JRC = 14	183
Figure C.13 Shear stress –shear displacement plot with JRC = 16	183
Figure C.14 Shear stress –shear displacement plot with JRC = 18	184
Figure C.15 Shear stress –shear displacement plot with JRC = 20	184
Figure C.16 Shear stress –shear displacement plot with JCS = 40 MPa	185
Figure C.17 Shear stress –shear displacement plot with JCS = 50 MPa	185
Figure C.18 Shear stress –shear displacement plot with JCS = 60 MPa	186
Figure C.19 Shear stress –shear displacement plot with JCS = 70 MPa	186
Figure C.20 Shear stress –shear displacement plot with JCS = 90 MPa	187
Figure C.21 Shear stress –shear displacement plot with JCS = 100 MPa	187
Figure C.22 Shear stress –shear displacement plot with JCS = 110 MPa	188
Figure C.23 Shear stress –shear displacement plot with JCS = 120 MPa	188
Figure C.24 Shear stress –shear displacement plot with JCS = 130 MPa	189
Figure C.25 Shear stress –shear displacement plot with JCS = 140 MPa	189
Figure C.26 Shear stress –shear displacement plot with $\sigma_n = 0.5$ MPa ..	190

Figure C.27 Shear stress –shear displacement plot with $\sigma_n = 3$ MPa	190
Figure C.28 Shear stress –shear displacement plot with $\sigma_n = 4$ MPa	191
Figure C.29 Shear stress –shear displacement plot with $\sigma_n = 5$ MPa	191
Figure C.30 Shear stress –shear displacement plot with $\sigma_n = 6$ MPa	192
Figure C.31 Shear stress –shear displacement plot with $\sigma_n = 7$ MPa	192
Figure C.32 Shear stress –shear displacement plot with $\sigma_n = 8$ MPa	193
Figure C.33 Shear stress –shear displacement plot with $\sigma_n = 9$ MPa	193
Figure C.34 Shear stress –shear displacement plot with $\sigma_n = 10$ MPa ...	194
Figure D.1 Graph of Shear displacement vs dilation and shear stress vs shear displacement ($\phi_r = 20^\circ$, $\sigma_c = 150$ MPa, $JRC_0=16$, $JCS_0=100$ MPa and $\sigma_n = 5$ MPa)	196

LIST OF SYMBOLS

τ_{peak} = peak shear strength

τ_{residual} = residual shear strength

τ_{ult} = ultimate shear strength

τ_m = bounding shear stress

c = cohesion

σ_n = normal stress

σ_{nmax} = maximum normal stress

σ_c = uniaxial compressive strength

σ_i = initial normal stress

\emptyset_p = peak friction angle of the discontinuity

\emptyset_r = residual friction angle of the discontinuity

\emptyset_b = basic friction angle of the discontinuity

\emptyset_p' = peak drained friction angle of the discontinuity

JRC_o = lab scale joint roughness coefficient

JRC_n = insitu size joint roughness coefficient

JRC_{mob} = mobilized joint roughness coefficient

JCS_o = lab scale joint wall compressive strength

JCS_n = insitu size joint wall compressive strength

r = Schmidt rebound on weathered rock surface

R = Schmidt rebound on unweathered rock surface

d_{peak} = peak dilation angle

α = tilt angle

γ = rock density

K = bulk modulus

G = shear modulus

δ = shear displacement

δ_{peak} = peak shear displacement

L_o = lab scale block length

L_n = insitu block length

K_n = joint normal stiffness

K_{ni} = initial joint normal stiffness

K_s = joint shear stiffness

n_j = shear stiffness exponent

ΔV = normal displacement

V_m = Maximum joint closure

a_j = mechanical joint aperture

K_j = shear stiffness number

R_f = failure ratio

A_c = Area of joint face

F^n = normal force

ΔF^n = normal force increment

F^s = shear force

ΔF^s = shear force increment

ΔV^i = normal displacement increment

$\Delta \delta$ = shear displacement increment

$\Delta \delta^p$ = plastic shear displacement increment

F = tangent modulus factor (3DEC continuously yielding joint model)

a_n = joint normal stiffness (3DEC continuously yielding joint model)

a_s = joint shear stiffness (3DEC continuously yielding joint model)

e_n = joint normal stiffness exponent (3DEC continuously yielding joint model)

e_s = joint shear stiffness exponent (3DEC continuously yielding joint model)

CHAPTER 1

INTRODUCTION

1.1 General Description

Discontinuities are the key elements that affect the mechanical behaviour of rock masses disturbed by the engineering structures such as tunnel, rock slope etc. Therefore, it is very important to understand the failure mechanism of the discontinuities around such engineering structures.

In a discontinuous rock mass, the stability of geotechnical structures can be controlled by the behavioural characteristics of the discontinuities rather than by the properties of rock mass. Therefore, discontinuity constitutive models have an essential role in numerical modelling of discontinuous media. A discontinuous medium is distinguished from a continuous medium by the existence of interfaces or contacts between the discrete bodies that comprise the system (Anon, 2007).

Numerical methods are very useful tools to model the discontinuities in rock masses, since closed form solutions rarely exist. Among these methods, distinct element method is the commonly used one since it considers the large deformation of discontinuities.

In numerical analyses of discontinuous rock masses, the failure is usually expected from the discontinuities. Therefore, the behaviour of the discontinuities under normal and shear stresses should be modelled truly.

Because of this reason, the shear strength criterion used for the stability purposes in discontinuous rocks becomes crucial.

1.2 Statement of the Problem

In geotechnical engineering, numerical programs are widely used for stability analyses purposes. The discontinuous rock masses are most effectively modelled by numerical programs working with discrete element methods. Two dimensional numerical analyses programs work in plane strain assumption that is the state of strain in which the strain normal to the sectional plane are assumed to be zero. Modelling the environment in three dimension is important since it also considers modelling the stress distribution and deformation characteristics in a more realistic way.

In most of the numerical analyses which use distinct element method, the most widely used shear strength criterion is the Mohr-Coulomb criterion. Mohr-Coulomb criterion relates the shear strength with cohesive strength, normal stress and internal friction angle, which may not represent totally the real shear behaviour on rock discontinuities. Besides the strength parameters, discontinuity surface characterization plays an important role on the shear strength of discontinuities. Studies of Barton (1973), Barton and Choubey (1977), Bandis et al. (1981), Barton and Bandis (1982), Bandis et al. (1983) and Barton et al. (1985) showed clearly that, under low levels of normal stress, discontinuity roughness and the strength of the asperities along the discontinuities significantly affect the shear behaviour of discontinuities. Not only the shear behaviour but also the normal deformation of a discontinuity has not been truly expressed by the conventional Coulomb criterion.

The need for combining those two aspects mentioned above, namely shearing and surface properties of discontinuities have always been an interest for investigators. Distinct element method better represents the

discontinuity behaviour since it considers large displacements of discontinuities. Therefore, distinct element modelling together with the Barton-Bandis failure criterion is the crucial topic for researchers who focus on the shear behaviour of rock discontinuities under low level of normal stresses and where the discontinuity surface characterization becomes important.

Additionally, discontinuity behaviour should be considered in three dimensions to get rid of assumptions of 2D analysis. Not only the dip angle of the discontinuity but also the dip direction and strike are also important factors that may affect the stability.

Three dimensional distinct element programs usually use Mohr-Coulomb slip criterion for discontinuity analyses. However, for totally representing the real shear behaviour of discontinuities, a non-linear shear strength criterion such as Barton-Bandis criterion should be used. There are two dimensional numerical programs which gives Barton-Bandis shear strength criterion as an option is available. However, the effect of third dimension in representing the insitu stresses is also an important factor. Thus a three dimensional numerical analyses method that works with discrete element method and based on Barton-Bandis failure criterion should be needed to represent large scale failure of discontinuities.

1.3 Objective of the Thesis

The objective of this study is to develop a methodology for implementing Barton-Bandis shear strength failure criterion into the 3 dimensional distinct element code, 3DEC, for analyzing discontinuity failure mechanism. 3DEC allows users to apply Mohr-Coulomb discontinuity slip model and continuously yielding joint model into discontinuity deformation studies. However, Barton-Bandis failure criterion can express several behaviours of discontinuities such as sliding and separating of discontinuities, by using

surface properties (surface roughness and surface strength), in a more realistic way.

Following the development of the numerical 3DEC model for the analysis of discontinuity failure based on Barton-Bandis criterion, three different large scale failure occurred at Turkish Coal Enterprises' (TKI) lignite mines were utilized to verify the developed model. In the verification, the input parameters of those actual cases were obtained from back analysis with Mohr-Coulomb slip model.

1.4 Methodology of the Thesis

Introducing the Barton-Bandis shear strength criterion, which also considers the geometry and slip property of the discontinuity surface is the first step to modelling. 3-dimensional distinct element code (3DEC) allows users to implement user defined discontinuity constitutive models that are derived in C++ and compiled into the main executable part. The models should exist as a runtime dynamic link library (DLL) files. Barton-Bandis shear strength failure criterion was coded by compiling a dynamic link library file which was written in C++.

Following that, a numerical direct shear test model was prepared in order to verify the numerically developed mechanical model by empirical relations.

After developing the model, the failure conditions occurred at Turkish Coal Enterprises (TKI) open pit lignite mines were used to verify the model numerically. The flowchart of the study is given in Figure 1.1.

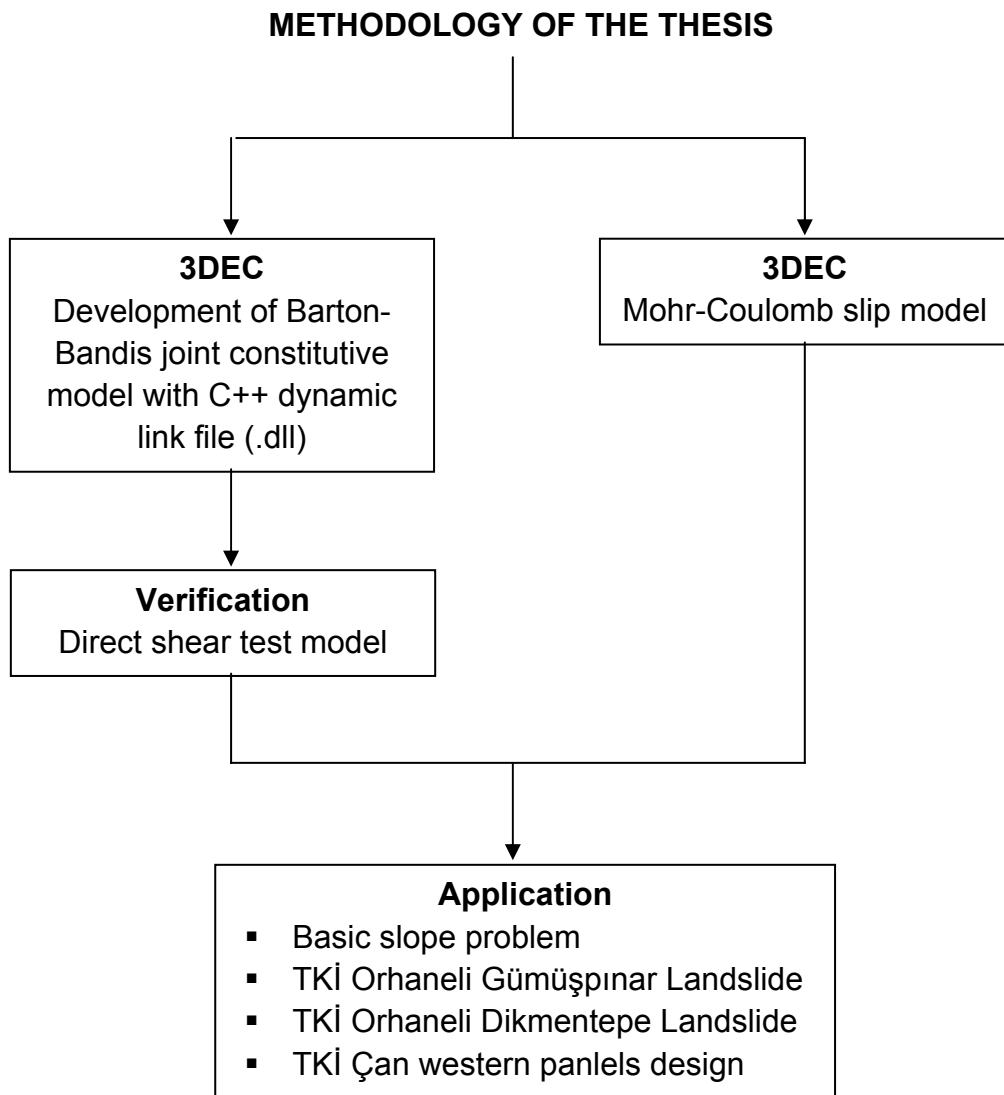


Figure 1.1 Flowchart representing the methodology of the thesis

1.5 Organization of the Thesis

Following the introductory chapter, a comprehensive study about the slope failure mechanisms, rock discontinuities and shear failure criterion along the discontinuities is presented. Besides this, the Barton-Bandis constitutive model is examined. The normal stress-closure relations and shear behaviour of the discontinuities and mechanical discontinuity

properties (i.e. joint wall compressive strength, joint roughness coefficient etc.) that affect failure mechanism are examined. Also a study about numerical models and 3 dimensional distinct element code 3DEC is presented in Chapter 2. The theory and the background of the program is briefly explained.

In Chapter 3, the development of the Barton-Bandis model for 3DEC is presented. How a C++ dynamic link library file (DLL) works and how it is implemented into 3DEC is explained in detail. The major commands for the discontinuity failure criterion are given in this chapter.

Chapter 4 presents the empirical verification of the Barton-Bandis model for 3DEC. First, a direct shear test model is presented and by monitoring the normal stress-normal closure and shear stress-shear displacement behaviour, different tests are conducted in order to verify the discontinuity behaviour under different normal stresses. For the verification process, the empirical relations developed by Bandis et al. (1983) were used.

Chapter 5 deals with the application of the proposed methodology in real case discontinuous mine slopes. The case studies were carried out with 3DEC within the years 2005 – 2007 in different open pit mines of Turkish Coal Enterprises (TKİ). There are total of three case studies related to behaviour of discontinuous rock slopes. The analysis were first carried out with Mohr-Coulomb slip model and with the application of the proposed Barton-Bandis model, the results from different models were compared.

The major conclusions drawn from this study along with the recommendations for further studies are summarized in Chapter 6.

CHAPTER 2

BASIC MECHANICS OF DISCONTINUITIES

2.1 Introduction

All rock masses contain discontinuities such as bedding planes, joints, shear zones and faults. At shallow depth, where stresses are low, the behaviour of the rock mass is controlled by sliding on the discontinuities rather than rock mass itself. In order to analyze the stability of this system of individual rock blocks, it is necessary to understand the factors that control the shear strength of the discontinuities which separate the blocks (Hoek, 2007). In this Chapter, it is intended to investigate the basic mechanics of discontinuities under normal and shear stresses.

2.2 Slope Failure Mechanisms

Based on the geological structure and the stress state in the rock mass, some failure modes appear to be more common. These can be summarized as plane failure, wedge failure, circular failure and toppling.

2.2.1 Plane failure

One of the discontinuity governed failure types is the plane failure. Plane failure is comparatively rarely seen in rock slopes because there are

geometrical conditions that should satisfy for the failure to happen. The general conditions for a slope to slide along a single plane are;

- The strike of the sliding plane should be within $\pm 20^\circ$ of the slope face,
- The dip of the failure plane should be less than the dip of the slope face,
- The dip of the failure plane should be greater than the friction angle of this plane,
- Release surfaces which enable the sliding that defines the lateral extends of the sliding mass. (Hoek and Bray, 1981)

The geometry of a plane failure is given in Figure 2.1.

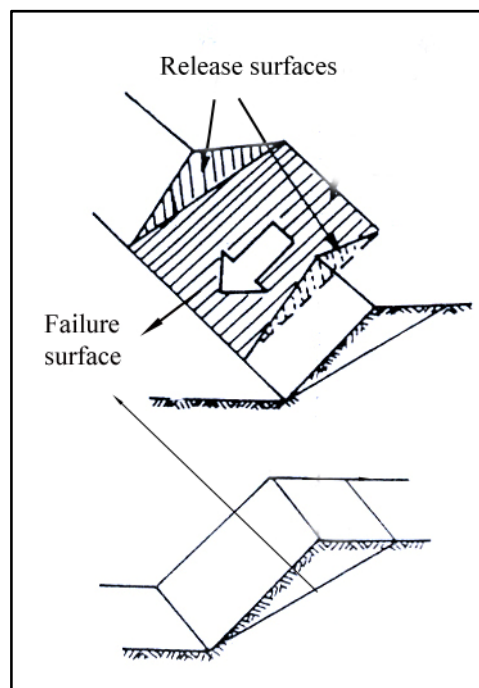


Figure 2.1 Geometry of plane failure (Hoek and Bray, 1981)

2.2.2 Wedge failure

Another failure mode that is governed by discontinuities is wedge failure. It is different than plane failure in the way that the discontinuities which sliding takes place, strikes across the slope crest. And sliding takes place along the line of intersection of two planes. A pictorial view of a wedge failure is given in Figure 2.2 and a section view is given in Figure 2.3.

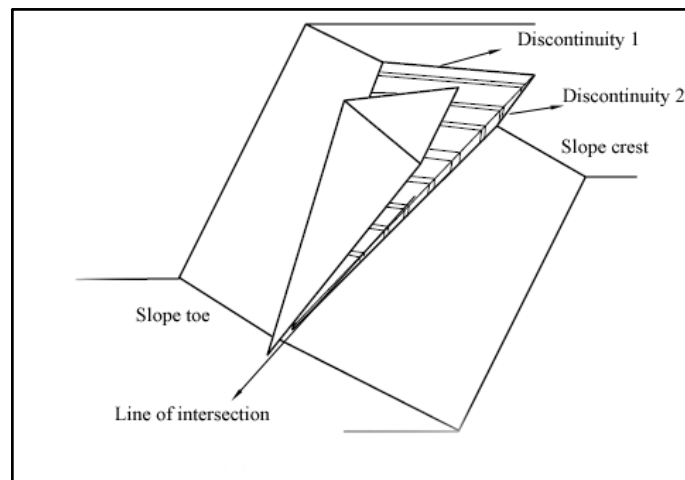


Figure 2.2 Geometry of wedge failure (Hoek and Bray, 1981)

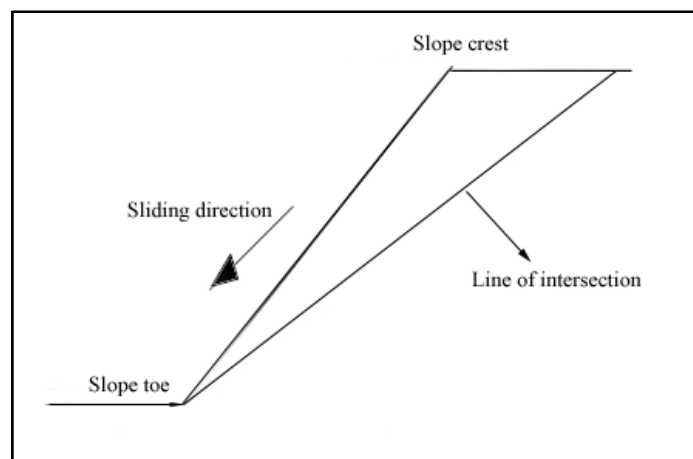


Figure 2.3 Section view of wedge failure (Hoek and Bray, 1981)

2.2.3 Circular failure

Circular failure mode of failure is also called rotational shear failure and the failure takes place along a circular arc and this is the typical failure mode in soils. As Hoek and Bray (1981) pointed out, circular failure could also occur in rock slopes if there are no strong structural patterns in the slope, for example, heavily discontinuous or highly weathered rock slope. A pictorial view of a circular failure is given in Figure 2.4 and simple cross sectional view of a circular failure surface is given in Figure 2.5.

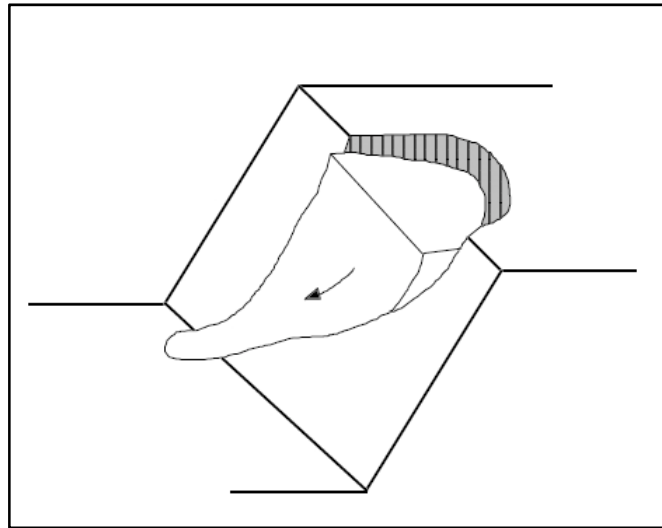


Figure 2.4 General circular slope failure (Hoek and Bray, 1981)

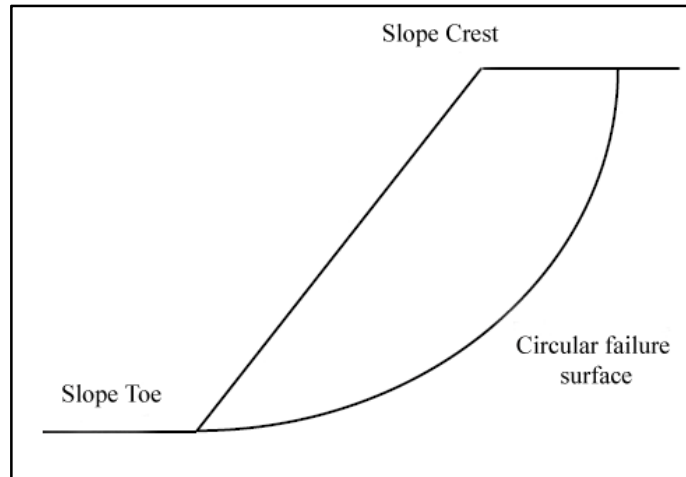


Figure 2.5 Circular slope failure surface, section view (Hoek and Bray, 1981)

2.2.4 Toppling failure

Another group of failure modes is the toppling failure. Toppling corresponds to overturning of columns of rock formed by steeply dipping discontinuities and defined as primary toppling. Figure 2.6 presents the primary toppling of a slope. Characteristic of toppling failure is that a successive breakdown of the rock slope occurs (Sjöberg, 1996).

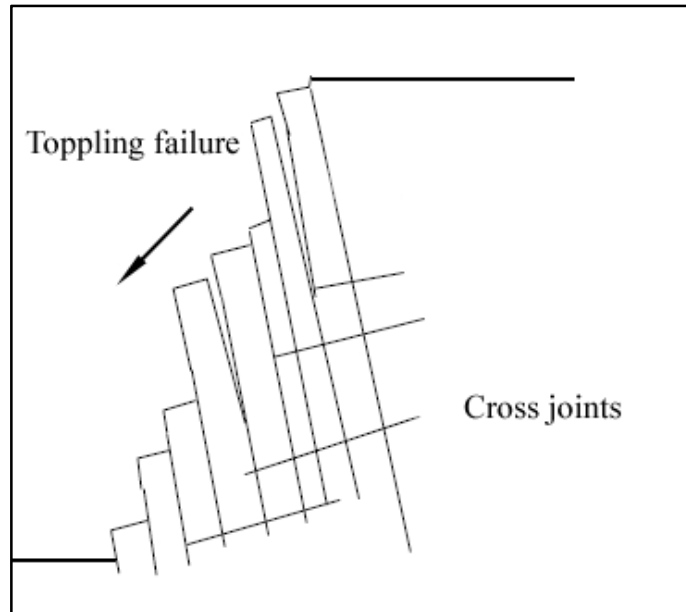


Figure 2.6 Primary toppling

The failure can also be initiated by crushing the slope toe and this is called secondary toppling (Hoek and Bray, 1981). In situ stresses in relation to the rock strength are important in this failure mode. The stress concentration at the slope toe increases with the slope height. Therefore these types of failures are more common in deep slopes. A toppling failure caused by crushing of the toe is given in Figure 2.7.

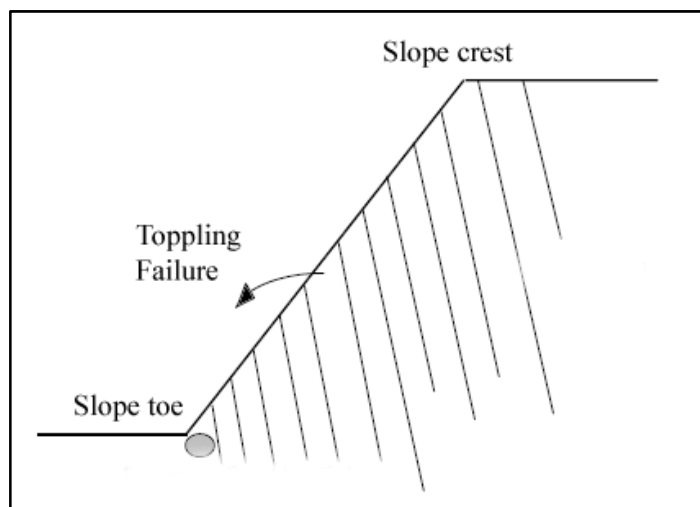


Figure 2.7 Secondary toppling

From the general description of the failure mechanism of slopes, it is seen that discontinuity governed slope failure mechanism has extensive types. If the rock is not a highly weathered and discontinuous, then the precaution that should be taken against a circular failure can easily be taken with arranging overall slope angle. On the contrary if a slope is to be produced in a discontinuous rock mass then discontinuity originated failure types should be considered. And to do this, the shear failure mechanism of rock discontinuities should be investigated in detail.

2.3 Shear Strength of Discontinuities

A discontinuity is a collective term referring to all structural breaks in rocks which usually have zero to low tensile strength. Discontinuities comprise joints, bedding, shears, contacts, veins, and faults (Mining Life Web Page).

Shear behaviour of rock discontinuities always take an important part in foundation stability studies both in surface and underground problems. There are several discontinuity shear failure criterion developed for the past half decade. The most common one is the linear Coulomb relation in which the peak shear (τ) strength is expressed in terms of the effective normal stress (σ_n), cohesion (c) and angle of friction (ϕ). The Mohr-Coulomb relation is given as;

$$\tau_{\text{peak}} = c + \sigma_n \tan \phi \quad (2.1)$$

This shear strength equation is derived by assuming that the discontinuity surface is planar. If such a surface is sheared at a constant normal stress at very small displacements, the surface behaves elastically, and so the shear stress acting on the discontinuity surface increases rapidly till the peak shear strength is reached. After that the stress required to continue sliding drops and becomes constant at the level which is called as residual

shear strength. Equation (2.1) can be expressed to give the residual shear strength as;

$$\tau_{\text{residual}} = \sigma_n \tan \phi_r \quad (2.2)$$

Where the residual friction angle (ϕ_r) is approximately equal to the basic friction angle (ϕ_b), which is usually measured with sawn rock surfaces. However, a natural rock discontinuity may probably have some asperities that directly affect the shear strength of the discontinuity. As the discontinuity is under shear loading, the shear displacement will be on these asperities that causes the block move upward on the inclined surfaces of the asperities (dilation). For this reason the roughness component (i) should be added to the basic friction angle (ϕ_b) (ϕ_b+i), where 'i' is the angle of the inclined surface of the asperities.

The condition of sliding along the asperity faces can occur only under very low normal stress. If the normal stress is increased, then the shear force tends to break or wear out the asperities and so the effect of discontinuity wall properties should also be considered.

Barton-Bandis failure criterion includes discontinuity surface properties besides the effective normal stress and friction angle of the discontinuity. Barton (1973) derived an empirical relationship for determining the shear strength of discontinuities. It is written as follows:

$$\tau = \sigma_n \tan \left[\text{JRC} \times \log_{10} \left(\frac{\text{JCS}}{\sigma_n} \right) + \phi_b \right] \quad (2.3)$$

Where;

σ_n = effective normal stress

JRC = joint roughness coefficient

JCS = joint wall compressive strength

ϕ_b = basic friction angle (obtain from residual shear tests on flat unweathered rock surfaces)

2.3.1 Joint wall compressive strength (JCS)

The joint wall compression strength (JCS) is known to generally reduce with water saturation compared to the dry state (Barton, 2007). This is because of the researched effect of moisture on the uniaxial compressive strength (σ_c). The value of JCS can be predicted from Schmidt hammer tests (ISRM, 1978).

The measurement of this parameter is of major importance in rock engineering because it is largely the thin layers of rock adjacent to discontinuity walls that control the strength and deformation properties of the rock mass as a whole (Barton and Choubey, 1977). Generally detection of JCS parameter becomes an important aspect if the discontinuity walls are weathered. If the discontinuity walls are unweathered completely then it is expected that JCS will be equal to uniaxial compressive strength (σ_c) of the unweathered rock (Barton and Choubey, 1977).

The depth of penetration of weathering into discontinuity walls probably depends on rock type, especially on its permeability. If the rock is permeable, it is expected that the rock is weakened throughout. On the other hand, an impermeable rock will just develop weakened discontinuity walls (Barton and Choubey, 1977). Barton and Choubey (1977) summarized the weathering in the following stages and determination methods of JCS:

1. Discontinuity in intact rock; $JCS = \sigma_c$
2. Reduction of joint wall strength if discontinuities are water-conducting; $JCS < \sigma_c$
3. Weathered, water conducting discontinuities, impermeable rock blocks between; $JCS = \sigma_c \times n$, where $n < 1$
4. Weathering starts to affect the rock; JCS continues to reduce slowly, σ_c reduces progressively,
5. Advance stage of weathering; $\sigma_c = JCS$, rock mass permeable throughout

For the stages 1 and 5, JCS can be obtained by conventional unconfined compression tests on intact cylinders, point load tests on irregular lumps. Point load tests can be performed on core discs down to a few centimetres in thickness; it might also be possible to use this test for stage 4. However, for stages 2 and 3 cannot be evaluated by standard rock mechanics tests. For these cases, the determination of JCS of weathered discontinuities can best be done by Schmidt hammer index test.

2.3.2 Basic friction angle (ϕ_b) and residual friction angle (ϕ_r)

Another major components of the shear strength criterion are the basic friction angle (ϕ_b) of unweathered artificial, planar, dry rock surfaces and the residual friction angle (ϕ_r) applying to flat, non-dilatant, saturated, well sheared surfaces, i.e. $\phi_r \leq \phi_b$. The friction angles obtained from flat unweathered rock surfaces, which were most frequently prepared by diamond saw, will not be applicable to weathered rock discontinuities unless the effective normal stress is high enough for the thin layers of weathered rock to be worn away (Richards, 1975, in Barton and Choubey, 1977). Low levels of effective normal stress the thin layers of weathered material, perhaps less than 1 mm in thickness, may continue to control the shear strength, post peak strength and even for displacements up to residual strength. Richards' (1975) tests on weathered sandstone joints showed strong correlation between residual friction angles (ϕ_r) and Schmidt rebound value (Figure 2.8).

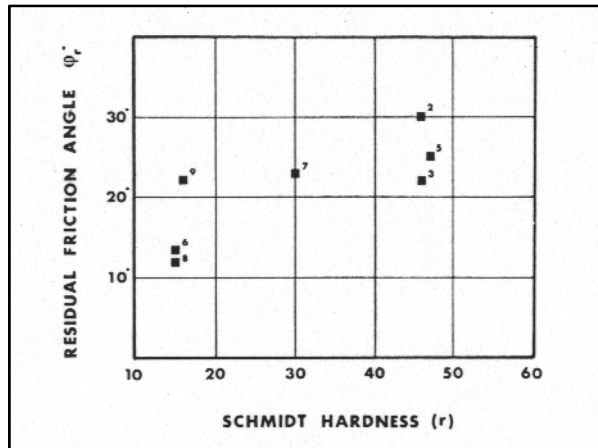


Figure 2.8 Relation between residual friction angle with Schmidt rebound value (Richards, 1975, in Barton and Choubey, 1977)

Richards' (1975) looked for a simple method of estimating ϕ_r from Schmidt hammer rebound values. The first empirical relationship tried was as follows:

$$\phi_r = 10^\circ + (r/R) (\phi_b - 10^\circ) \quad (2.4)$$

Where;

r = Schmidt rebound on weathered discontinuity surface

R = Schmidt rebound on unweathered discontinuity surface

Therefore the equation for shear strength (2.3) for the general case of weathered and unweathered discontinuities was rewritten as (Barton and Choubey (1977):

$$\tau_{\text{peak}} = \sigma_n \tan \left[\text{JRC} \log_{10} \left(\frac{\text{JCS}}{\sigma_n} \right) + \phi_r \right] \quad (2.5)$$

In the work of Barton and Choubey (1977), eight different rock types with total of 136 individual discontinuities were studied. The specimens were sawn from larger blocks containing throughgoing discontinuities. Following

this study another methodology for determining ϕ_r by residual tilt test was introduced, which is basically a shear test under very low normal stress (Figure 2.9). In this test, pair of flat and sawn surfaces were mated, and the pair of blocks tilted until sliding occurred.

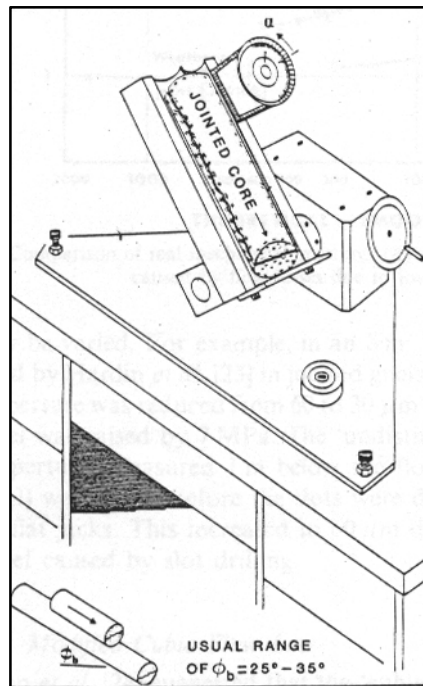


Figure 2.9 Mechanism of residual tilt test (Bandis et al., 1985)

An empirical equation was obtained from residual tilt tests that enable to relate ϕ_r to ϕ_b ;

$$\phi_r = (\phi_b - 20^\circ) + 20(r/R) \quad (2.6)$$

Where;

ϕ_b = basic friction angle estimated from residual tilt tests on dry unweathered sawn surfaces

r = Schmidt hammer rebound value on the saturated joint wall,

R = Schmidt hammer rebound value on the dry, artificially cut rock surfaces

Eq. (2.6) is preferred since it allows for a range of ϕ_r values even when the discontinuity is highly weathered. Equation (2.3) tends to discount mineralogical differences since ϕ_r tends to a single minimum value of 10° when (r) value is zero.

2.3.3 Joint Roughness Coefficient (JRC)

The strength measured along individual discontinuities by direct shear methods is strongly dependent on the roughness of the discontinuity surfaces (Barton, 1973). The roughness parameter represents an index of the unevenness and waviness of the adjacent discontinuity rock wall (Giani, 1992). Barton (1973) defined the term joint roughness coefficient (JRC), which varies from 0 to 20. Unlike the JCS parameter, the JRC parameter is not significantly affected by the dry or wet condition, since it essentially represents a geometry (Barton, 2007). Figure 2.10 presents the laboratory-scale joint roughness profiles with their measured JRC values defined by Barton and Choubey (1977).

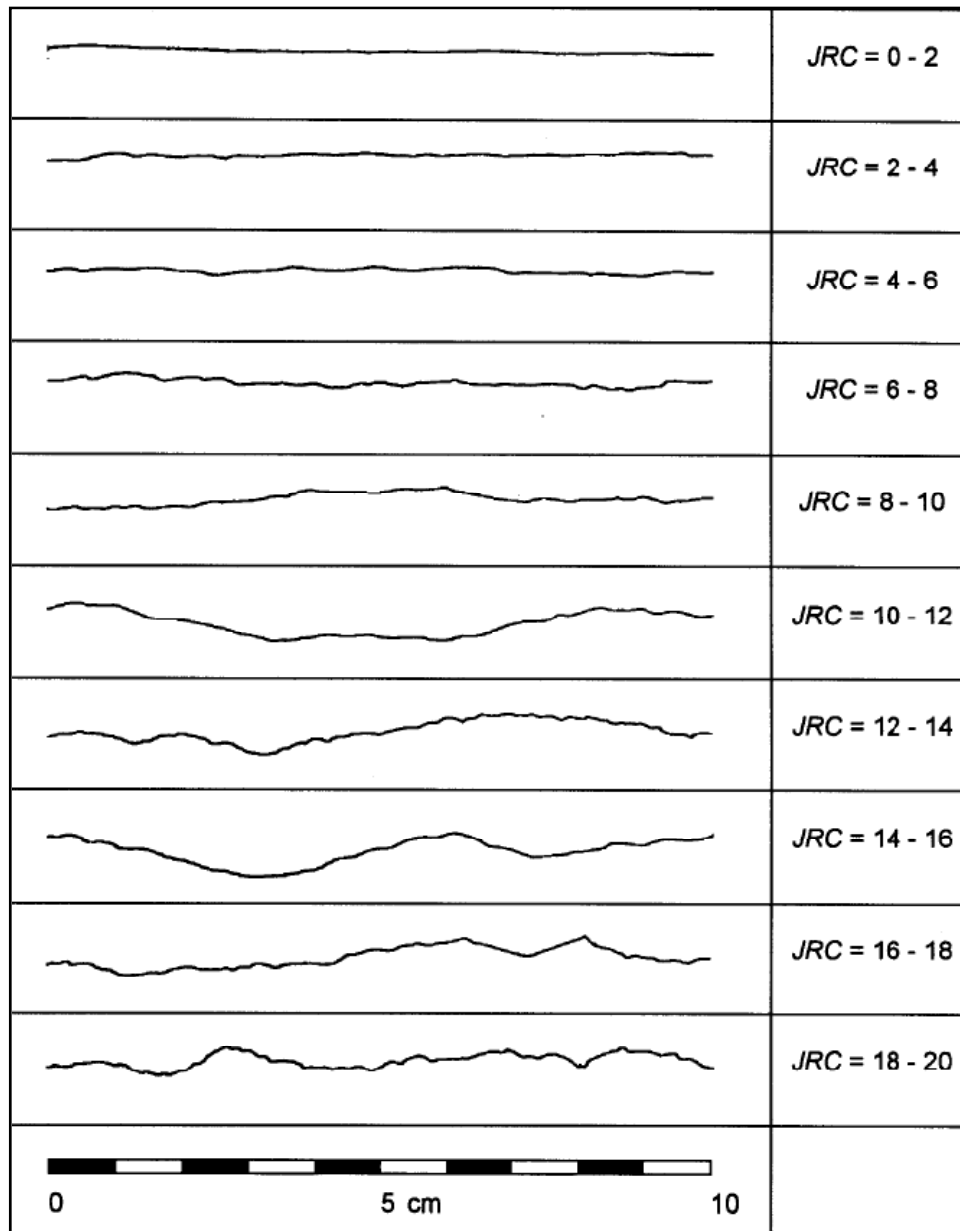


Figure 2.10 Laboratory scaled joint roughness profiles (Barton and Choubey, 1977)

Besides the joint roughness profiles, simple residual tilt test may help to obtain JRC indirectly. In a tilt test on a rough joint, the angle (α) at which sliding occurs may be 40° or 50° more than ϕ_b (higher than compared to ϕ_r) (Barton and Choubey, 1977). This additional shear strength is a result of discontinuity surface roughness. The maximum dilation angle (d_0) when

sliding occurs is probably given by the following simple relationship derived by Barton and Choubey, 1977).

$$d_o = \alpha - \phi_r \quad (2.7)$$

The tilt angle (α) is a function of shear stress and normal stress acting on the joint is given as:

$$\alpha = \arctan\left(\frac{T_0}{\sigma_0}\right) \quad (2.8)$$

The effective normal stress generated by the gravitational force acting on the upper half of the block is given as:

$$\sigma_n = \gamma h \cos \alpha \quad (2.9)$$

Where;

h = thickness of the top block (m)

γ = rock density (kN/m^3)

The JRC value is estimated from tilt tests using Eq. (2.5), by substituting α and σ_{n0} results in:

$$\text{JRC} = \frac{\alpha - \phi_r}{\log_{10}\left(\frac{\text{JCS}}{\sigma_n}\right)} \quad (2.10)$$

Barton and Choubey (1977) recommended “push” or “pull” tests in order to determine the JRC values of rougher discontinuities. In “push” or “pull” test the top block is pushed or pulled parallel to the discontinuity plane. First applying a dry tilt test then a dry push or pull test, it was found to be possible to test whole spectrum of joint roughness (0-20). However, they mentioned the fact that, discontinuous joints and discontinuities with cross jointing cannot be tested by such methods.

Another method for determining JRC was presented by Barton and Bandis (1982) by considering the amplitudes of the asperities of the discontinuity surface as shown in Figure 2.11.

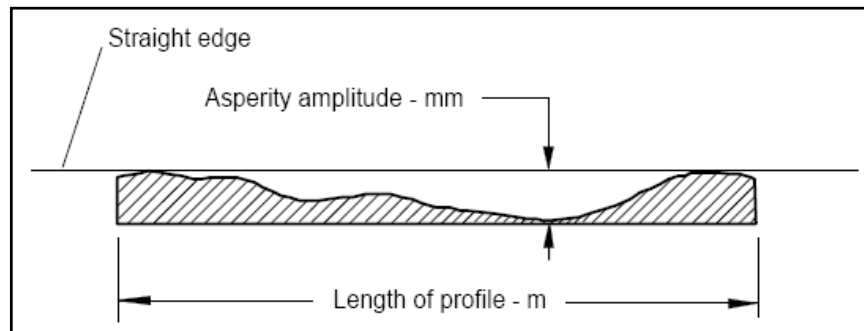


Figure 2.11 Measurement of asperity amplitude for determining joint roughness (Barton and Bandis (1982), in Hoek (2007))

After determining the asperity amplitude and the sample length the chart which is shown in Figure 2.12 can be used to determine JRC.

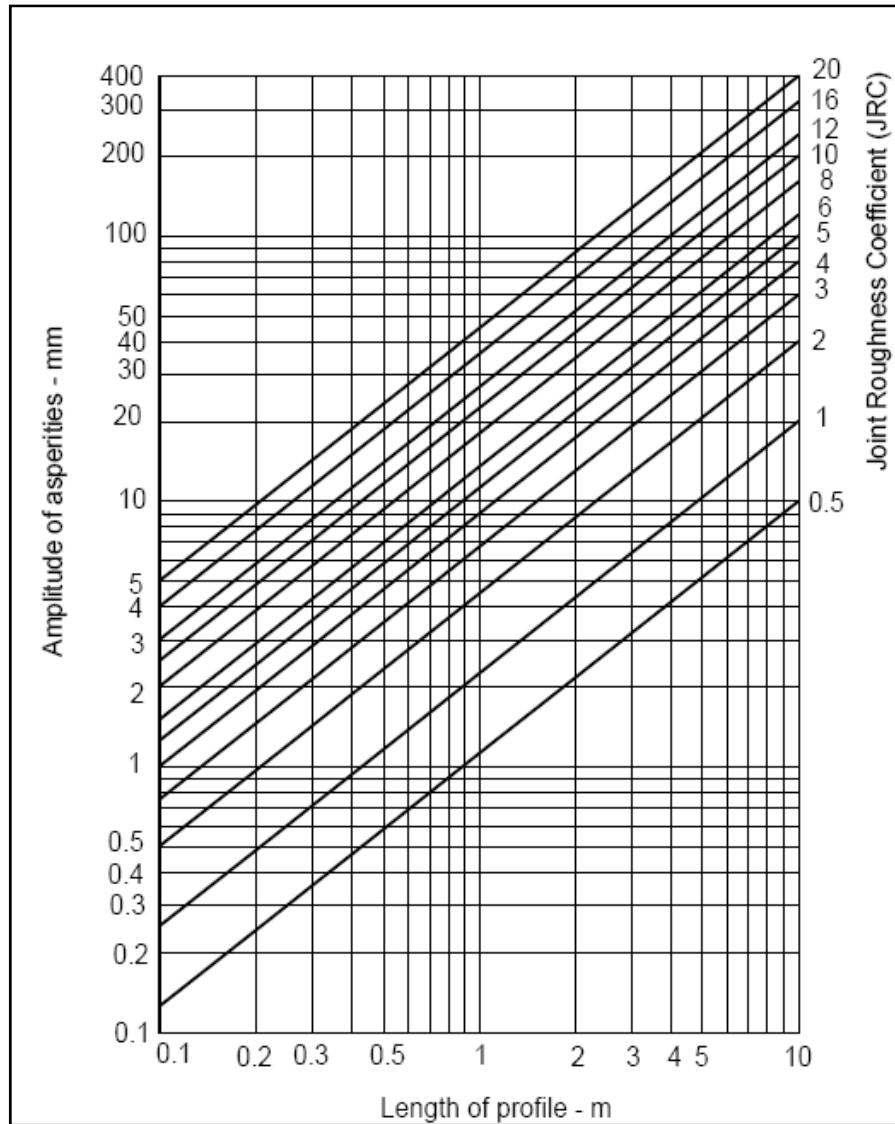


Figure 2.12 Chart for determining joint roughness coefficient from asperity amplitude and profile length (Barton and Bandis (1982), in Hoek (2007))

The chart of Barton and Bandis (1982) is a useful tool for determining joint roughness coefficient. From the chart the relation between asperity height, discontinuity length and joint roughness coefficient can be summarized as;

$$\text{Asperity height} = 2 \times \text{JRC} \times \text{Discontinuity length} \quad (2.11)$$

2.3.4 Dilation

If the shearing of a non-planar discontinuity occurs, the asperities on either side of the discontinuity slide over each other and cause an increase in aperture which is called dilation. This process requires a finite displacement to get started, and occurs at an increasing rate as peak strength is approached (Barton et al., 1985). The peak dilation angle, d_{peak} , is the maximum dilation angle which occurs more or less at the same time with peak shear resistance (Barton and Choubey, 1977) and it is defined as:

$$d_{\text{peak}} = 1/2 \times \text{JRC} \times \log_{10} \left(\frac{\text{JCS}}{\sigma_n} \right) \quad (2.12)$$

2.3.5 Scale effects

The choice of an appropriate discontinuity size during a shear strength investigation is generally based on both economic and technical considerations (Bandis et al., 1981). Because of these scale restrictions in the experimental procedure, scaling of the laboratory determined discontinuity properties into the field has always been an interesting phenomenon.

Pratt et al. (1974) (in Bandis et al. (1981)) studied the effect of scale on shear strength and concluded that the reduction in peak shear strength was due to the decrease in actual contact area. Their prediction was that, the scale effect would be negligible if the discontinuities are unweathered, perfectly mating under high normal stresses. Barton (1976) also interpreted similar results of scale effect on joint wall compressive strength (JCS). The study of Barton and Choubey (1977) showed that different lengths of discontinuities affect joint roughness coefficient (JRC) and thus the shear strength of the discontinuity.

Bandis et al. (1981) studied the scale effect on the shear strength of discontinuities with eleven types of discontinuities, of which was divided into four groups according to their roughness (Figure 2.13). The peak total friction angles ($\phi_p = \tan^{-1}(\tau/\sigma_n)$) are described with different discontinuity lengths (Table 2.1). It is seen that ϕ_p values decreases by approximately 8° - 20° as the length of individual blocks increases from 5-6 cm to 36-40 cm. Besides this another remarkable effect of scale can be seen in the mean peak shear stress vs. average discontinuity area plots in Figure 2.14.

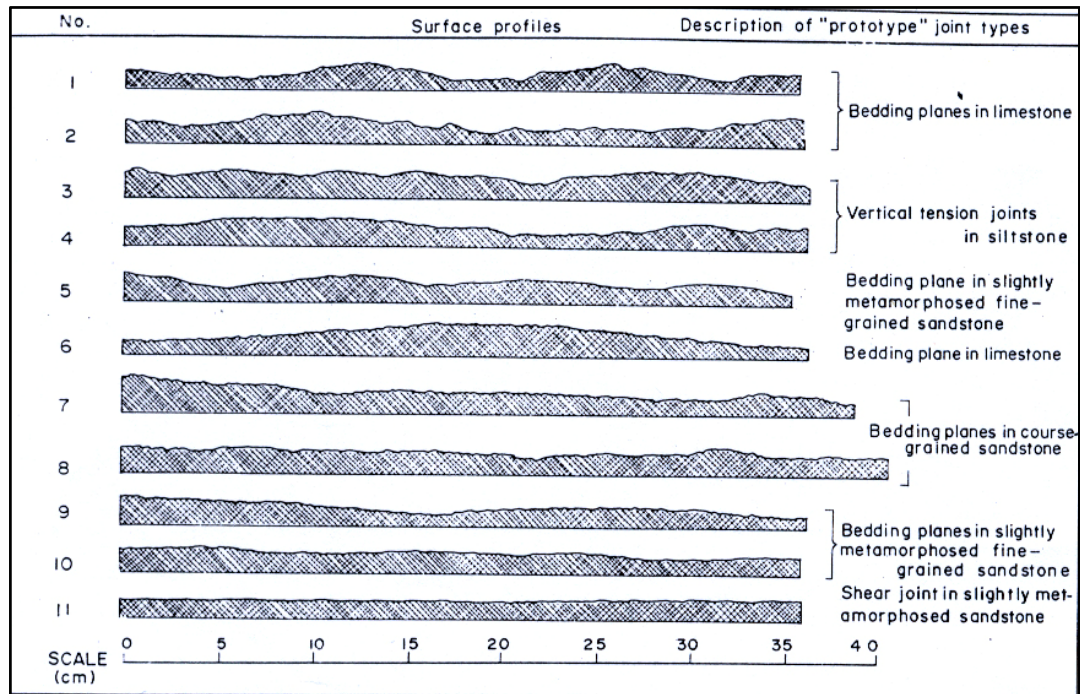


Figure 2.13 Groups of discontinuity types according to their roughness
(Bandis et al., 1981)

Table 2.1 Summary of results of work of Bandis et al. (1981) for scale effects

Discontinuity length (L)		Description of joint roughness			
Model (cm) [M]	Prototype (m) [P]	Strongly undulating, rough	Strongly undulating, moderately rough	Moderately undulating, very rough	Moderately undulating to almost planar, moderately rough to almost smooth
Model no		1, 2, 3	4, 5	6, 7, 8	9, 10, 11
5, 6	1.5, 1.8	64.5°±6.8°	58.4°±8.3°	64.3°±6.3°	49.8°±6.4°
10, 12	3.0, 3.6	59.4°±7.9°	58.7°±5.6°	60.7°±6.3°	46.1°±6.1°
18, 20	5.4, 6.0	56.2°±3.8°	53.4°±3.2°	52.1°±5.9°	43.0°±5.02°
36, 40	10.8, 12.0	51.9°±4.1°	48.1°±	45.5°±1.6°	41.5°±2.6°

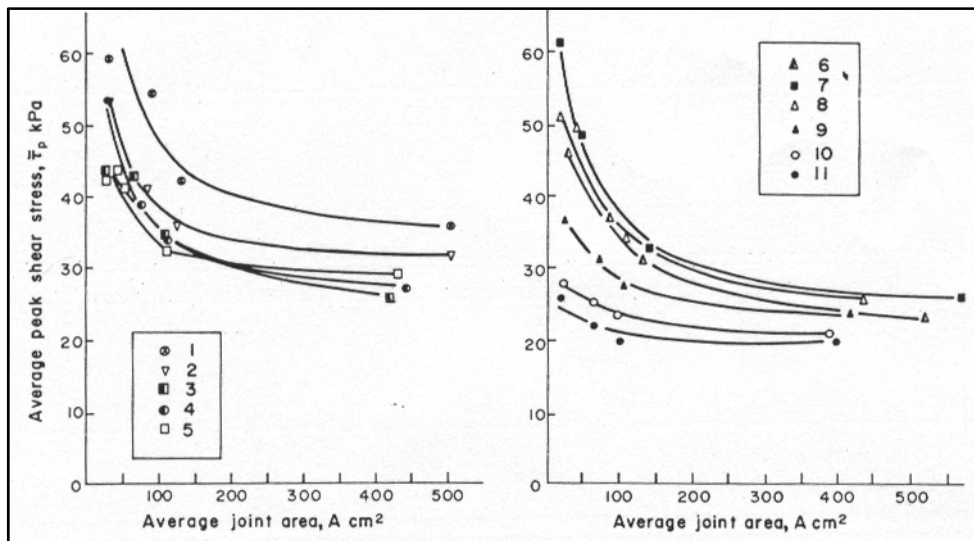


Figure 2.14 Graphs of mean peak shear stress vs. average joint area (Bandis et al., 1981)

This study also showed that the peak shear displacement ($\bar{\delta}_{peak}$) is affected from scale differences of discontinuities. The plots of $\bar{\delta}_{peak}$ vs discontinuity length showed that surface roughness has also an effect as the discontinuity size increases as shown in Figure 2.15. Peak shear

displacement is a measure of the distance that a discontinuity has to cover till the effective contact is made between the asperities controlling the peak resistance (Bandis et al., 1981).

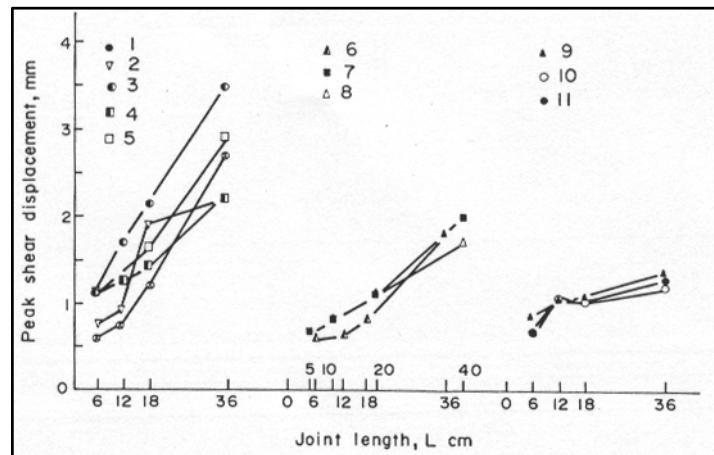


Figure 2.15 Graphs of peak shear displacement vs discontinuity length (Bandis et al., 1981)

2.3.6 Empirical equations for the scale effects on the shear behaviour of rock discontinuities

Studies of Barton and Bandis (1982) concluded with some empirical relations for the scale effects on the joint wall compressive strength, joint roughness coefficient and peak shear displacement. They developed some empirical relations for predicting the large scale joint wall compressive strength (JCS_n), joint roughness coefficient (JRC_o) from lab scale values (JCS_o , JRC_o) and the peak shear displacement (δ_{peak}) of the discontinuity.

The effects of scale on the dry or saturated state of the discontinuities are expressed below;

Large-scale joint wall compressive strength (Barton and Bandis (1982), in Barton et al. (1985)) is:

$$JCS_n = JCS_o \times \left(\frac{L_n}{L_o}\right)^{-0.03JRC_o} \quad (2.13)$$

Large-scale joint roughness (Barton and Bandis (1982), in Barton et al. (1985)) is:

$$JRC_n = JRC_o \times \left(\frac{L_n}{L_o}\right)^{-0.02JRC_o} \quad (2.14)$$

Displacement at the peak strength (Barton and Bandis (1982), in Barton et al. (1985)) is:

$$\delta_{peak} = \frac{L_n}{500} \times \left(\frac{JRC_n}{L_o}\right)^{\frac{1}{3}} \quad (2.15)$$

Where;

L_n = in situ block size (m)

L_o = lab scale sample length (m)

Assuming that the lab scale sample length is 0.1 meters, then the empirical relation for joint roughness coefficient would be limited with a joint length of 1.5 meters at most. Figure 2.16 represents the change of joint roughness coefficients with different lengths of joints with this scale correction relation.

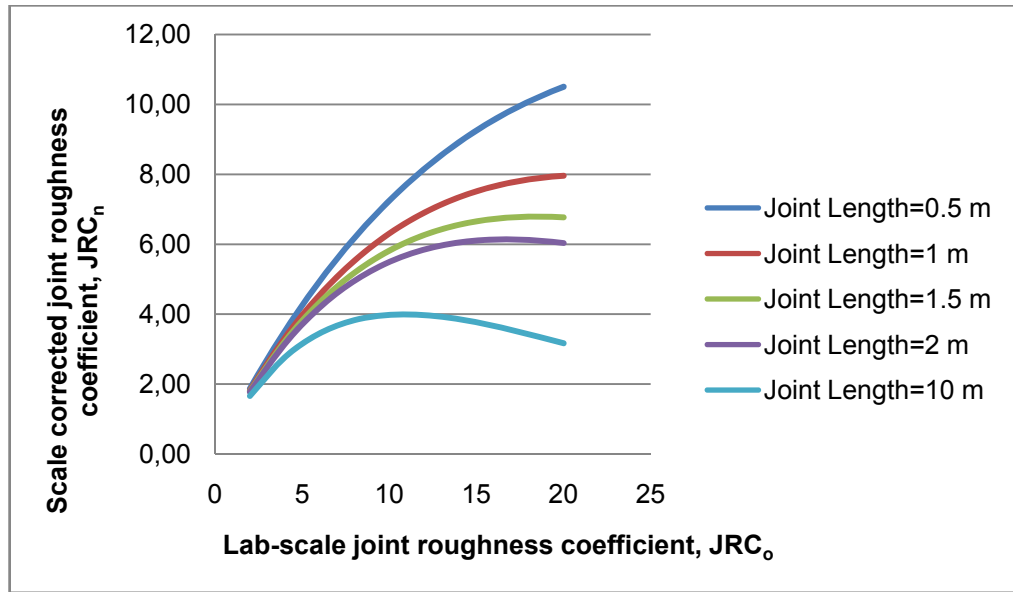


Figure 2.16 Sensitivity of scale correction for joint roughness coefficient with a lab scale sample of 0.1 meters

It can be seen from the scale corrected joint roughness coefficients plot of discontinuities with different length, the logic breaks down from 1.5 meters (when considering that the lab scale length is 0.1 m). In the field with large scale discontinuous rock slopes, this amount of discontinuity length would probably be unimportant to consider as a stability threat. Because of that reason, a more realistic joint roughness determination for large scale discontinuities, which has no limitation, should be used. The study of Barton and Bandis (1982) also offers a methodology for predicting large scale joint roughness coefficients from asperity amplitudes (height of undulations of the discontinuities), which was mentioned in Figure 2.11-12 and Eq. (2.11).

2.3.7 Mobilization of roughness during shear

As introduced earlier, JRC is specifically related to the peak shear strength and the corresponding peak drained friction angle was expressed as (Barton et al., 1985):

$$\phi_p' = \text{JRC} \times \log_{10} \left(\frac{\text{JCS}}{\sigma_n} \right) + \phi_r \quad (2.16)$$

This peak strength is mobilized following a peak shear displacement (δ_{peak}) which is frequently about 1 % of the joint sample length (Barton et al. (1985). During this peak shear displacement first residual friction angle (ϕ_r) is mobilized and then the roughness is mobilized causing dilation. Shear displacements larger than this range causes roughness gradually destroy or worn out. Rate of dilation also decreases continuously. Barton et al. (1985) formulated the case generally as:

$$\phi_p'(\text{mob}) = \text{JRC}(\text{mob}) \times \log_{10} \left(\frac{\text{JCS}}{\sigma_n} \right) + \phi_r \quad (2.17)$$

The gradual decrease in JRC was formulated by Barton et al. (1985). According to this study, $\text{JRC}_{\text{mob}}/\text{JRC}_n$ corresponds to different values with respect to shear displacement to peak shear displacement ratio (i.e. $\left(\frac{\delta}{\delta_{\text{peak}}} \right)$). The relation between them is illustrated in Table 2.2. For the calculation of mobilized roughness a relation called roughness contribution was introduced as;

$$\text{RUFF} = \text{JRC}_n \cdot \log_{10} \left(\frac{\text{JCS}_n}{\sigma_n} \right) \quad (2.18)$$

Table 2.2 Values used for calculation of JRC_{mob} (Anon, 2005)

A $\left(\frac{\delta}{\delta_{peak}}\right)$	B $\left(\frac{JRC_{mob}}{JRC_n}\right)$
0.00	$-\phi_r / RUFF$
0.20	$(-0.25) \cdot \phi_r / RUFF$
0.30	0.00
0.45	0.50
0.60	0.75
0.80	0.90
1.00	1.00
1.50	0.90
2.00	0.85
3.00	0.75
4.00	0.70
6.00	0.60
8.00	0.55
10.00	0.50
20.00	0.40
40.00	0.30
60.00	0.20
80.00	0.10
100.00	0.00

So the JRC_{mob} parameter is found as;

$$JRC_{mob} = B \cdot JRC_n \quad (2.19)$$

Introducing the mobilization of roughness, dilation angle of the discontinuity also mobilizes. Eq. (2.12) becomes for the dilation angle;

$$d_{\text{mob}} = 1/2 \times \text{JRC}_{\text{mob}} \times \log_{10} \left(\frac{\text{JCS}}{\sigma_n} \right) \quad (2.20)$$

2.3.8 Rock discontinuity deformation

Under changing stress conditions, discontinuity deformation is a principal component of the behaviour of the discontinuous rock mass (Bandis et al., 1985). The terms of joint normal stiffness and joint shear stiffness were defined in order to analyse the deformation characteristics of the joints.

Normal stiffness (K_n) is defined as the normal stress increment required for a small closure of a joint or fracture, at a given level of effective stress. Similarly the shear stiffness (K_s) is taken as the average slope up to the shear strength-peak shear displacement curve. The units of joint stiffness values are stress/displacement (e.g. MPa/mm, MPa/m etc.). Therefore it is usually expected that K_n values get larger value than the shear stiffness K_s values (Barton, 2007). Typical normal stress-normal closure and shear stress-shear displacement curves are given in Figure 2.17.

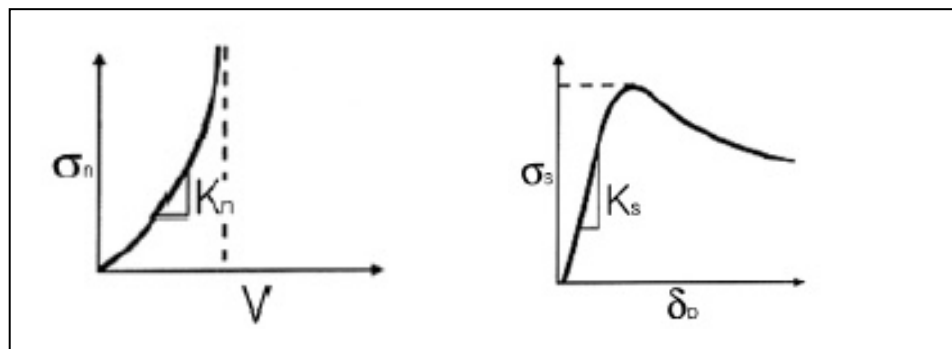


Figure 2.17 Typical graphs of normal stress-normal closure and shear stress-shear displacement (Choi and Chung (2004))

Normal deformation

Previous experimental studies show that, unlikely the Coulomb model the normal stress-normal closure and shear stress-shear displacement curves follow a non-linear path (Barton (1973), Barton and Choubey (1977), Bandis et al. (1981), Barton and Bandis (1982), Bandis et al. (1983) and Barton et al. (1985)). Therefore the normal stiffness of a discontinuity cannot be defined as a single value. For each increment of normal stress, the corresponding K_n value must be obtained.

Experimental studies of Bandis et al. (1983) showed that normal stress-normal closure relations for natural and unfilled discontinuity types are invariably non-linear. Goodman (1976) (in Bandis et al. (1983)) developed a relation between normal stress, initial normal stress and normal closure. The relation is given below;

$$\frac{\sigma_n - \sigma_i}{\sigma_i} = C \left[\frac{\Delta V}{V_m - V} \right]^t \quad (2.21)$$

Where;

C and t are constants,

σ_n is normal stress,

σ_i is initial normal stress,

V_m is maximum allowable closure,

ΔV is joint closure.

Bandis et al.(1983) developed that relation for normal stress;

$$\sigma_n = \frac{V_j}{a - b\Delta V} \quad \text{or} \quad \sigma_n = \frac{1}{\frac{a}{\Delta V} - b} \quad (2.22)$$

Where a and b are constants that a/b =asymptote to the hyperbola = V_m (maximum closure). Initial normal stiffness is defined as $1/a$ and hence Eq.(2.22) becomes for the discontinuity normal stiffness at point ΔV ;

$$K_n = \frac{K_{ni}}{\left(1 - \frac{\Delta V}{V_m}\right)^2} \quad (2.23)$$

Where;

K_{ni} = initial normal stiffness

Maximum closure

As mentioned above, the total deformation curve of a discontinuous block eventually becomes asymptotic to a limiting value of maximum allowable closure (V_m). Studies of Bandis et al. (1983) resulted to a relation between V_m and strength and geometrical properties of the discontinuities. According to the authors, maximum closure with similar aperture thickness (a_j) depended mainly on the joint wall compressive strength (JCS). Figure 2.18 presents the effect of the JCS and a_j on V_m .

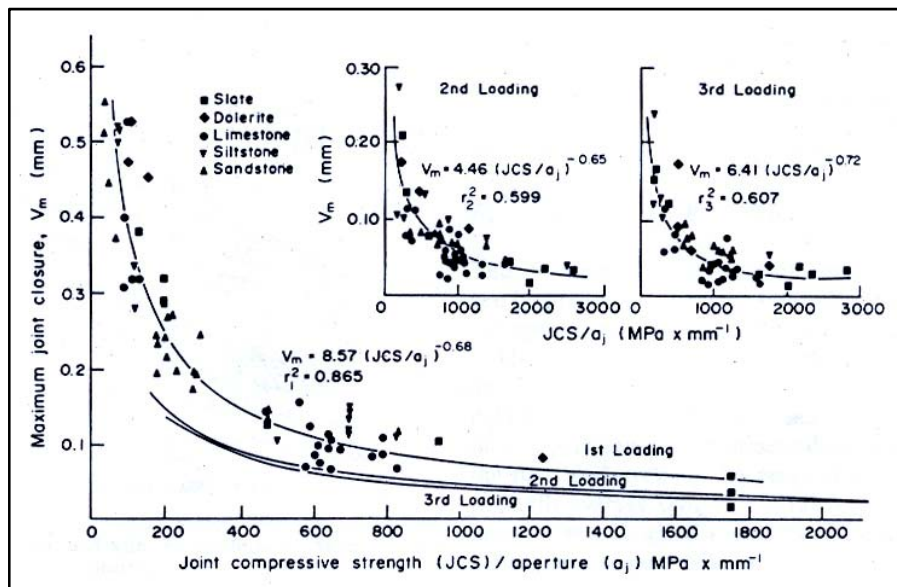


Figure 2.18 Effects of the joint wall compressive strength (JCS) and mechanical aperture (a_j) on maximum closure (V_m) (Bandis et al., 1983)

As it can be seen from the Figure, curve fitting of the results yield an empirical result between V_m , JCS and a_j which is;

$$V_m = C \left(\frac{JCS}{a_j} \right)^D \quad (2.24)$$

Where $C = 8.57$ and $D = -0.68$ $R^2 = 0,865$ for the first loading cycle,

$C = 4.46$ and $D = -0.65$ $R^2 = 0.599$ for the second loading cycle,

$C = 6.41$ and $D = -0.72$ $R^2 = 0.607$ for the third loading cycle,

Where; JCS is in MPa and a_j is in mm.

Besides these results, authors investigated the relation between V_m and JRC. Figure 2.19 shows the well defined relation between them that is V_m decreases as the JRC increases. The authors came to a conclusion that explains this effect as: “upon initiation of loading, discontinuities undergo a rapid closure through readjustment of their initial seating condition. As σ_n increases, discontinuity closure depends almost exclusively on the deformability of asperities. The tight mechanical interlock between the protrusions of a rough surface creates a very effective confined environment, thus stiffening the deformational response of the asperities” (Bandis et al., 1983).

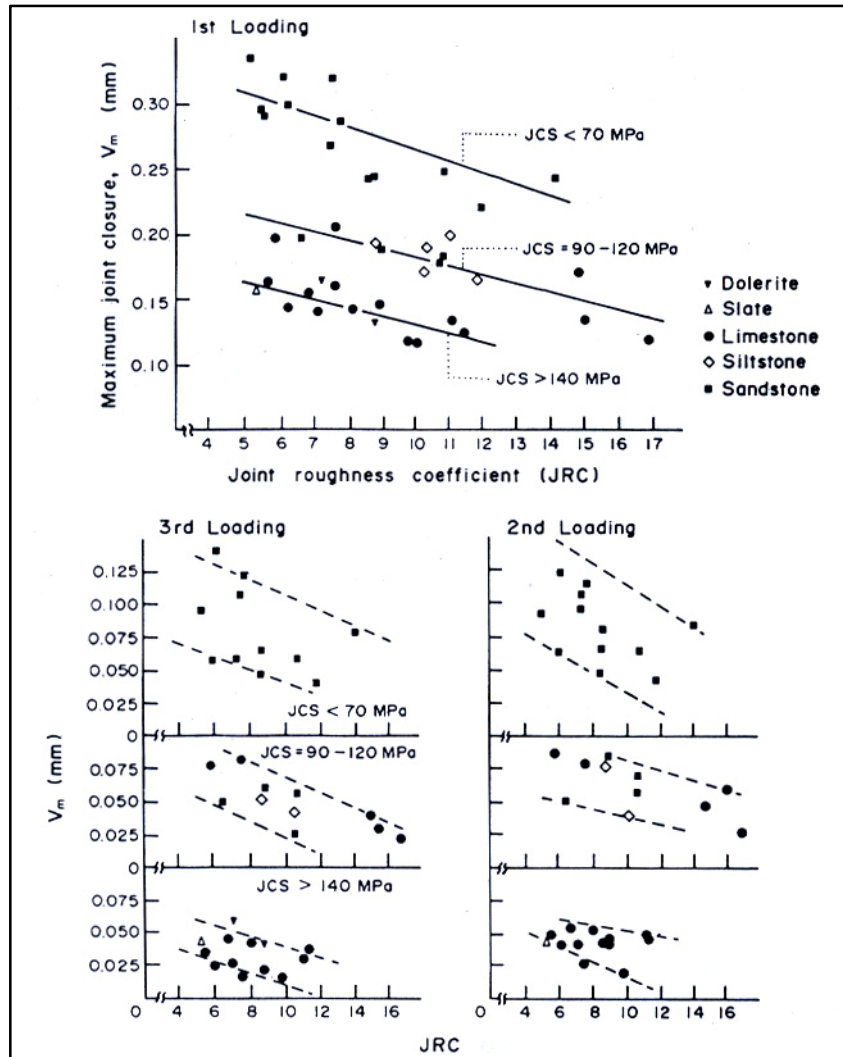


Figure 2.19 Relation between maximum closure (V_m) and joint roughness coefficient (JRC) (Bandis et al., 1983)

The relations derived between V_m , a_j , JCS and JRC were combined and the following empirical equation were obtained;

$$V_m = A + B(JRC) + C \left(\frac{JCS}{a_j} \right)^D \quad (2.25)$$

Where;

$A = -0.2960$ $B = -0.0056$ $C = 2.2410$ $D = -0.2450$ $R^2 = 0.675$ for the first cycle

A = -0.1005 B = -0.0073 C = 1.0082 D = -0.2301 R² = 0.546 for the second cycle

A = -0.1032 B = -0.0074 C = 1.1350 D = -0.2510 R² = 0.589 for the third cycle

Bandis et al. (1983) empirically defined the mechanical aperture (a_j) in mm as:

$$a_j = \frac{JRC}{5} \left(0.2 \frac{\sigma_c}{JCS} - 0.1 \right) \quad (2.26)$$

Where;

σ_c = Uniaxial compressive strength of the rock.

Shear deformation

The non-linear stress - shear displacement behaviour of sheared discontinuities in the pre-peak range were frequently expressed by hyperbolic functions (Bandis et al., 1983). Kulhaway (1975) (in Bandis et al., 1983) refers to the relation;

$$\tau = \frac{\bar{\delta}}{m+n\bar{\delta}} \quad (2.27)$$

Where $\bar{\delta}$ is the shear displacement at a given shear stress level and m and n are constants of the hyperbola. Constant m is the reciprocal of the initial shear stiffness and constant n is the reciprocal of the horizontal asymptote τ_{ult} to the hyperbolic τ - $\bar{\delta}$ curve. Development of Eq.(2.27) results with the following relation for shear stiffness;

$$K_s = K_j (\sigma_n)^{n_j} \left(1 - \frac{\tau R_f}{\tau_p} \right)^2 \quad (2.28)$$

Where;

K_j = stiffness number,

n_j = stiffness exponent,

$R_f = \text{failure ratio} = \tau / \tau_{ult}$

$\tau_p = \text{peak shear strength.}$

The indices R_f , n_j and K_j describes the non-linearity in discontinuity shear behaviour. The stiffness exponent n_j is the slope of log-log relation between initial shear stiffness K_{si} and σ_n with a unit of $(\text{MPa})^2/\text{mm}$. Also the experimental studies Bandis et al. (1983) showed that stiffness number K_j (intercept of the log-log relation between initial shear stiffness K_{si} and σ_n) can be written empirically as;

$$K_j = -17.19 + 3.86 \text{ JRC} \quad (2.29)$$

With $R = 0,835$ for $\text{JRC} > 4,5$.

The summary of the experimental discontinuity shear stiffness parameters of Bandis et al. (1983) are given in Figure 2.21.

Rock type	Weathering state of joint samples	Range of normal stress (MPa)	Initial K_s (MPa)	Stiffness k_j (MPa/mm)	Stiffness exponent (n_j) (MPa) ² /mm	Failure ratio R_f	Secant peak K_s (MPa/mm)
Sandstone	Fresh (3 samples)	0.25–2.36	2.2–37.6	13.02	0.674	0.748	0.56–4.50
	Slightly weathered (1 sample)	0.25–2.07	8.7–41.9	24.49	0.714	0.738	1.23–4.74
	Moderately weathered (2 samples)	0.24–2.04	1.2–6.2	3.88	0.725	0.810	0.47–1.73
	Weathered (3 samples)	0.50–1.96	2.1–6.5	3.49	0.831	0.887	0.56–1.35
Limestone	Slightly weathered (1 sample)	0.23–1.84	8.0–50.5	30.19	0.799	0.830	1.65–6.87
	Moderately weathered (1 sample)	0.24–1.90	4.1–17.3	9.73	0.698	0.731	1.12–3.13
	Weathered (1 sample)	0.25–1.53	1.0–10.5	5.04	1.118	0.788	0.66–1.89
Dolerite	Slightly weathered (1 sample)	0.26–2.11	8.2–19.0	17.74	0.615	0.652	1.75–4.98
	Weathered (1 sample)	0.28–1.11	3.6–9.1	9.02	0.674	0.778	0.86–2.19
Slate	Fresh (3 samples)	0.54–2.28	= K_s	—	0	0	5.6–12.6
	Weathered (3 samples)	0.40–1.45	2.8–7.5	5.72	0.760	0.870	0.64–1.27

Figure 2.20 Summary of experimental joint shear stiffness parameters (Bandis et al. (1983))

2.4 Distinct Element Modelling

In geotechnical engineering applications there are several numerical modelling methods for the analysis of stress, deformation, fracture and breakage in mechanical systems. The most popular methods are;

- Finite Element Method
- Finite Difference Method
- Boundary Element Method
- Discrete Element Method

Many continuum mechanics software (e.g., finite element and Lagrangian finite-difference programs) can simulate the variability in material types and non-linear constitutive behaviour associated with a rock mass successively. However, presenting the discontinuities in the system

requires a discontinuum-based formulation. Finite element, boundary element and finite difference codes may have interface elements that are limited to model discontinuous media in one or more of the following ways;

1. The logic may break down when many intersecting interfaces are used,
2. There may not be an automatic scheme for recognizing new contacts,
3. The formulation may be limited to small displacements. (Anon, 2007)

For these reasons, continuum codes with interface elements are restrictive in their applicability for analysis of surface and underground excavations in discontinuous rock. Codes based upon a discontinuum mechanics formulation, which is described as discrete element codes, provides the capability of analyzing the motion of multiple intersecting discontinuities explicitly. Cundall and Hart (1992) provide the following conditions for a computer program to be represented as a discrete element method:

- (a) the method should allow finite displacements and rotations of discrete bodies, including complete detachment; and
- (b) the method should recognize new contacts automatically as the calculation progresses. (Anon, 2007)

Cundall and Hart (1992) identify the following classes of codes which adopt discrete element method:

1. Distinct element programs – use an explicit time-marching scheme to solve the equations of motion directly. Bodies may be rigid or deformable (by subdivision into elements); contacts are deformable. Representative codes are TRUBAL (Cundall and Strack 1979a, in Anon 2007), UDEC (Cundall 1980 and Cundall and Hart 1985, in Anon 2007, Anon 2005),

3DEC (Cundall 1988, Hart et al., 1988, in Anon 2007), DIBS (Walton 1980, in Anon 2007), 3DSHEAR (Walton et al., 1988, in Anon 2007) and PFC (Itasca 2005, in Anon 2007).

2. Modal methods – are similar to the distinct element method in the case of rigid blocks, but, for deformable bodies, modal superposition is used. This method appears to be better-suited for loosely packed discontinua; in dynamic simulation of dense packing, eigenmodes are apparently not revised to account for additional contact constraints. A representative code is CICE (Hocking et al., 1985, in Anon 2007).

3. Discontinuous deformation analysis – assumes that contacts are rigid bodies, and bodies may be rigid or deformable. The condition of no-penetration is achieved by an iterative scheme; the deformability comes from superposition of strain modes. The relevant computer program is DDA (Shi 1989, in Anon 2007).

4. Momentum-exchange methods – assume both the contacts and bodies to be rigid: momentum is exchanged between two contacting bodies during an instantaneous collision. Friction sliding can be represented.

The distinct element technique was originally developed by Cundall (1971) and has resulted in formulation and development of three dimensional distinct element code (3DEC) and it progressed over a period of 35 years (Anon, 2007).

3DEC is a three-dimensional numerical program based on the distinct element method for modelling discontinuous medium subjected to static or dynamic loading. A discontinuous medium is distinguished from a continuous medium by the existence of contacts between the discrete bodies that comprise the system (Anon, 2007).

3DEC is based on a dynamic (time-domain) algorithm that solves the equations of motion of the block system by an explicit finite difference method. At each time step, the law of motion and the constitutive equations are applied. For both rigid and deformable blocks, sub-contact force-

displacement relations are prescribed. The integration of the law of motion provides the new block positions, and therefore the contact displacement increments (or velocities). The sub-contact force-displacement law is then used to obtain the new sub-contact forces, which are to be applied to the blocks in the next time step. The cycle of mechanical calculations is illustrated in Figure 2.21 (Anon, 2007).

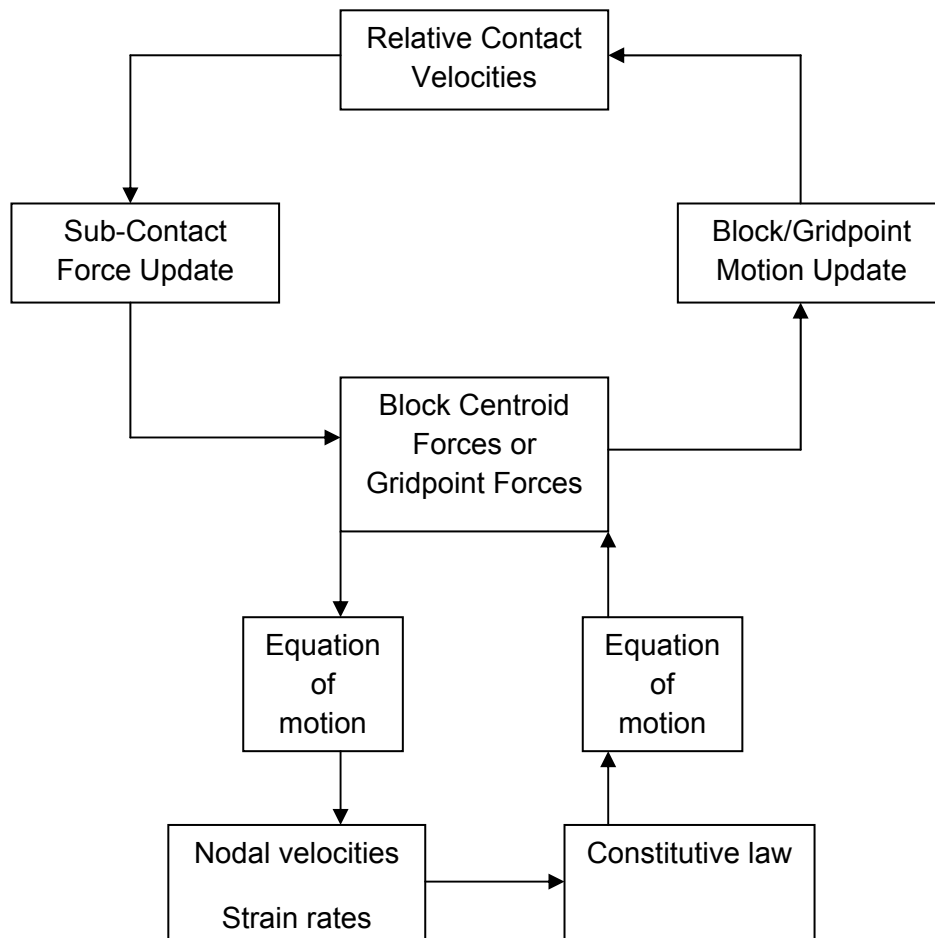


Figure 2.21 The calculation cycle of 3DEC program (Anon, 2007)

3DEC also has a built in programming language called FISH which can be used for user specific purposes.

3DEC has two constitutive models for analyzing discontinuity behaviour. The first one is the generalization of Coulomb friction law. This law works similarly for sub-contacts between both rigid and deformable blocks. Both shear and tensile failure is considered. In elastic range the model behaviour is governed by discontinuity normal stiffness and discontinuity shear stiffness.

The force increments are found by using displacement increment and the input discontinuity stiffness. The normal force increment ΔF^n is found as;

$$\Delta F^n = -K_n \Delta V^i A_c \quad (2.30)$$

And the shear force increment is found as;

$$\Delta F^s = -K_s \Delta \delta A_c \quad (2.31)$$

Where;

ΔV^i = Normal displacement increment

A_c = Area of contact

$\Delta \delta$ = Shear displacement increment

The total normal and shear forces, F^n and F^s are then updated for the next cycle as;

$$F^n = F^n + \Delta F^n \quad (2.32)$$

And,

$$F^s = F^s + \Delta F^s \quad (2.33)$$

For tensile failure;

$$F^n < T_{\max}, \text{ then } F^n = T_{\text{residual}} \quad (2.34)$$

Where;

$$T_{\max} = -T A_c \quad (2.35)$$

$$T_{\text{residual}} = -T_{\text{residual}} A_c \quad (2.36)$$

T_{max} = Peak tensile strength

T_{residual} = Residual tensile strength

For shear failure;

$$F^s < F_{\text{max}}^s, \text{ then } F^s = F^s \left(\frac{F_{\text{max}}^s}{F^s} \right) \quad (2.37)$$

Where;

$$F_{\text{max}}^s = c A_c + F^n \tan \phi \quad (2.38)$$

Shear displacement leads to a dilation that is;

$$\Delta V(\text{dil}) = \Delta \delta \tan(d) \quad (2.39)$$

Where d is the dilation angle specified.

Then the normal force is corrected to consider the effect of dilation as;

$$F^n = F^n + K_n A_c \Delta \delta \tan(d) \quad (2.40)$$

The second constitutive model of 3DEC for discontinuities is the continuously yielding joint model. The model attempts to account for some nonlinear behaviour observed in physical tests. The model generates the discontinuity shearing damage, normal stiffness dependence and decrease in dilation angle with plastic shear displacement.

The normal stress is found incrementally as;

$$\Delta \sigma_n = K_n \Delta V^i \quad (2.41)$$

Where the normal stiffness K_n is given by;

$$K_n = a_n \sigma_n^{e_n} \quad (2.42)$$

Where a_n and e_n are model input parameters

For shear loading, the shear stress increments calculated as;

$$\Delta\tau = Fk_s \Delta\delta \quad (2.43)$$

Where the shear stiffness K_s is given by;

$$K_s = a_s \sigma_n^{e_s} \quad (2.44)$$

And where e_s and a_s are model input parameters and F is the tangent modulus factor which depends on the distance from the actual stress curve to the target or bounding strength;

$$F = \frac{(1 - \tau/\tau_m)}{1 - r} \quad (2.45)$$

Where;

r is the stress ratio at the last reversal and it is limited to 0.75 in order to avoid numerical noise.

τ_m is the bounding strength and found as;

$$\tau_m = \sigma_n \tan \phi_m \Delta\delta \quad (2.46)$$

ϕ_m is the friction angle at which the discontinuity is dilating at the maximum dilation angle and it is continuously reduced according to the equation;

$$\Delta\phi_m = -\frac{1}{R} (\phi_m - \phi) \Delta\delta^p \quad (2.47)$$

R is the model input parameter defines the surface roughness,

The plastic increment $\Delta\delta^p$ is found as;

$$\Delta\delta^p = (1 - F) |\Delta\delta| \quad (2.48)$$

Studies related to 3DEC were mostly conducted by Coulomb slip model rather than continuously yielding joint model (Kulatilake et al. (1993), Konietzky et al. (2001), Hutri and Antikainen (2002), Corkum and Martin (2004). The reason for that would probably be the easiness of the

parameter determination. Only the discontinuity cohesion and discontinuity friction angle should be determined for the Coulomb slip model.

Universal distinct element code (UDEC) is a two dimensional numerical program that offers users to use Barton-Bandis failure criterion in discontinuity behaviour analyses. Researchers, who were interested in discontinuity failure in detail, prefer to use Barton-Bandis failure criterion rather than Coulomb slip model, usually used UDEC for their numerical analyses (Bhasin and Hoeg (1997), Chryssanthakis et al. (1997), Hökmark (1998), Choi and Cung (2004), Bhasin and Kaynia (2004), Vardakos et al (2006), Kveldevisk et al. (2007)).

Within these studies, some researchers investigated the difference between the Coulomb slip model and the Barton-Bandis model. Choi and Chung (2004) investigated a failed slope by both methods and concluded that Barton-Bandis method showed more realistic results.

In the study of Kveldevisk et al. (2007), a back analyses of a 100 000 m³ landslide was conducted and main focus was given to determination of roughness parameter (JRC). The authors had used limit equilibrium analyses together with UDEC. From the limit equilibrium analyses JRC was found to be the most effective parameter on the factor of safety. Also the probabilistic calculations showed that JRC was found to be the most important contributor to the total uncertainty over the whole set of variables.

From the detailed information about the behaviour of rock discontinuities and recent numerical studies about discrete element modelling, it can be concluded that not only the strength parameters of discontinuities but also the surface characterization of them are important. The Barton-Bandis failure criterion includes the discontinuity surface properties into the shear failure such as joint wall compressive strength (JCS) and joint roughness coefficient (JRC).

In cases where the normal stress on discontinuity surface is low, linear Coulomb constitutive model appears to be inadequate in reflecting both the normal and shear deformation characteristics of discontinuities. Barton-Bandis failure criterion allows the non-linear behaviour of the normal deformation until a limited amount (maximum allowable closure), shear behaviour with mobilization of roughness under shear stress and the dilation angle with the shear displacement of rock blocks.

Another point is that, a great variety of numerical analyses programs are being developed. Different type of programs are available for different kinds of problems (e.g. distinct element programs for discontinuum analyses, finite difference programs for continuum based analyses, finite element programs for small displacement problems). An important point is that the choice of appropriate program and the related constitutive model among many kinds of these in order to obtain best results from the numerical analyses.

Barton-Bandis failure criterion which is used within discrete element models is only available in two dimensional distinct element code (UDEC). In simulating the field stresses three dimensional programs yield to more realistic results. The application of Barton-Bandis approach in a three dimensional discrete element model is required for geotechnical applications.

Another point that can be concluded from the detailed literature survey is that, the scale correction for the field discontinuity sets is restricted to some extent. In case of discontinuity lengths longer than 1,5 meters (with a 0.1 meters lab scale discontinuity length), the scale correction logic breaks down for the joint roughness coefficient and another methodology for determining field scale joint roughness coefficient is needed for the practical slope problems related to large scale discontinuities (e.g. 500 m). The study of Barton et al. (1982) was extended for large scale roughness determination.

CHAPTER 3

DEVELOPMENT OF THE NUMERICAL MODEL

3.1 Introduction

3DEC allows users to implement user defined discontinuity constitutive models that are derived in C++ and compiled into the main executable part. The models should exist as a runtime dynamic link library (DLL) files that can be loaded whenever it is needed. The files that contain shareable routines are called dynamic link libraries (DLLs). Dynamic link libraries contain predefined functions that are linked with an application program when it is loaded (dynamically), instead of when the executable file is generated (statically) (Murray, 2002). In this chapter, the implementation of Barton-Bandis discontinuity constitutive model to 3DEC by constructing a dynamic link library file is explained.

3.2 Basic Structure of the Program

The main function of the model is to return new forces with the given displacement increments. However, the model must also provide other information, such as names, and perform operations such as writing and reading save files (Anon, 2007).

In the C++ language, the emphasis is on an object-oriented approach to program structure, using classes to represent objects. The possibility to

orientate programming to objects allows the programmer to design applications from a point of view more like a communication between objects rather than on a structured sequence of code. In addition it allows a greater reusability of code in a more logical and productive way (C++ Resources Network).

The data associated with an object is encapsulated by itself and is invisible outside it. Communication with the object is by member functions that operate on the encapsulated data. In addition, there is strong support for a hierarchy of objects: new object types may be derived from a base object, and the base-object's member functions may be superseded by similar functions provided by the derived objects. This arrangement confers a distinct benefit in terms of program modularity. For example, the main program may need access to many different varieties of derived objects in many different parts of the code; but it is only necessary to make reference to base objects, not to the derived objects. The runtime system automatically calls the member functions of the appropriate derived objects (Anon, 2007).

A base class provides a framework for actual constitutive models, which are classes derived from the base class. The base class, called JointModel, is termed an "abstract" class because it declares a number of "pure virtual" member functions. This means that no object of this base class can be created, and that any derived-class object must supply real member functions to replace each one of the pure virtual functions of JointModel. Partial listing of base class JointModel is given in Table A.1 in Appendix A.

The model class definition should also contain a constructor that must invoke the base constructor (Anon, 2007). Initialization of data members may be performed by the constructor. Model constructor is illustrated in Table A.2 in Appendix A.

The most important link between the 3DEC main code and the developed model is the member-function Run (UByte nDim, State *ps), which computes the mechanical response of the model during cycling. A structure, State is used to transfer information to and from the model. The members of State are summarized in Table A.3 in Appendix A.

The main task of member-function Run () is to compute new forces from displacement increments. In a slipping discontinuity, it is also useful to communicate the internal state of the model, so that the state may be plotted and printed. For example, the presented model indicates whether they are currently yielding or have yielded in the past. Both shear and tensile failure may occur together in the model.

3.3 Implementation of the model

In this section, the implementation of the algorithm of Barton-Bandis criterion into 3DEC with C++ dynamic link library is explained. The input parameters and calculation steps of the algorithm is explained in detail.

3.3.1 Input data of the Barton-Bandis criterion

The input parameters for the Barton-Bandis criterion into 3DEC are given below;

- Joint initial normal stiffness, jkn,
- Joint shear stiffness number, jks,
- Joint residual friction angle, ϕ_r ,
- Lab scale Joint compressive strength (JCS_o), jcso,
- Lab scale Joint roughness coefficient (JRC_o), jrco,
- Intact rock uniaxial compressive strength, sigmac,
- Normal stress exponent, nj,
- Lab scale joint length, lo,
- In-situ joint length, ln.

3.3.2 Execution stage

As the code starts to execute, first of all the size corrections were applied in the algorithm. In this part, the scale corrections of JCS and JRC parameters were done according to the results of the studies of Barton and Bandis (1982). As mentioned in Section 2.3.6 the scale correction for joint roughness coefficient, the logic breaks down for a 1.5 meters discontinuity length with a 0.1 meters lab scale discontinuity length. For large scale discontinuities, it was mentioned in Section 2.3.6 that using Eq.(2.11) for joint roughness coefficient determination would be appropriate.

In addition to this, by using Eq.(2.13) for the scale correction, joint wall compressive strength value would get very small values as the discontinuity length reaches to few hundred meters. Because of this, it was decided that using a joint wall compressive strength value without scale correction would be appropriate. Therefore, an option was developed for deciding which joint roughness coefficient and joint wall compressive strength values are going to be used for the rest of the analyses. An optional input parameter namely "large" was defined. If the user does not enter the large parameter, the program continues with the algorithm that uses Eq.(2.13) and Eq.(2.14) for the scale correction. On the contrary, if the user decides to use the asperity related algorithm for joint roughness coefficient and joint wall compressive strength value without scale correction, the "large" input should be entered. The routine for introducing the "large" option is given in Table A.4 in Appendix A.

Following that, normal and shear stiffness values were found in order to calculate the normal and shear force increments. Bandis et al. (1983) described the normal stiffness as given in Eq. (2.23) and shear stiffness as in Eq. (2.28). In order to calculate the normal stiffness dynamically, maximum closure value should be calculated first. Eq. (2.25) was used for determining the value of maximum closure (V_m). The empirical equation for determining V_m contains the parameter that represents the mechanical

aperture (a_j) which was calculated by Eq. (2.26). The calculation of normal stiffness is given in Table A.5 in Appendix A.

The stiffness relation (Eq.(2.28)) that was derived by Bandis et al. (1983) contains peak shear strength parameter in the denominator. The yield strength relation (i.e. Eq.(2.5)) contains normal stress component in it. As the cycling of the program starts the average normal stress across the contact is initially zero. As the normal stress is zero then the shear stiffness relation goes to infinity. Because of this reason, a numerical instability occurs. To overcome this weakness, Bandis et al. (1985) had yielded a bi linear shear stiffness relation that change with respect to the shear relative displacement (Anon, 2005). The relation is given below;

$$K_s = \sigma_n \left(\frac{\tan(0.75)\phi_{\text{residual}}}{0.2\delta_{\text{peak}}} \right) L \quad \text{for} \left(\frac{\delta}{\delta_{\text{peak}}} \right) < 0.20 \quad (3.1)$$

and

$$K_s = \sigma_n \left(\frac{\tan(0.25)\phi_{\text{residual}}}{0.1\delta_{\text{peak}}} \right) L \quad \text{for} \left(\frac{\delta}{\delta_{\text{peak}}} \right) > 0.20 \quad (3.2)$$

(Anon, 2005)

The peak displacement was found by Eq.(2.13).

For the initial loading steps (approximately $\left(\frac{\delta}{\delta_{\text{peak}}}\right) < 0.002$) the shear stiffness relation that is described in Eq.(3.1) was used and after the normal stress of the contact was established the relation which was given in Eq. (2.28) was used. The ultimate shear strength parameter in Eq.(2.28) was taken equal to the peak shear strength value. The execution steps of the shear stiffness relation in the code are given in Table A.6 in Appendix A.

Then the execution part of mobilization of joint roughness coefficient (JRC_{mob}) parameter was inserted to the code. The values for determining the JRC_{mob} was given in Table 2.1. The JRC_{mob} values for the

corresponding $\left(\frac{\delta}{\delta_{\text{peak}}}\right)$ values are defined by an if-else if statement. The JRC_{mob} calculation steps are given in Table A.7 in Appendix A.

After the preliminary calculations of the Barton-Bandis model is finished, the calculation of the forces and the failure conditions are specified. First step is to calculate the normal force acting on the contact (discontinuity face). Program uses the previously determined k_{na} value and the normal displacement increment (which is found from the law of motion after the first cycle) to find the normal force increment. After that the resultant normal force increment value is added to the normal force value found in the previous cycle. The normal force calculation is given in Table A.8 in Appendix A.

When the normal force is calculated, the discontinuity is then checked for a tensile failure. If the discontinuity is stable against tension then the discontinuity behaviour under shear load is examined. The shear force found similarly with the normal force. The shear displacement increment and non-linear shear stiffness relation is used to calculate shear force increment. And the found value is added to the shear force that was calculated in the previous cycle.

After determining the shear stress, then the shear strength value is calculated for the given discontinuity parameters. Every cycle, the current shear stress and the yield value is compared in order to determine if the discontinuity starts slipping. If the yield strength is obtained then the state of the discontinuity changes and the failure state of the discontinuity can be monitored from the display properties of 3DEC.

The modelling procedure of the tensile and shear behaviour is given in Table A.9 in Appendix A.

When the peak shear stress is achieved, dilation starts. The dilation angle is mobilized as previously mentioned and the relation was given in Eq. (2.20). Then the normal force is corrected according to the dilatational

component of the normal displacement as given in Eq.(2.40). The relation for calculating the corrected normal force is given below;

The procedure of updating the normal force with respect to dilation is given in Table A.10 in Appendix A. The flowchart of the execution stage is given in Figure 3.1.

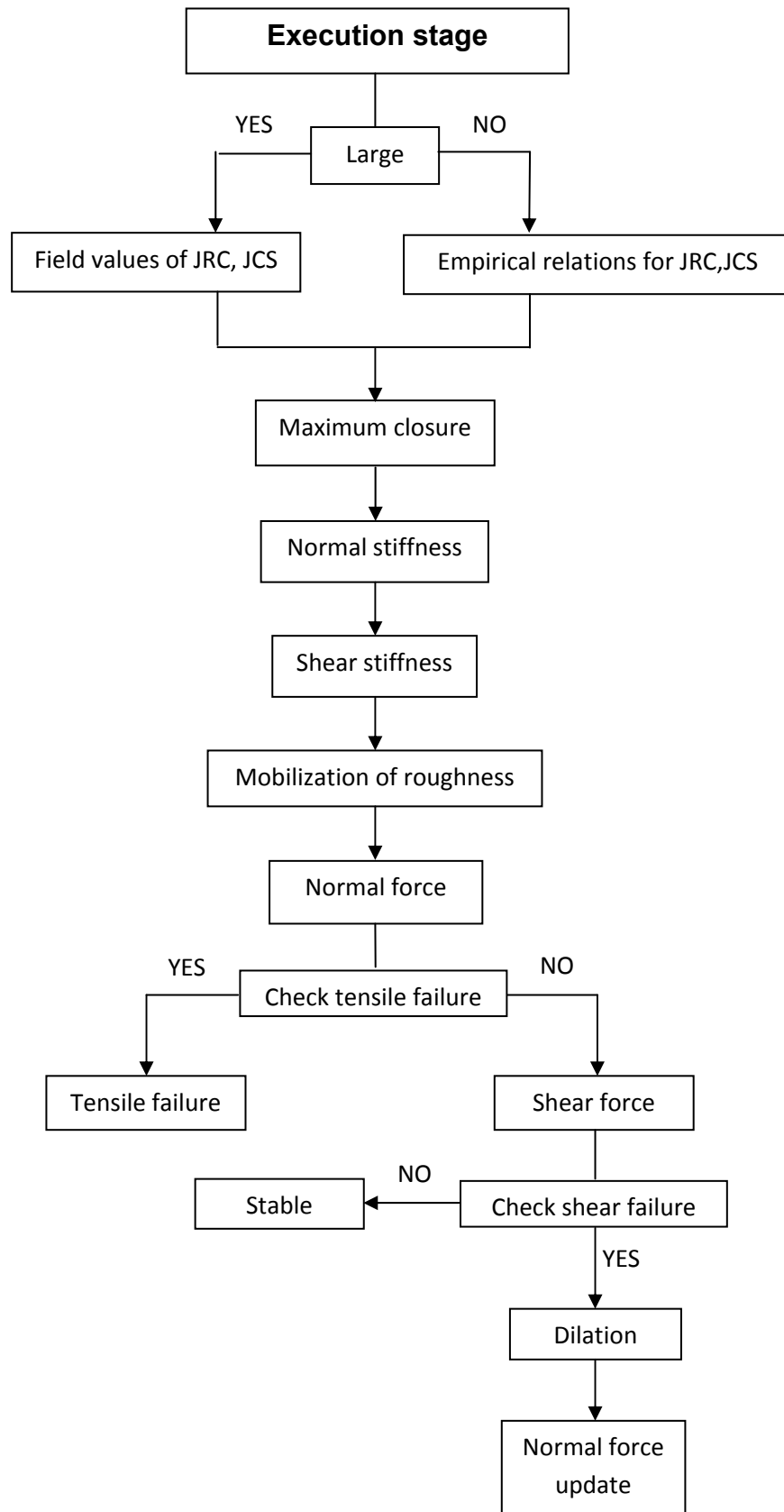


Figure 3.1 Flowchart of the execution part of the model

CHAPTER 4

EMPIRICAL VERIFICATION OF THE NUMERICAL MODEL

4.1 Introduction

The proposed methodology for implementing the Barton-Bandis failure criterion into three dimensional distinct element code (3DEC) needs to be checked for reliability purposes. In this chapter, the empirical verification of the developed methodology is presented.

The empirical relations that were derived from the empirical results of Barton (1973), Barton and Choubey (1977), Bandis et al. (1981), Barton and Bandis (1982), Bandis et al. (1983), Barton et al. (1985) were used for the verification.

A simple direct shear test model was prepared in 3DEC for the verification of the numerically developed model. The block and discontinuity parameters were determined and several direct shear test modelling were carried out.

At first, the normal deformation characteristics of the discontinuities were analyzed. Emphasis was given to maximum closure, discontinuity normal stiffness and irrecoverable closure values, and the numerically obtained values were compared with the results found from the empirical relations.

Following that, the shear deformation behaviour was examined. The shear stiffness, peak shear displacement, peak shear strength and residual shear

strength values using different discontinuity properties were compared with the empirical results.

4.2 Direct-shear Test Model

For the empirical verification, a simple direct shear test model was prepared. The model consists of two deformable blocks with a defined discontinuity face between them. A normal stress is applied from the top block and the shear force is generated by applying a constant velocity in x-direction to the upper block. The model geometry is given in Figure 4.1. The upper block's dimensions are 0.2 meters in length and in height, 0.1 meters in width. The lower block's dimensions are 0.3 meters in length, 0.2 meters in height and 0.1 meters in width. When the numerical model is in progress, the average normal stress, average shear stress, average normal and shear displacements were monitored. The direct shear model blocks were zoned (finite difference mesh) and both blocks have nodes only at the corners. For the measurement purposes, the average values of the nodes in the contact are taken by a simple FISH function. The executable code of the direct shear test model is given in Appendix B. All the input discontinuity surface parameters that are joint roughness coefficient (JRC) and joint wall compressive strength (JCS) were considered as lab scale parameters. Therefore, the verification of the empirical scale correction of the model was also tested.

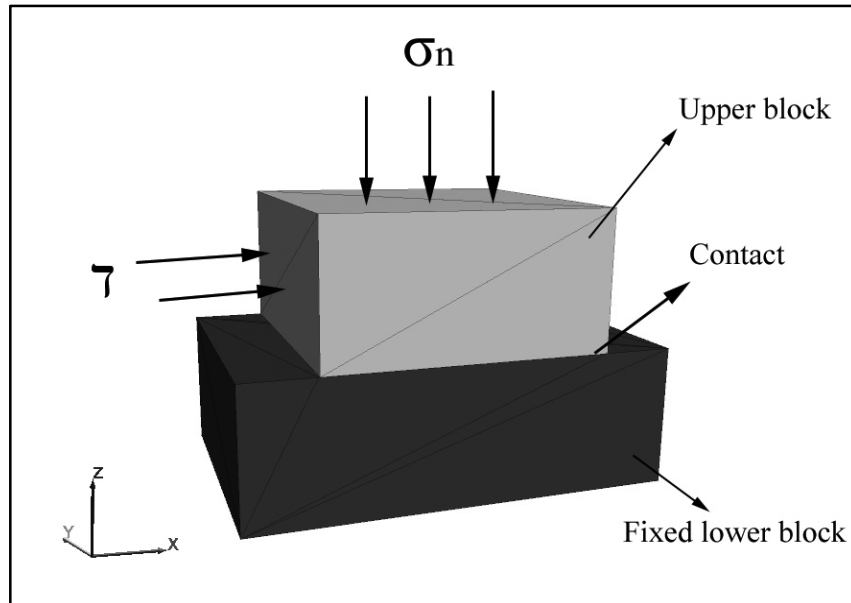


Figure 4.1 Direct shear test model used in the verification of the numerical model

4.3 Normal Deformation of the Discontinuity Model

In this section, the normal closure behaviour of the discontinuity is investigated in detail and verified according to the theory of empirical results. The normal stress-normal closure relation is explained. In addition, the effect of discontinuity surface properties such as joint roughness coefficient (JRC), joint wall compressive strength (JCS) and rock material property uniaxial compressive strength (σ_c) on the maximum closure behaviour on the discontinuity are investigated and verified with the empirical results.

4.3.1 Normal stress – normal closure

The theory and empirical approaches for the normal closure behaviour of discontinuities was presented in Chapter 2. The normal deformation characteristic of a discontinuity is governed mostly by the amount of maximum allowable closure. Various studies (Barton (1973), Barton and

Choubey (1977), Bandis et al. (1981), Barton and Bandis (1982), Bandis et al. (1983), Barton et al. (1985)) showed that the normal stress vs normal closure plots have non-linear behaviour that is different from the Mohr-Coulomb model in. And the path followed by this plot is governed by the non-linear normal stiffness relation. The empirical relation of maximum allowable closure was given in Eq.(2.24) and the relation of normal stiffness was given in Eq.(2.22) in Chapter 2.

The amount of maximum closure mainly depends on the JRC, JCS and mechanical aperture (a_j) parameters. Aperture also depends on the JRC, JCS and σ_c values. As a result JRC, JCS and σ_c are the main properties that affect the amount of maximum allowable closure.

For the verification of this behaviour, first JRC values were changed and JCS and σ_c were kept constant. The maximum allowable closure (V_m) was calculated both empirically and numerically by making model runs. The results of both methods were plotted and the amount of difference between two calculations was determined. The same procedure was repeated for the constant JRC- σ_c and JRC-JCS cases.

Following that, the normal stiffness values were again calculated numerically and empirically for a set of discontinuity properties (i.e. JRC, JCS and σ_c). The results of the calculations were plotted and the corresponding Difference amount was calculated.

In this part of the verification, the interest is given mainly to the normal deformation of the discontinuity rather than shear deformation. The normal stress was increased continuously, and the shear load was set to zero. For the application of the normal load displacement boundary condition was used in the program that is the normal force was formed by applying a constant velocity to the upper block.

The model input properties for the blocks and the discontinuity between them are given in Table 4.1.

Table 4.1 Material and discontinuity properties of the direct shear test model

Block Properties	Block mass density = 2600 kg/m ³ Bulk modulus of block, K = 4 GPa Shear modulus of block, G = 3 GPa
Discontinuity Properties	Initial discontinuity normal stiffness, $k_n = 100$ GPa Discontinuity shear stiffness number, $k_s = 10$ GPa Discontinuity stiffness exponent, $n_j = 0.8$ (MPa) ² /m Residual friction angle, $\phi_r = 20^\circ$ Discontinuity length of lab scale sample, $L_o = 0.1$ m Discontinuity length of the model, $L_n = 0.2$ m

The discontinuity stiffness exponent parameter, n_j was selected as 0.8 by assuming the direct shear test model has a slightly weathered discontinuity with correspondence to Figure 2.22.

Effect of joint roughness coefficient (JRC) on discontinuity normal closure

For the comparison of the numerical and empirical values, JCS_o and σ_c values were kept constant and different JRC_o values were tried. For the JCS_o value 100 MPa and for the σ_c value 150 MPa were selected. The results are given in Figure 4.2 and the corresponding data are given in Table 4.2.

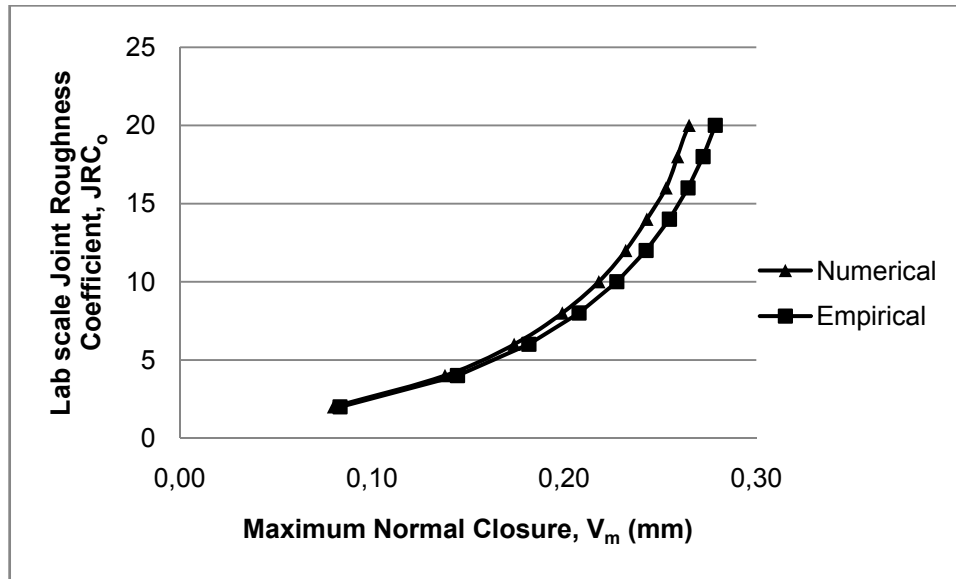


Figure 4.2 Graph of maximum normal closure (V_m) vs lab scale joint roughness coefficient (JRC_o)

Table 4.2 Results of maximum closure (V_m) analyses with varying joint roughness coefficient (JRC_o) ($\theta_r = 20^\circ$, $JCS_o=100\text{MPa}$ and $\sigma_c=150\text{ MPa}$)

JRC_o	V_m (empirical) (mm)	V_m (numerical) (mm)	Difference (%)
2	0.083	0.080	3.61
4	0.144	0.138	4.17
6	0.182	0.174	4.40
8	0.208	0.198	4.81
10	0.227	0.218	3.97
12	0.243	0.232	4.53
14	0.255	0.243	4.71
16	0.264	0.253	4.17
18	0.272	0.259	4.78
20	0.279	0.265	5.02
		Average	4.42

From Figure 4.2 and Table 4.2, it can be seen that the numerical response of the program gives an average of 4.42 % difference in the maximum allowable closure value. The difference between the results may have some possible reasons. First of all, 3DEC do not have any option that outputs the maximum allowable closure. After the normal stress-normal closure graph was generated, the maximum allowable closure amount was recorded by simply reading from the graph. There may be some errors while recording the actual amounts. Another reason can be stated as, for the calculation time hardware limitation, the mesh density was kept at minimum. By generating a finer mesh, the results can be closer. Despite these reasons, the results can be considered as acceptable.

Effect of joint wall compressive strength (JCS) on discontinuity normal closure

After determining the response of the numerical model to the change in JRC_0 parameter, the response to the change in JCS_0 parameter was analyzed in a similar way. Using constant values of JRC_0 and σ_c with different JCS_0 values, model runs were carried out. For the JRC_0 value, 8 was used and the σ_c value was selected as 150 MPa. The results are given in Figure 4.3 and the corresponding data is presented in Table 4.3.

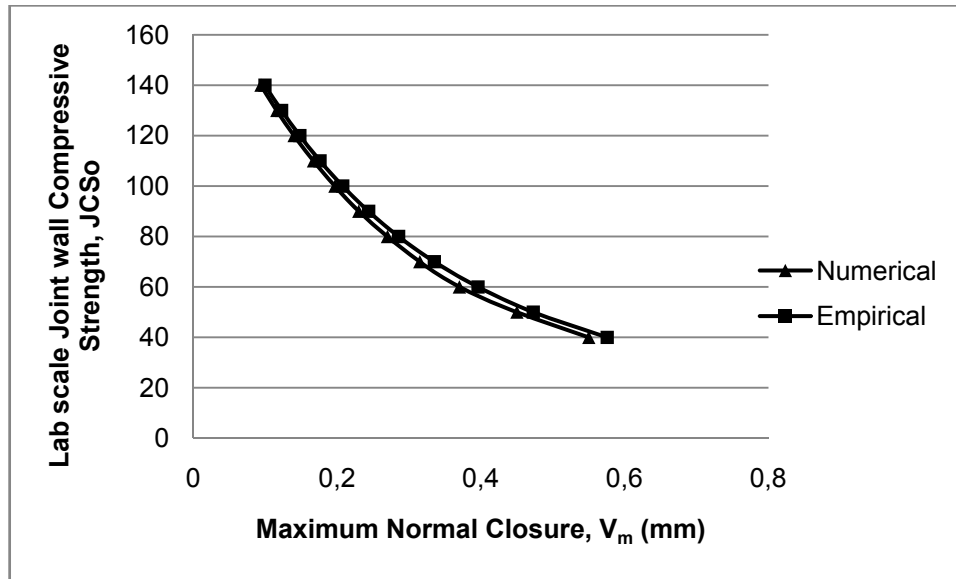


Figure 4.3 Graph of maximum normal closure (V_m) vs lab scale joint compressive strength (JCS_o)

Table 4.3 Results of maximum closure (V_m) analyses with varying joint wall compressive strength (JCS_o) values ($\varnothing_r = 20^\circ$, $JRC_o=8$ and $\sigma_c=150$ MPa)

JCS_o (MPa)	Empirical V_m (mm)	Numerical V_m (mm)	Difference (%)
40	0.58	0.55	5.17
50	0.47	0.447	4.89
60	0.40	0.37	7.50
70	0.34	0.315	7.35
80	0.29	0.27	6.90
90	0.24	0.23	4.17
100	0.21	0.198	5.71
110	0.18	0.167	5.99
120	0.15	0.14	6.67
130	0.12	0.116	3.33
140	0.10	0.094	6.00
		Average	5.79

The corresponding data of varying JCS_0 shows that the numerical models' responses have an average of 5.79 % difference with respect to the empirical results. Also the plots of JCS_0 vs normal closure show very similar trends with respect to each other. The possible errors for the differences can be restated as the recording errors of the numerical results and the mesh density of the block. This difference can also be considered as acceptable.

Effect of uniaxial compressive strength (σ_c) on discontinuity normal closure

The third parameter that affects the amount of maximum allowable closure is the unconfined compressive strength (σ_c) of the rock material. The same way was followed to see the response of the program to the change in σ_c . Constant JRC_0 and JCS_0 values were selected as 8 and 50 MPa respectively. Figure 4.4 shows the results and the corresponding data are given in Table 4.4.

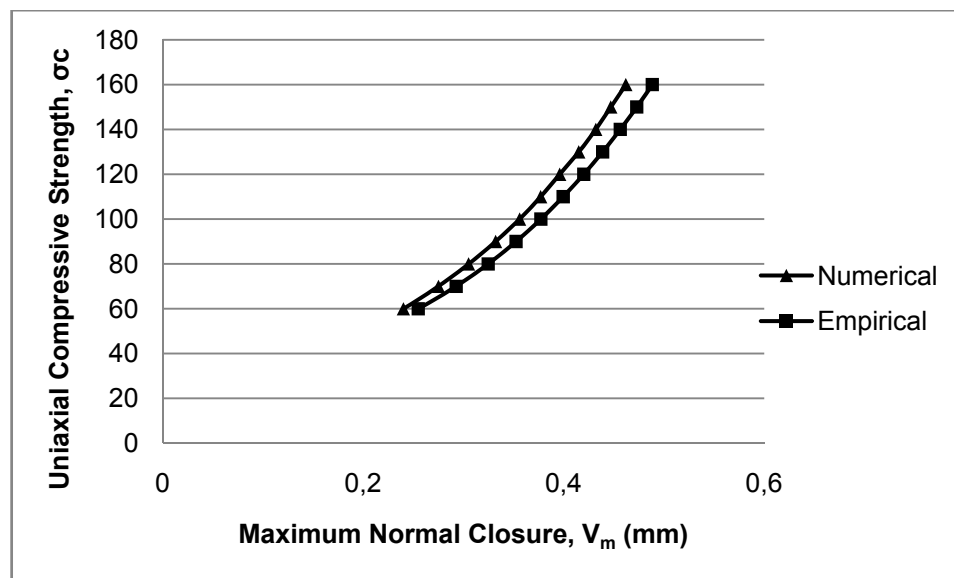


Figure 4.4 Graph of maximum normal closure (V_m) vs uniaxial compressive strength σ_c

Table 4.4 Results of maximum closure (V_m) analyses with varying uniaxial compressive strength (σ_c) values ($JRC_0=8$ and $JCS_0=50$ MPa)

σ_c (MPa)	V_m (empirical) (mm)	V_m (numerical) (mm)	Difference (%)
60	0.25	0.24	4.00
70	0.29	0.275	5.17
80	0.32	0.305	4.69
90	0.35	0.332	5.14
100	0.38	0.356	6.32
110	0.40	0.377	5.75
120	0.42	0.396	5.71
130	0.44	0.415	5.68
140	0.46	0.432	6.09
150	0.47	0.447	4.89
160	0.49	0.462	5.71
		Average	5.38

Results show that the program response to the change in σ_c has an average difference of 5.38 % when compared to the empirical results. And the corresponding plots have a similar trend for the empirical and numerical computations.

4.3.2 Discontinuity normal stiffness

As explained in Section 2.3.8, the nonlinear discontinuity closure behaviour is mainly governed by the ratio of current normal displacement to the maximum closure. From the discontinuity normal stiffness relation (Eq.(2.23)), it can be seen that, as the normal displacement approaches to the maximum closure value, the stiffness equation converges to infinity. As a result the normal deformation stops and the normal stress increases

rapidly. A typical normal stress-normal closure plot of a specific discontinuity is given in Figure 4.5.

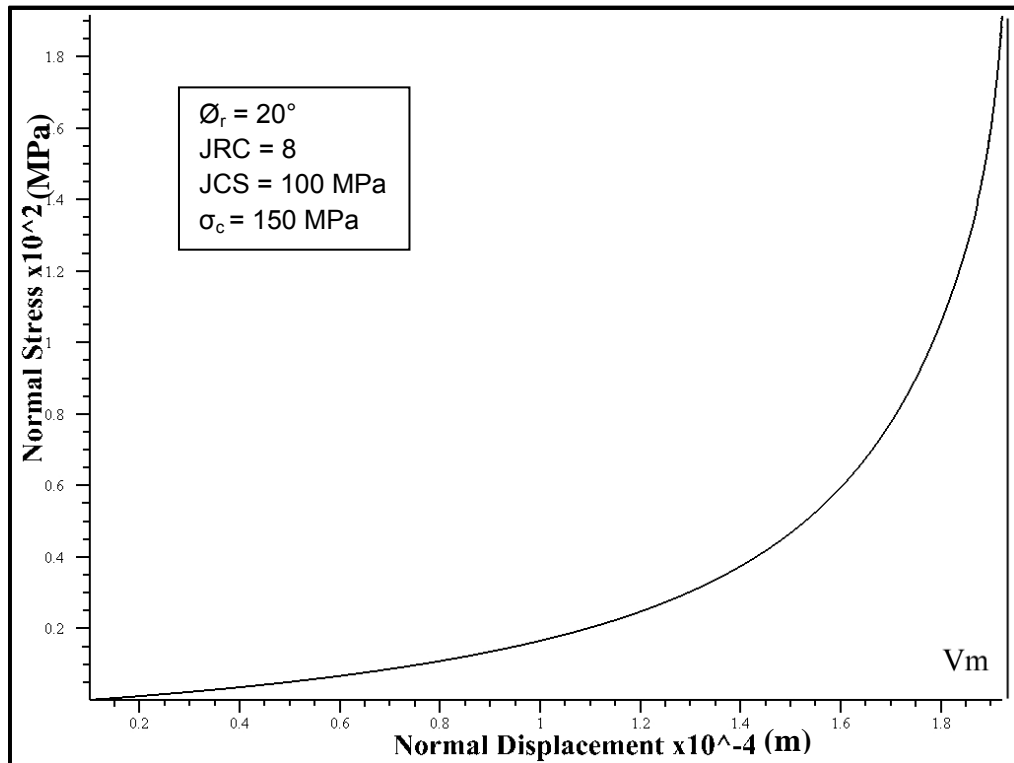


Figure 4.5 Graph of normal stress vs normal closure with $\varnothing_r = 20^\circ$, $JRC_o = 8$, $JCS_o = 100$ MPa, $\sigma_c = 150$ MPa

For the comparison procedure, the discontinuity properties, which were used in previous analyses (Figure 4.5), were assigned to the model. When the discontinuity normal deformation reaches to the maximum closure point, cycling was stopped. From the graph of normal stress vs. normal displacement, slopes from nine different points were taken and the results were compared to the empirical ones. The numerical and empirical results of normal stiffness-normal closure data were plotted and the difference between them was found. Figure 4.6 presents the results of numerical and empirical methods and Table 4.5 gives the corresponding data.

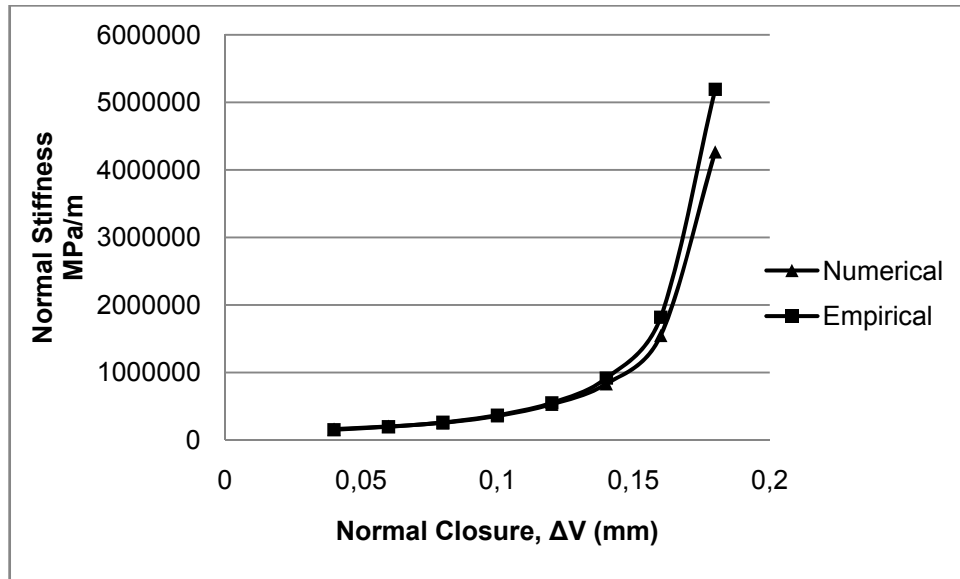


Figure 4.6 Graph of normal stiffness (K_n) vs normal closure ΔV ($\theta_r = 20^\circ$, $JRC_o = 8$, $JCS_o = 100$ MPa, $\sigma_c = 150$ MPa)

Table 4.5 Empirical and numerical results of normal stiffness (K_n)

Normal Closure (mm)	Normal Stiffness (empirical) (MPa/m)	Normal Stiffness (numerical) (MPa/m)	Difference %
0.04	162727	152939	6.02
0.06	203939	196752	3.52
0.08	253720	262490	3.46
0.10	359565	367654	2.25
0.12	530212	551458	4.01
0.14	832889	917475	10.16
0.16	1548759	1819283	17.47
0.18	4267200	5193935	21.72
	Average		8.58

Results show that, the difference between the empirical ones and the manually calculated numerical results increases as the stiffness increases.

The reason for that can be stated as, the manual drawing of the slopes become more difficult as the normal stress-normal closure graph becomes asymptotic. The increasing trend of the differences towards the maximum closure point is because of this reason. However, the results before the asymptote value show little difference. So the normal closure behaviour of the model can be considered as acceptable.

4.4 Shear Behaviour of the Discontinuity Model

Experimental studies of Bandis et al. (1983) showed that discontinuity shear stress – shear displacement behaviour mostly shows a non-linear behaviour in the pre-peak range, and the discontinuity shear stiffness that governs this non-linearity was empirically defined as given in Eq.(2.28). In this relation, as the shear stress increases, the discontinuity shear stiffness is reduced smoothly and the non-linearity is established. The peak shear stress was defined empirically in Eq.(2.5) in Chapter 2. From these relations, it can be seen that the parameters that govern the shear behaviour can be stated as;

- Normal stress, σ_n
- Residual friction angle, ϕ_r
- Joint roughness coefficient, JRC
- Joint compressive strength, JCS

In the verification procedure, a similar way as the normal deformation behaviour was followed. Every effective parameter was changed, and compared to the results obtained from empirical expressions. The corresponding differences were calculated.

First, the effect of normal stress acting on the discontinuity face was examined. Peak shear strength and residual shear strength values were determined and the differences were calculated.

Second, the effect of JRC was studied in the same way and the shear strength values were found and compared with the results obtained from empirical expressions and the differences were calculated again.

Following that, the effect of JCS was studied and the same critical values were determined with the resulting differences.

Finally, the shear stiffness values obtained from numerical model were compared to the values obtained from empirical expressions and the differences were evaluated.

In the modelling section, the same direct shear test model, which was presented in Figure 4.1, was used. The interest was given to the shear behaviour of the discontinuity, so the normal stress was applied as a boundary condition with a constant value. The shear stress on the discontinuity was generated by applying a constant velocity to the upper block in the shear direction, and the shear stress along the discontinuity was monitored.

4.4.1 Shear strength behaviour of the model

The shear strength values were determined under the effect of different normal stress levels and residual friction angles, JCS and JRC parameters. The same block properties were used in the analyses as described in Table 4.1.

Effect of normal stress on shear strength

The most important factor in the shear strength of a rock discontinuity is the magnitude of the normal stress acting across the discontinuity. In the Barton-Bandis shear strength failure criterion, it affects the shear strength as a linear factor.

For the verification of the normal stress effect, the direct shear model was tested under different normal stress levels, and the peak shear stress values were compared with the empirical results. The differences between the results were determined. In the analyses, joint roughness coefficient was set to 8, joint wall compressive strength was set to 100 MPa, residual friction angle was set to 20° and uniaxial compressive strength was set to 150 MPa.

Figure 4.7 shows the relation between peak shear strength values of numerical and empirical results. Figure 4.8 illustrates the graphs of numerical peak shear strength and empirical peak shear strength values vs normal stress. Table 4.6 gives the results of the analyses. Figure 4.9 presents the plot of shear stress – shear displacement of the model with normal stress level of 2 MPa. The rest of the graphs are given in Appendix B.

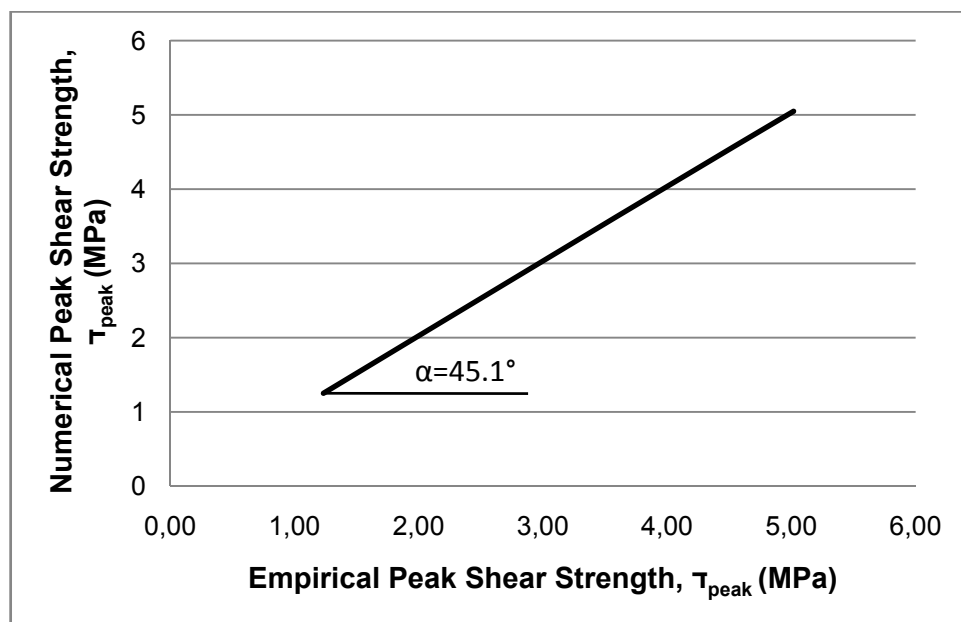


Figure 4.7 Graph of peak shear strength of empiric results vs numerical results under different normal stress levels

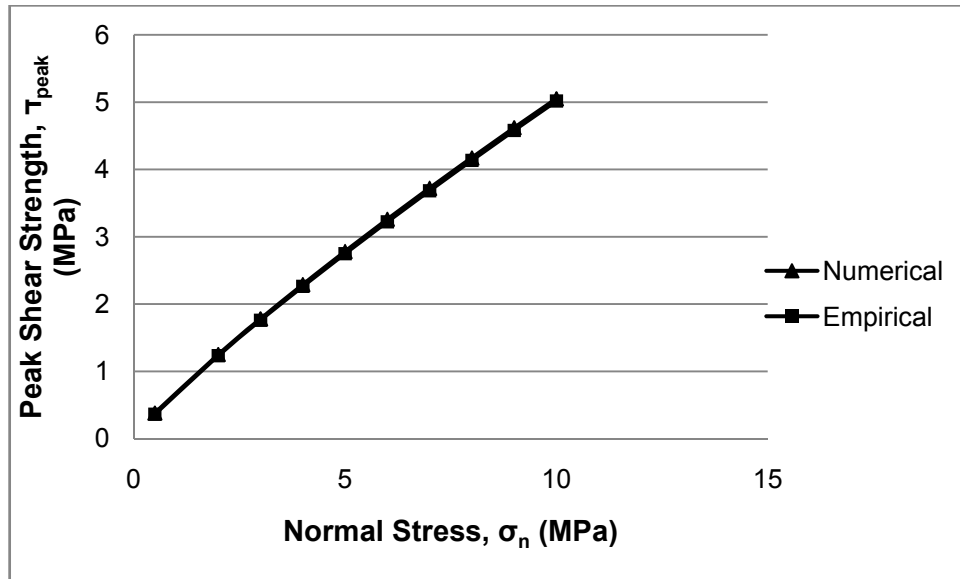


Figure 4.8 Graph of normal stress vs peak shear strength

Table 4.6 Results of peak shear strength analyses under different normal stresses (σ_n) values ($\phi_r = 20^\circ$, $\sigma_c = 150$ MPa, $JRC_o=8$ and $JCS_o=100$ MPa)

σ_n (MPa)	τ_{peak} (empirical) (MPa)	τ_{peak} (numerical) (MPa)	Difference (%)
0.5	0.36	0.38	5.26
2	1.23	1.25	1.63
3	1.76	1.78	1.14
4	2.26	2.29	1.33
5	2.75	2.78	1.09
6	3.22	3.26	1.24
7	3.68	3.72	1.09
8	4.14	4.17	0.73
9	4.58	4.62	0.87
10	5.02	5.05	0.60
		Average	1.50

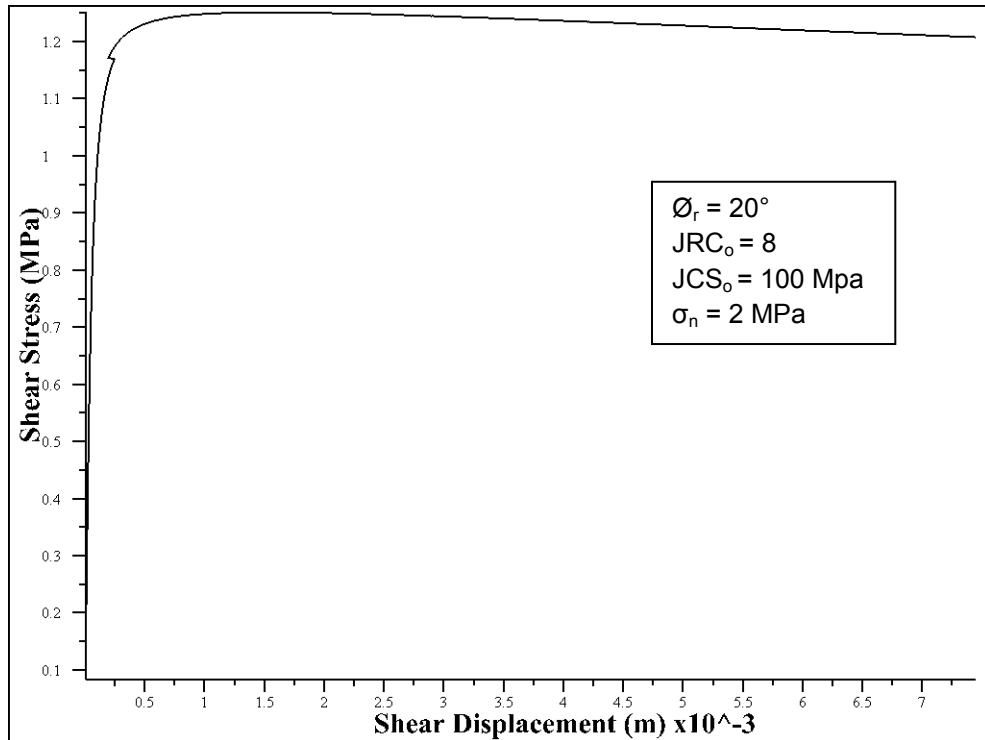


Figure 4.9 Graph of shear stress – shear displacement ($\phi_r = 20^\circ$, $\sigma_n = 2$ MPa, $JRC_o=8$ and $JCS_o=100$ MPa)

From Figure 4.7, the relation between the numerical and empirical peak shear strength values under different normal stresses can be found by finding the angle of the linear plot, α . The angle of the line can be found using the data in Table 4.6 as;

$$\alpha = \tan^{-1} \frac{(5.05 - 0.38)}{(5.02 - 0.36)} = 45.1^\circ$$

It can be concluded that, the numerical response of the program is slightly different from the empirical model, which can be considered as acceptable with an average difference of 1.50 %. The effect of normal stress on the discontinuity face was verified with the empirical results with the numerical model. Also the model shows consistency with the empirical results when normal stress acting on the discontinuity changes.

Effect of joint roughness coefficient (JRC) on shear strength

Joint roughness has a significant effect on the shear strength of a discontinuity. Not only it affects the shear strength, but also the joint roughness controls the post peak behaviour as it mobilizes after peak value and the roughness is completely destroyed as explained in Section 2.3.7.

In this part of the verification, the other parameters except the lab scale joint roughness coefficient (JRC_o) were kept constant. With the variation of JRC_o , different peak shear strength values were determined and compared to the empirical results.

JRC mobilizes and it also controls the behaviour of the discontinuity after peak strength is passed. Because of that reason, the residual strength values of the model were also studied.

Figure 4.10 shows the relation between the peak shear strength values of numerical results and empirical results with a joint wall compressive strength of 100 MPa, residual friction angle of 20° and under a normal stress of 5 MPa with uniaxial compressive strength of 150 MPa. Figure 4.11 presents the graphs of numerical peak shear strength and empirical peak shear strength values vs lab scale joint roughness coefficient (JRC_o). Table 4.7 presents the corresponding data.

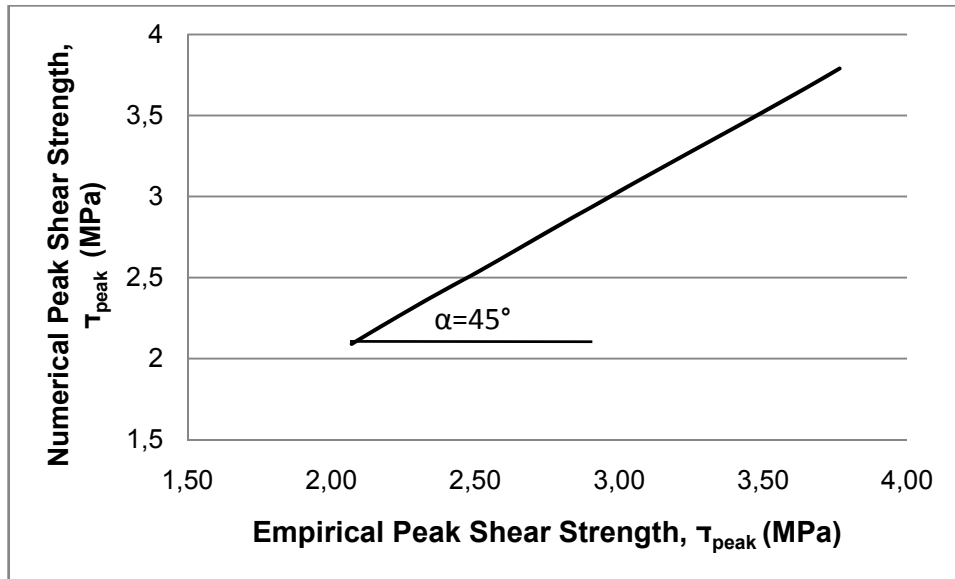


Figure 4.10 Graph of peak shear strength (τ_{peak}) of empirical results vs numerical results with different joint roughness coefficients (JRC_o)

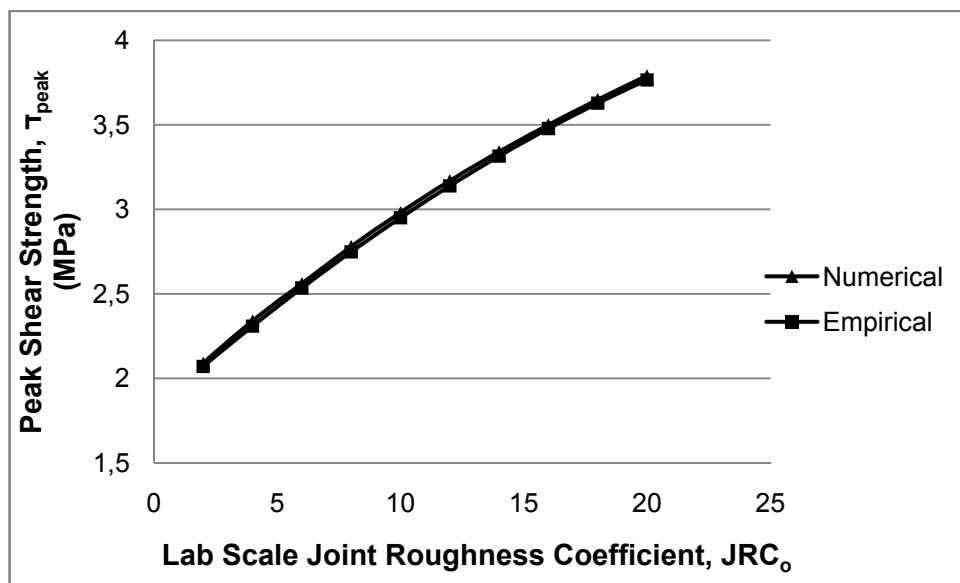


Figure 4.11 Graph of lab scale joint roughness coefficient vs peak shear strength

Table 4.7 Results of peak shear strength (τ_{peak}) analyses under different joint roughness coefficients (JRC) values ($\theta_r = 20^\circ$, $\sigma_c = 150$ MPa, $\sigma_n = 5$ MPa and $JCS_o = 100$ MPa)

JRC_o	τ_{peak} (empirical) (MPa)	τ_{peak} (numerical) (MPa)	Difference (%)
2	2.07	2.09	0.97
4	2.31	2.34	1.30
6	2.53	2.56	1.19
8	2.75	2.78	1.09
10	2.95	2.98	1.02
12	3.14	3.17	0.96
14	3.31	3.34	0.91
16	3.48	3.5	0.58
18	3.63	3.65	0.55
20	3.77	3.79	0.53
		Average	0.91

The shear stress-shear displacement plot of the case with $JRC_o = 8$ is given in Figure 4.12. Graphs of other cases are given in Appendix C.

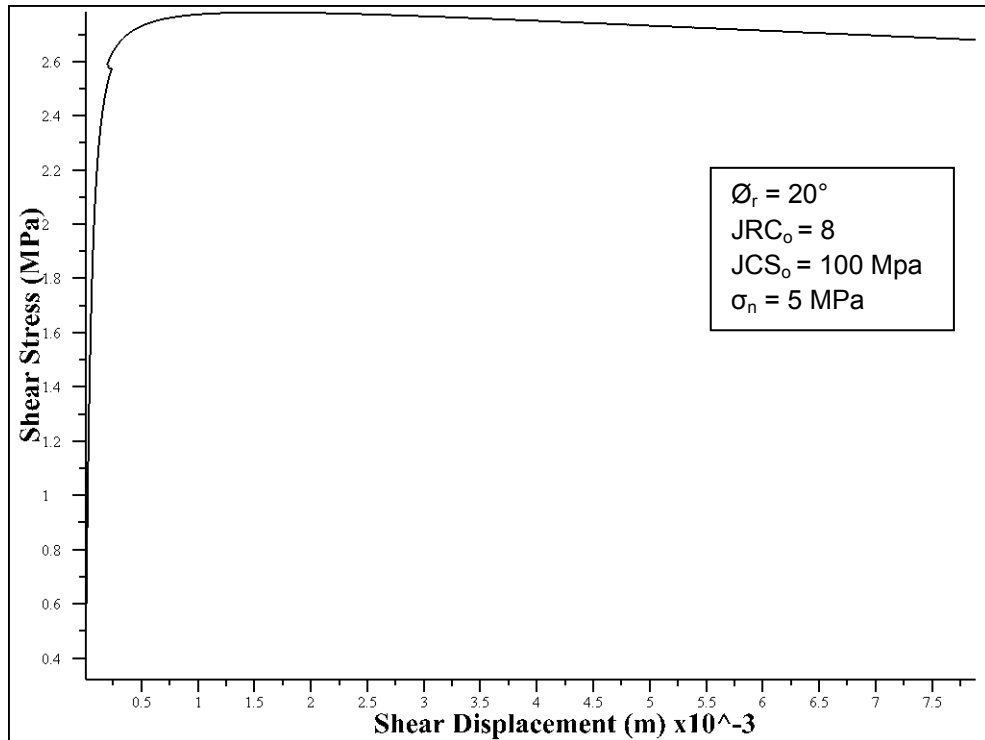


Figure 4.12 Graph of shear stress – shear displacement ($\phi_r = 20^\circ$, $\sigma_c = 150 \text{ MPa}$, $\sigma_n = 5 \text{ MPa}$ and $JCS_o = 100 \text{ MPa}$)

The relation between the numerical and empirical peak shear strength values under different lab scale joint roughness coefficients can be found by finding the angle of the linear plot, α in Figure 4.10. The angle of the line can be found using the data in Table 4.6 as;

$$\alpha = \tan^{-1} \frac{(3.79 - 2.09)}{(3.77 - 2.07)} = 45^\circ$$

The results show that, the numerical results are very close the empirical ones, which can be considered as acceptable with an average difference of less than 1 % and can be considered as acceptable. The effect of joint roughness coefficient on the discontinuity face was verified with the empirical results with the numerical model. The response of the program is also consistent with the empirical results when joint roughness coefficient changes.

As mentioned in Section 2.3.7, the joint roughness is mobilized as the peak shear strength is reached. As the shear displacement continues the joint roughness approaches to zero. From the Barton-Bandis shear strength criterion relation Eq.(2.5), when the joint roughness coefficient becomes zero the shear stress becomes;

$$\tau_r = \sigma_n \tan \phi_r$$

According to the theory of the mobilization of the roughness, the joint roughness coefficient would become totally worn out (zero) at the $\left(\frac{\delta}{\delta_{peak}}\right)$ ratio of 100. So the direct shear test model was needed to be modified. The lower block length was increased to 0.4 meters.

The verification of this behaviour is done on a model with a residual friction angle of 10° , JRC of 8, JCS of 100 MPa and a uniaxial compressive strength of 150 MPa and the normal force was set to 5 MPa. Figure 4.13 shows the plot of shear stress vs shear displacement plot and Table 4.7 gives the results of it.

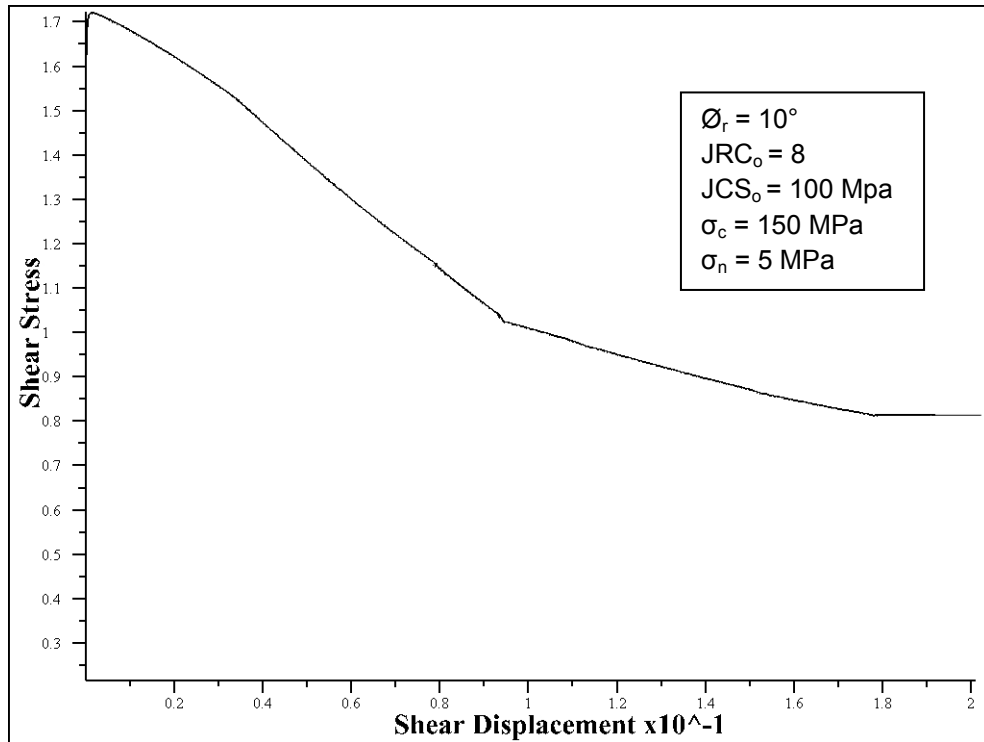


Figure 4.13 Graph of shear stress – shear displacement (ϕ_r , $\sigma_c = 150$ MPa, $JRC_0=8$ and $JCS_0=100$ MPa, $\sigma_n = 5$ MPa)

Table 4.7 Results of residual shear strength analyses ($\phi_r = 10^\circ$, $\sigma_c = 150$ MPa, $\sigma_n=5$ MPa and $JCS_0=100$ MPa)

T_{residual} (empirical) (MPa)	T_{residual} (numerical) (MPa)	Difference (%)
0.88	0.82	6.82

The result of residual shear strength test was resulted with a difference of 6.82 %. The reason for this difference, which is higher than the average difference in peak shear strength, was considered to be because of the model geometry. As the lower block size was changed and this resulted with a mesh problem. However, the difference can still be considered as acceptable.

Effect of joint wall compressive strength (JCS) on shear strength

The effect of JCS parameter on the normal stress response was verified in the normal deformation part. For the shear deformation verification, the same procedure was followed. Model runs were conducted with different values of lab scale joint wall compressive strength (JCS_o) values and the relation between the empirical and numerical values were obtained. In the analyses the joint roughness coefficient was set to 8, residual friction angle was set to 20° and the normal stress was set to 5 MPa. Figure 4.14 shows the plot of empirical results vs numerical results. Figure 4.15 presents the graphs of numerical peak shear strength and empirical peak shear strength values vs lab scale joint roughness coefficient (JCS_o) and Table 4.8 gives the corresponding data.

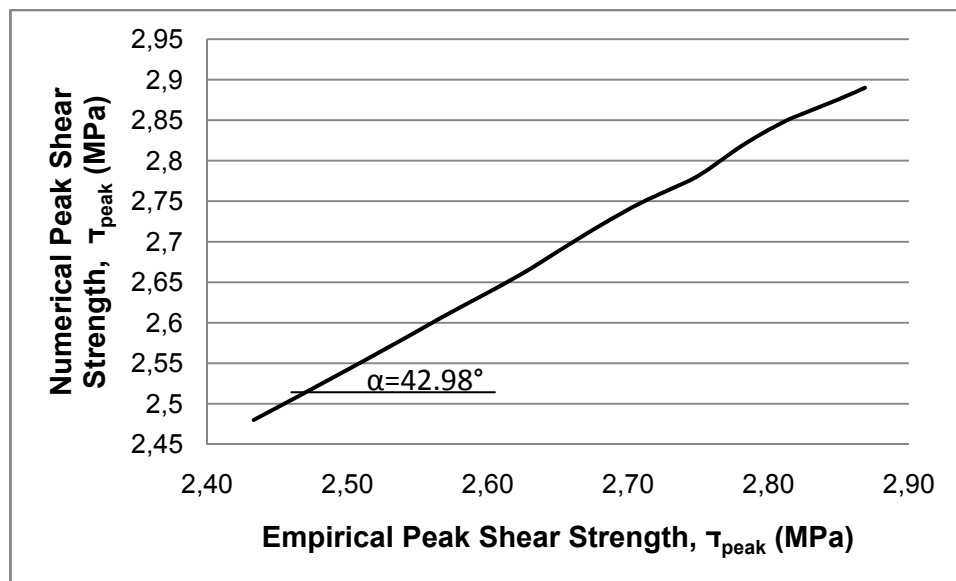


Figure 4.14 Graph of peak shear strength of empiric results vs numerical results with different joint compressive strengths (JCS_o)

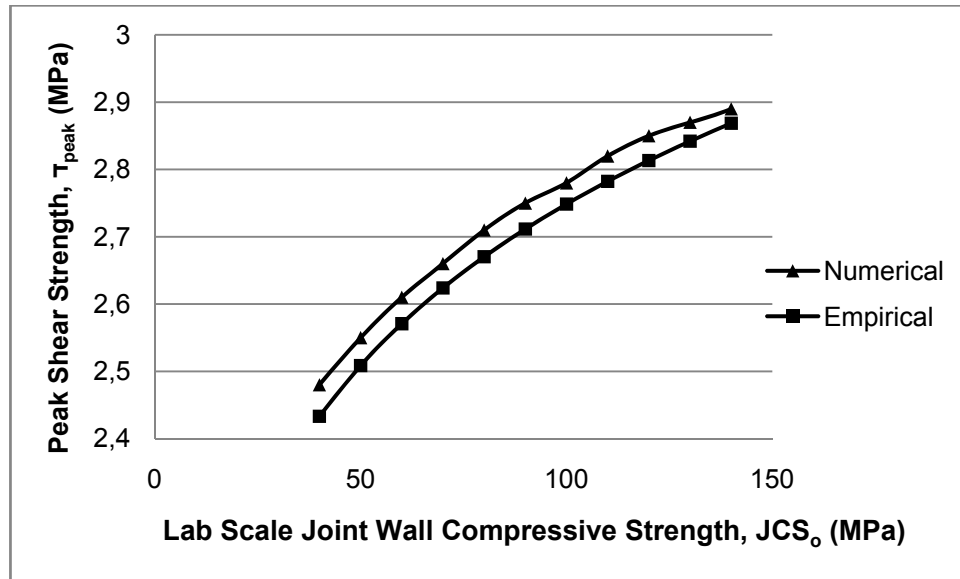


Figure 4.15 Graph of lab scale joint wall compressive strength vs peak shear strength

Table 4.9 Results of peak shear strength (τ_{peak}) analyses under different joint wall compressive strength (JCS_o) values ($\phi_r = 20^\circ$, $\sigma_c = 150$ MPa, JRC_o=8 and $\sigma_n=5$ MPa)

JCS _o (MPa)	τ_{peak} (empirical) (MPa)	τ_{peak} (numerical) (MPa)	Difference (%)
40	2.43	2.48	2.06
50	2.51	2.55	1.59
60	2.57	2.61	1.56
70	2.62	2.66	1.53
80	2.67	2.71	1.50
90	2.71	2.75	1.48
100	2.75	2.78	1.09
110	2.78	2.82	1.44
120	2.81	2.85	1.42
130	2.84	2.87	1.06
140	2.87	2.89	0.70
		Average	1.41

The shear stress-shear displacement plot of the case with $JCS_o = 80$ MPa is given in Figure 4.16. Graphs of other cases are given in Appendix C.

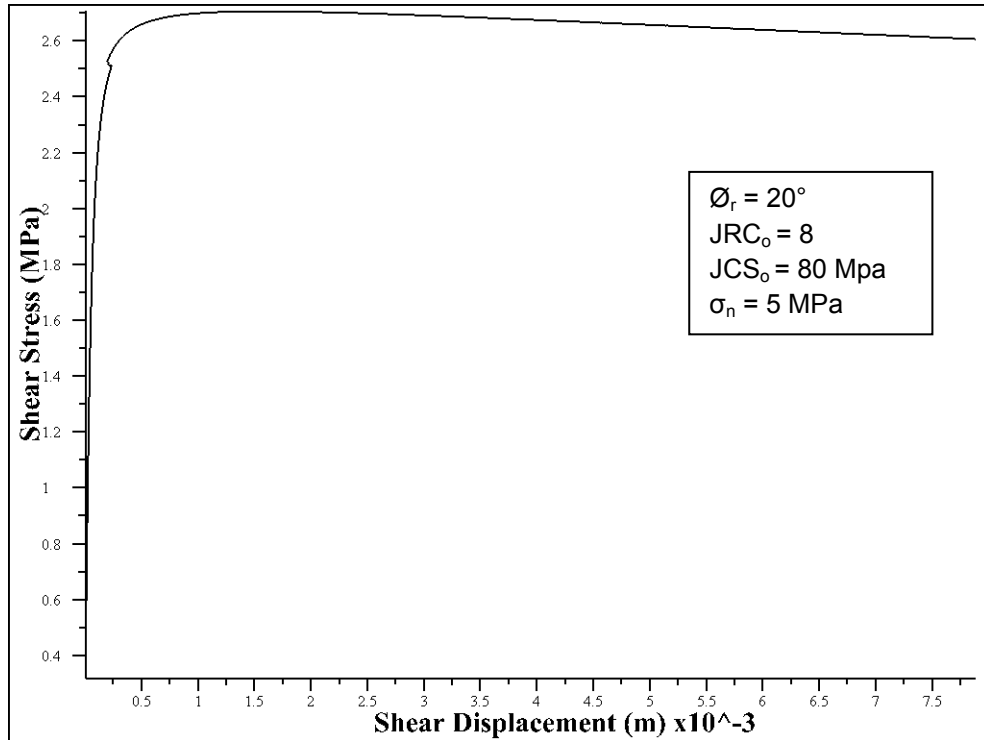


Figure 4.16 Graph of shear stress – shear displacement

The relation between the numerical and empirical peak shear strength values under different lab scale joint roughness coefficients can be found by finding the angle of the linear plot, α in Figure 4.10. The angle of the line can be found using the data in Table 4.6 as;

$$\alpha = \tan^{-1} \frac{(2.89-2.48)}{(2.87-2.43)} = 42.98^\circ$$

The effect of change in joint wall compressive strength was verified with the numerical model with an average difference of 1.41 %. This difference can be considered as acceptable. This small difference can be considered as negligible and in the limits of numerical response of the program. Also

the response of the program with different joint wall compressive strength values is consistent with the empirical results. The angle in the plot in Figure 4.14 is approximately 43°.

Effect of residual friction angle on shear strength

Another factor that has major effect in shear strength of discontinuities is the residual friction angle. The verification of the model was done with different residual friction angles. The joint roughness coefficient was set to 8, joint wall compressive strength was set to 100 MPa and the normal stress was set to 5 MPa. Figure 4.17 shows the relation between the empirical and numerical values and Table 4.10 shows the corresponding data.

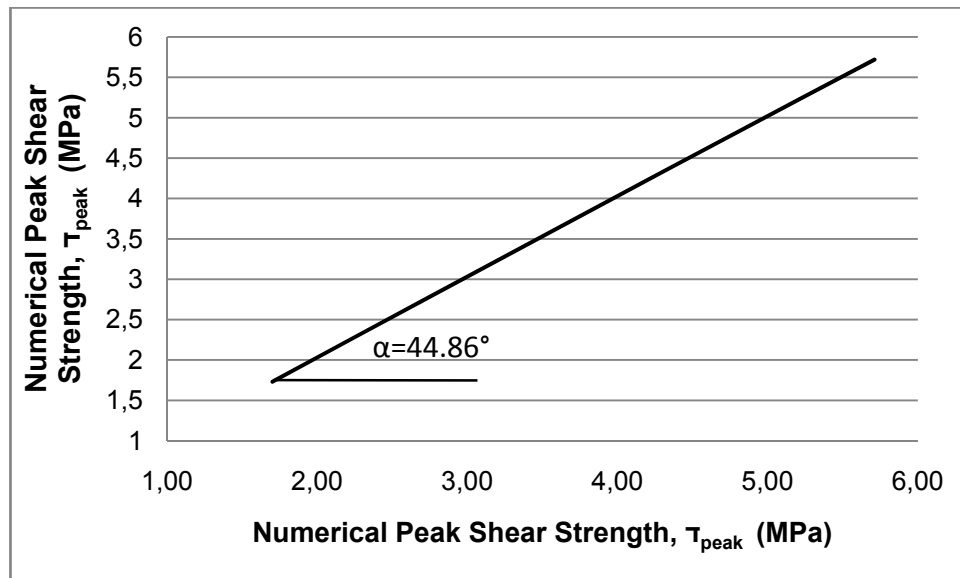


Figure 4.17 Graph of maximum shear stress of empiric results vs numerical results with different discontinuity residual friction angles (ϕ_r)

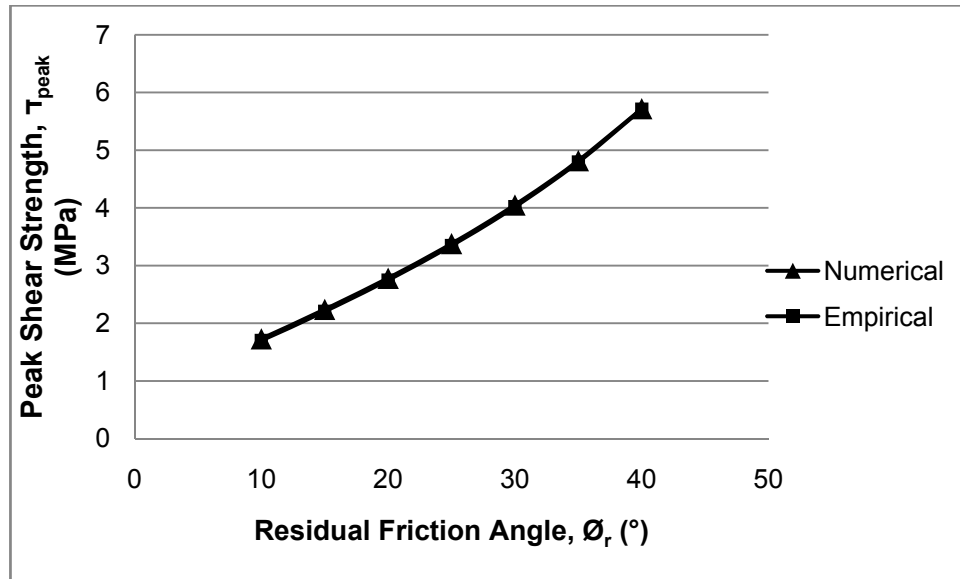


Figure 4.18 Graph of residual friction angle vs peak shear strength

Table 4.10 Results of peak shear strength (τ_{peak}) analyses under different residual friction angle (\emptyset_r) values ($\sigma_c = 150$ MPa, $JRC_o=8$ and $JCS_o=100$ MPa)

\emptyset_r (°)	τ_{peak} (empirical) (MPa)	τ_{peak} (numerical) (MPa)	Difference (%)
10	1.70	1.73	1.77
15	2.21	2.24	1.36
20	2.75	2.78	1.09
25	3.35	3.38	0.90
30	4.02	4.05	0.75
35	4.79	4.82	0.63
40	5.71	5.72	0.18
		Average	0.95

The shear stress-shear displacement plot of the case with $\emptyset_r = 25^\circ$ is given in Figure 4.19. Graphs of other cases are given in Appendix C.

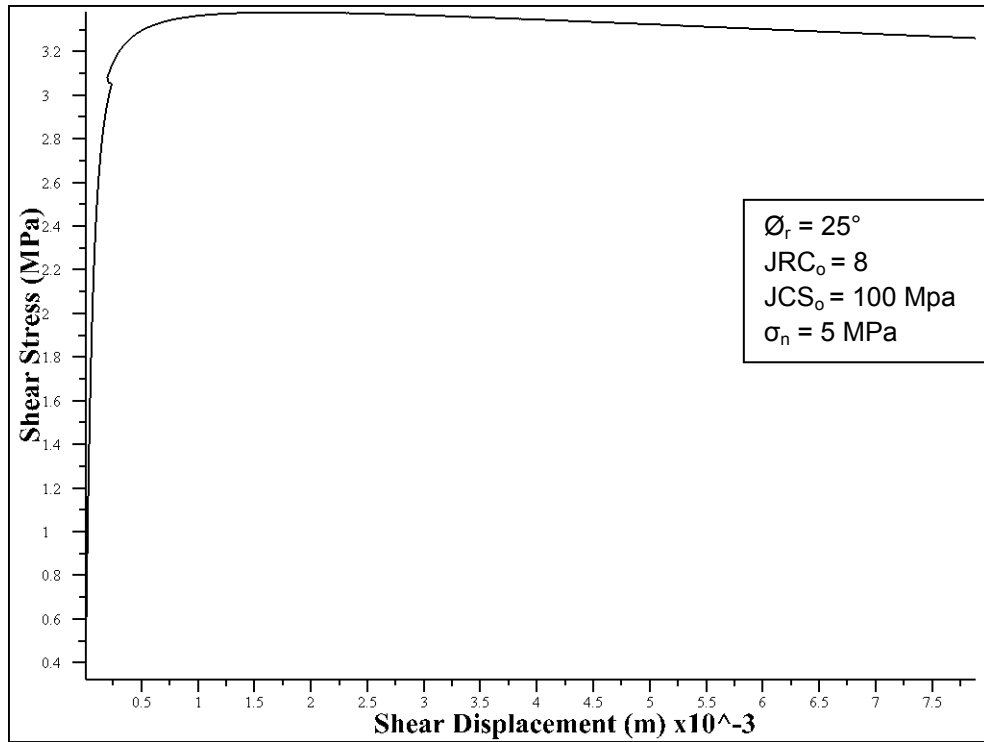


Figure 4.19 Graph of shear stress – shear displacement ($\phi_r = 25^\circ$, $\sigma_c = 150 \text{ MPa}$, $JRC_o=8$ and $JCS_o=100 \text{ MPa}$)

The angle α in Figure .17, which shows the relation between the numerical and empirical peak shear strength values with different residual friction angles, can be found by using the data in Table 4.6 as;

$$\alpha = \tan^{-1} \frac{(5.72-1.73)}{(5.71-1.70)} = 44.86^\circ$$

The effect of change in joint wall compressive strength was verified with the numerical model with an average difference of 0.96 %. This difference can be considered as acceptable. This small difference can be considered as negligible and in the limits of numerical response of the program. Also the numerical response of the program shows consistency with the empirical results as the residual friction angle changes as can be seen from the angle of the plot in Figure 4.17.

4.4.2 Dilation

As mentioned in Section 2.3.7, mobilization of roughness causes the dilation angle to mobilize. Therefore the maximum angle of dilation should occur as the peak shear strength is reached. The verification of this behaviour was verified with a model with joint roughness coefficient of 12, joint wall compressive strength of 100 MPa, residual friction angle of 20° , a uniaxial compressive strength of 150 MPa and under a normal stress of 5 MPa. Figure 4.20 illustrates the dilatational behaviour of the test. From the figure, it can be seen that the peak dilation angle coincides with the peak shear displacement.

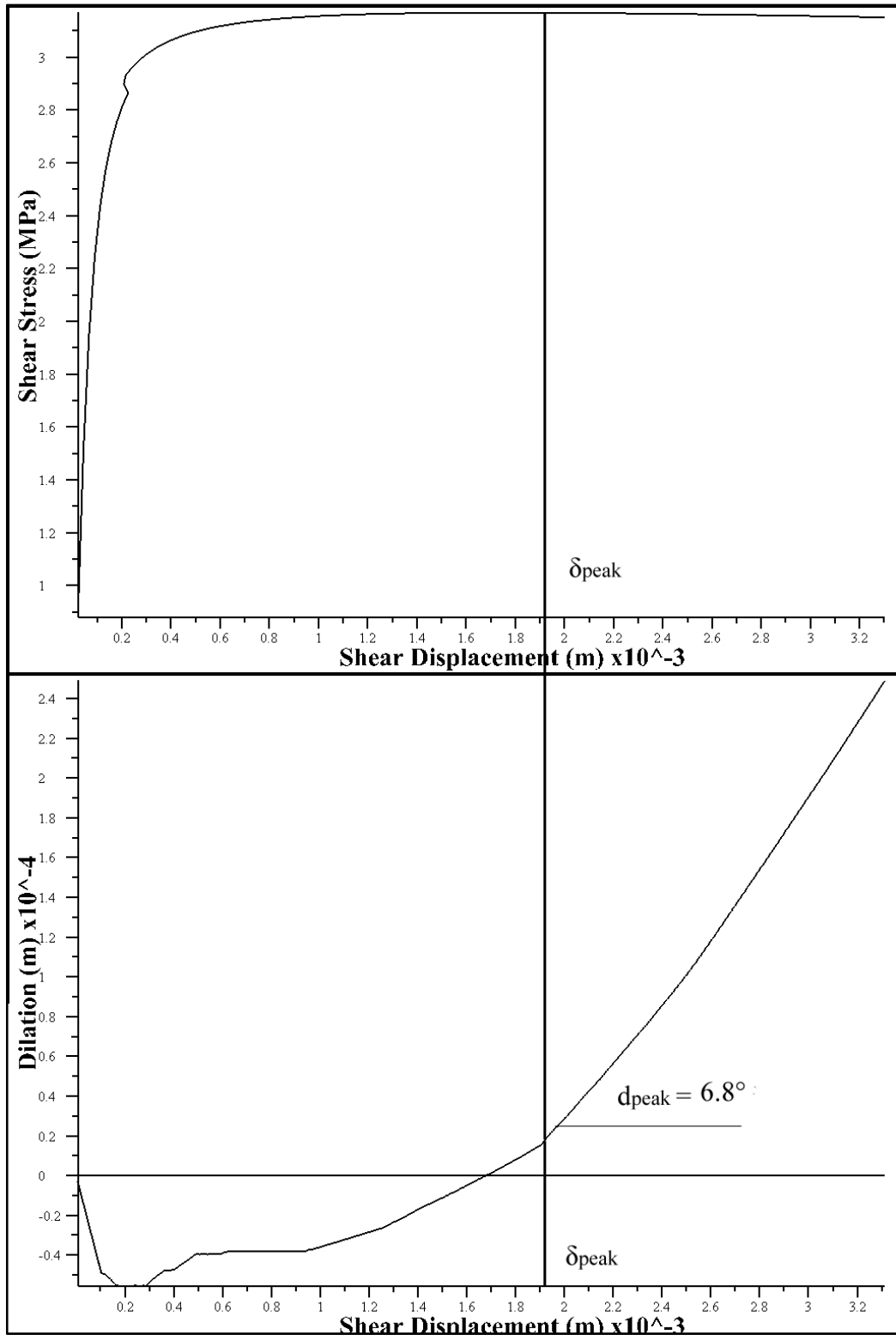


Figure 4.20 Graph of shear displacement vs dilation and shear stress vs shear displacement ($\phi_r = 20^\circ$, $\sigma_c = 150$ MPa, $JRC_0=12$, $JCS_0=100$ MPa and $\sigma_n = 5$ MPa)

From empirical relation for calculating dilation angle Eq.(2.20) was used and from this relation peak dilation angle can be found as;

$$d_{\text{peak}} = 1/2 \times JRC_{\text{npeak}} \times \log_{10} \left(\frac{JCS}{\sigma_n} \right)$$

By using Eq.(2.14) scale corrected joint roughness coefficient (JRC_n) becomes;

$$JRC_n = JRC_o \times \left(\frac{L_n}{L_o} \right)^{-0.02JRC_o}$$

$$JRC_n = 12 \times \left(\frac{0.2}{0.1} \right)^{-0.02 \times 12}$$

$$JRC_n = 10.2$$

Similarly by using Eq.(2.13) joint wall compressive strength becomes;

$$JCS_n = JCS_o \times \left(\frac{L_n}{L_o} \right)^{-0.03JRC_o}$$

$$JCS_n = 100 \times \left(\frac{0.2}{0.1} \right)^{-0.03 \times 12}$$

$$JCS_n = 77.92 \text{ MPa}$$

Then Eq. (2.20) becomes;

$$d_{\text{peak}} = 1/2 \times 10.2 \times \log_{10} \left(\frac{JCS}{\sigma_n} \right)$$

$$d_{\text{peak}} = 6.1^\circ$$

From the results the difference between the results was calculated as 11.5 %. Considering the numerical response, mesh formation and calculation of dilation angle from the plot, the difference can be considered as acceptable. The dilation vs shear displacement graphs of models with joint roughness coefficients of 16 is given in Appendix D.

4.4.3 Discontinuity shear stiffness

It was mentioned in Section 2.3.8 that discontinuities under shear show a non-linear load-deformation behaviour in the pre-peak range. Hyperbolic functions were frequently used for expressing this behaviour empirically. In this section it is intended to compare the results of shear stiffness values to results obtained from empirical expressions. For the verification Eq.(2.27) was used to calculate shear stiffness empirically. Numerical results were calculated by drawing tangent lines to the shear stress shear displacement curves. The results were plotted and the differences between them were found. In the numerical analyses, joint roughness coefficient was set to 8, joint wall compressive strength was set to 100 MPa, uniaxial compressive strength of the rock was set to 150 MPa and the residual friction angle was set to 20°. The shear stiffness vs shear displacement plot is given in Figure 4.21 and Table 4.11 gives the data of the analyses.

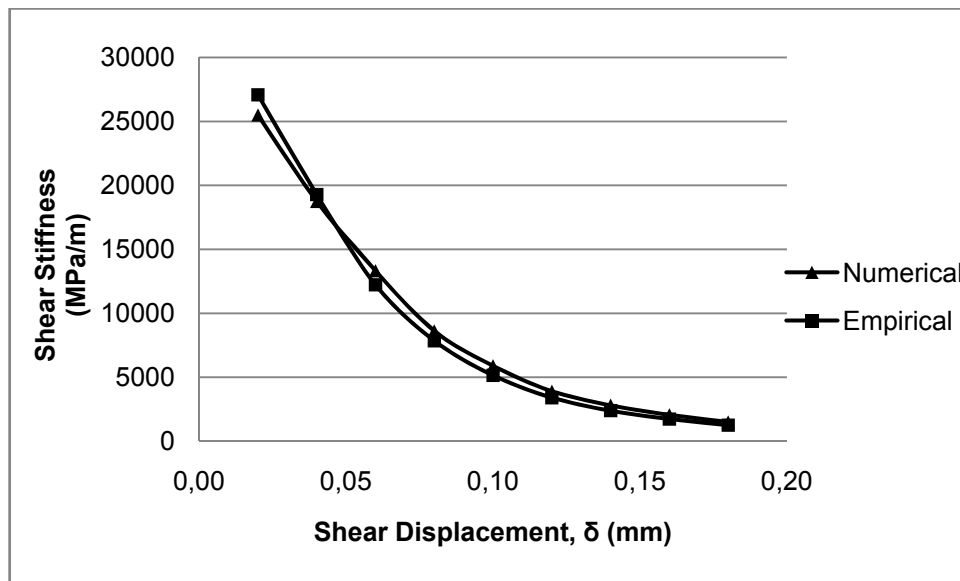


Figure 4.21 Graph of shear stiffness (K_s) vs shear displacement

Table 4.11 Empirical and numerical results of shear stiffness (K_s)

Shear displacement ΔU (mm)	Shear Stiffness (empirical) (MPa/m)	Shear Stiffness (numerical) (MPa/m)	Difference %
0.02	27078	25500	5.83
0.04	19291	18750	2.80
0.06	12234	13333	8.98
0.08	7862	8625	9.71
0.10	5160	5900	14.34
0.12	3406	3910	14.80
0.14	2399	2817	17.42
0.16	1741	2063	18.50
0.18	1264	1510	19.46
		Average	12.43

The results show that as the shear stress is approaching to its peak value the error percentage increases. The possible reason for that can be stated as the shear stiffness values converge to zero as peak shear stress is approaching. And taking slopes from these points become difficult so the possibility of drawing errors increases.

4.5 Results and Discussion

From the detailed analyses carried out, it can be concluded that the implementation of Barton-Bandis approach in three dimensional distinct element code (3DEC) was successfully implemented.

In all direct shear test model analyses, the joint normal and shear displacements and discontinuity normal and shear stress values were calculated by a FISH function which takes the average of the values in each node.

The percentage difference of the shear strength values, which were obtained by model runs with different discontinuity properties, were very low (approximately 1%) and the reason for that may be explained by the numerical response of the software.

The results of the normal deformation behaviour of the discontinuity were very close to the empirical results. The percentage difference was approximately 5. As mentioned above, the values were obtained by taking average of the four nodes. Probably a finer mesh can give closer results to the empirical results, but this occasion has a deficiency of slowing down the analyses and limiting down the total step number that can be reached in an efficient way. Despite of this, the results can be considered as acceptable.

The difference in verification of the normal and shear stiffness values of the discontinuities seemed to be increasing because of the reason that the results of numerical analyses were obtained by calculating slopes manually. The stiffness values which were close to the asymptotic values, drawing slopes manually gets difficult. A very small deviation can result with a great difference. Because of this reason, the results can be considered as acceptable.

CHAPTER 5

APPLICATION OF THE PROPOSED NUMERICAL MODEL FOR FIELD SCALE SLOPE PROBLEMS

5.1 Introduction

In this chapter, results of the application of the proposed Barton-Bandis method into large scale slope models are presented, some of which are real case studies. First, the method was applied to a basic slope model. A methodology for converting Mohr-Coulomb parameters to Barton-Bandis parameters was developed. The basic slope model was used to check the reliability of that methodology. Also the effect of discontinuity surface properties on the shear strength of the discontinuity, which is both in equilibrium and sliding, were examined. Following that, some previously failed open pit mine slopes are verified.

In the first part, a basic slope model with plane failure geometry was modelled. With this basic slope model, Mohr-Coulomb slip model and Barton-Bandis model was compared for the equilibrium condition. After that Barton-Bandis model was examined for the failure condition and the effect of joint roughness on the sliding behaviour was examined.

Second part includes case studies from Orhaneli open pit lignite mine which belongs to Bursa Lignite Establishments (BLİ) and Çan Lignites Establishments (ÇLİ) of Turkish Coal Enterprises (TKİ) were used. In these studies, Karpuz et al. (2006) studied the reasons of Gümüşpınar landslide (A-6 panel) and Karpuz et al. (2007) studied the reasons of Dikmentepe (A-

5 panel) landslide in the mine. The former failure was governed by two intersecting faults from sides and a weak contact layer from the bottom. In Dikmentepe landslide, a similar mechanism was also seen in the field but the major difference is that the side faults were not intersecting each other. The south border of the landslide was formed by unconformity zone that was formed by the neogene basin border formations.

Karpuz et al. (2007) studied the stability of the slopes of the western panels in Çan open pit mine. These panels were planned to be on production in year 2009. Two main faults which have unfavourable dips and dip directions exist in the field. Minimum distance between the crest of the slope and the faults and the stripping plans were examined in this study. The material properties were obtained from back analyses studies of Karpuz et al.(2005). All three cases were analyzed by Barton-Bandis criterion and verified.

5.2 Basic Slope Model

A simple slope model with plane failure geometry was generated by 3DEC. A 70° dipping 50 m height slope was cut with a 25° dipping discontinuity plane as seen in Figure 5.1. The model was run with Mohr-Coulomb slip model and Barton-Bandis model, and the displacement on the slope crest (Point A) was monitored.

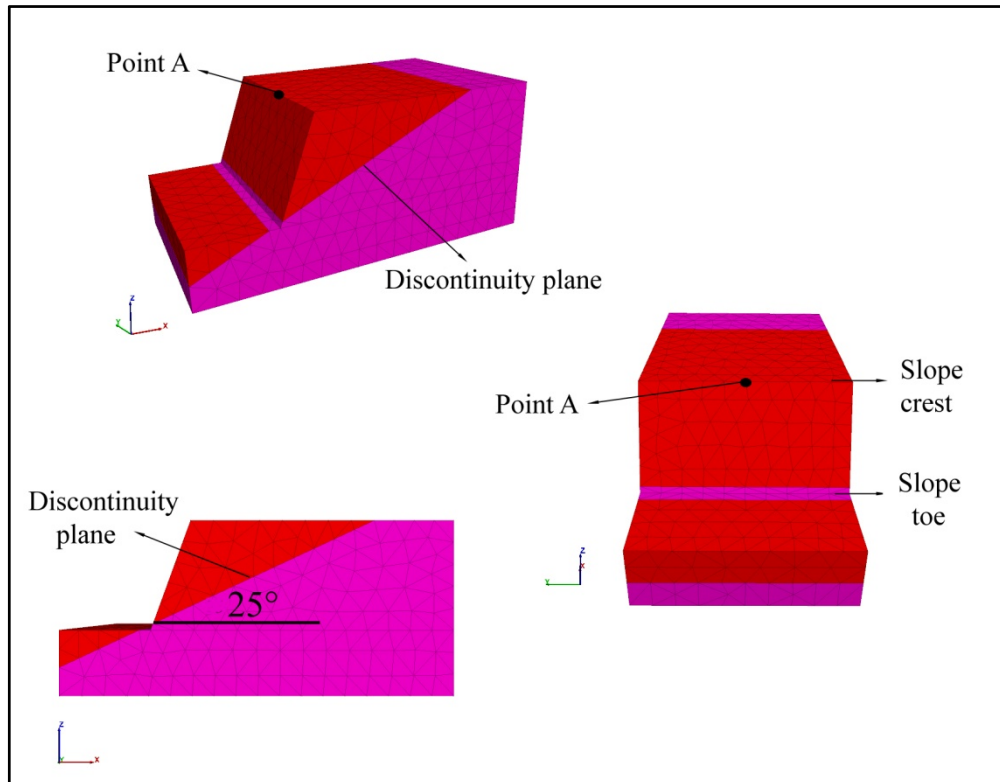


Figure 5.1 Geometry of basic slope model

Table 5.1 Material and discontinuity parameters of the basic slope model with Mohr-Coulomb slip criterion

Material	
Material density	2000 kg/m ³
Material bulk modulus	4 GPa
Material shear modulus	3 GPa
Material cohesion	5 MPa
Material internal friction angle	50°
Discontinuity	
Discontinuity normal stiffness	100 GPa/m
Discontinuity shear stiffness	100 GPa/m
Discontinuity friction angle	25°
Discontinuity cohesion	0

In order to run the model with Barton-Bandis discontinuity constitutive model, the relevant parameters (i.e. joint roughness coefficient, joint wall compressive strength and residual friction angle) should be determined. The residual friction angle of the discontinuity can be estimated approximately. In general the residual friction angles are between the 80-100 % of the peak friction angle. For the field scale joint roughness coefficient determination, the chart which was illustrated in Figure 2.12 can be used with the corresponding equation Eq.(2.11). The joint wall compressive strength of the faults in the field can be found by Schmidt hammer rebound tests or if the weathering at the discontinuity plane is known, an approximation from the uniaxial compressive strength of the intact rock can be used.

In a case of which the joint wall compressive strength parameter cannot be measured and, if the Mohr-Coulomb parameters cohesion and peak friction angle is known, the shear stresses from both criterions can be equated and the unknown parameter can be determined. For this procedure the maximum normal stress acting on the discontinuity plane should be determined because for both criterions the main parameter affecting the shear strength is the normal stress acting on the discontinuity plane. The maximum normal stress acting on the discontinuity wall can be calculated from the geometry of the slope and the discontinuity plane.

Calculation of the normal stress acting on the discontinuity plane is controlled by the gravitational force of the upper block. So the weight of the upper block must be calculated. Following that the discontinuity face area should be used to calculate the normal stress acting on it. The sectional view of the slope geometry is given in Figure 5.2.

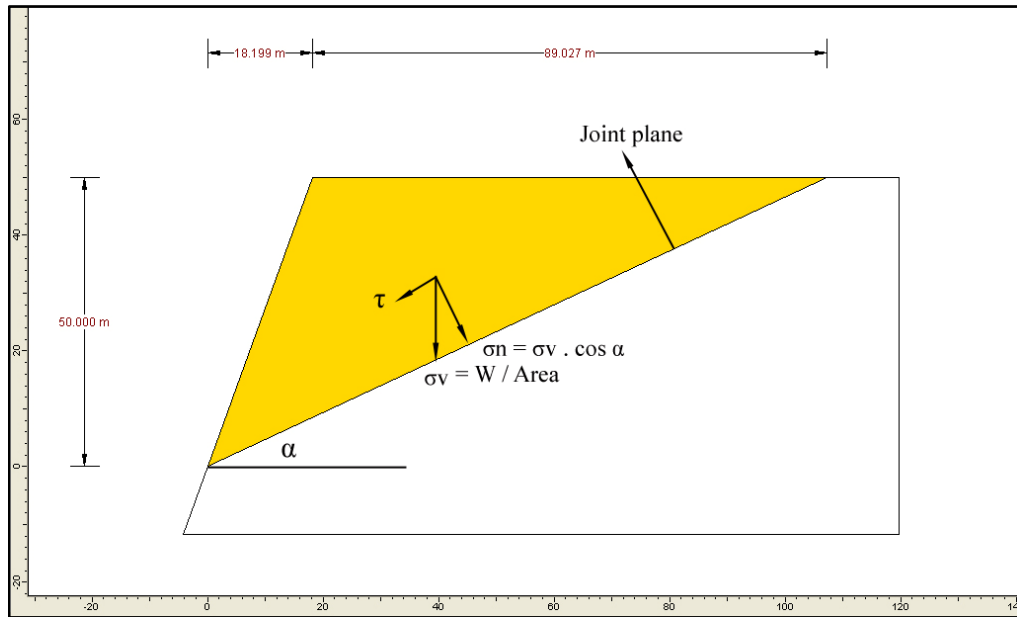


Figure 5.2 Sectional view of the basic slope geometry

The weight of the upper block is calculated as;

$$W = \text{Area}_{\text{section}} \times \gamma \times t \quad (5.1)$$

Where;

$\text{Area}_{\text{section}}$ = Cross sectional area of upper block,

γ = unit weight (kg/m^3)

t = thickness of the model

$$\text{Area}_{\text{section}} = \frac{b \times h}{2} = \frac{(18.199 + 89.027) \times 50}{2} = 2680.65 \text{ m}^2$$

Therefore;

$$W = 2680.65 \times 2000 \times 100 = 536130000 \text{ kg} = 5259435300 \text{ Newtons}$$

$$\text{Area}_{\text{discontinuity}} = 118 \times 100 = 11800 \text{ m}^2$$

$$\sigma_v = \frac{W}{\text{Area}_{\text{discontinuity}}} = 445714.86 \text{ Pa} = 0.45 \text{ MPa} \quad (5.2)$$

$$\sigma_n = \sigma_v \times \cos \alpha \quad (5.3)$$

Therefore;

$$\sigma_n = 0.45 \times \cos 25^\circ = 0.41 \text{ MPa}$$

After the normal stress acting on the discontinuity was determined, the shear stress acting on the discontinuity plane should be equal with the two methods;

$$\tau = c + \sigma_n \tan \phi = \sigma_n \tan \left(\phi_r + \text{JRC} \times \log_{10} \left(\frac{\text{JCS}}{\sigma_n} \right) \right) \quad (5.4)$$

For a cohesionless discontinuity Eq.(5.2) becomes;

$$\phi = \phi_r + \text{JRC} \times \log_{10} \left(\frac{\text{JCS}}{\sigma_n} \right)$$

Where;

ϕ_r is accepted as the 90 % of the peak friction angle that is approximately 22° ,

The discontinuity was assumed to be planar and the joint roughness coefficient was assumed to be 2.

So turning back to Eq.(5.3) and the joint wall compressive strength for the discontinuity plane is found as;

$$\phi = \phi_r + \text{JRC} \times \log_{10} \left(\frac{\text{JCS}}{\sigma_n} \right)$$

$$25 = 22 + 2 \times \log_{10} \left(\frac{\text{JCS}}{0.41} \right)$$

$$\text{JCS} = 12.97 \text{ MPa}$$

5.2.1 2-D verification of parameter determination

The basic slope model was also modelled in Slide program to check the parameters reliability. Slide program is capable of determining safety factors for both Mohr-Coulomb models and Barton-Bandis models. Slide program is a 2D limit equilibrium slope stability program for evaluating the stability of circular or non-circular failure surfaces in soil or rock slopes. the program do not have any discontinuity or interface options so the discontinuity plane was generated by a thin layer with discontinuity properties and a non-circular failure plane was passed along it for the analyses of a failure along it. The safety factors for Mohr-Coulomb and Barton-Bandis analyses are given in Figures 5.3 and 5.4 respectively.

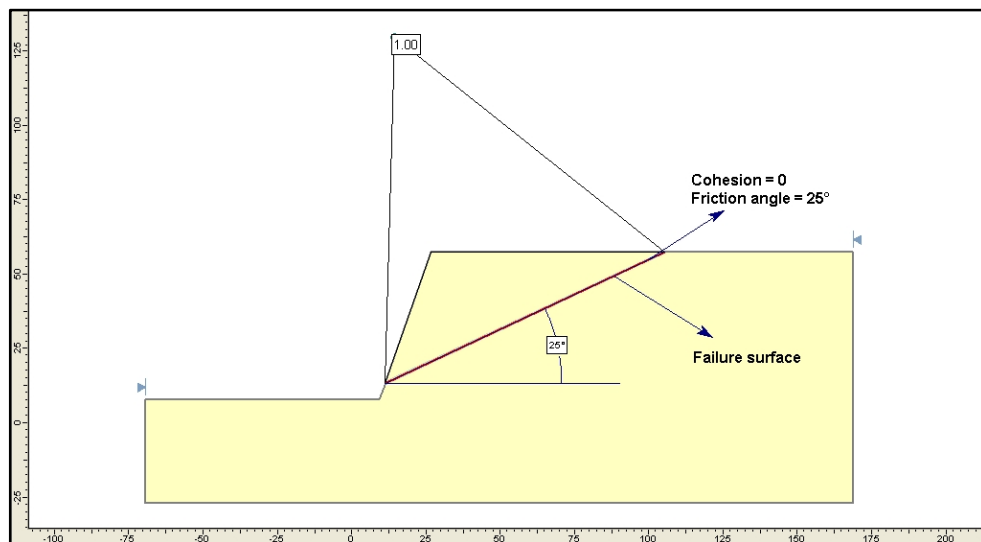


Figure 5.3 2-D Limit equilibrium factor of safety analyses with Mohr-Coulomb parameters

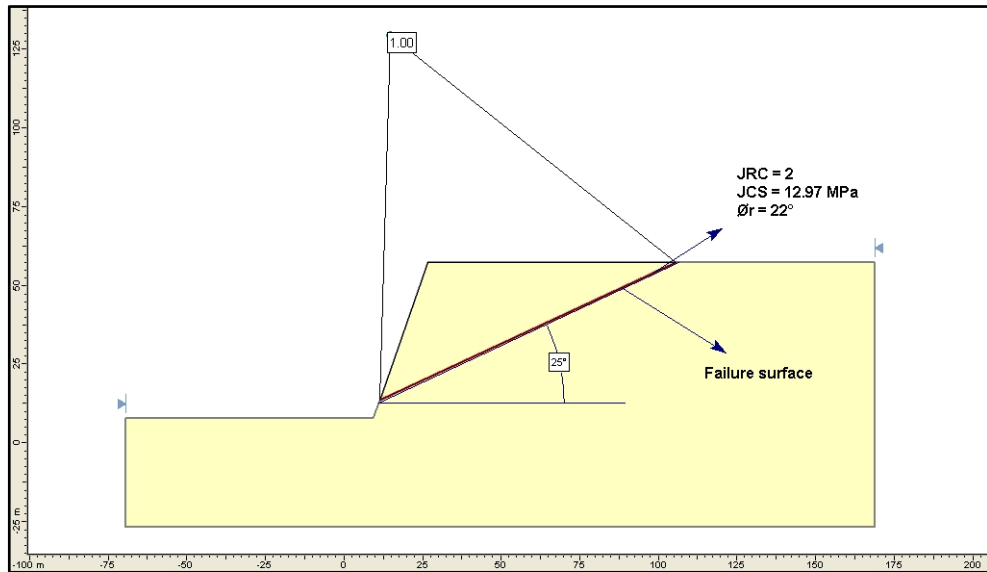


Figure 5.4 2-D Limit equilibrium factor of safety analyses with Barton-Bandis parameters

From the two dimensional safety factor analyses, it can be concluded that the methodology for determining Barton-Bandis joint wall compressive strength from existing Mohr-Coulomb parameters is accurate.

5.2.2 3-D verification of parameter determination

First the basic slope model was run with Mohr-Coulomb parameters with the equilibrium conditions (i.e. zero cohesion and friction angle is equal to discontinuity dip angle) that were verified with the two dimensional Slide analyses. Following that the basic slope model was run with Barton-Bandis model in 3DEC with the equilibrium conditions that were again verified with Slide analyses.

First the model was run with elastic model properties to set the insitu stresses. When the vertical displacement was stabilized and the unbalanced force had become zero the stresses were set and the model was ready to plastic analyses. The model was run with previously mentioned material and discontinuity parameters (Table 5.1). The

displacements were reset to zero before starting to plastic run. The shear displacement graphs of point A for the equilibrium state are given in Figure 5.5.

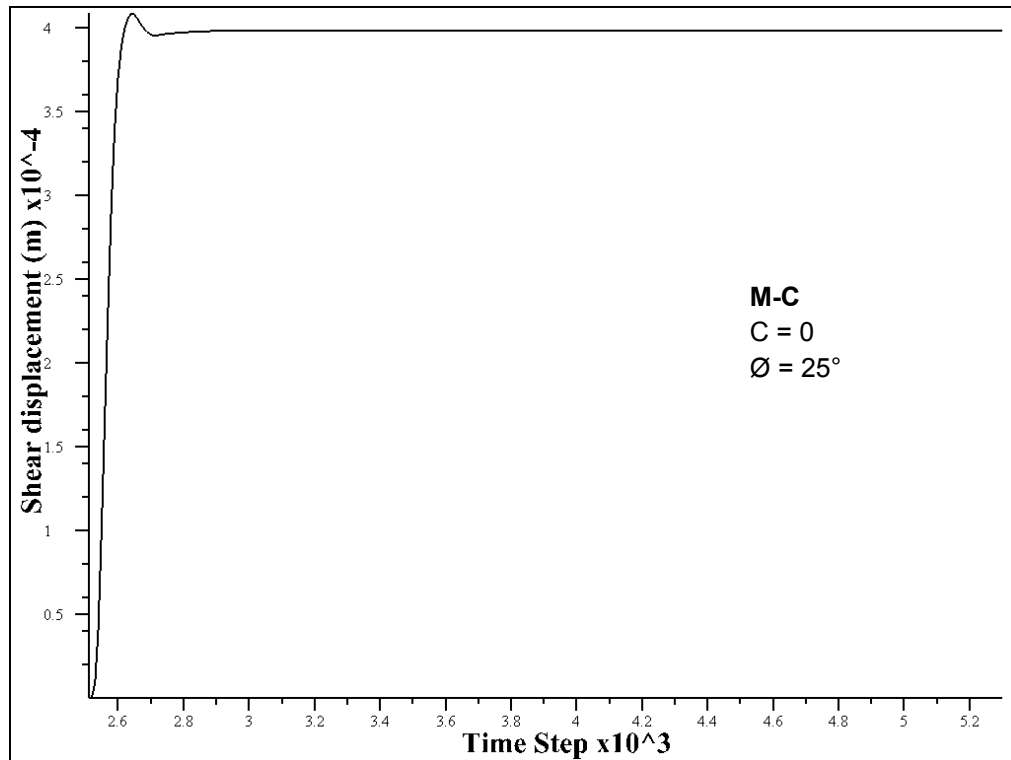


Figure 5.5 Shear displacement of point A with Mohr-Coulomb criterion
($c=0$, $\varnothing = 25^\circ$)

From the analyses with Mohr-Coulomb slip model, it can be seen that the slope stays in equilibrium along the discontinuity. This result confirms the theory that, if the friction angle of the cohesionless discontinuity is equal to the discontinuity dip angle, then the block stays in equilibrium.

Following the Mohr-Coulomb slip model analyses, the basic slope model was run with different Barton-Bandis model parameters to see the effect of discontinuity surface properties JRC and JCS on the stability of the discontinuity. The analyses were carried out after the elastic model run in

order to generate the stresses. The parameters of the Barton-Bandis model are given in Table 5.2.

Table 5.2 Discontinuity parameters of the basic slope model for Barton-Bandis criterion

Discontinuity normal stiffness	100 GPa/m
Discontinuity shear stiffness	100 GPa/m
Discontinuity residual friction angle	22°
Joint roughness coefficient	2
Joint wall compressive strength	12.97 MPa

Barton-Bandis model was run after the elastic run process for the generation of insitu stresses. Point A was again monitored for shear displacement (Figure 5.6). The Barton-Bandis model was run with the large option that was mentioned in Section 3.3.2. For the peak shear displacement calculation from Eq.(2.15) the lab scale discontinuity length was assumed as 0.1 meters. In general, direct shear testing apparatus can be done to samples with lengths between 0.10 – 0.30 meters in laboratory or up to 0.70 meters for insitu tests (ISRM, 1974). In this section, the lab scale discontinuity length was assumed to be 0.1 meters and the response of the developed model was examined according to this assumption.

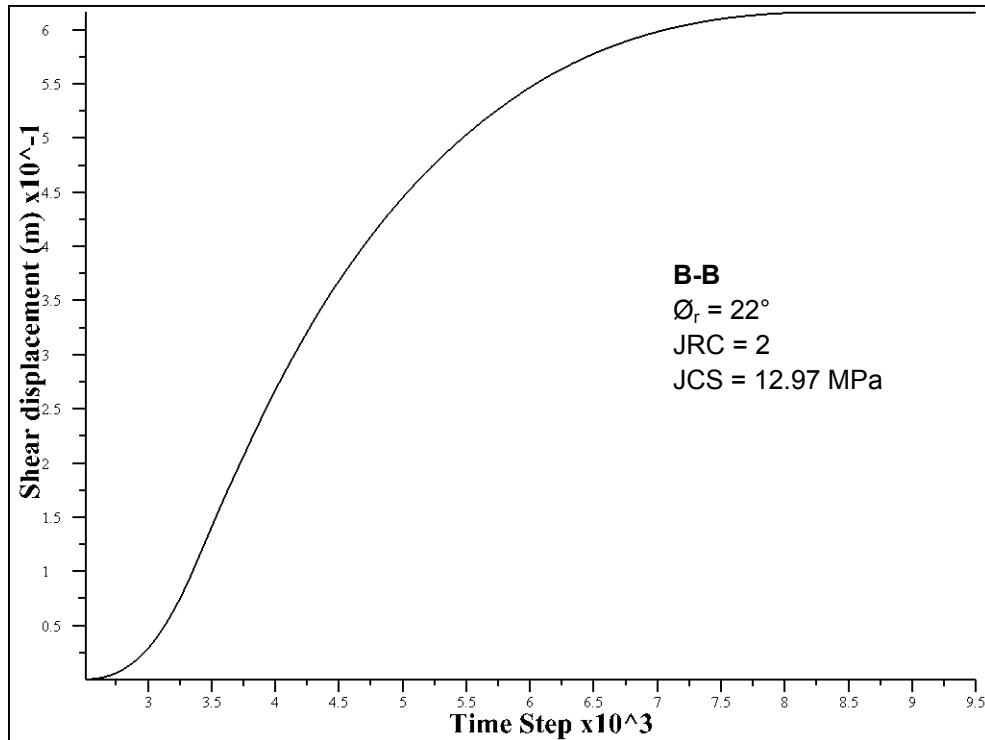


Figure 5.6 Shear displacement of Point A with Barton-Bandis criterion ($\phi_r = 22^\circ$, JRC = 2, JCS = 12.97 MPa)

The analyses showed that besides the two dimensional limit equilibrium analyses; three dimensional distinct element code 3DEC also verifies the Barton-Bandis criterion parameter determination from existing Mohr-Coulomb parameters and for the equilibrium condition the model was verified with the basic slope model. The discontinuity with approximately 100 meters in length would have approximately 0.55 meters peak shear displacement from Eq.(2.15). The analyses showed that the block slips until the discontinuity's roughness gets its peak value at the peak shear displacement and then remains stable. Therefore the mobilization of roughness behaviour and the peak shear strength criterion was also verified with this example.

5.3 Effect of discontinuity surface properties on slope stability

The joint roughness coefficient (JRC) and joint wall compressive strength (JCS) has significant effect on the shear behaviour of discontinuities. In a discontinuous slope, the residual friction angle of the discontinuity may be much smaller than the discontinuity dip angle. However, if the discontinuity surface is very rough, then this drawback may be tolerated by the roughness. Similarly, joint wall strength also affects the stability of such a case. Basic slope model was used to test different discontinuity parameters to verify the effect of them on stability of the slope.

First the effect of joint roughness was examined. For 25° discontinuity dip angle, the discontinuity properties for the equilibrium state were previously found as;

$$\phi_r = 22^\circ$$

$$\text{JRC} = 2$$

$$\text{JCS} = 12.97 \text{ MPa}$$

A rock discontinuity may have a low residual friction angle but may also have a rough and undulating surface. In such a case, the discontinuity may still be stable. Following analyses shows the results of a discontinuity with the following properties;

$$\phi_r = 17^\circ$$

$$\text{JRC} = 8$$

$$\text{JCS} = 12.97 \text{ MPa}$$

Another property that represents the discontinuity surface is the joint wall compressive strength (JCS). A similar occasion with the previous case that a discontinuity with higher joint wall compressive strength with less joint roughness coefficient as;

$$\phi_r = 17^\circ$$

$$\text{JRC} = 5$$

$$\text{JCS} = 80 \text{ MPa}$$

Shear displacement plot of Point A (Figure 5.7) for both conditions verifies that the block is still in equilibrium.

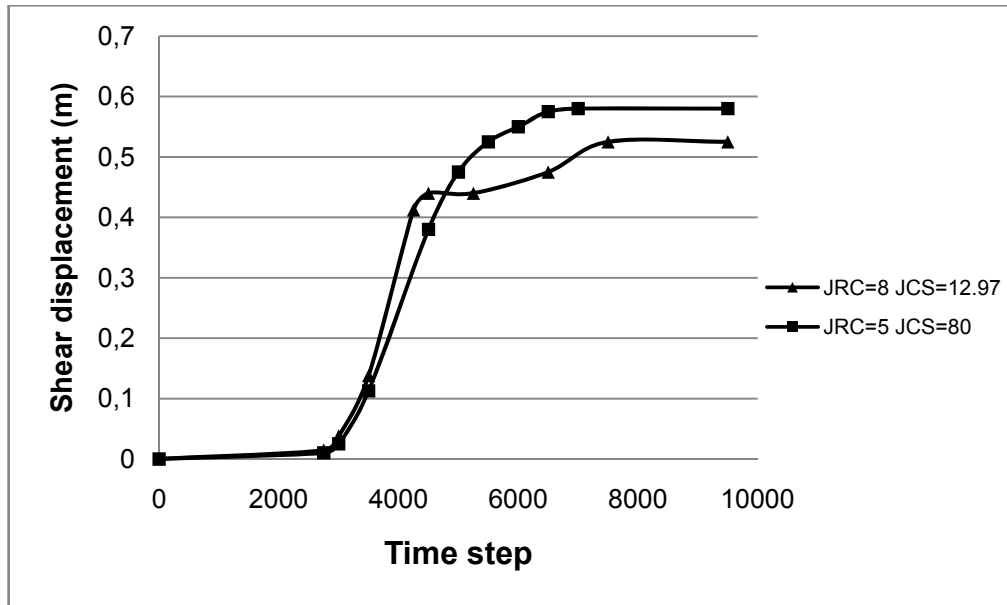


Figure 5.7 Shear displacement of Point A with Barton-Bandis criterion

From the analyses above, it can be concluded that discontinuity surface properties had significant effect on the shear behaviour of a rock discontinuity. Besides the direct shear test model that was mentioned in Chapter 4, this behaviour was also verified by the field scale basic slope model. Also the mobilization of roughness until the peak shear displacement concept was also verified again with these analyses.

5.4 Example for large scale slope deformation behaviour – Sliding block

In this section, large scale deformation behaviour of the sliding block in the basic slope model is presented. Different joint roughness coefficient values were analyzed with the basic slope model by monitoring the displacement amounts under specific time step of the program.

For the sensitivity analyses of the joint roughness coefficient parameter, a discontinuity with specific residual friction angle and joint wall compressive strength values was selected and the difference of the shear displacement amounts in the basic slope model were analyzed. The residual friction angle was selected as 13° in order to force the block to slide. The joint wall compressive strength was selected as 100 MPa. The joint roughness coefficient was changed between 2 and 6 and the shear displacement of the sliding block was recorded every time. Figure 5.8 represents the shear displacement amounts of the sliding block with different joint roughness coefficients.

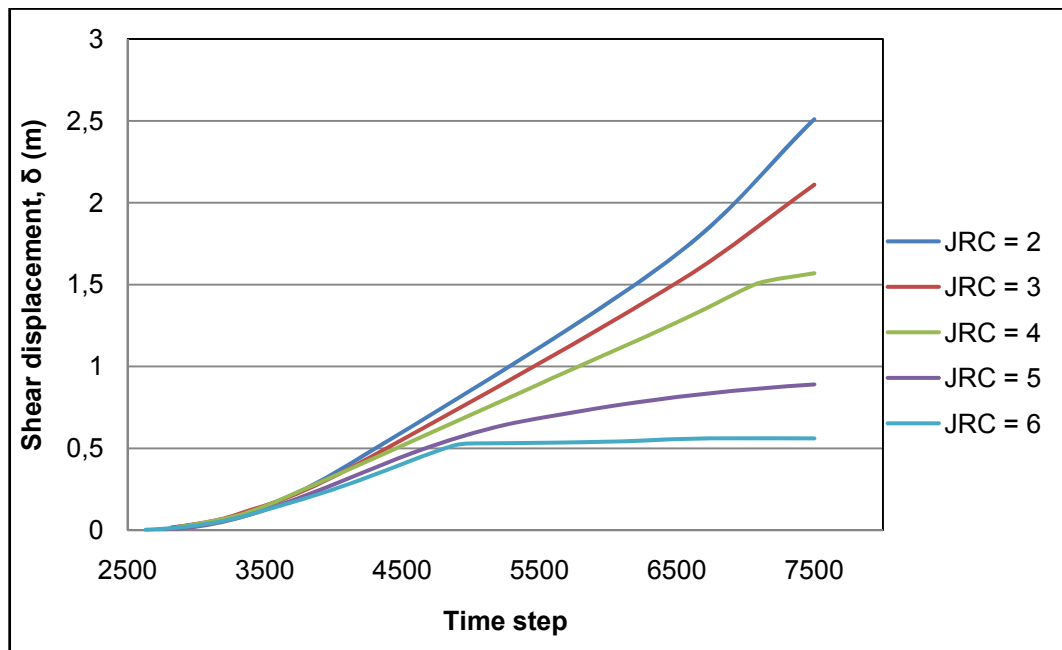


Figure 5.8 Shear displacement of the sliding block under different joint roughness coefficients

From the plot it can be seen that joint roughness coefficient has significant effect on the discontinuity when it starts to slip. As mentioned in Chapter 2, the joint roughness coefficient is a mobilized parameter. It gets its peak value at the peak shear displacement. The discontinuity length is

approximately 100 meters and from Eq.(2.15) the peak shear displacement of the block can be calculated. For $JRC = 6$ the peak shear displacement becomes approximately 0.77 meters (assuming the lab scale discontinuity length is 0.1 meters) and the block becomes stable just before it reaches the peak shear displacement value.

It is also clear that, as the peak shear displacement is passed, the displacement increases continuously as the joint roughness is mobilized and shear strength decreases continuously.

5.5 Orhaneli Gümüşpınar (A-6 panel) Slope Failure

Orhaneli open pit lignite mine is located in Orhaneli district of Bursa, which is approximately 65 km from city centre (Figure 5.9). Gümüşpınar Village is approximately 22 km from Orhaneli district.

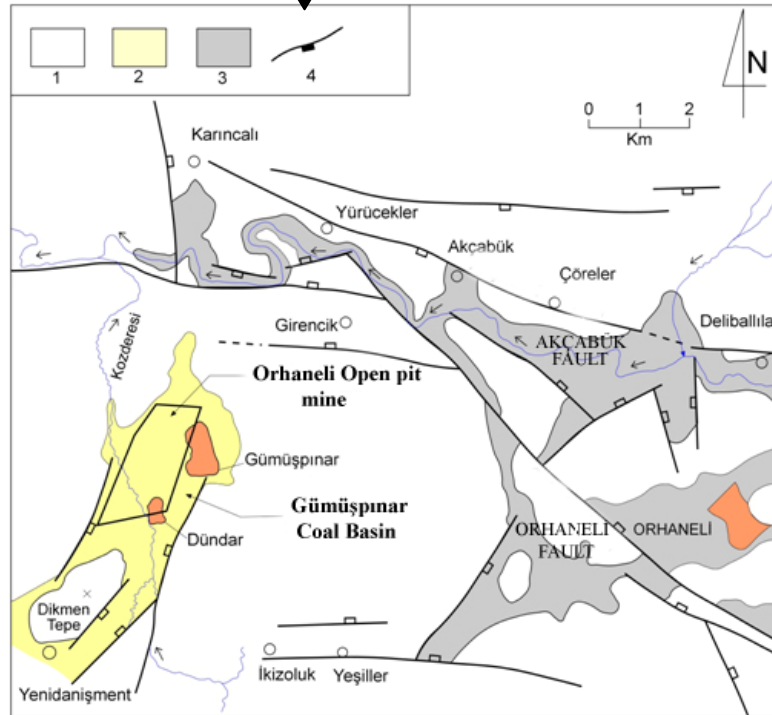
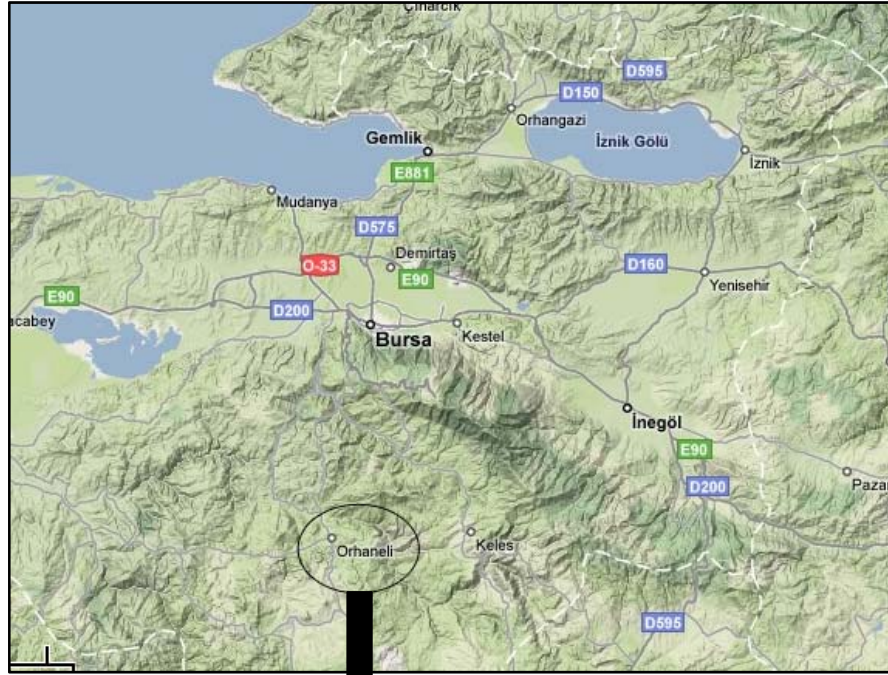


Figure 5.9 Location and geological map of Orhaneli district (Karpuz et al.(2006)

(1. Jurassic cretaceous aged limestone, 2. Gümüşpınar miocene basin stowage, 3. Quaternary alluvium, 4. Normal fault)

In year 2004, the slope of A-6 panel of Orhaneli open pit lignite mine had failed. Operating with high slope angles in the fault zones had caused this failure. The failure mechanism was governed by two intersecting faults Fault 11 (F11) and Fault 12 (F12) (Figure 5.10). Besides these faults which determine the lateral borders of the slump, weak contact layer right above the lignite seam had caused the slump to slide along it. The weak contact layer thickness was 2-4 meters with a very low friction angle. So in numerical analyses this zone was simulated as a discontinuity. The lithological section of the Orhaneli miocene basin is given in Figure 5.11. The two dimensional section view of the landslide is illustrated in Figure 5.12. As it can be seen from cross section (S-S') in Figure 5.12, water table level was assigned to the model approximately 10 meters below from the surface.



Figure 5.10 Orhaneli A-6 panel slope failure

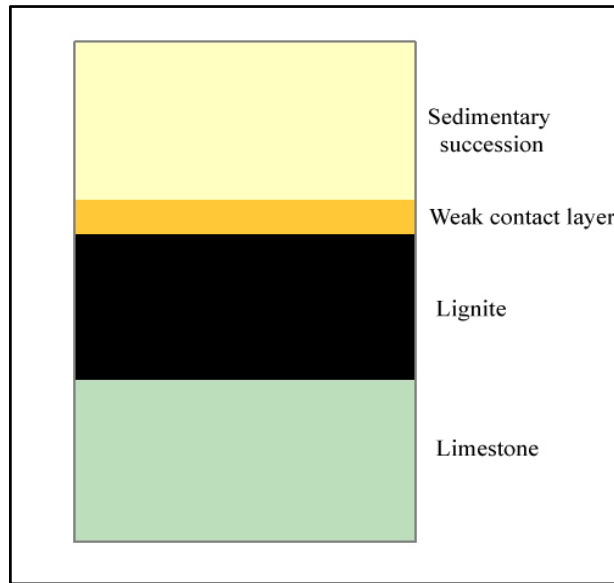


Figure 5.11 Lithological section of Orhaneli miocene basin

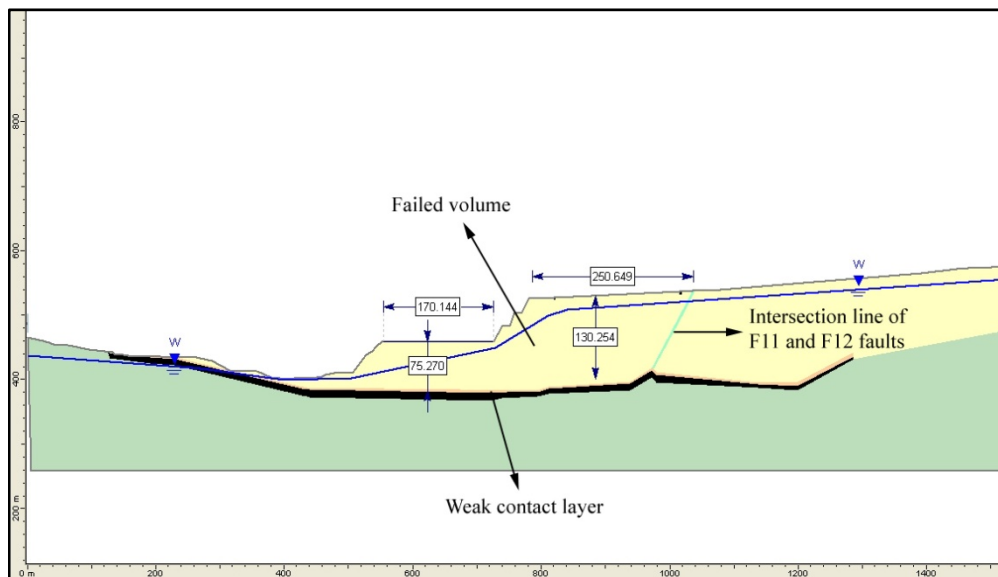


Figure 5.12 Cross section (S-S') of the A-6 panel landslide

Karpuz et al. (2006) studied the reasons of the landslide, progressive mechanism and the material and discontinuity properties in order to use for design purposes in the field. As the failure was governed by discontinuities the numerical studies had been done by 3DEC in order to obtain large

displacements along the discontinuities in the back analyses as observed in the field.

The parameter determination for rock mass and discontinuities were done in 3DEC by back analyses of the failure. The corresponding model geometry is given in Figure 5.13.

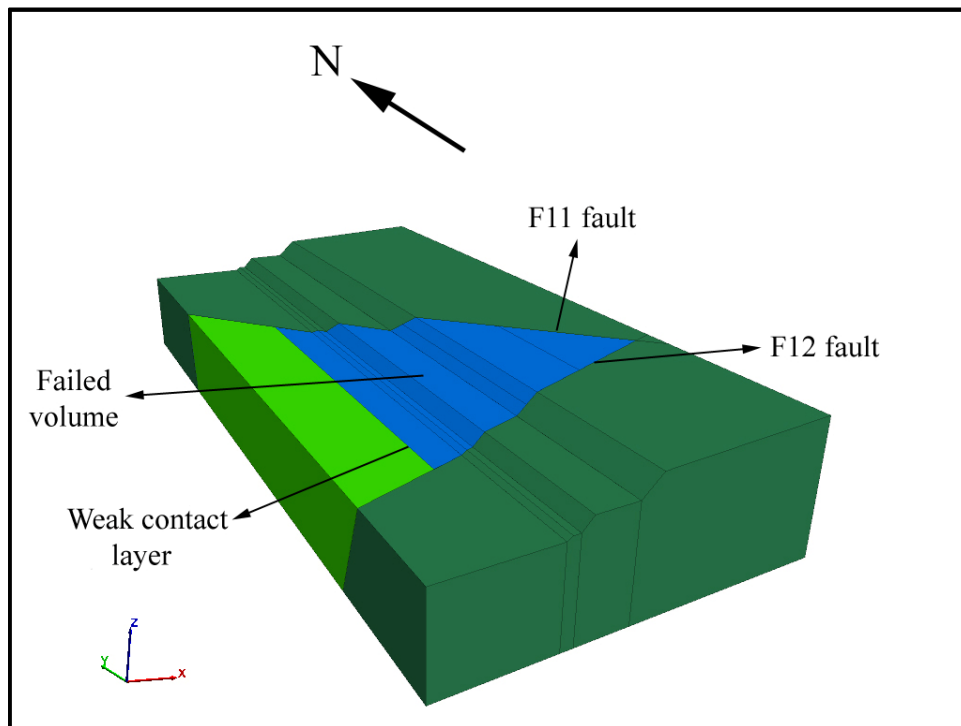


Figure 5.13 Gümüşpınar 3DEC model geometry

In the field studies, extend of the failure was examined. At the point of intersection of F11 and F12 faults a vertical displacement of approximately 5 m was observed. Horizontal displacements of the slope toe had reached to 30 meters. Different displacement monitoring points were determined in order to compare the behaviour of the model with the field results. The displacement monitoring points and the location of the cross section S-S' are given in Figure 5.14.

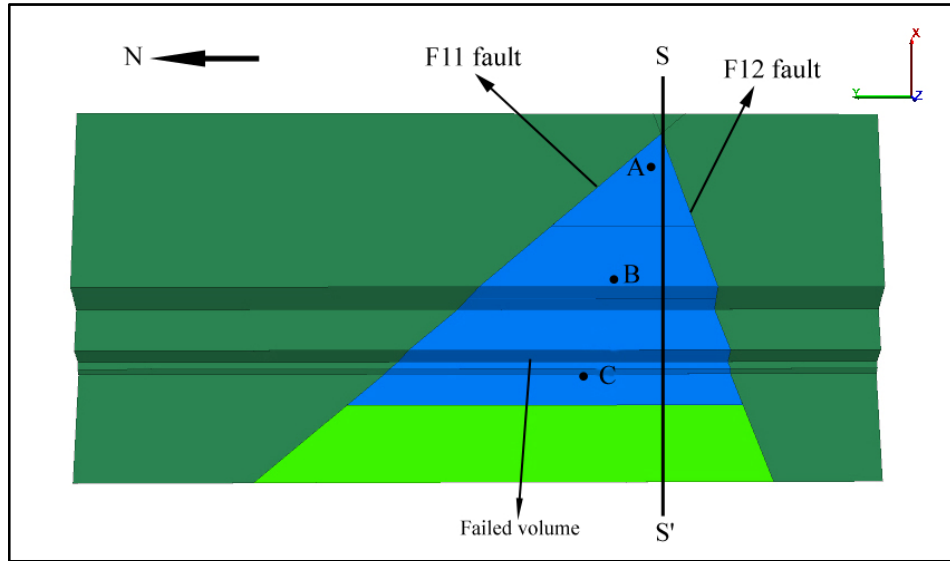


Figure 5.14 Gümüşpınar model displacement monitoring points

The result of studies concluded the input parameters for the material and discontinuity properties of the Mohr-Coulomb model. The parameters for rock mass and discontinuities are given in Table 5.3 and Table 5.4 respectively. The corresponding horizontal and vertical displacement graphs are given in Figure 5.15 and Figure 5.16 respectively.

Table 5.3 Material properties of Gümüşpınar landslide obtained from back analyses

Property	Overburden	Lignite	Footwall
Density	1667 kg/m ³	1500 kg/m ³	2000 kg/m ³
Young's modulus	50 MPa	500 MPa	20 GPa
Poisson's' ratio	0,2	0,2	0,2
Cohesion	55 kPa	500 kPa	5MPa
Internal friction angle	26°	25°	35°

Table 5.4 Discontinuity properties of Gümüşpınar landslide obtained from back analyses

Property	F11	F12	Weak contact layer
Length	1500 m	1000 m	1055 m
Normal stiffness	160 MPa/m	160 MPa/m	400 MPa/m
Shear stiffness	160 MPa/m	160 MPa/m	400 MPa/m
Cohesion	5 kPa	5 kPa	5 kPa
Friction angle	20°	20°	11°

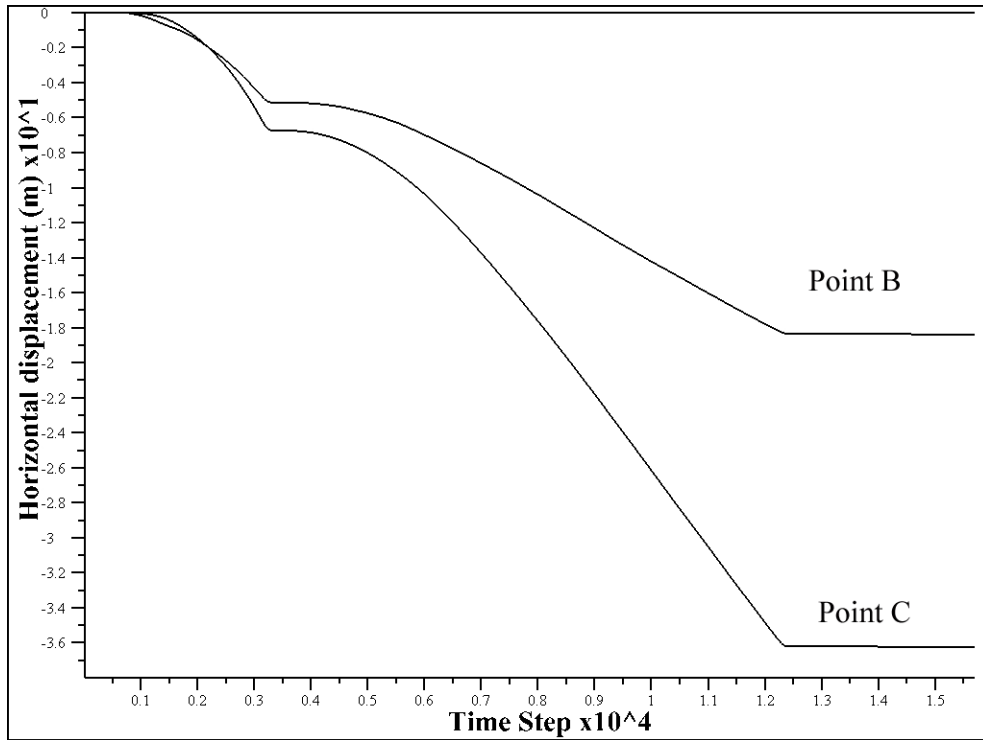


Figure 5.15 Horizontal displacement plots of monitoring points with Mohr-Coulomb model

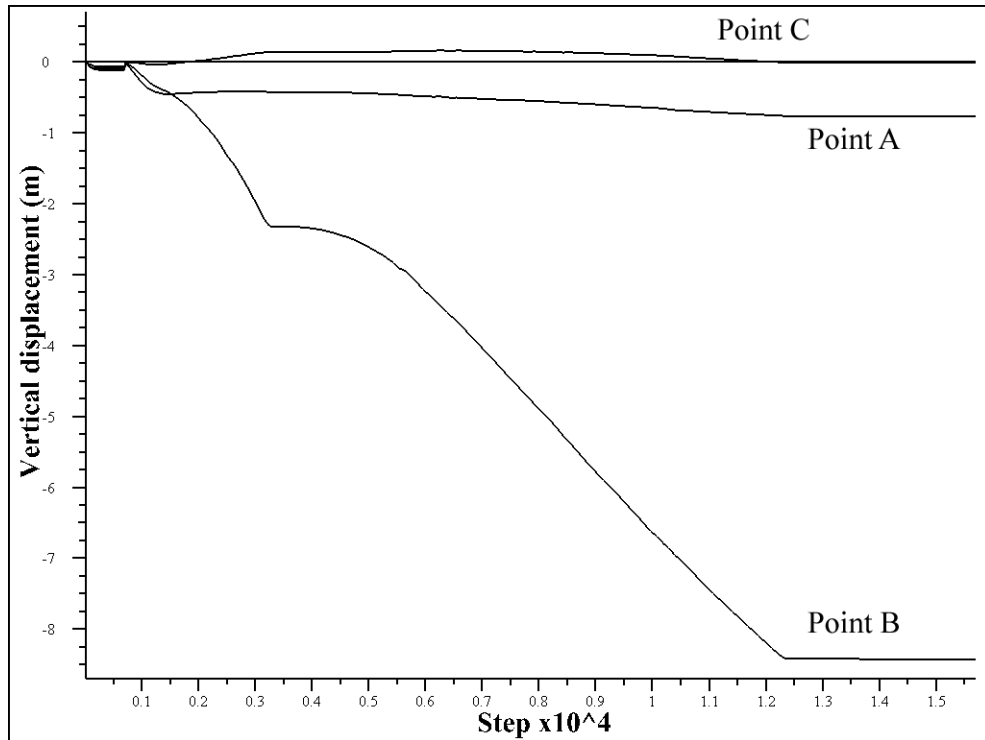


Figure 5.16 Vertical displacement plots of monitoring points with Mohr-Coulomb model

After generating the field conditions in the model, the model was run with Barton-Bandis criterion. The critical part for this analysis is the determination of the discontinuity parameters. From the field studies the asperity amplitudes were obtained and the joint roughness coefficients were determined by using Eq. (2.11).

From the field studies, the amplitude of the asperity (caused by undulation) for fault F11 was found to be at most 6,6 meters and F12 was found to be at most 4,4 meters. From the Eq.(2.11) the joint roughness parameters can be found as;

$$JRC_{F11} = \frac{6600}{(1500 \times 2)} = 2,2$$

$$JRC_{F12} = \frac{4400}{(1000 \times 2)} = 2,2$$

The joint roughness coefficient of the weak contact layer was assumed to be a lower value because of the stratification of the formations and it is not expected to have undulations. Thus the joint roughness coefficient for the weak contact layer was assumed to be 1.5.

The residual friction angle was assumed to be 90 % of the peak value. And the joint wall compressive strength value was back calculated as it was done in the basic slope model. For the back calculation of the joint wall compressive strength, the maximum normal stress acting on the discontinuity was calculated for the slope geometry that is shown in Figure 5.17 the maximum overburden depth in the Gümüşpınar landslide geometry was 150 meters.

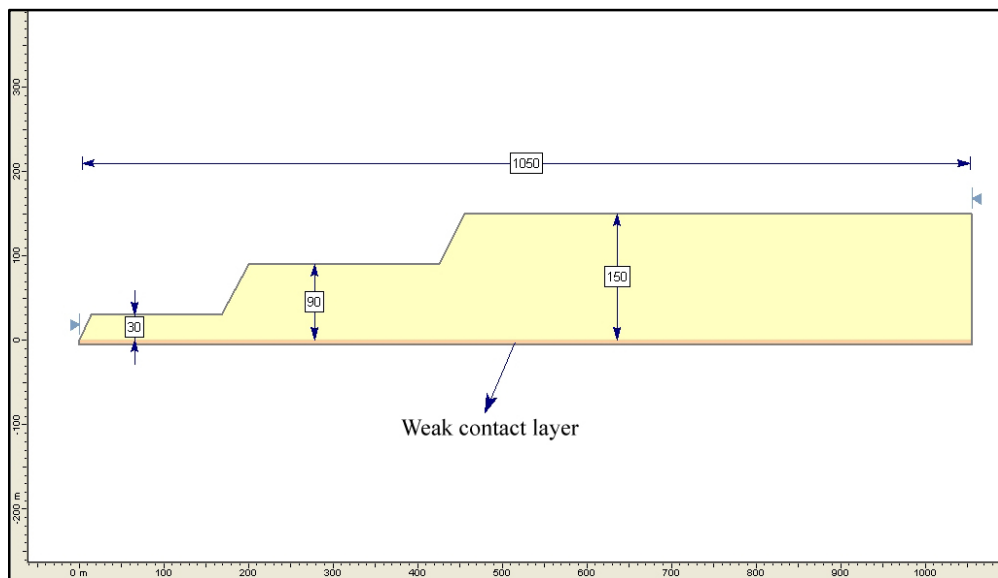


Figure 5.17 Gümüşpınar landslide cross sectional model geometry

The maximum normal stress acting on the weak contact layer was calculated from Eq. (5.2) as;

$$\sigma_{nmax} = \frac{150 \times 1667 \times 9,81}{10^6} = 2,45 \text{ MPa}$$

Then by using the JRC parameter, residual friction angle and the average normal stress acting on the discontinuity plane, the shear stresses with Mohr-Coulomb and Barton-Bandis criterion were equated and the joint wall compressive strength was calculated.

After the normal stress acting on the discontinuity was determined, the shear stress on the discontinuity should be equal with the two methods. Therefore Eq.(5.4) becomes;

$$0.005+2.45 \times \tan 11 = 2.45 \times \tan \left(\phi_r + \text{JRC} \times \log_{10} \left(\frac{\text{JCS}}{\sigma_n} \right) \right)$$

Where;

$$\text{JRC}_{\text{weak contact layer}} = 1.5 \text{ MPa},$$

$$\phi_r = 10^\circ$$

So the relation becomes;

$$0.48 = 2.45 \times \tan \left(10 + 1.5 \times \log_{10} \left(\frac{\text{JCS}}{2.45} \right) \right)$$

Then $\text{JCS}_{\text{weak contact layer}}$ becomes;

$$\text{JCS}_{\text{weak contact layer}} = 12.95 \text{ MPa}$$

The normal stress calculation for a fault line which outcrops at surface is different than the horizontal lying bedding plane. The vertical stress affects the fault plane with the cosine of the dipping angle as previously shown in Figure 5.2.

The normal stress acting on the F11 and F12 faults were calculated with this manner. The faults were dipping with 85° and 70° respectively. The maximum height of the overburden was 150 meters. So the maximum normal stresses acting on the F11 and F12 faults were calculated from Eq.(5.3) as;

$$\sigma_{n\max F11} = \frac{150 \times 1667 \times 9,81}{10^6} \times \cos 85^\circ = 0.21 \text{ MPa}$$

$$\sigma_{n\max F12} = \frac{150 \times 1667 \times 9,81}{10^6} \times \cos 70^\circ = 0.84 \text{ MPa}$$

Therefore by using Eq.(5.4) JCS for F11 fault becomes;

$$0.005 + 0.21 \times \tan 20 = 0.21 \times \tan \left(\phi_r + \text{JRC} \times \log_{10} \left(\frac{\text{JCS}}{\sigma_n} \right) \right)$$

$$0.081 = 0.21 \times \tan \left(18 + 2.2 \times \log_{10} \left(\frac{\text{JCS}}{0.21} \right) \right)$$

$$\text{JCS}_{F11} = 5.95 \text{ MPa}$$

And JCS for F12 fault becomes;

$$0.005 + 0.84 \times \tan 20 = 0.84 \times \tan \left(\phi_r + \text{JRC} \times \log_{10} \left(\frac{\text{JCS}}{\sigma_n} \right) \right)$$

$$0.311 = 0.84 \times \tan \left(18 + 2.2 \times \log_{10} \left(\frac{\text{JCS}}{0.84} \right) \right)$$

$$\text{JCS}_{F12} = 9.49 \text{ MPa}$$

The uniaxial compressive strength values were taken as equal to the joint wall compressive strength values. The final Barton-Bandis discontinuity properties are given in Table 5.5. The shear stiffness exponent, η_j , was selected as 0.9 with reference to Figure 2.20, considering the discontinuities were weathered.

Table 5.5 Barton-Bandis discontinuity geotechnical properties of the Gümüşpınar landslide

Property	F11 fault	F12 fault	Weak contact layer
Length	1500 m	1000 m	1055 m
Initial normal stiffness	160 MPa/m	160 MPa/m	400 MPa/m
Shear stiffness number	160 MPa/m	160 MPa/m	400 MPa/m
Stiffness exponent (η_j)	0.9	0.9	0.9
JRC	2,2	2,2	1,5
JCS	5.95	9.49	12.95
Residual friction angle	18°	18°	10°

The horizontal and vertical displacement amounts are given in Figure 5.18 and Figure 5.19.

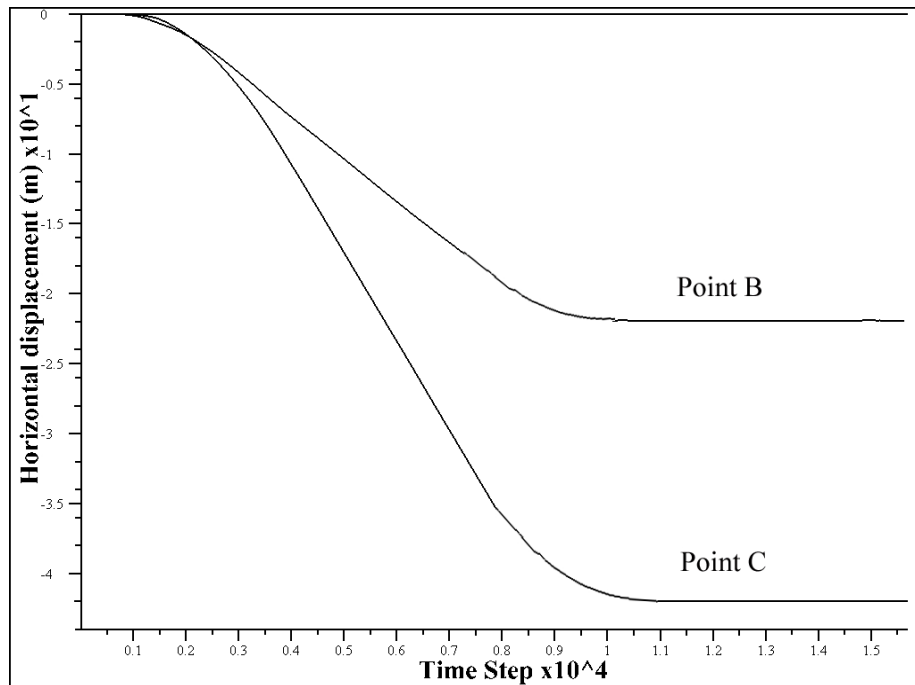


Figure 5.18 Horizontal displacement plots of monitoring points with Barton-Bandis model

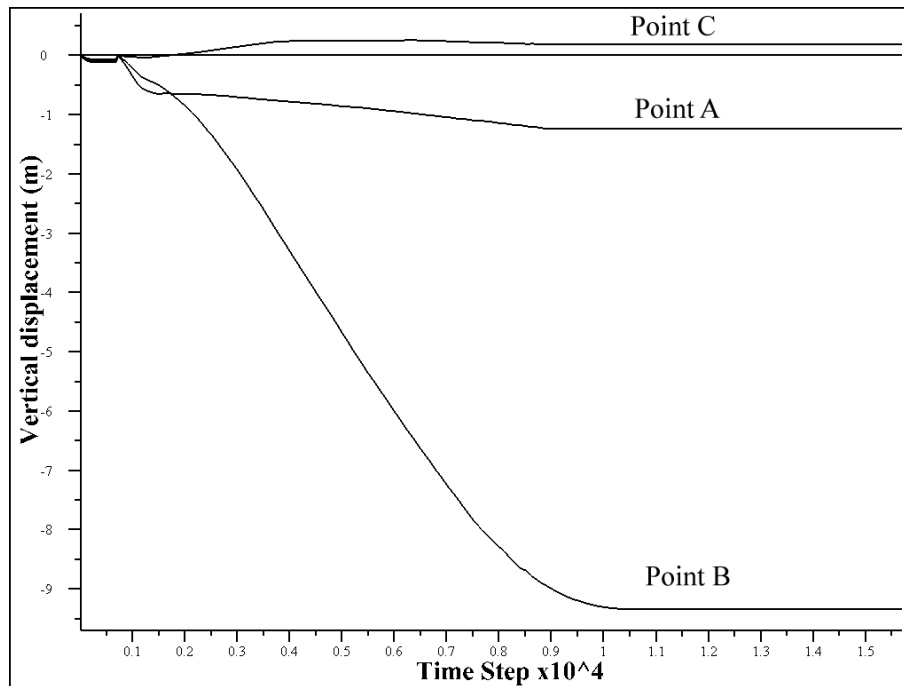


Figure 5.19 Vertical displacement plots of monitoring points with Barton-Bandis model

The failure mechanism of Gümüşpınar landslide was in the form of rotating of the failed volume by slipping along the weak contact layer and breaking into slices.

From the analyses, it can be concluded that the displacement amounts of Barton-Bandis model is higher than the Mohr-Coulomb's. The horizontal extend of the slope was approximately 1100 meters. The horizontal displacement was found to be approximately 3.3 % from Mohr-Coulomb model and 3.9 % from Barton-Bandis model with respect to the total length of the slope. The reason can be stated as the shear strengths of the discontinuities were reduced as the shear failure occurs. Therefore higher amounts in displacements had been expected. Besides the slip along the discontinuities, the weak rock material also fails so the displacement amounts had become that much.

5.6 Orhaneli Dikmentepe (A-5 panel) Slope Failure

In year 2006, A-5 panel slopes of the Orhaneli open pit lignite mine had failed along the neogene contact of the coal basin which extends over 600 m along the slope crest. The lateral extends of the mobilized slump was limited by two main faults of the area, which were Bayırpınar fault from the west and D1 fault from the east as seen in Figure 5.20.

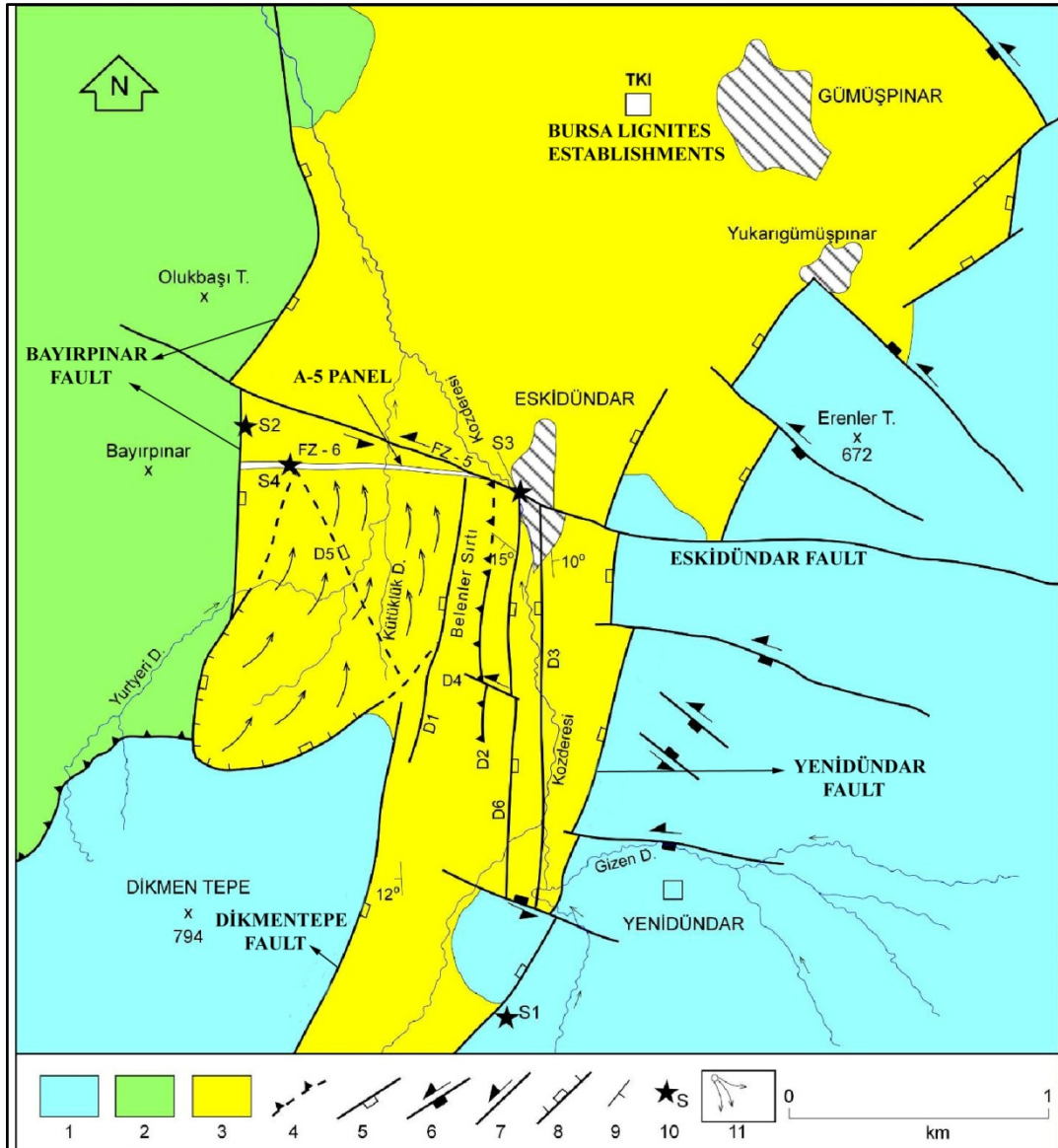


Figure 5.20 Geological map of Orhaneli coal basin (Karpuz et al.,2007)

- (1. Jurassic cretaceous aged limestone, 2. Late cretaceous offiolite, 3. Miocene basin stowage, 4. Reverse fault, 5. Normal fault, 6. Strike slip fault, 7. Strike slip fault with normal component, 8. Dikmentepe slump slip surfaces, 9. Bedding dip, 10. Slip vectors measurement stations, 11. Dikmentepe slump)

The simple cross sectional (T-T') model geometry of Dikmentepe landslide is given in Figure 5.21. As seen from Figure 5.21 the water table was assigned to the model approximately 10 meters below from the surface. The 3DEC model geometry is given in Figure 5.22.

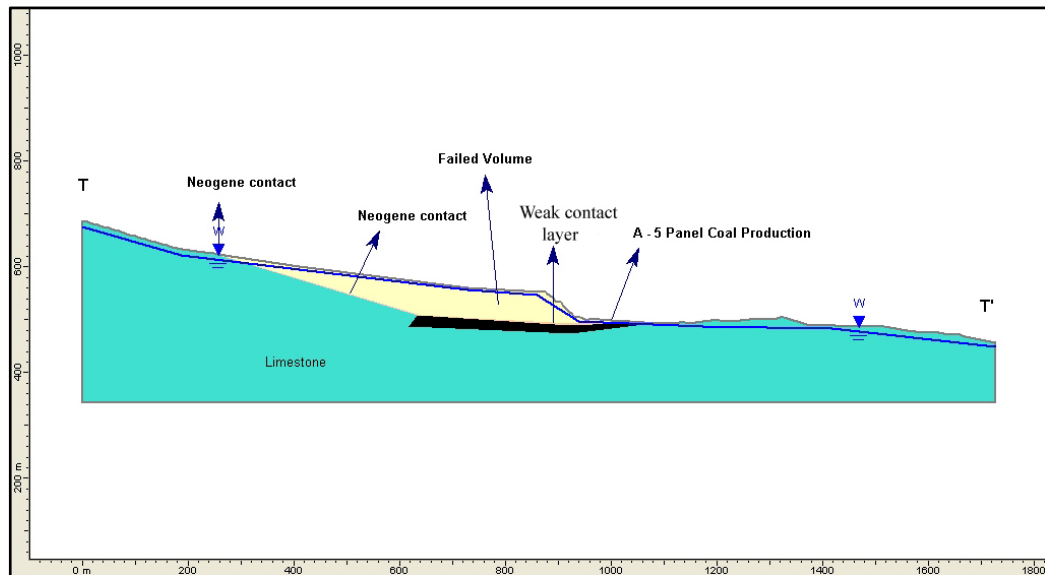


Figure 5.21 Cross section of the Dikmentepe (A-5 panel) landslide (T-T')

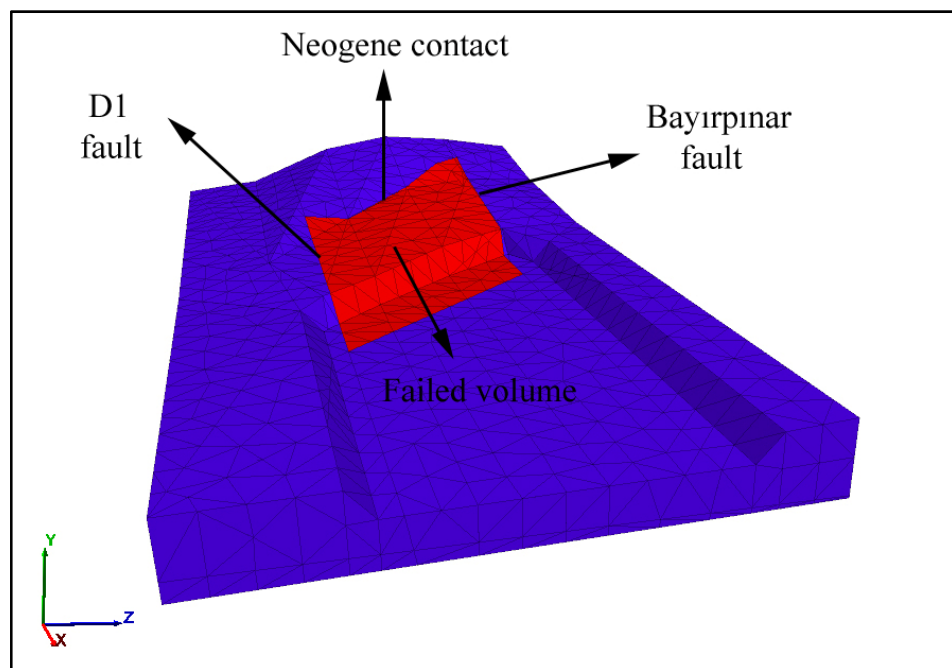


Figure 5.22 Dikmentepe 3DEC model geometry

In the field, the displacements were observed at the outcrop neogene contact of the landslide was approximately 15 meters and at the toe of the slope 10 meters. Different displacement monitoring points were determined in order to compare the behaviour of the model with the field results. The displacement monitoring points are given in Figure 5.23.

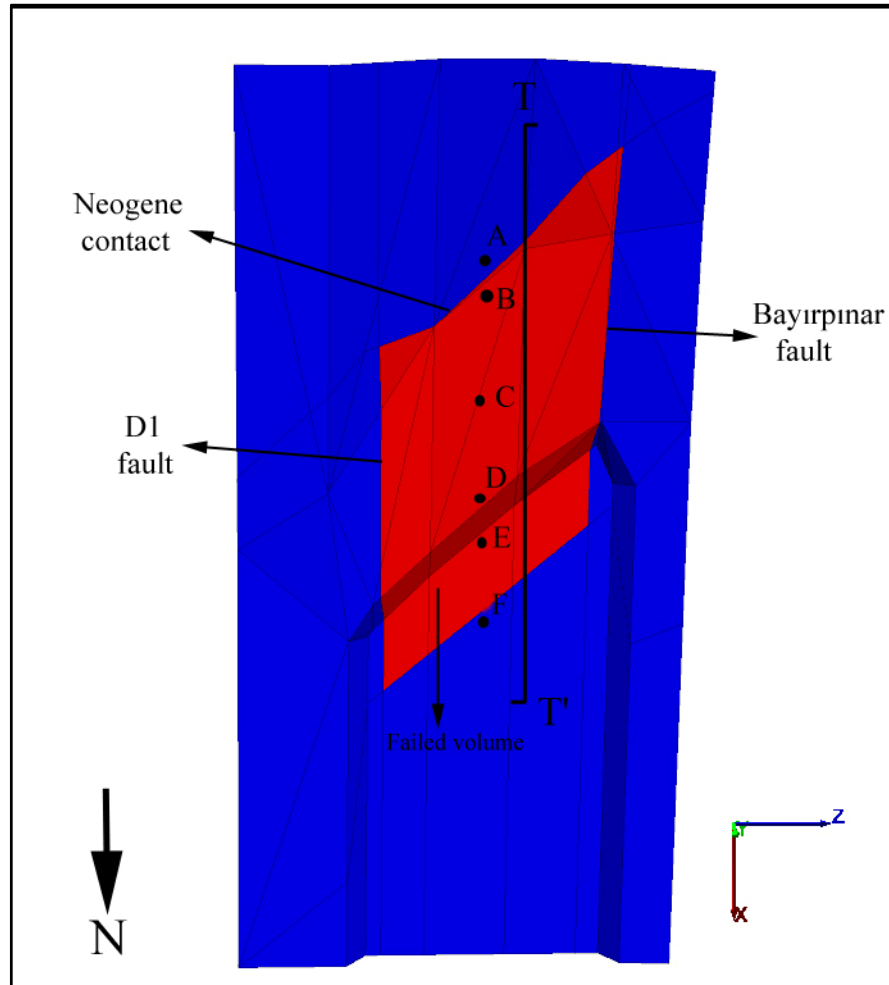


Figure 5.23 Dikmentepe displacement monitoring points (Top view)

The studies about the back analyses concluded the input parameters for the material and discontinuity properties of the Mohr-Coulomb model. The parameters for rock mass for the Orhaneli open pit mine were given in Table 5.3 previously and discontinuities are given in Table 5.6. The

corresponding horizontal and vertical displacement graphs are given in Figure 5.24 and Figure 5.25 respectively.

Table 5.6 Discontinuity properties of Dikmentepe landslide obtained from back analyses

Property	D1 fault	Bayırpınar fault	Weak contact layer
Length	820 m	880 m	1150 m
Normal stiffness	160 MPa/m	160 MPa/m	400 MPa/m
Shear stiffness	160 MPa/m	160 MPa/m	400 MPa/m
Cohesion	5 kPa	5 kPa	5 kPa
Friction angle	20°	20°	11°

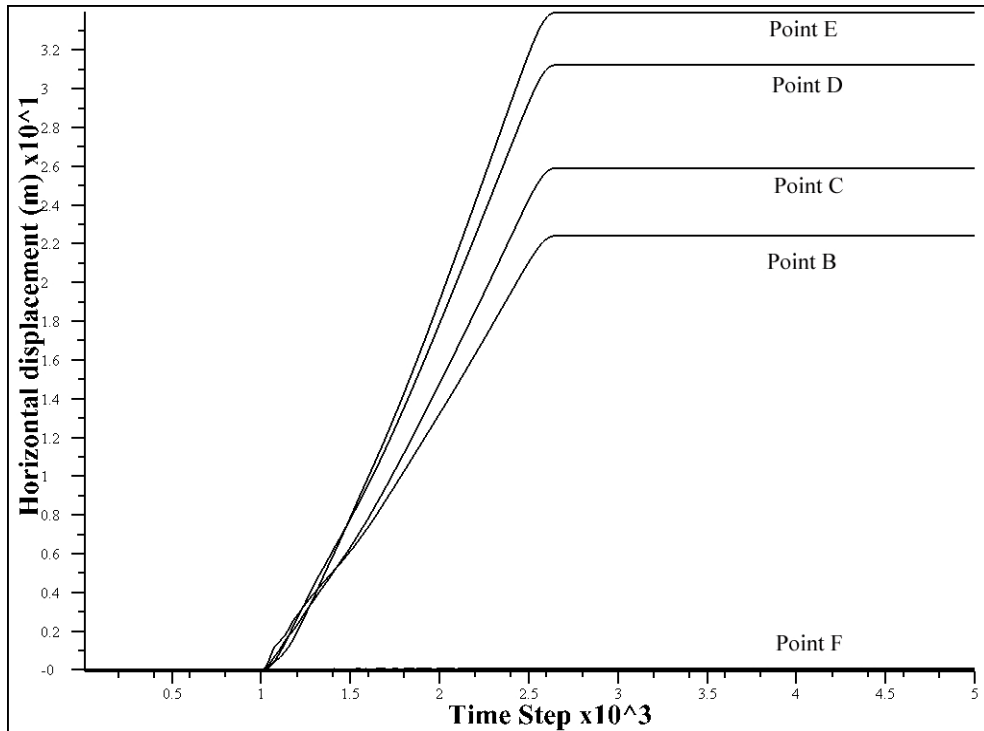


Figure 5.24 Horizontal displacement plots of monitoring points with Mohr-Coulomb model

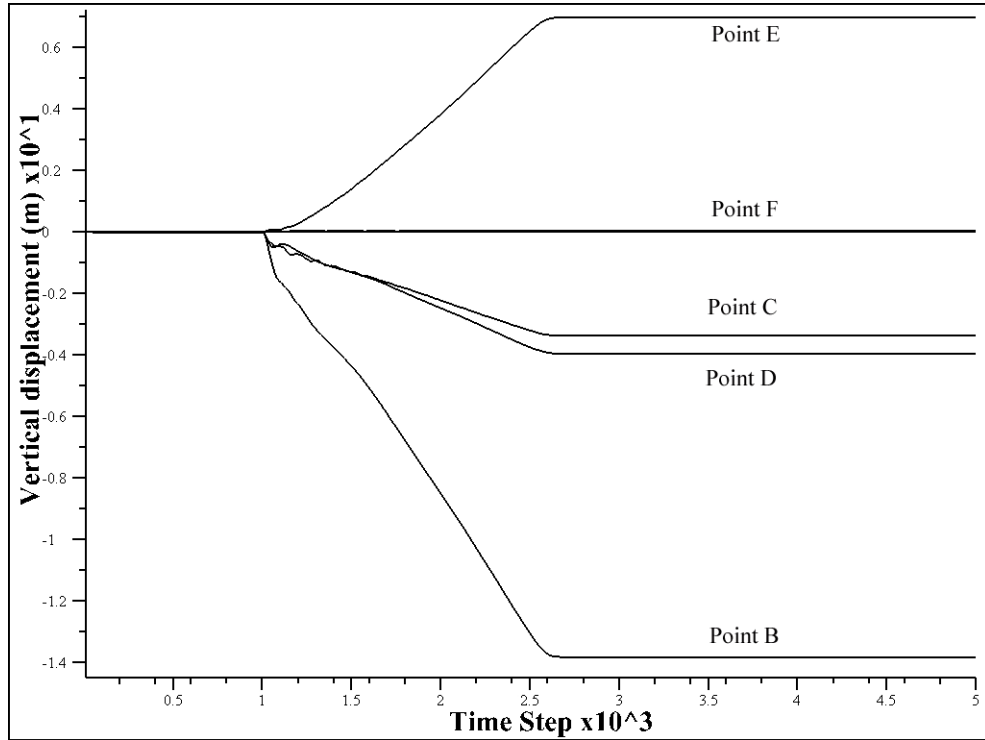


Figure 5.25 Vertical displacement plots of monitoring points with Mohr-Coulomb model

For the Barton-Bandis parameter determination, first the joint roughness coefficients were calculated from the field measurements of the asperity amplitudes. Similar to the previous case, the joint roughness coefficient was assumed to be 1.5 for the weak contact layer and the neogene contact and the residual friction angle is 10° . And joint roughness coefficient for the Bayırpınar fault and the D1 fault was calculated from Eq. (2.11). The field measurements of asperity (undulation) amplitudes for the faults were resulted with maximum 3.5 meters. The faults were approximately 850 meters in length. So the joint roughness coefficients were found as;

$$JRC_{\text{faults}} = \frac{3500}{(850 \times 2)} \cong 2$$

The maximum normal stress acting on the weak contact layer is calculated by using the cross sectional view of the model as given in Figure 5.26.

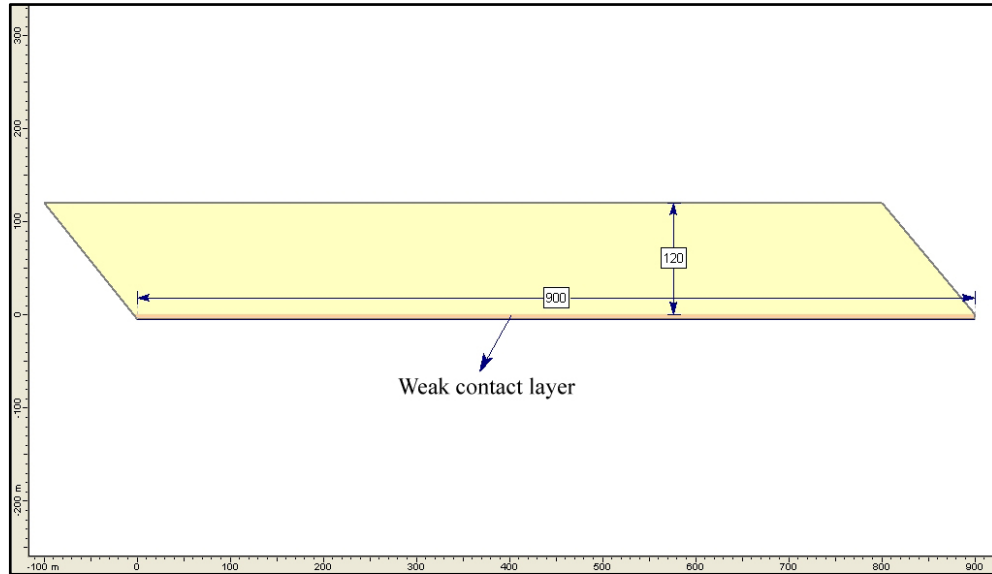


Figure 5.26 Simplified cross sectional model geometry of Dikmentepe model

From Figure 5.26, it can be seen that the maximum depth on the discontinuity plane is 120 meters. So the maximum normal stress acting on the weak contact layer was found from Eq.(5.2) as;

$$\sigma_{n\max} = \frac{120 \times 1667 \times 9,81}{10^6} = 1,96 \text{ MPa}$$

After determining the joint roughness coefficients and normal stress acting on the discontinuity plane, joint wall compressive strength values were found by substituting the determined parameters in Eq.(5.4) as;

$$0.005 + 1.96 \times \tan 11 = 1.96 \times \tan \left(10 + 1.5 \times \log_{10} \left(\frac{\text{JCS}}{1.96} \right) \right)$$

Then;

$$\text{JCS}_{\text{weak contact layer}} = 11.3 \text{ MPa,}$$

The normal stress acting on the D1 and Bayırpınar faults were calculated in this manner. The faults were dipping with 80°. The maximum height of the overburden was 120 meters. So the maximum normal stresses acting on the D1 and Bayırpınar faults were calculated from Eq.(5.3) as;

$$\sigma_{n\max\text{faults}} = \frac{120 \times 1667 \times 9,81}{10^6} \times \cos 80 = 0.34 \text{ MPa}$$

After determining the maximum normal stress acting on the fault planes, the joint wall compressive strength of the faults were calculated from Eq.(5.4) as;

$$0.005 + 0.34 \times \tan 20 = 0.34 \times \tan \left(18 + 2 \times \log_{10} \left(\frac{\text{JCS}}{0.34} \right) \right)$$

Then;

$$\text{JCS}_{\text{faults}} = 7.98 \text{ MPa}$$

The uniaxial compressive strength values were taken as equal to the joint wall compressive strength values. The final Barton-Bandis discontinuity properties are given in Table 5.7.

Table 5.7 Barton-Bandis discontinuity properties of the Dikmentepe landslide

Property	D1 fault	Bayırpınar fault	Weak contact layer
Initial normal stiffness	160 MPa/m	160 MPa/m	400 MPa/m
Shear stiffness number	160 MPa/m	160 MPa/m	400 MPa/m
Stiffness exponent (n_j)	0.9	0.9	0.9
JRC	2	2	1,5
JCS	7.98	7.98	11.3
Residual friction angle	18°	18°	10°

The horizontal and vertical displacement amounts are given in Figure 5.27 and Figure 5.28.

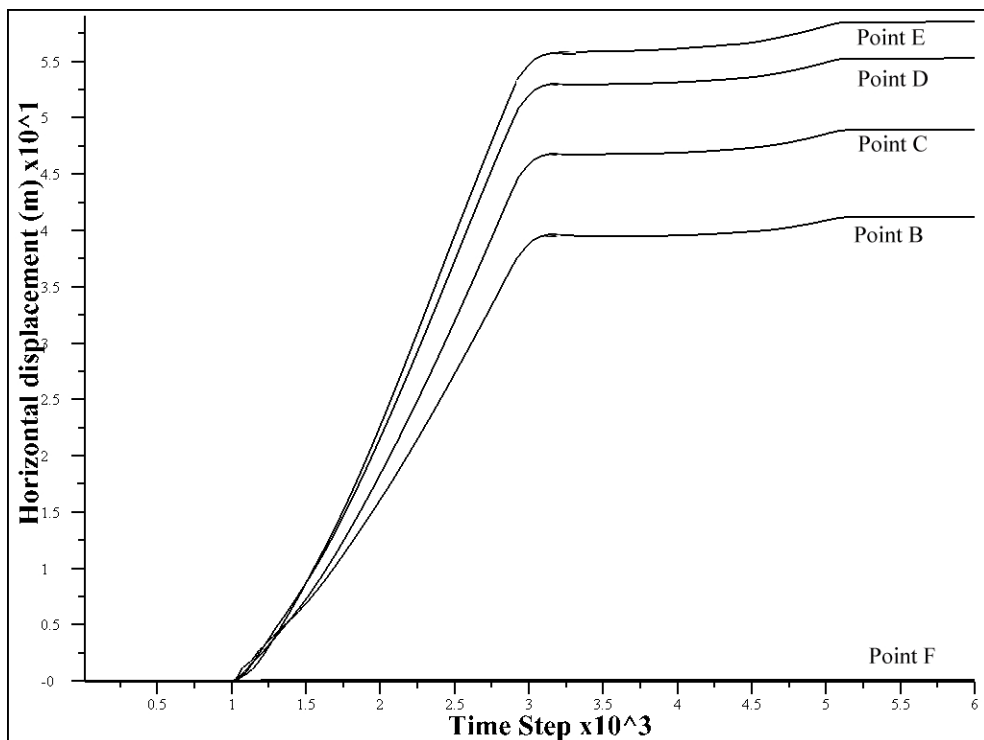


Figure 5.27 Horizontal displacement plots of monitoring points with Barton-Bandis model

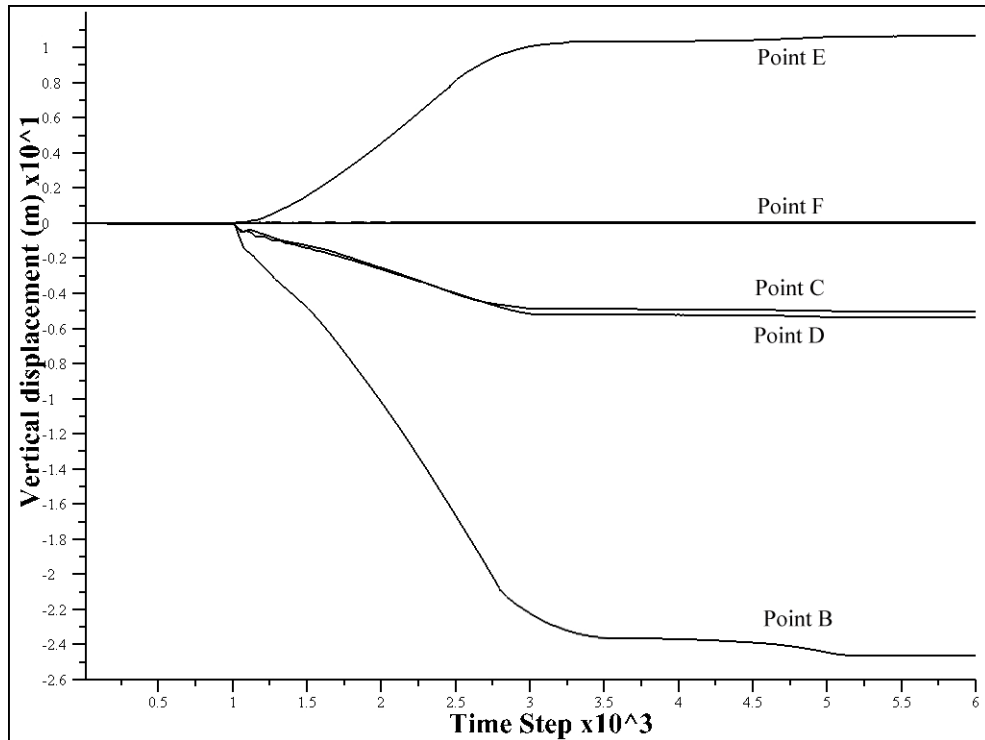


Figure 5.28 Horizontal displacement plots of monitoring points with Barton-Bandis model

Similar to the Gümüşpınar landslide, the displacement amounts with Barton-Bandis model were higher than those of Mohr-Coulomb model. The horizontal extend of the slope was approximately 1150 meters. The horizontal displacement was found to be approximately 3 % from Mohr-Coulomb model and 5.2 % from Barton-Bandis model with respect to the total length of the slope. The difference in the failure mechanism from the previous model was that the dip direction and the dip amount of the weak contact layer were in an unfavourable position which was forcing to slide. Because of this reason, the differences between the two models become higher. However, the result can be considered as acceptable.

5.7 Çan Open Pit Mine Western Panel Slopes

Çan open pit lignite mine is located in Çan district of Çanakkale, which is approximately 55 km from city centre (Figure 5.29).

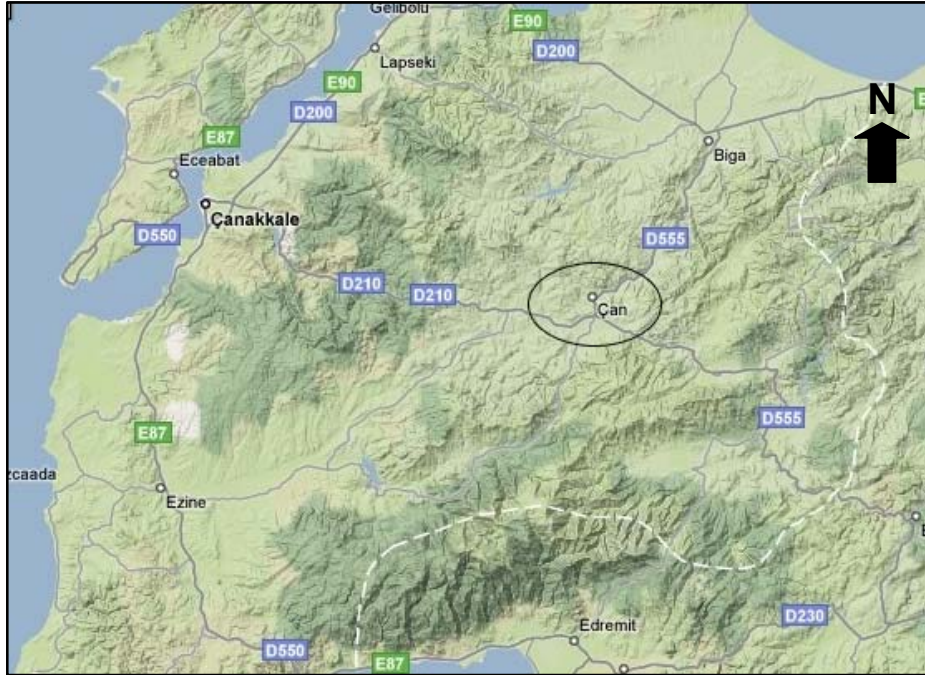


Figure 5.29 Location map of Çan district

In the future development plans of the mine management; a need for detailed stability analyses was arised. In some panels the total depth exceeds 200 meters. In the development stage of the western panels, some critical faults were examined in the field by geophysical studies of Karpuz et al. (2006). Because of this reason a stability analyses with respect to discontinuities (besides rock mass) was needed. A similar slope stability study was also carried out by Paşamehmetoğlu et al. (1991) at the other panels of the Çan lignite mine.

The western panel is located just besides the basin border. A basin border fault and another fault (F5), which was intersecting it perpendicularly was dipping in an unfavourable position (forcing failure). Besides these, a

similar formation with the Orhaneli coal basin, a weak contact layer was lying beneath the lignite seam. The critical distance of slope crest to the outcrop of F5 fault was wound with SLIDE program and then the details of that critical position was analyzed (i.e. the amounts of total deformation) with 3DEC. The lithological section of Çan coal miocene basin is given in Figure 5.30. The cross sectional model geometry and factor of safety of the western panel slope is given in Figure 5.31. The 3DEC model geometry is given in Figure 5.32. The top view of the model which also shows displacement monitoring points is given in Figure 5.33. As shown from Figure 5.30 the water table was assigned to the model approximately 15 meters below from the surface.

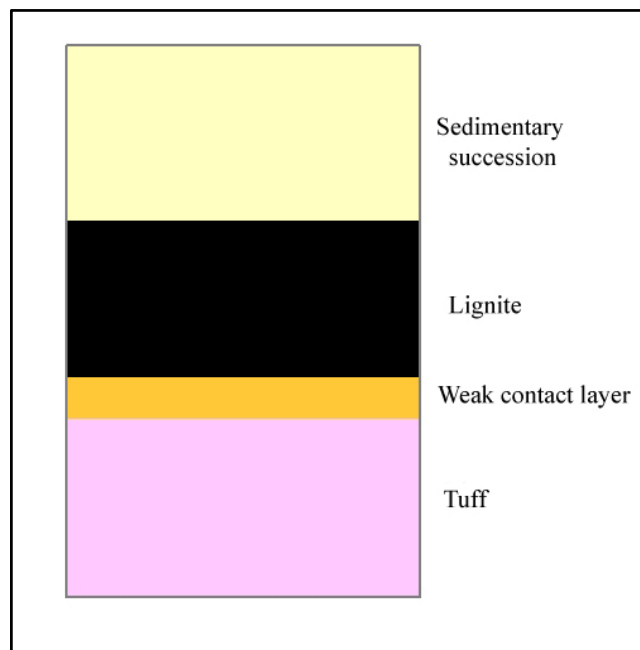


Figure 5.30 Lithological section of Çan miocene basin

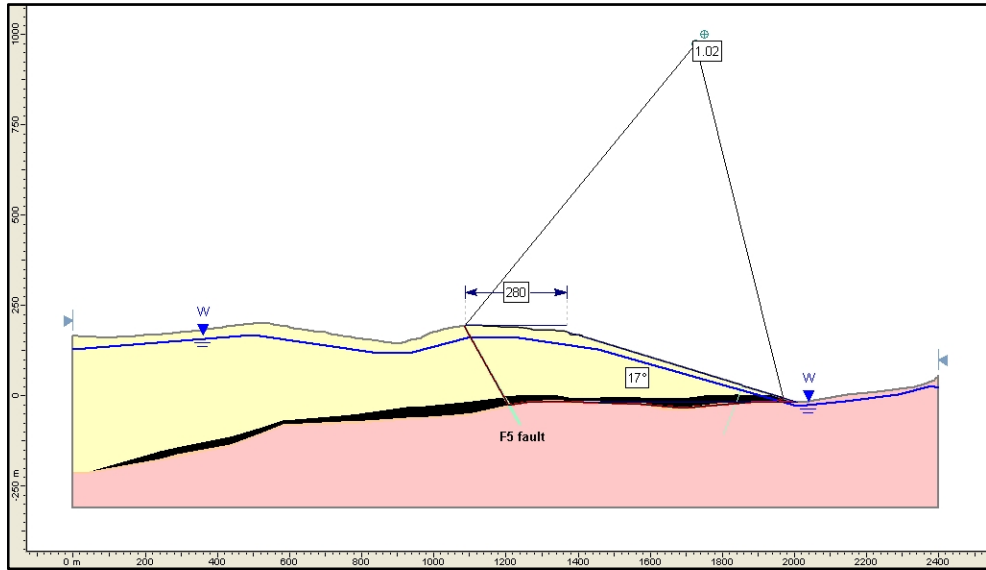


Figure 5.31 Cross section of Çan western panel slopes (U-U')

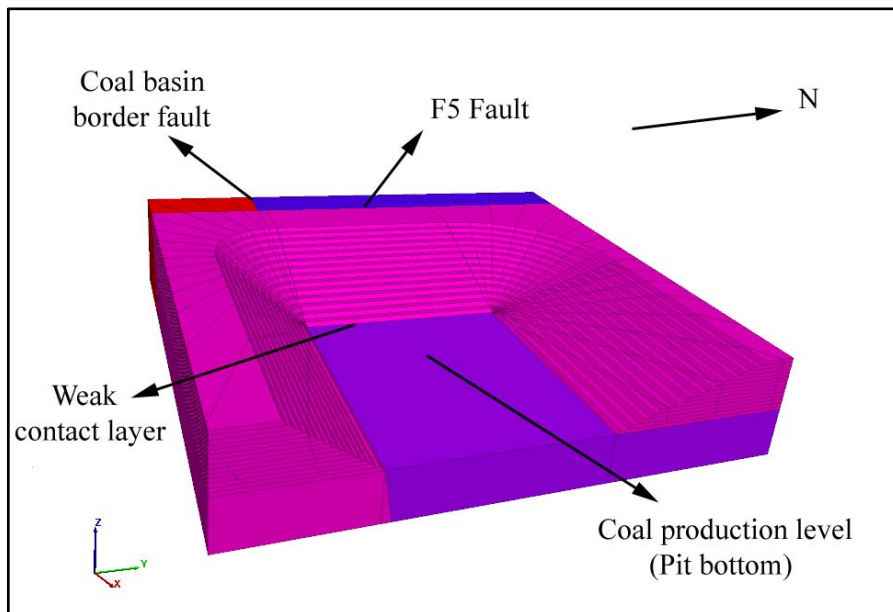


Figure 5.32 Çan western panel slopes 3DEC model

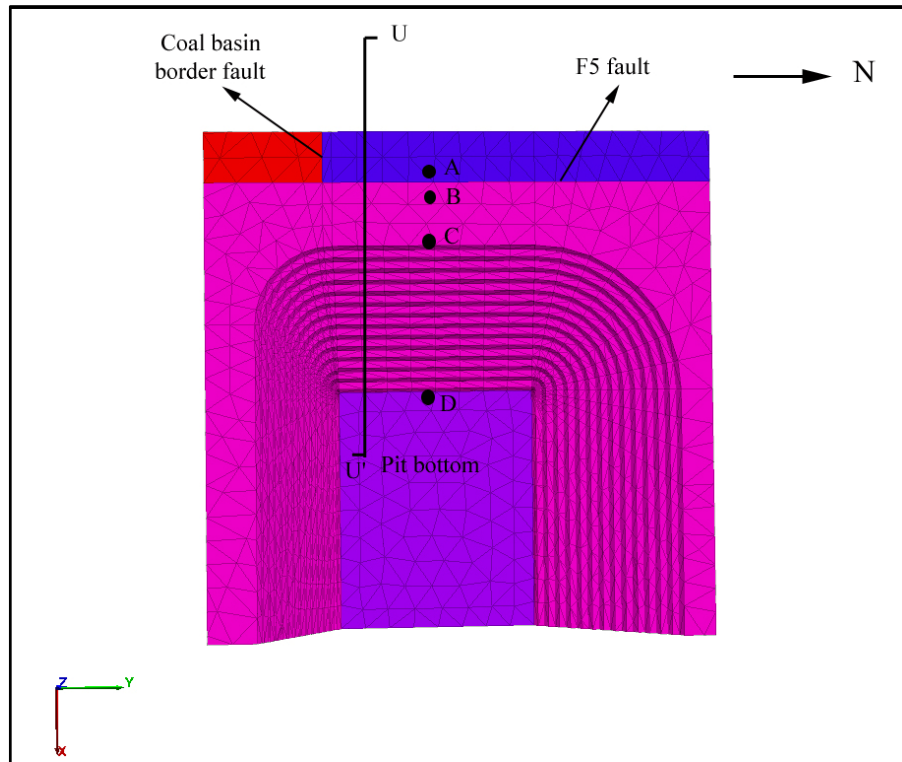


Figure 5.33 Çan western panel slopes model with displacement monitoring points (top view)

The Mohr-Coulomb material and discontinuity properties were determined by Karpuz et al. (2006) by back analyses, which were obtained from previously failed Çan-5 panel, are given in Table 5.8 and Table 5.9 respectively. The corresponding horizontal and vertical displacement graphs are given in Figure 5.34 and Figure 5.35 respectively.

Table 5.8 Material properties of Çan open pit coal basin from back analyses

Property	Overburden	Lignite	Footwall
Density	1661 kg/m ³	1500 kg/m ³	2000 kg/m ³
Young's modulus	100 MPa	500 MPa	25 GPa
Poisson's ratio	0,2	0,2	0,2
Cohesion	16 kPa	500 kPa	5 MPa
Internal friction angle	20°	25°	35°

Table 5.9 Discontinuity properties of Çan open pit coal basin from back analyses

Property	F5	Basin border fault	Weak contact layer
Length	250 m	840 m	700 m
Normal stiffness	160 MPa/m	160 MPa/m	400 MPa/m
Shear stiffness	160 MPa/m	160 MPa/m	400 MPa/m
Cohesion	5 kPa	5 kPa	9.87 kPa
Friction angle	20°	20°	8°

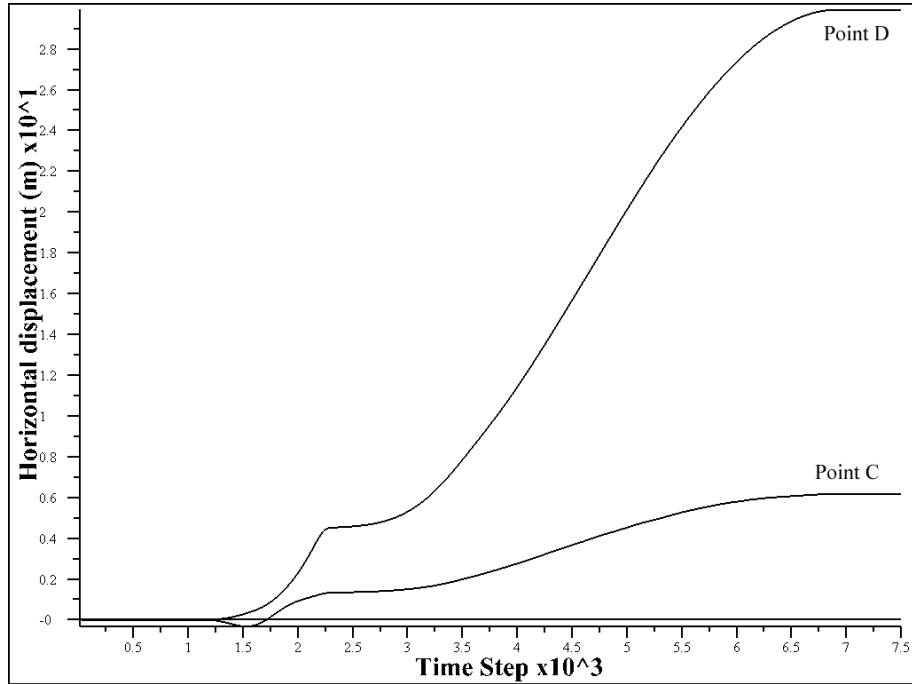


Figure 5.34 Horizontal displacement plots of monitoring points with Mohr-Coulomb model

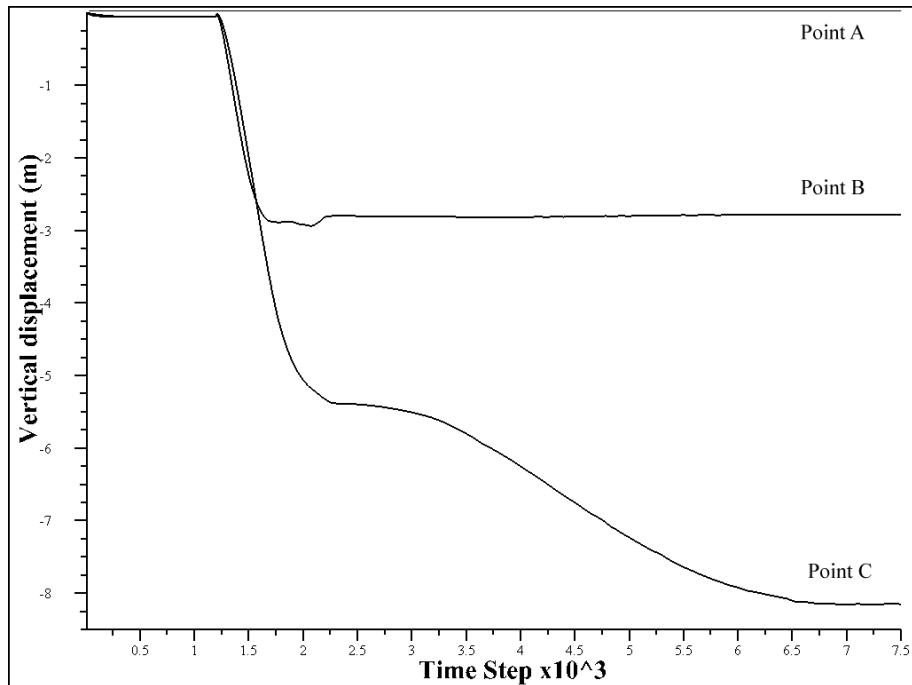


Figure 5.35 Vertical displacement plots of monitoring points with Mohr-Coulomb model

From the field studies, the amplitude of the asperity (caused by undulation) for fault F5 was found to be at most 6 meters and basin border fault was found to be at most 4.6 meters. From the Eq.(2.11) the joint roughness parameters can be found as;

$$JRC_{F5} = \frac{6000}{(1500 \times 2)} = 2$$

$$JRC_{\text{basin border}} = \frac{4600}{(1000 \times 2)} = 2.3$$

Similar to the previous cases, the joint roughness coefficient of the weak contact layer was assumed to be a lower value because of the stratification of the formations. Thus the joint roughness coefficient for the weak contact layer was assumed to be 1.5.

The residual friction angle was assumed to be 90 % of the peak value as 18° for the faults and 7° for the weak contact layer. And the joint wall compressive strength value was back calculated as it was done in the previous cases. For the back calculation of the joint wall compressive strength, the maximum normal stress acting on the discontinuity was calculated for the slope geometry that is shown in Figure 5.36 the maximum overburden depth in the Çan western panels geometry was 200 meters.

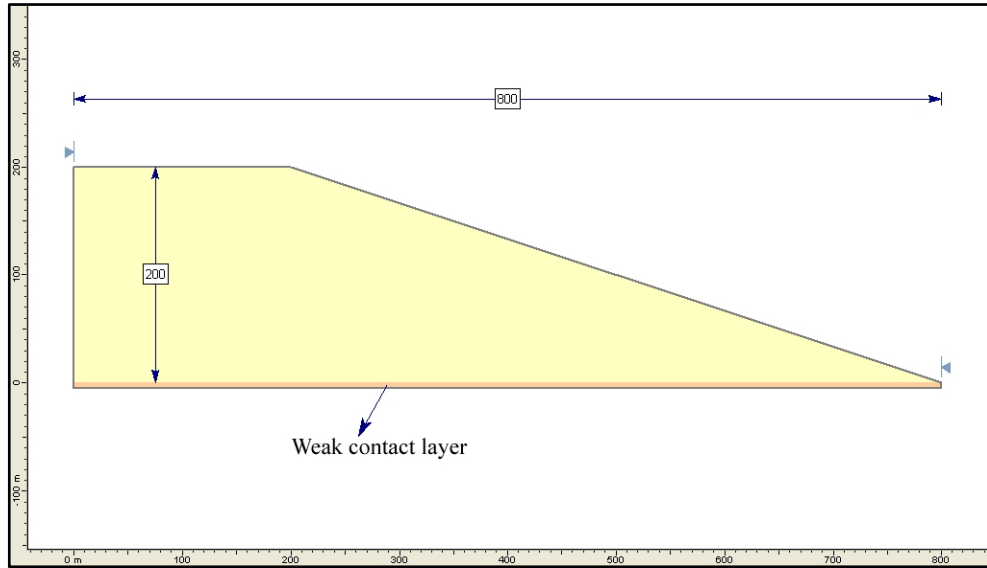


Figure 5.36 Simplified cross sectional model geometry of Çan western panel slope

The maximum normal stress acting on the weak contact layer was calculated from Eq. (5.2) as;

$$\sigma_{n\max} = \frac{200 \times 1661 \times 9.81}{10^6} = 3.26 \text{ MPa}$$

Then by using the JRC parameter, residual friction angle and the average normal stress acting on the discontinuity plane with respect to the Mohr-Coulomb parameters which were listed in Table 5.9, similar to the previous cases, by equating the shear stresses with Mohr-Coulomb and Barton-Bandis criterion the analyses for determining the joint wall compressive strength were carried out.

After the normal stress acting on the discontinuity was determined, the shear stress on the discontinuity should be equal with the two methods. Therefore Eq.(5.4) becomes;

$$0.00987+3.26 \times \tan 8 = 3.26 \times \tan \left(\phi_r + \text{JRC} \times \log_{10} \left(\frac{\text{JCS}}{\sigma_n} \right) \right)$$

Where;

$$\text{JRC}_{\text{weak contact layer}} = 1.5 \text{ MPa},$$

$$\phi_r = 7^\circ$$

So the relation becomes;

$$0.47 = 3.26 \times \tan \left(7 + 1.5 \times \log_{10} \left(\frac{\text{JCS}}{3.26} \right) \right)$$

Then $\text{JCS}_{\text{weak contact layer}}$ becomes;

$$\text{JCS}_{\text{weak contact layer}} = 20.69 \text{ MPa}$$

F5 and basin border faults were dipping with 60° and 80° respectively. The maximum height of the overburden was 200 meters. So the maximum normal stresses acting on the F5 and basin border faults were calculated from Eq.(5.3) as;

$$\sigma_{n\text{maxF5}} = \frac{200 \times 1661 \times 9,81}{10^6} \times \cos 60^\circ = 1.63 \text{ MPa}$$

$$\sigma_{n\text{maxbasinborderfault}} = \frac{200 \times 1661 \times 9,81}{10^6} \times \cos 80^\circ = 0.57 \text{ MPa}$$

Therefore by using Eq.(5.4), JCS of F5 fault becomes;

$$0.005 + 1.63 \times \tan 20 = 1.63 \times \tan \left(\phi_r + \text{JRC} \times \log_{10} \left(\frac{\text{JCS}}{\sigma_n} \right) \right)$$

$$0.60 = 1.63 \times \tan \left(18 + 2 \times \log_{10} \left(\frac{\text{JCS}}{0.21} \right) \right)$$

$$JCS_{F5} = 2.67 \text{ MPa}$$

JCS for basin border fault;

$$0.005 + 0.57 \times \tan 20 = 0.57 \times \tan \left(\phi_r + JRC \times \log_{10} \left(\frac{JCS}{\sigma_n} \right) \right)$$

$$0.21 = 0.57 \times \tan \left(18 + 2.3 \times \log_{10} \left(\frac{JCS}{0.84} \right) \right)$$

$$JCS_{\text{basin border}} = 7.79 \text{ MPa}$$

The uniaxial compressive strength values were taken as equal to the joint wall compressive strength. The final Barton-Bandis discontinuity properties are given in Table 5.10.

Table 5.10 Barton-Bandis discontinuity properties of the Çan western panel slopes

Property	F5 fault	Basin border fault	Weak contact layer
Initial normal stiffness	160 MPa/m	160 MPa/m	400 MPa/m
Shear stiffness number	160 MPa/m	160 MPa/m	400 MPa/m
Stiffness exponent (n_j)	0.9	0.9	0.9
JRC	2	2,3	1,5
JCS	2.67	7.79	20.69
Residual friction angle	18°	18°	7°

The horizontal and vertical displacement amounts are given in Figure 5.37 and Figure 5.38.

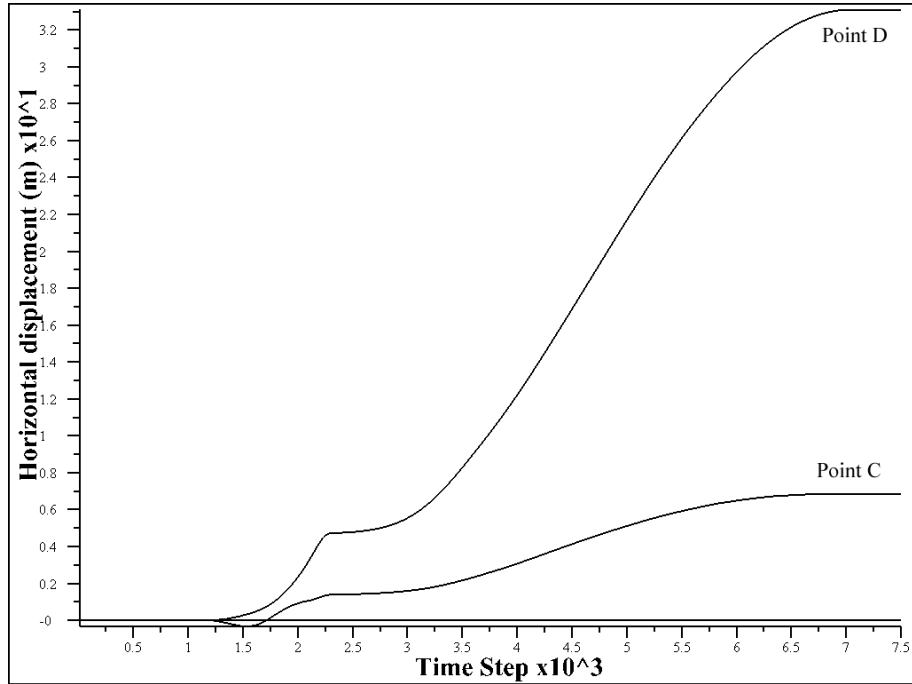


Figure 5.37 Horizontal displacement plots of Çan open pit mine western panel slope monitoring points with Barton-Bandis model

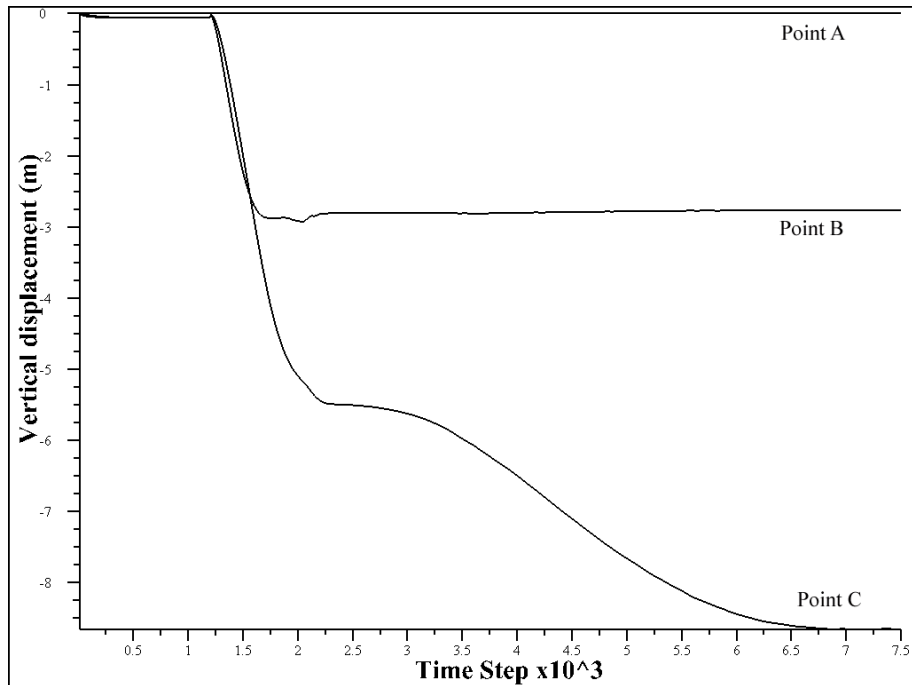


Figure 5.38 Vertical displacement plots of Çan open pit mine western panel slope monitoring points with Barton-Bandis model

From the analyses carried out for Çan open pit mine western panel slopes, it can be seen that the amounts of displacements with two methods are close to each other. The horizontal extend of the slope was approximately 840 meters. The horizontal displacement of the slope was approximately 3.5 % with Mohr-Coulomb model and 3.9 % with the Barton-Bandis model with respect to total length of the slope. The result can be considered as acceptable.

5.8 Results and Discussion

Besides the lab scale test model, it was intended to verify the discontinuity behaviour with large scale slope models.

Barton-Bandis constitutive model presents the mobilization of joint roughness coefficient before and after the peak shear displacement. The roughness reaches its peak value at the peak shear displacement. From the basic slope model, this behaviour was verified for equilibrium condition. Before reaching its peak shear displacement value, the block had significantly higher shear displacement than Mohr-Coulomb model and then remains stable with the same shear strength.

For the slipping condition of the block, the effect of joint roughness coefficient was also verified. As the joint roughness coefficient increases, the amount of shear displacement occurred within a fixed time step decreases.

The model was then used for real case large scale slope problems. The open pit lignite mines of Bursa Lignite Establishments (BLİ) and Çan Lignite Establishments (ÇLİ). The cases were run with previously determined Mohr-Coulomb discontinuity and rock mass properties by Karpuz et al. (2006) and Karpuz et al. (2007). The parameters were determined from back analyses in all three cases. After that the Barton-Bandis shear parameters were determined. The joint roughness

coefficients were determined from the field measurements of the undulations of the discontinuities. After that the maximum normal stress acting on the discontinuity plane was calculated and the joint wall compressive strength values that would equate the shear strengths to the ones obtained from Mohr-Coulomb parameters. From the results, it can be concluded that the models with Barton-Bandis parameters resulted with more deformation with respect to Mohr-Coulomb models. The average maximum horizontal displacement value of Mohr-Coulomb model was 3.27 % when considering the total length of the slopes of the three cases. However, the Barton-Bandis model had resulted with an average of 4.33 % horizontal displacements of these cases. The reason for this can be stated as the mobilization of the joint roughness coefficient after the peak shear displacement has reached. The shear strengths of the discontinuities were continuously decreasing as the shear displacement increases. Besides the reduction of the shear strength, all three cases had weak rock masses. The failure mechanisms did not governed only by the discontinuities. The failure mechanisms of the three cases were the combination of discontinuity failure and rock mass failure following that. As the slipping along the discontinuities had occurred, rock masses were failed because of the rotational movement of the body.

CHAPTER 6

CONCLUSIONS AND RECOMMENDATIONS

Main conclusions derived from this study and recommendations are outlined below;

1. A methodology has been developed based on Barton-Bandis shear strength failure criterion in the three dimensional distinct element code 3DEC. A code in C++ was written for calculation steps of discontinuity surfaces of three dimensional models.
2. The developed model better represents the discontinuity failure, since it considers discontinuity geometrical properties as well as non-linear nature of loading towards failure along discontinuities.
3. A numerically developed mechanical model for direct shear testing was used to verify the behaviour of the discontinuity under normal and shear stresses. The results obtained from numerically developed direct shear test model were found to be within acceptable limits and therefore the reliability of the developed model was verified.
4. The developed model was also verified by modelling three actual discontinuity originated slope failures from different open pit lignite mine sites of TKI.
5. From the case study analyses, the Mohr-Coulomb failure model resulted with an average displacement of 3.27 % when the total length of

slope was considered, while the developed Barton-Bandis failure model resulted with an average displacement of 4.33 %. This behaviour can be explained with the mobilization of discontinuity roughness as the shear displacement along the discontinuity increases, since the shear strength of the discontinuity decreases.

6. The developed model also includes an option for using joint roughness coefficient and joint wall compressive strength values either with the scale correction relations or with large scale field values.
7. The model should also be verified by a case which it's Mohr-Coulomb and Barton-Bandis parameters are determined separately.
8. The model should also be verified for hard rock discontinuous rock slope.

REFERENCES

- Anon, 2005. UDEC v.4.0 Users' Manual, Itasca Consulting Group, Inc. Minneapolis, Minnesota, USA.
- Anon, 2007. 3DEC v.4.1 Users' Manual, Itasca Consulting Group, Inc. Minneapolis, Minnesota, USA.
- Bandis, S., Lumsden, A. C., and Barton, N., 1981. Experimental studies of scale effects on the shear behaviour of rock joints. *International Journal of Rock Mechanics, Mining Sciences and Geomechanics Abstracts*, Vol.18, pp 1-21.
- Bandis, S., Lumsden, A. C., and Barton, N., 1983. Fundamentals of rock joint deformation. *International Journal of Rock Mechanics, Mining Sciences and Geomechanics Abstracts*, Vol.20, No.6, pp 249-268.
- Barton, N., 1973. Review of a new shear strength criterion for rock joints. *Engineering Geology*, Vol.7, pp 287-332.
- Barton, N.R., 1976. The shear strength of rock and rock joints. *International Journal of Rock Mechanics, Mining Sciences and Geomechanics Abstracts*. Vol. 13, No. 10, pp 1-24.
- Barton, N., 2007. *Rock Quality, Seismic Velocity, Attenuation and Anisotropy*. Taylor & Francis Group, London, U.K, p 728.
- Barton, N.R. and Bandis, S.C., 1982. Effects of block size on the the shear behaviour of jointed rock. 23rd U.S. symp. on rock mechanics, Berkeley, pp 739-760.
- Barton, N., Bandis, S., and Bakhtar, K., 1985. Strength, deformation and conductivity coupling of rock joints. *International Journal of Rock*

Mechanics and Mining Sciences and Geomechanics Abstracts,
Vol.22, No.3, pp 121-140.

Barton, N., and Choubey, V., 1977. The shear strength of rock joints in theory and practice. *Rock Mechanics*, Vol.10, pp 1-54.

Bhasin, R., and Hoeg, K., 1997. Numerical modelling of block size effects and influence of joint properties in multiply jointed rock. *Tunnelling and Underground Space Technology*, Vol.12, No.3, pp 407-415.

Bhasin, R., and Kaynia, A. M., 2004. Static and dynamic simulation of a 700-m high rock slope in western Norway. *Engineering Geology*, Vol.71, pp 213-226.

C++ Resources Network. <http://www.cplusplus.com>. Last accessed date: 20 August 2008.

Choi, S. O., and Chung, S. K., 2004. Stability analysis of jointed rock slopes with the Barton-Bandis constitutive model in UDEC. *International Journal of Rock Mechanics and Mining Sciences*, Vol.41, pp 469-474.

Chryssanthakis, P., Barton, N., Lorig, L., and Christianson, M., 1997. Numerical simulation of fiber reinforced shotcrete in a tunnel using the discrete element method. *International Journal of Rock Mechanics and Mining Sciences*, Vol.34, No.3-4, Paper No. 054.

Corkum, A. G., and Martin, C. D., 2004. Analysis of a rock slide stabilized with a toe-berm: a case study in British Columbia, Canada. *International Journal of Rock Mechanics and Mining Sciences*, Vol.41, pp 1109-1121.

Cundall, P. A., 1971. A Computer Model for Simulating Progressive Large Scale Movements in Blocky Rock Systems. *Proceedings of the Symposium of the International Society of Rock Mechanics (Nancy, France, 1971)*, Vol. 1, Paper No. II-8.

- Cundall P. A., 1980. UDEC — A Generalized Distinct Element Program for Modelling Jointed Rock. Report PCAR-1-80, Peter Cundall Associates Report, European Research Office, U.S. Army, Contract DAJA37-79-C-0548.
- Cundall, P. A., 1988. Formulation of a Three-Dimensional Distinct Element Model—Part I: A Scheme to Detect and Represent Contacts in a System Composed of Many Polyhedral Blocks. International Journal of Rock Mechanics, Mineral Sciences & Geomechanics Abstracts, Vol. 25, pp 107-116.
- Cundall, P. A., and R. D. Hart, 1985. Development of Generalized 2-D and 3-D Distinct Element Programs for Modeling Jointed Rock. Itasca Consulting Group; Misc. Paper SL-85-1, U.S. Army Corps of Engineers.
- Cundall P. A., and O. D. L. Strack., 1979a. The Distinct Element Method as a Tool for Research in Granular Media, Part I. University of Minnesota, Department of Civil and Mineral Engineering, Report to National Science Foundation, Grant ENG 76-20711.
- Cundall, P. A., and Hart, R. D., 1992. Numerical modeling of discontinua. Engr. Comp., Vol.9, No.2, pp 101-113.
- Giani, G. P., 1992. Rock Slope Stability Analysis. Rotterdam; Brookfield, A. A. Balkema, p 361.
- Goodman, R., E., 1976. Methods of Geological Engineering in Discontinuous Rock; West, New York, p 472.
- Hart, R., Cundall, P. and Lemos, J., 1988. Formulation of a Three-Dimensional Distinct Element Model — Part II: Mechanical Calculations for Motion and Interaction of a System Composed of Many Polyhedral Blocks. International Journal of Rock Mechanics, Mineral Sciences & Geomechanics Abstracts. Vol. 25, pp 117-126.

- Hocking, G., Mustoe, G., G., W., and Williams, J., R., 1985. CICE Discrete Element Code — Theoretical Manual. Lakewood, Colorado: Applied Mechanics Inc.
- Hoek, E., 2007. Practical Rock Engineering. Dr. Evert Hoek's Rock Engineering Course notes. Unpublished, p 313.
- Hoek, E., and Bray, J., 1981. Rock Slope Engineering. The Institution of Mining and Metallurgy, London.
- Hökmark, H., 1998. Numerical study of the performance of tunne plugs. Engineering Geology, Vol.49, pp 327-335.
- Hutri, K. L., and Antikainen, J., 2002. Modelling of the bedrock response to glacial loading at the Olkiluoto site, Finland. Engineering Geology, Vol.67, pp 39-49.
- ISRM, 1974. Suggested methods for determining shear strength. International Journal of Rock Mechanics Mineral Sciences and Geomechanics Abstracts. Vol.15, pp 89-97.
- ISRM, 1978. Suggested methods for determining hardness and abrasiveness of rocks. International Journal of Rock Mechanics Mineral Sciences and Geomechanics Abstracts. Vol.15, pp 89-97.
- Itasca Consulting Group, Inc., 2005. Particle Flow Code in 2 Dimensions and Particle Flow Code in 3 Dimensions, Version 3.1. Minneapolis: ICG.
- Karpuz, C., Tutluođlu, L., Koçal, A., Önal, K., 2005. Türkiye Kömür İşletmeleri Kurumu TKİ, Çan İşletmesi açık ocakları Çan/B panolarında şev tasarımı. Report to Turkish Coal Enterprises (TKİ), Project Code: 04-03-05-2-00-11, p 108.
- Karpuz, C., Koçyiğit, A., Tutluođlu, L., Koçal, A., Erdem, E., Alkılıçgil, Ç., 2006. Türkiye Kömür İşletmeleri Kurumu TKİ, Orhaneli İşletmesi Açık Ocakları A-1, A-5 ve Gümüşpınar panolarında Şev Tasarımı

ve Dragline Çalışma Sisteminin Belirlenmesi. Report to Turkish Coal Enterprises (TKİ), Project Code: 05-03-05-2-00-13, p 100.

Karpuz, C., Koçyiğit, A., Tutluoğlu, L., Koçal, A., Alkılıçgil, Ç., Deveci, Ş., 2007. Türkiye Kömür İşletmeleri Kurumu TKİ, Orhaneli İşletmesi açık ocakları Dikmentepe civarında şev tasarımı yapılması. Report to Turkish Coal Enterprises (TKİ), Project Code: 06-03-05-2-00-10, p 43.

Karpuz, C., Koçyiğit, A., Tutluoğlu, L., Düzgün, H. Ş., Koçal, A., Alkılıçgil, Ç., Deveci, Ş., 2007. Türkiye Kömür İşletmeleri Kurumu TKİ, Çan İşletmesi açık ocaklarında Kocabaş Çayı ile ocak arası ve batı panolarında şev tasarımı yapılması. Report to Turkish Coal Enterprises (TKİ), Project Code: 06-03-05-2-00-13, p 103.

Konietzky, H., Kamp, L.te, Hammer, H., Niedermeyer, S., 2001. Numerical modelling of insitu stress conditions as an aid in route selection for rail tunnels in complex geological formations in South Germany. Computers and Geotechnics. Vol. 28, pp 495-516.

Kulatilake, P., H., S., W., Wang, S., Stephansson, O., 1993. Effect of finite size joints on the deformability of jointed rock in three dimension. International Journal of Rock Mechanics, Mining Sciences and Geomechanics Abstracts. Vol. 30, No. 5, pp 479-501.

Kulhaway, F. H., 1978. Geomechanical model for rock foundation settlement. Journal of Geotechnical Division, Proceedings of American Society of Civil Engineers, Vol.106(GT2), pp 221-227.

Kveldsvik, V., Nilsen, B., Einstein, H. H., and Nadim, F., 2007. Alternative approaches for analyses of a 100,000 m³ rock slide based on Barton-Bandis shear strength criterion. Landslides, Vol. 5, No. 2, pp. 161-176.

Mining Life Web Page. <http://www.mininglife.com>. Last accessed date: 27 August 2008.

- Murray, W. H., 2002. Visual C++.NET: The Complete Reference. McGraw-Hill/Osborne, U.S.A, p 1073.
- Paşamehmetoğlu, A.G., Özgenoğlu, A., Karpuz, C., Sarı, D., 1991. Çan Linyit İşletmesi açık ocaklarında şev stabilitesi çalışmaları. Report to Turkish Coal Enterprises (TKİ), No: 89-03-05-01-07, p 111.
- Pratt, H., R., Black, A., D., and Brace, W., F., 1974. Friction and deformation of jointed quartz diorite. Proceedings of 3rd Congress of International Society for Rock Mechanics, Denver, CO. Vol. IIA, pp 306-310.
- Richards, L. R., 1975. The shear strength of joints in weathered rock. PhD Thesis, University of London, Imperial College, p 427.
- Shi, G.-H., 1989. Discontinuous Deformation Analysis — A New Numerical Model for the Statics and Dynamics of Block Systems. Lawrence Berkeley Laboratory, Report to DOE OWTD, Contract AC03-76SF0098, September 1988; also Ph.D. Thesis, University of California, Berkeley.
- Walton, O. R., 1980. Particle Dynamic Modeling of Geological Materials. Lawrence Livermore National Laboratory, Report UCRL-52915.
- Walton, O. R., Braun, R., L., Mallon, R., G., and Cervelli, D., M., 1988. Particle-Dynamics Calculations of Gravity Flows of Inelastic, Frictional Spheres. Micromechanics of Granular Material. pp 153-161. Amsterdam: Elsevier Science Publishers.
- Sjöberg, J., 1996. Large scale slope stability – A review. Technical Report, Lulea University of Technology, Division of Rock Mechanics, p 229.
- Vardakos, S. S., Gutierrez, M. S., and Barton, N., 2006. Back-analysis of Shimizu Tunnel No.3 by distinct element modelling. Tunnelling and Underground Space Technology. Article in press.

APPENDIX A

STRUCTURE OF THE PROGRAM

The partial definition of the constitutive model, model constructor and execution part of the code is given in Table A.1-A11.

Table A.1 Partial class definition for base class, ConstitutiveModel

```
class JmodelBartonBandis : public JointModel {
public:
    JmodelBartonBandis();
    virtual String getName() const;
    virtual String getFullName() const;
    virtual UInt getMinorVersion() const;
    virtual String getProperties() const;
    virtual String getStates() const;
    virtual Variant getProperty(UInt index) const;
    virtual void setProperty(UInt index,const Variant &p);
    virtual JModelBartonBandis *clone() const { return new
JModelBartonBandis(); }
    virtual Double getMaxNormalStiffness() const { return kn_; }
    virtual Double getMaxShearStiffness() const { return ks_; }
    virtual void copy(const JointModel *mod);
    virtual void run(UByte dim,State *s);
    virtual void initialize(UByte dim,State *s);
```

Table A.2 Model constructor

JModelBartonBandis::JModelBartonBandis() :

```

    kn_(0),
    ks_(0),
    friction_(0),
    dilation_(0),
    tension_(0),
    zero_dilation_(0),
    jcso_(0),
    jrco_(0),
    sigmac_(0),
    nj_(0),
    lo_(0),
    ln_(0),
    res_friction_(0),
    res_dilation_(0),
    res_tension_(0),
    tan_friction_(0),
    tan_dilation_(0),
    tan_res_friction_(0),
    tan_res_dilation_(0),
    large_(0),
{
}

```

Table A.3 Summary of members of structure State

Double area_;	Contact area
Double normal_force_;	Contact normal force
DVect3 shear_force_;	Contact shear force
Double normal_disp_;	Normal displacement
DVect3 shear_disp_;	Shear displacement
Double normal_disp_inc_;	Normal displacement increment
DVect3 shear_disp_inc_;	Shear displacement increment
Double normal_force_inc_;	Normal force increment
DVect3 shear_force_inc_;	Shear force increment
Double dnop_;	Fraction of normal displacement increment that causes contact tension or separation

Table A.4 Scale correction step

```
Double exp1 = -0.02 * jrco_;
Double exp2 = -0.03 * jrco_;
Double ratio1 = ln_ / lo_;

Double jrcn;
Double jcsn;

    bool large_ = false;

        if (large_)
        {
            jrcn = jrco_;
            jcsn = jcso_;
        }
        else
        {

            jrcn = jrco_ * pow(ratio1,exp1);
            jcsn = jcso_ * pow(ratio1,exp2);
        }

```

Table A.5 Normal stiffness calculation step

```
// Normal stiffness
// Maximum allowable closure
Double ar = 0.2 * sigmac_ / jcso_;
Double ic = ar - 0.1;
Double aj = (jrco_/5) * ic;
Double vic = jcso_ / aj;
Double po = pow (vic,-0.245);
Double vm = -0.296 - (0.0056 * jrco_) + (2.241 * po);

//Normal stiffness equation for loading
Double frac = - (s->normal_disp_ *1000) / vm;
Double brac = 1 - frac;
Double power = pow (brac,2);
Double kna = kn_ / power;
Double kni = kna * s->area ;

```

Table A.6 Calculation steps for shear stiffness of the joint

```

Double ratio2 = jrcn / lo_ ;
Double peakdisp = (ln_ / 500) * pow(ratio2,0.33);

Double sheardisp = s->shear_disp_.mag();
Double dispratio = sheardisp / peakdisp ;

//shear stiffness conditions
Double ini = 0.75 * res_friction_ ;
Double tani = tan (ini * dDegRad);
Double div = tani / (0.2 * peakdisp);

//peak shear strength calculation
Double loga = log10 (jcsn / (s->normal_force_ / s->area_));
Double tanici = res_friction_ + jrcn * loga;
Double tanp = tan (tanici * dDegRad);
Double fsmax = (s->normal_force_ / s->area_) * tanp;

//current shear stress and shear strength ratio
Double fsm = s->shear_force_.mag() / s->area_ ;
Double rat = fsm / fsmax;

Double pran = pow(rat,2);
Double parant = 1 - rat;
Double povv = pow(parant,2);
Double normal = s->normal_force_ / s->area_ ;
Double normalpov = pow(normal,nj_);

//shear stiffness
Double ksi;
if (dispratio <= 0.002)
    ksi = normal * div * ln_ * s->area_ ;
else
    ksi = ks_ * normalpov * povv * s->area_ ;

```

Table A.7 Calculation steps for mobilization of roughness coefficient during shear

```

Double ratio3 = jcsn / normal;

Double ruff = jrcn * log10 (ratio3);

//Mobilization of roughness
Double jrcmob;
if ((0<=dispratio) &&
    (dispratio<0.2))
    {
        jrcmob = jrcn * (-res_friction_ / ruff);
    }
else if ((0.2<=dispratio) &&
    (dispratio<0.3))
    {
        jrcmob = jrcn * (-0.25 * res_friction_ / ruff);
    }
else if ((0.3<=dispratio) &&
    (dispratio<0.45))
    {
        jrcmob = jrcn * 0;
    }
else if ((0.45<=dispratio) &&
    (dispratio<0.6))
    {
        jrcmob = jrcn * 0.50;
    }
else if ((0.6<=dispratio) &&
    (dispratio<0.8))
    {
        jrcmob = jrcn * 0.75;
    }
else if ((0.8<=dispratio) &&
    (dispratio<1))
    {
        jrcmob = jrcn * 0.90;
    }
else if ((1<=dispratio) &&
    (dispratio<1.5))
    {
        jrcmob = jrcn * 1;
    }
else if ((1.5<=dispratio) &&
    (dispratio<2))

```

Table A.7 continued

```
{
    jrcmob = jrcn * 0.90;
}
else if ((2<=dispratio) &&
        (dispratio<3))
    {
        jrcmob = jrcn * 0.85;
    }
else if ((3<=dispratio) &&
        (dispratio<4))
    {
        jrcmob = jrcn * 0.75;
    }
else if ((4<=dispratio) &&
        (dispratio<6))
    {
        jrcmob = jrcn * 0.70;
    }
else if ((6<=dispratio) &&
        (dispratio<8))
    {
        jrcmob = jrcn * 0.60;
    }
else if ((8<=dispratio) &&
        (dispratio<10))
    {
        jrcmob = jrcn * 0.55;
    }
else if ((10<=dispratio) &&
        (dispratio<20))
    {
        jrcmob = jrcn * 0.50;
    }
else if ((20<=dispratio) &&
        (dispratio<40))
    {
        jrcmob = jrcn * 0.40;
    }
else if ((40<=dispratio) &&
        (dispratio<60))
    {
        jrcmob = jrcn * 0.30;
    }
}
```

Table A.7 continued

```

else if ((60<=dispratio) &&
        (dispratio<80))
    {
        jrcmob = jrcn * 0.20;
    }
else if ((80<=dispratio) &&
        (dispratio<100))
    {
        jrcmob = jrcn * 0.10;
    }
else
    {
        jrcmob = jrcn * 0;
    }

```

Table A.8 Normal force calculation

```

// normal force
s->normal_force_inc_ = -kni * s->normal_disp_inc_;
s->normal_force_ += s->normal_force_inc_;

```

Table A.9 Tensile failure decision step and shear force calculation steps

```

// tensile strength
Double ten;
if (s->state_)
    ten = -res_tension_ * s->area_;
else
    ten = -tension_ * s->area_;

// check tensile failure
Bool tenflag = false;
if (s->normal_force_ <= ten)
{
    s->normal_force_ = ten;
    if (!s->normal_force_)
    {
        s->shear_force_ = DVect3(0,0,0);
        tenflag = true; // tensile failure is completed
    }
}

```

Table A.9 continued

```

s->state_ |= tension_now;
  s->normal_force_inc_ = 0.0;
  s->shear_force_inc_ = DVect3(0,0,0);
}

// shear force
if (!tenflag)
{
  s->shear_force_inc_ = s->shear_disp_inc_ * -ksi;
  s->shear_force_ += s->shear_force_inc_;
  Double fsm = s->shear_force_.mag() / s->area_;

// shear strength
  Double loga = log10 (jcsn / (s->normal_force_ / s->area_));
  Double tanici = res_friction_ + jrccmob * loga;
  Double tanp = tan (tanici * dDegRad);
  Double fsmax;

  fsmax = (s->normal_force_ / s->area_) * tanp ;

  if (!s->state_)
    fsmax = (s->normal_force_ / s->area_) * tanp;
  else

{ // the residual value where jrc is totally worn out
  Double resamueff = tan_res_friction_;

  fsmax = s->normal_force_ / s->area_ * resamueff;
}

  if (fsmax < 0.0) fsmax = 0.0;

// check for slip
if (fsm >= fsmax)
{
  Double rat = 0.0;
  if (fsm) rat = fsmax / fsm;
  s->shear_force_ *= rat;
  s->state_ |= slip_now;
  s->shear_force_inc_ = DVect3(0,0,0);
}

```

Table A.10 Calculation steps for dilatational component of normal force

```
// dilation
  if (!dilation_)
  {
    Double zdd = zero_dilation_;
    Double usm = s->shear_disp_.mag();
    if (!zdd) zdd = 1e20;
    if (usm < zdd)
    {
      Double dusm = s->shear_disp_inc_.mag();
      Double dil = 0.0;

      if (!s->state_)
        dil = tan((0.5*jrcmob*log10(jcsn/(s->normal_force_ / s-
>area_))) * dDegRad);

      else
      {
        Double resdileff = tan((0.5*jrcmob*log10(jcsn/(s->normal_force_ /
s->area_))) * dDegRad);

        if (!resdileff) resdileff = tan((0.5*jrcmob*log10(jcsn/(s->normal_force_ / s-
>area_))) * dDegRad);
        dil = resdileff;
      }

      s->normal_force_ += kni * dil * dusm;
    }
  }

```

APPENDIX B

NORMAL DEFORMATION BEHAVIOUR

In this part, the executable code of the direct shear test model and the maximum closure plots with different joint roughness coefficients (JRC), joint wall compressive strength (JCS) and uniaxial compressive strength (σ_c) are given in Figure B.1-B.32;

The executable code for the direct shear test model is;

```
; direct shear test

config cppudm

;bottom block
poly brick -0.15,0.15 -0.10,0.10 -0.10,0.0
gen edge 1

;top block
poly brick -0.10,0.10 -0.1,0.10 0.0,0.10
gen edge 0.2

set jcondf 1
set jmatdf 1
prop mat 1 jkn 1e2 jks 1e4 jfric 10 jcoh 5e3

jmodel model exampled

;material property assignment
prop mat=1 density = 0.0026 k=4e3 g=3e3

;joint property assignment
jmodel jkn=1e5 jks=1e4 resfriction=20.0 jcso=100 jrco=15 sigmac=150 nj =
0.8 lo = 0.1 ln=0.2
hide range z 0 .1
```

```
bound xvel = 0 zvel=0 range zr -1 0.01
```

```
seek
```

```
; normal load 5MPa
```

```
bound str 0 0 -5 0 0 0 range z .09 .11
```

```
;time step for initial settling
```

```
step 1000
```

```
pl block
```

```
pl reset
```

```
;fish function for calculating average stresses and displacement for the joint  
plane
```

```
def av_str
```

```
whilestepping
```

```
sstav = 0.0
```

```
nstav = 0.0
```

```
njdisp = 0.0
```

```
sjdisp = 0.0
```

```
ncon = 0
```

```
jarea = 0.04
```

```
ic = contact_head
```

```
loop while ic # 0
```

```
icsub = c_cx(ic)
```

```
loop while icsub # 0
```

```
ncon = ncon + 1
```

```
sstav = sstav + cx_xsforce(icsub)
```

```
nstav = nstav + cx_nforce(icsub)
```

```
njdisp = njdisp + cx_ndis(icsub)
```

```
sjdisp = sjdisp + cx_xsdis(icsub)
```

```
icsub = cx_next(icsub)
```

```
endloop
```

```
if ncon # 0
```

```
sstav = sstav / jarea
```

```
nstav = nstav / jarea
```

```
njdisp = -1800 * njdisp / ncon
```

```
sjdisp = - sjdisp / ncon
```

```
endif
```

```
ic = c_next{ic}
```

```

endloop
end

reset disp
reset jdisp

; shear load
hide range z -.1 0
bound xvel=0.8 range z -.1 1.1
bound yvel=0.0 range z -.1 1.1
seek

; displacement and stress monitoring
hist unbal ncyc 5
hist @sstav @nstav @njdisp @sjdisp

hist sdis -1 -1 0 ndis -1 -1 0
hist sdis -1 1 0 ndis -1 1 0
hist sdis 0 0 0 ndis 0 0 0
histsstr -1 -1 0 nstr -1 -1 0
histsstr -1 1 0 nstr -1 1 0
histsstr 0 0 0 nstr 0 0 0
hist sfor -1 -1 0 nfor -1 -1 0
hist szz 0 0 0.1
hist zdisp 0 0 0.1
hist zdisp 0 0 0

hist label 2 'Shear Stress'
hist label 3 'Normal Stress'
hist label 4 'Normal Displacement'
hist label 5 'Shear Displacement'

cyc 20000
;
return

```

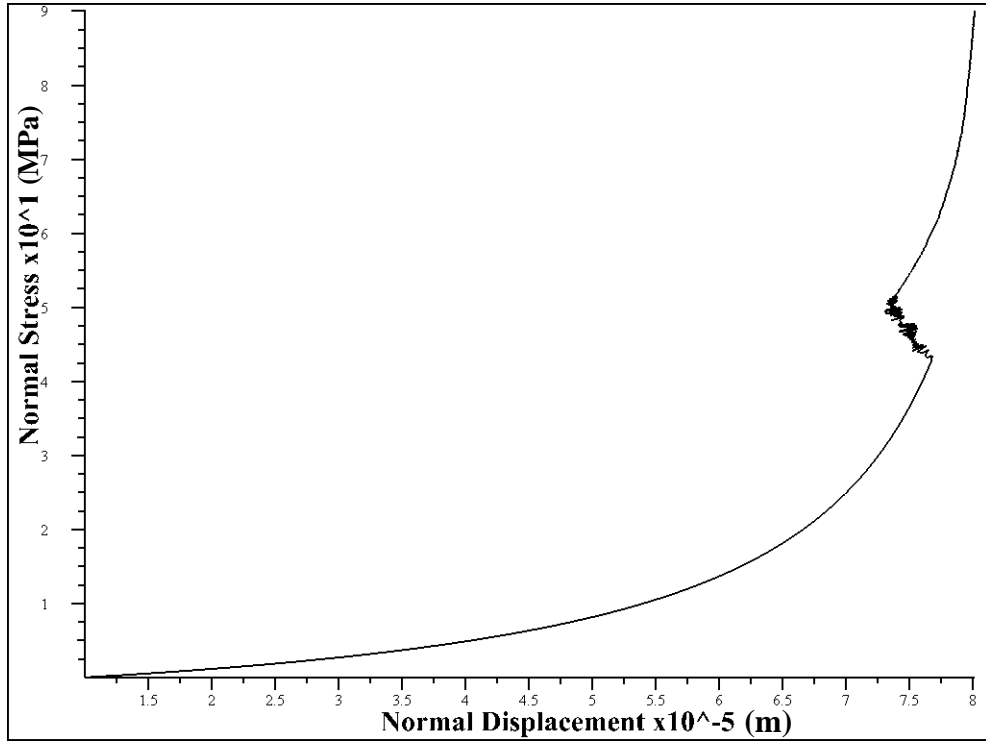


Figure B.1 Normal stress – normal closure plot with JRC = 2

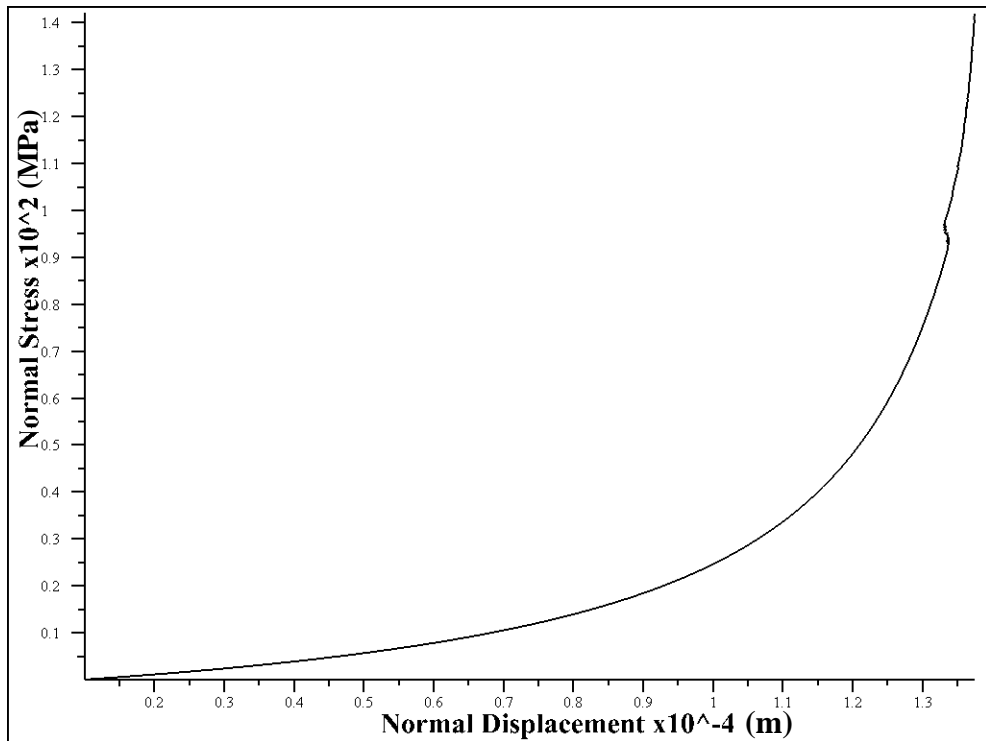


Figure B.2 Normal stress – normal closure plot with JRC = 4

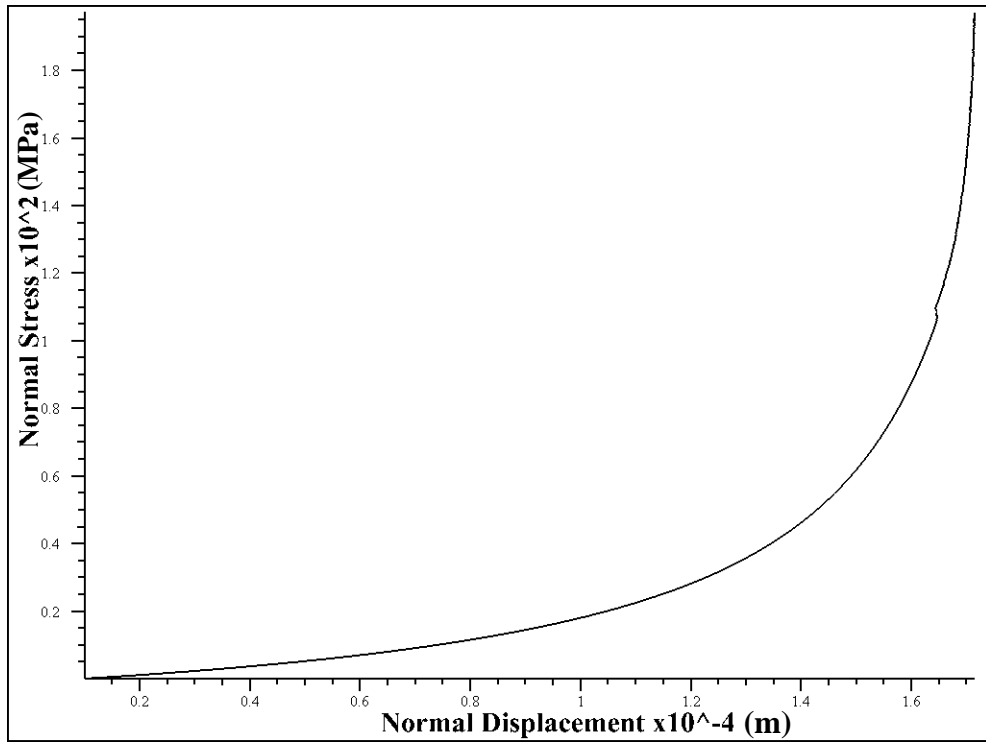


Figure B.3 Normal stress – normal closure plot with JRC = 6

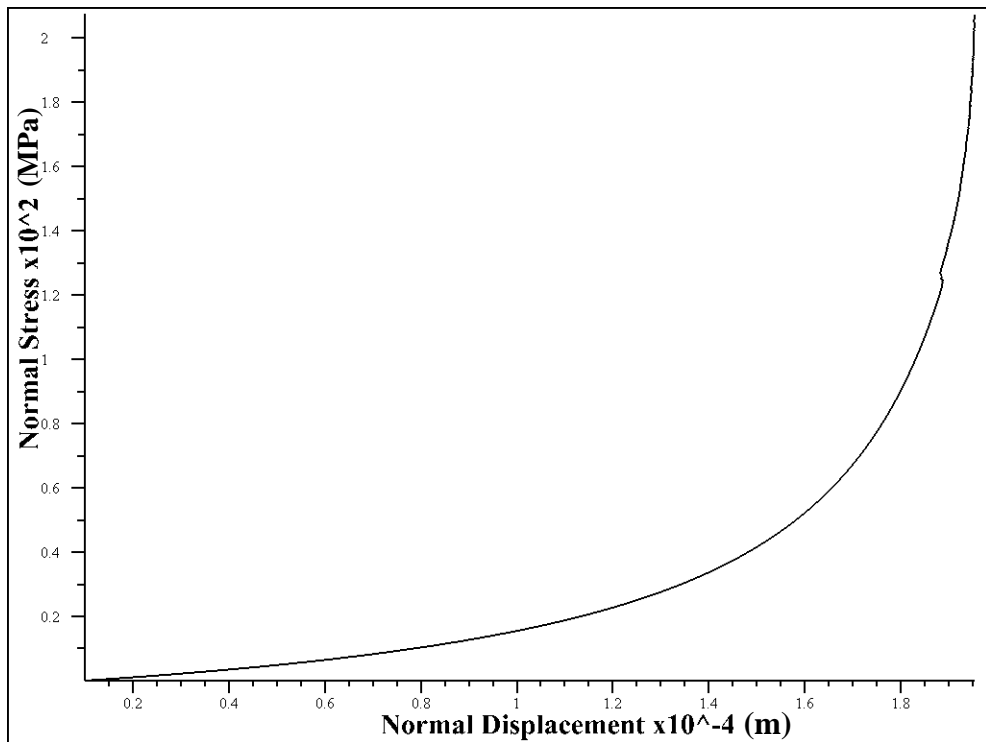


Figure B.4 Normal stress – normal closure plot with JRC = 8

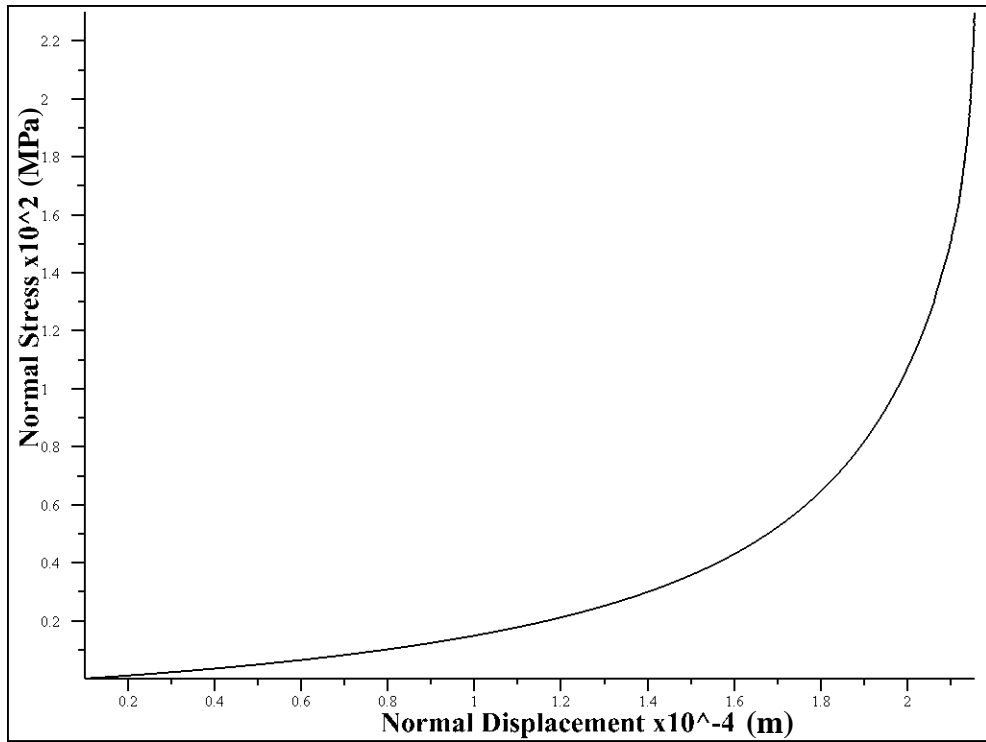


Figure B.5 Normal stress – normal closure plot with JRC = 10

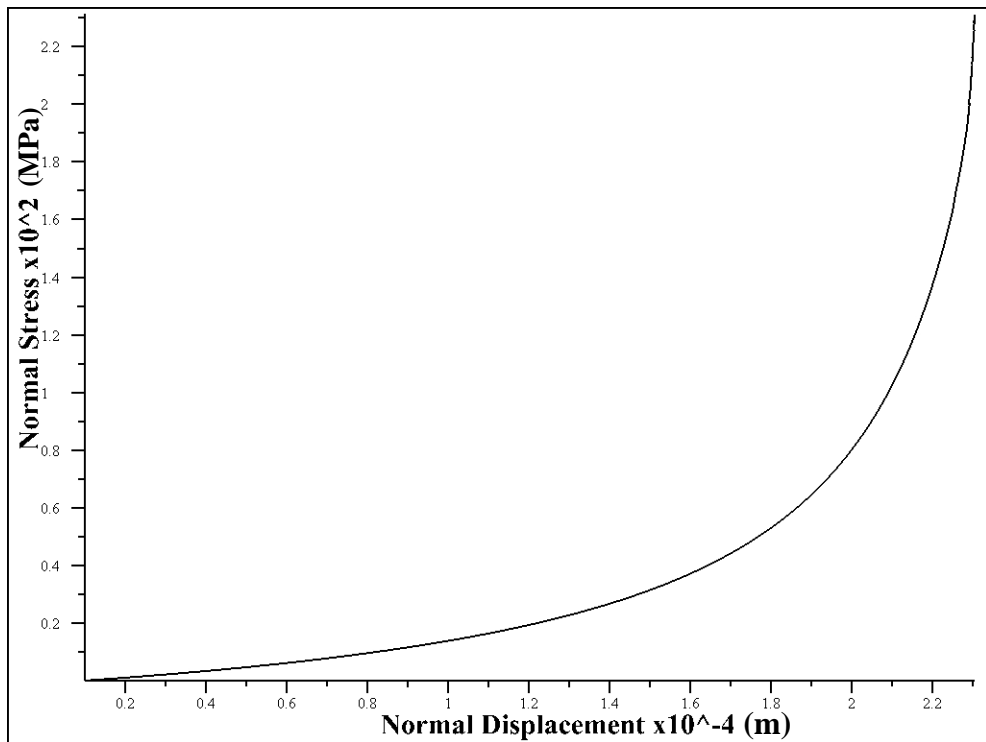


Figure B.6 Normal stress – normal closure plot with JRC = 12

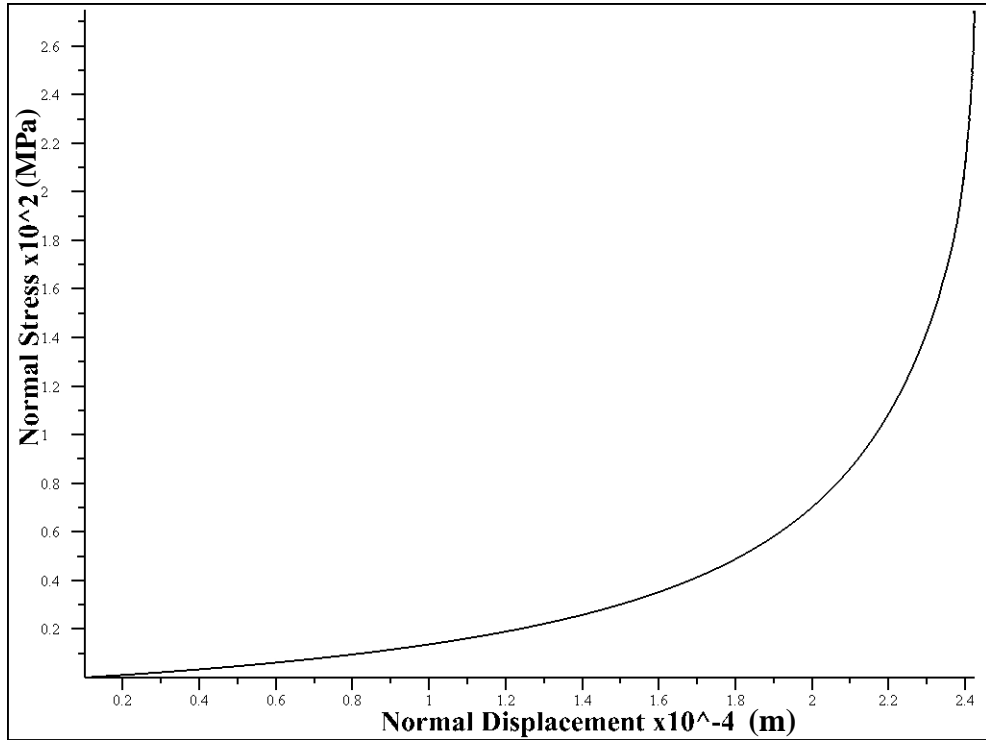


Figure B.7 Normal stress – normal closure plot with JRC = 14

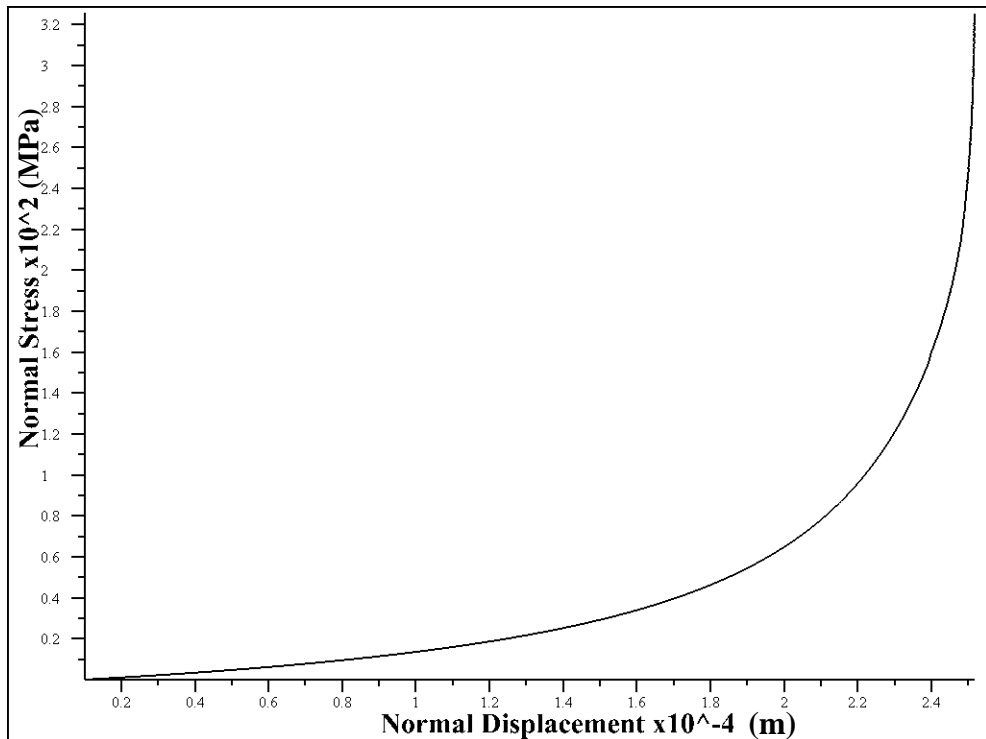


Figure B.8 Normal stress – normal closure plot with JRC = 16

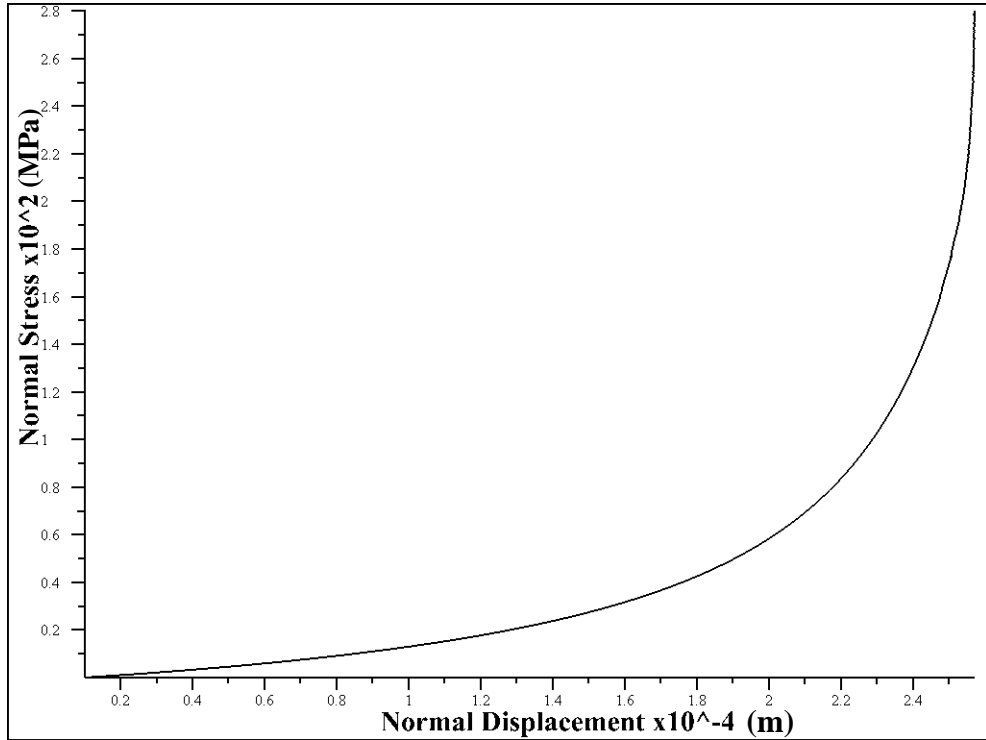


Figure B.9 Normal stress – normal closure plot with JRC = 18

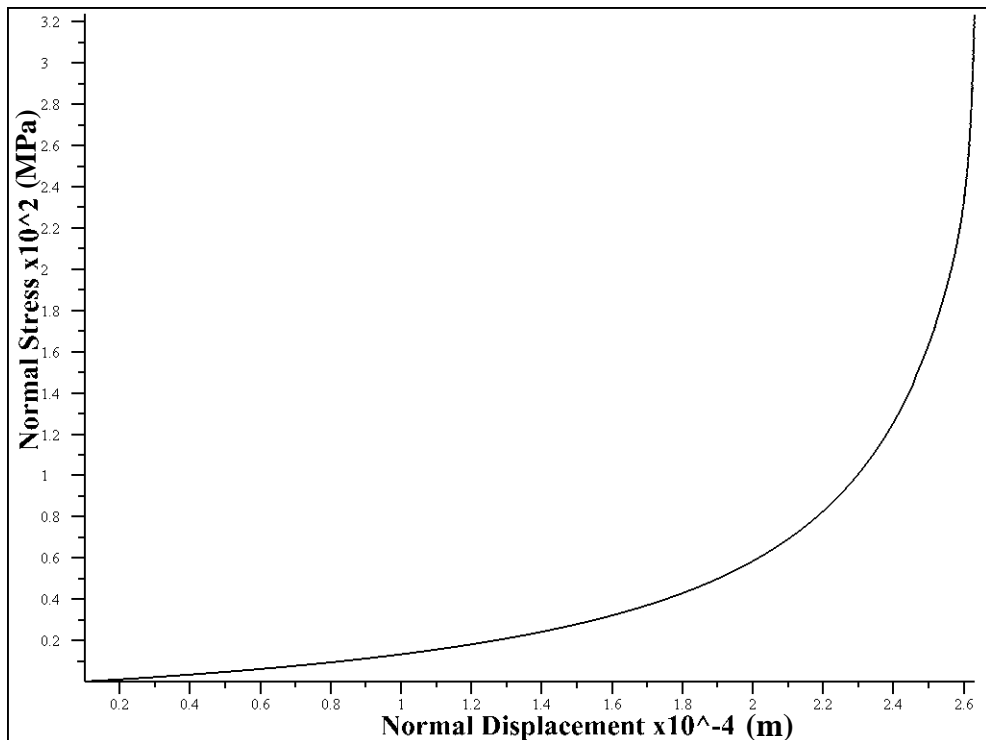


Figure B.10 Normal stress – normal closure plot with JRC = 20

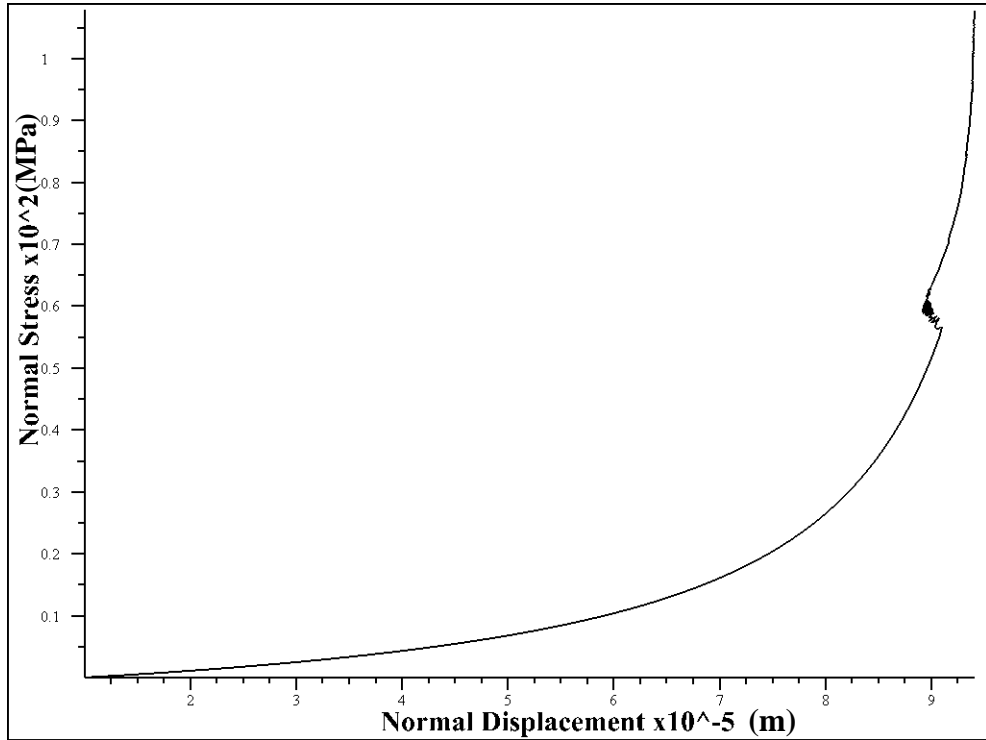


Figure B.11 Normal stress – normal closure plot with JCS = 40 MPa

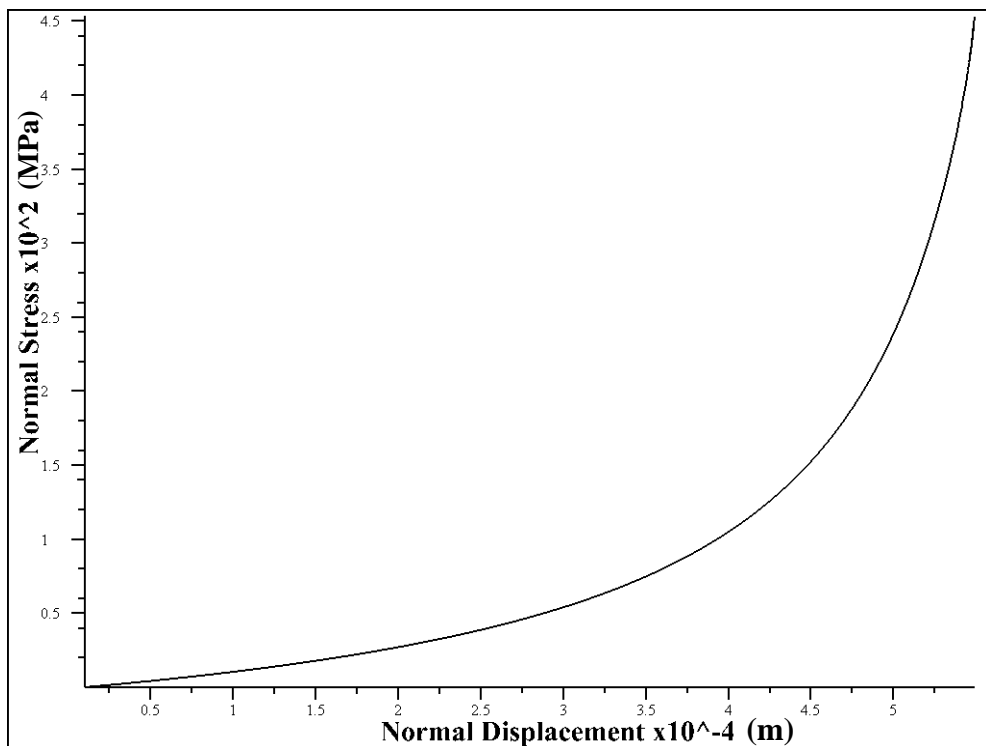


Figure B.12 Normal stress – normal closure plot with JCS = 50 MPa

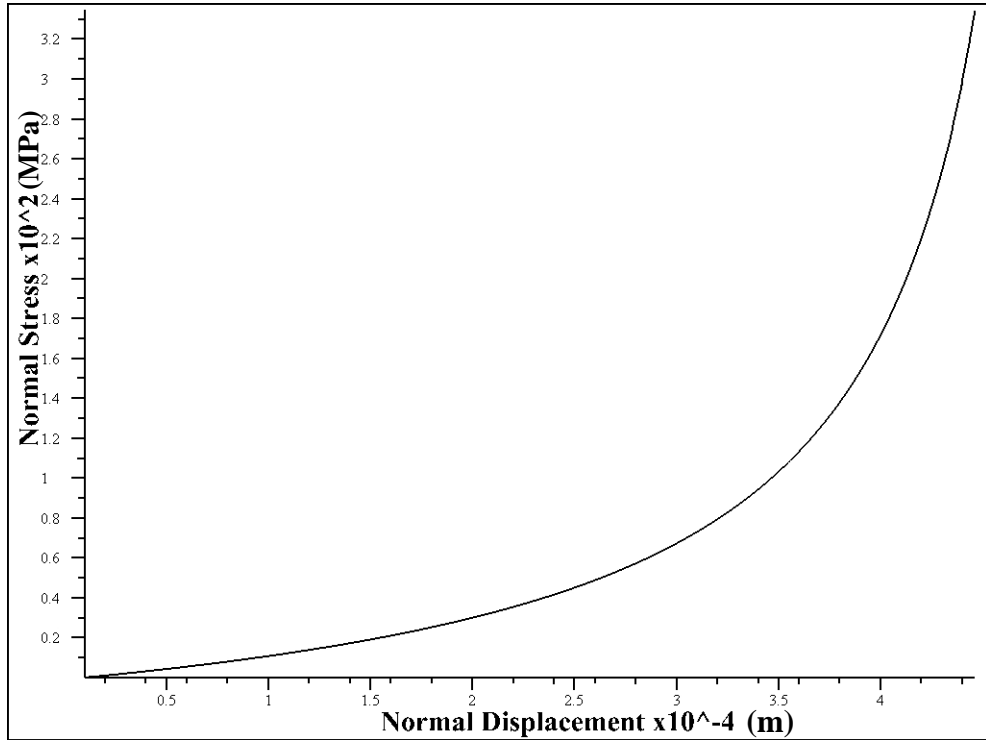


Figure B.13 Normal stress – normal closure plot with JCS = 60 MPa

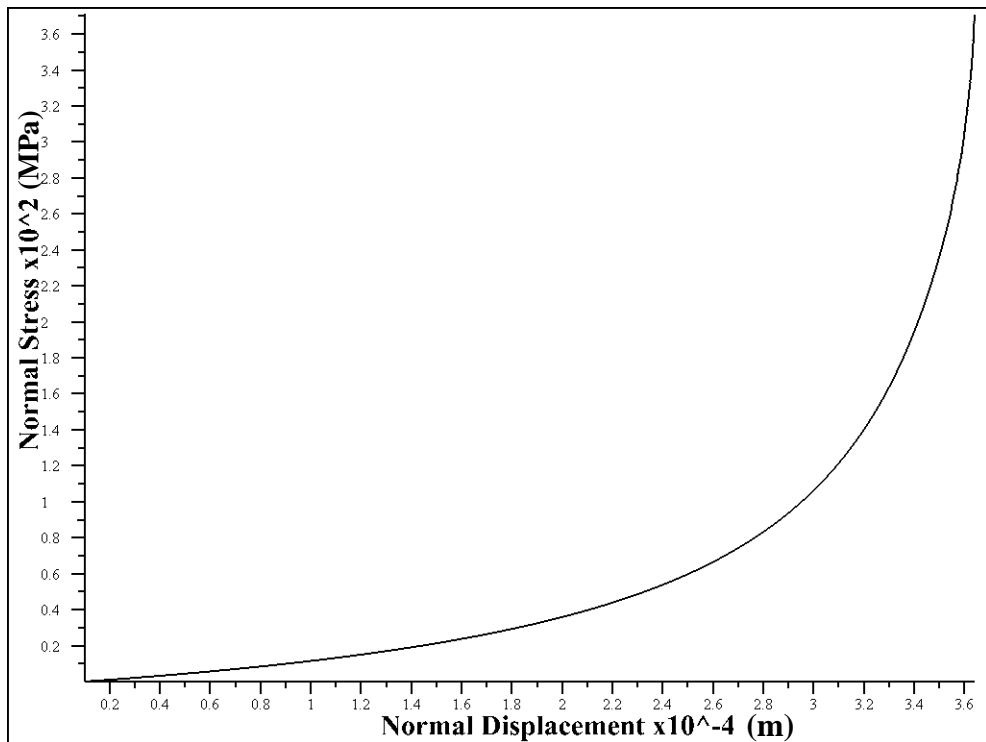


Figure B.14 Normal stress – normal closure plot with JCS = 70 MPa

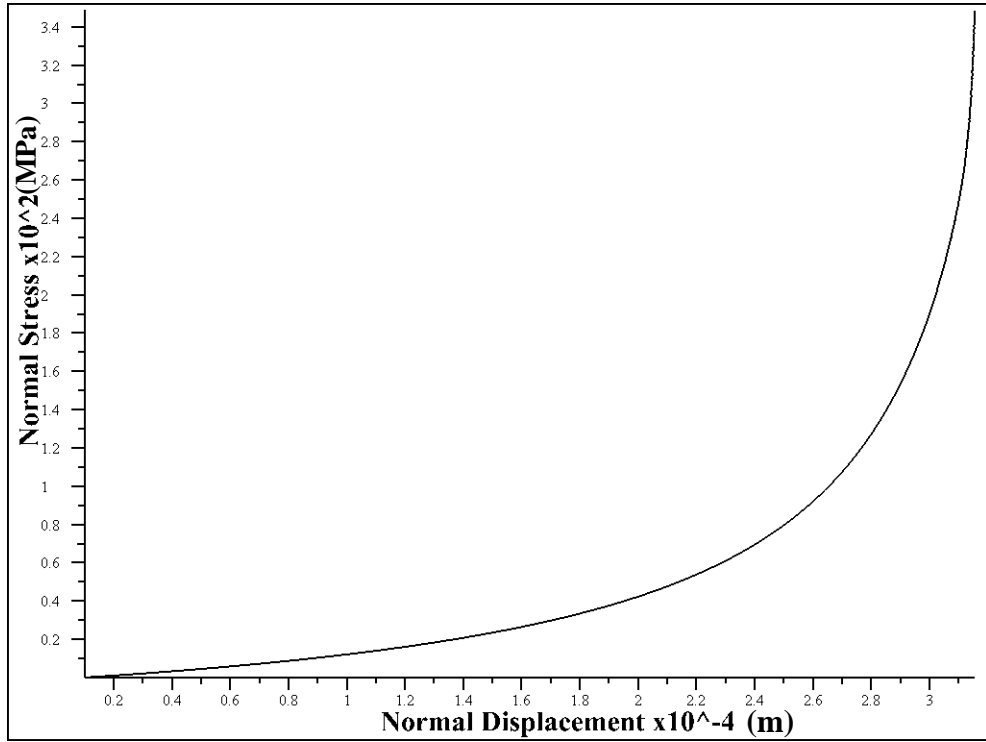


Figure B.15 Normal stress – normal closure plot with JCS = 80 MPa

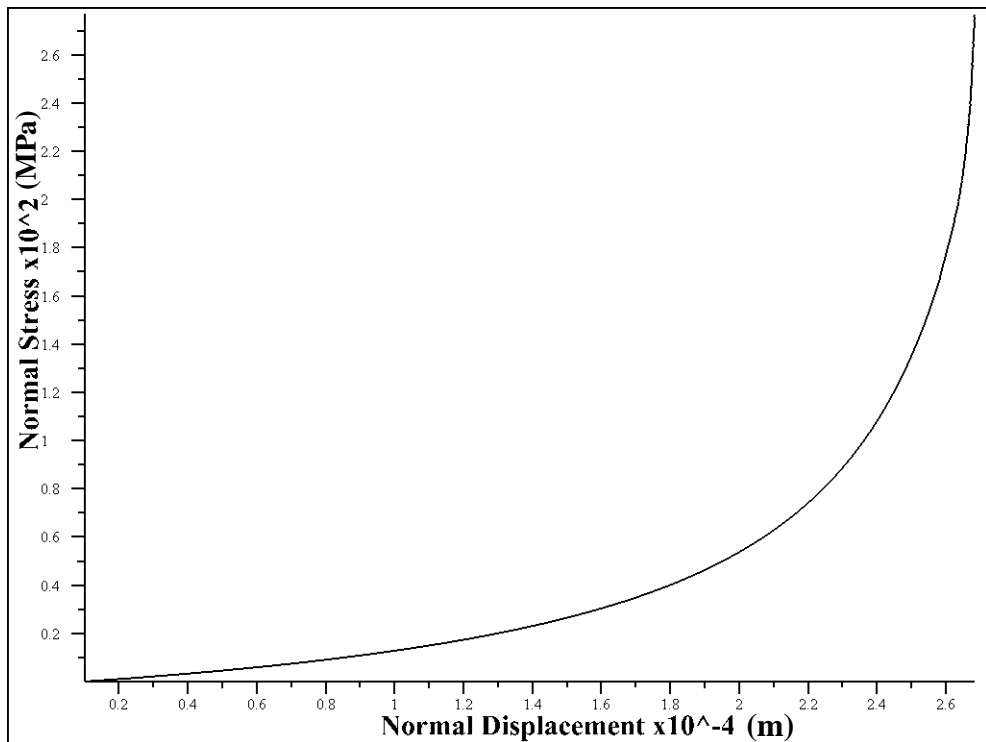


Figure B.16 Normal stress – normal closure plot with JCS = 90 MPa

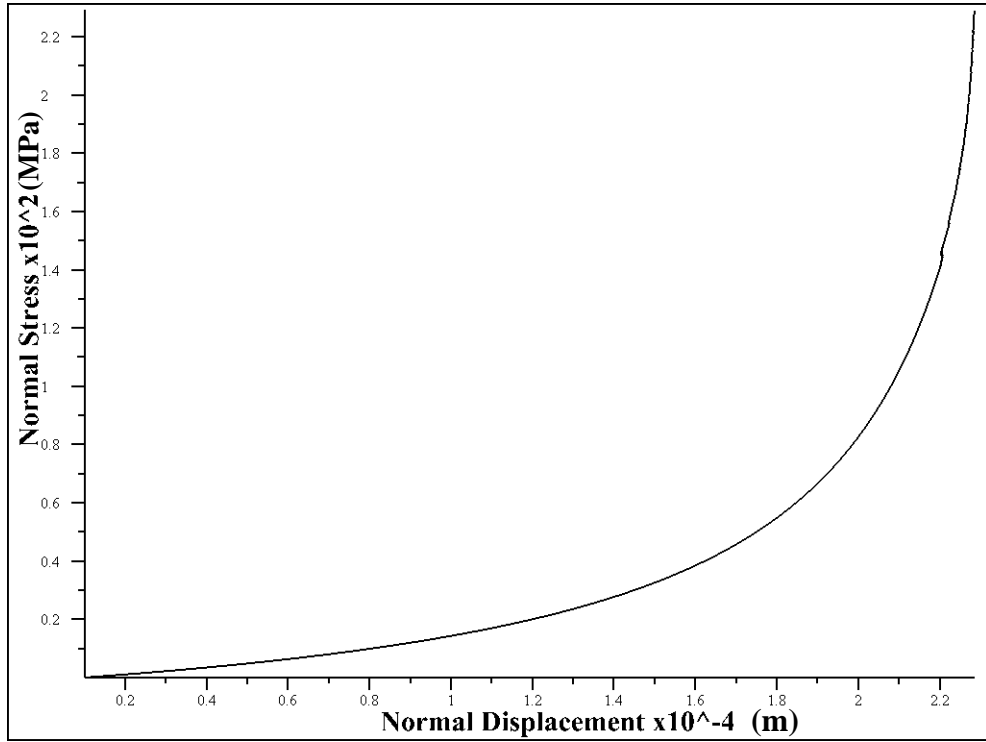


Figure B.17 Normal stress – normal closure plot with JCS = 100 MPa

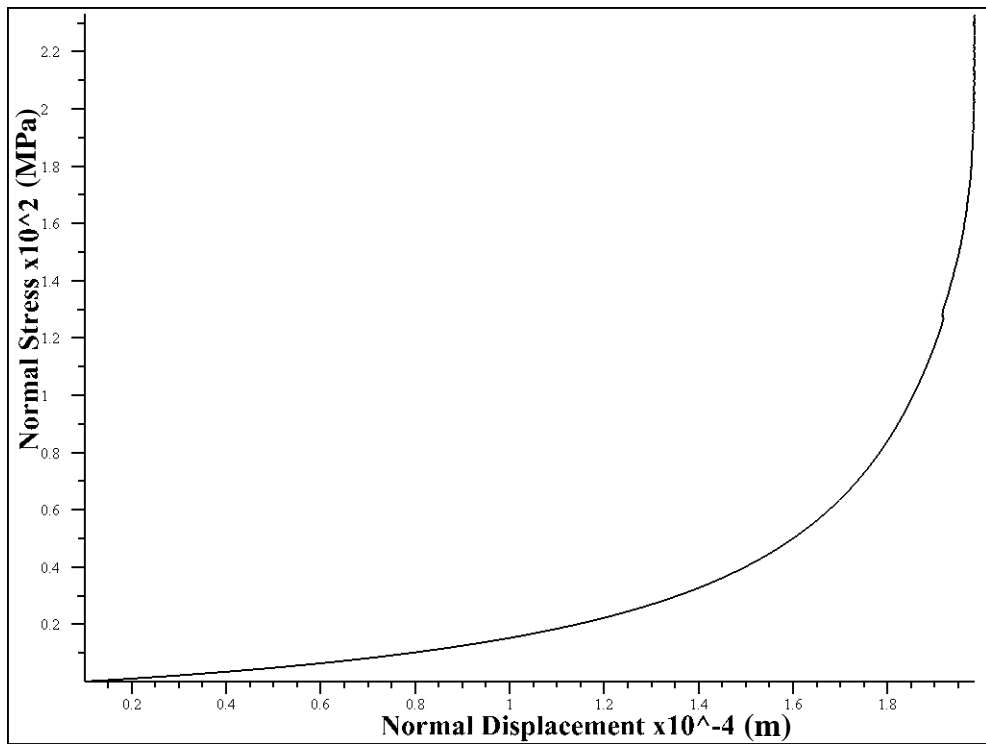


Figure B.18 Normal stress – normal closure plot with JCS = 110 MPa

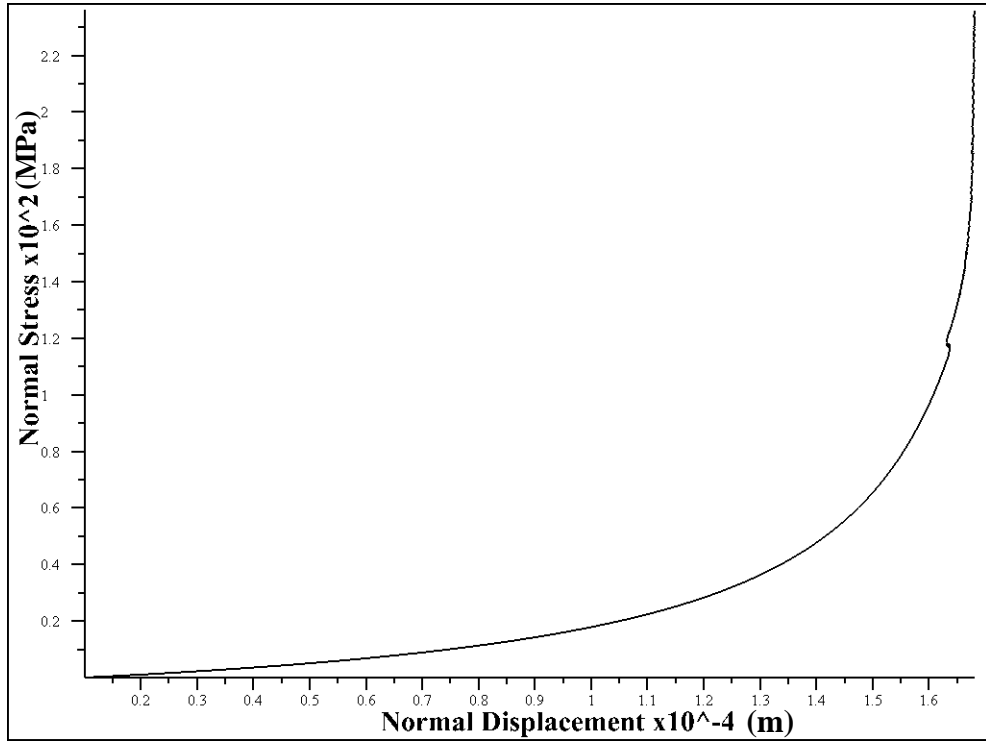


Figure B.19 Normal stress – normal closure plot with JCS = 120 MPa

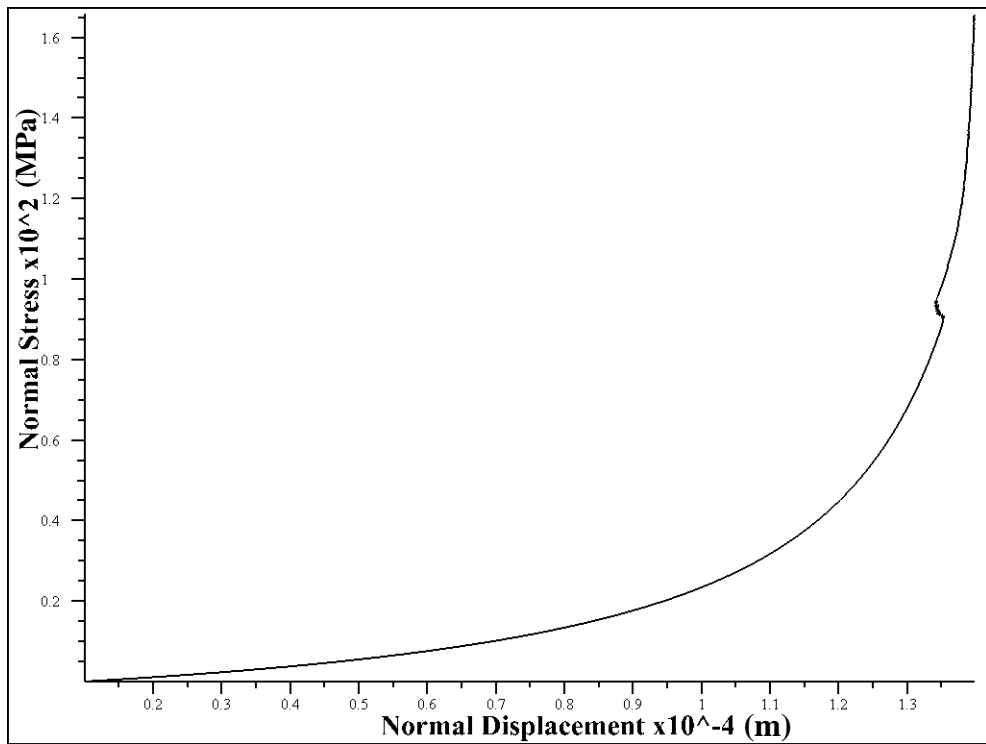


Figure B.20 Normal stress – normal closure plot with JCS = 130 MPa

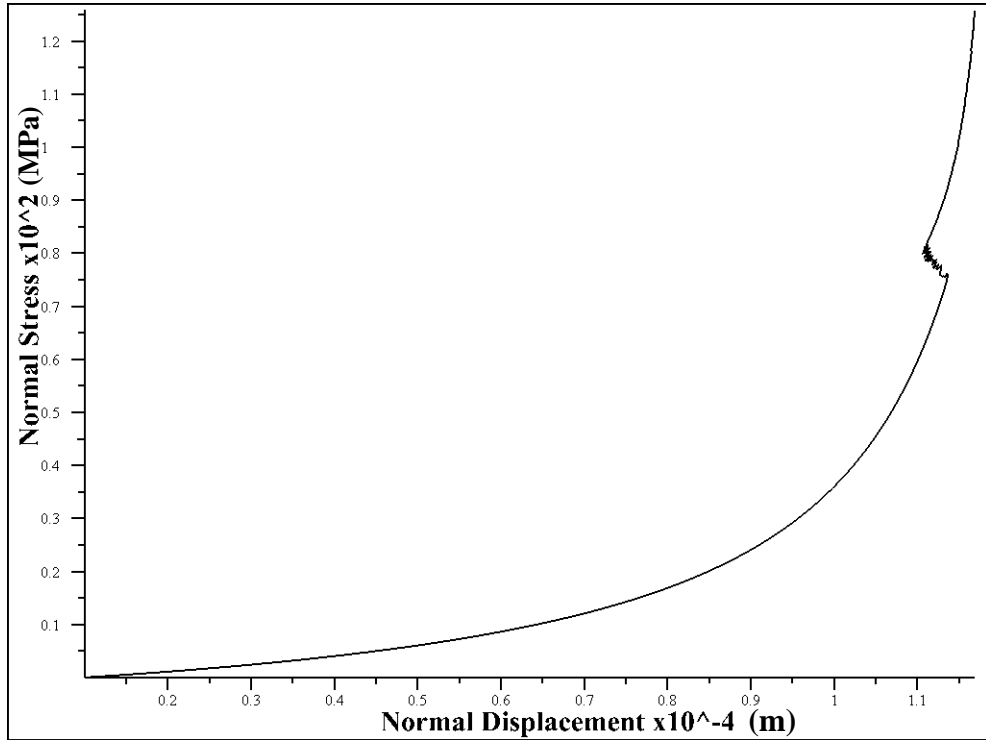


Figure B.21 Normal stress – normal closure plot with JCS = 140 MPa

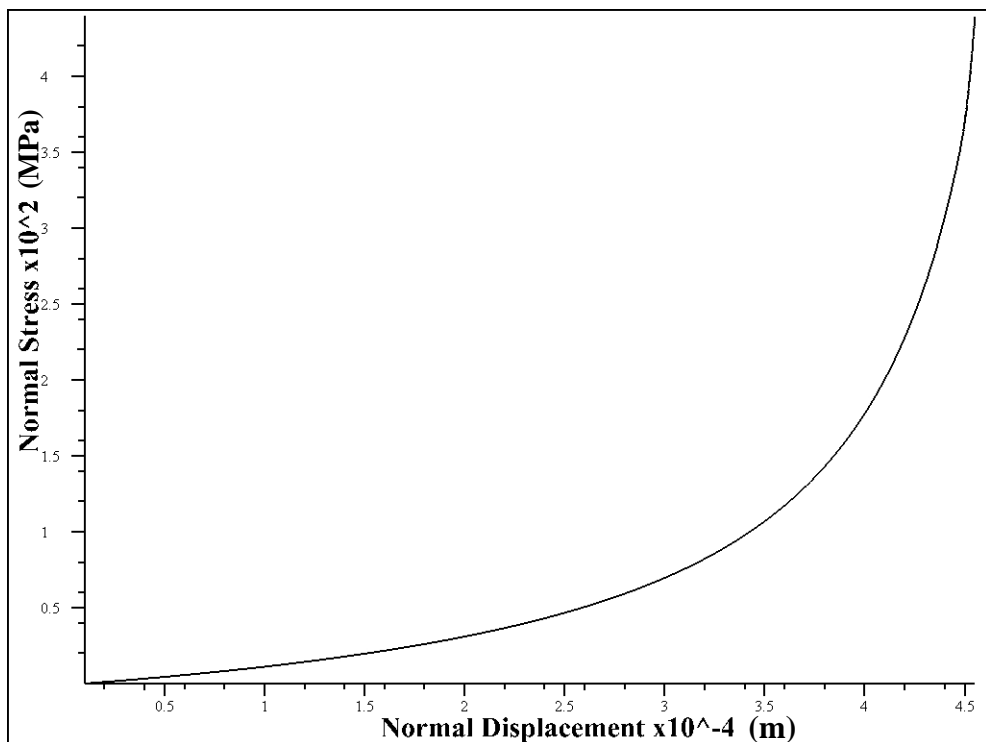


Figure B.22 Normal stress – normal closure plot with $\sigma_c = 60$ MPa

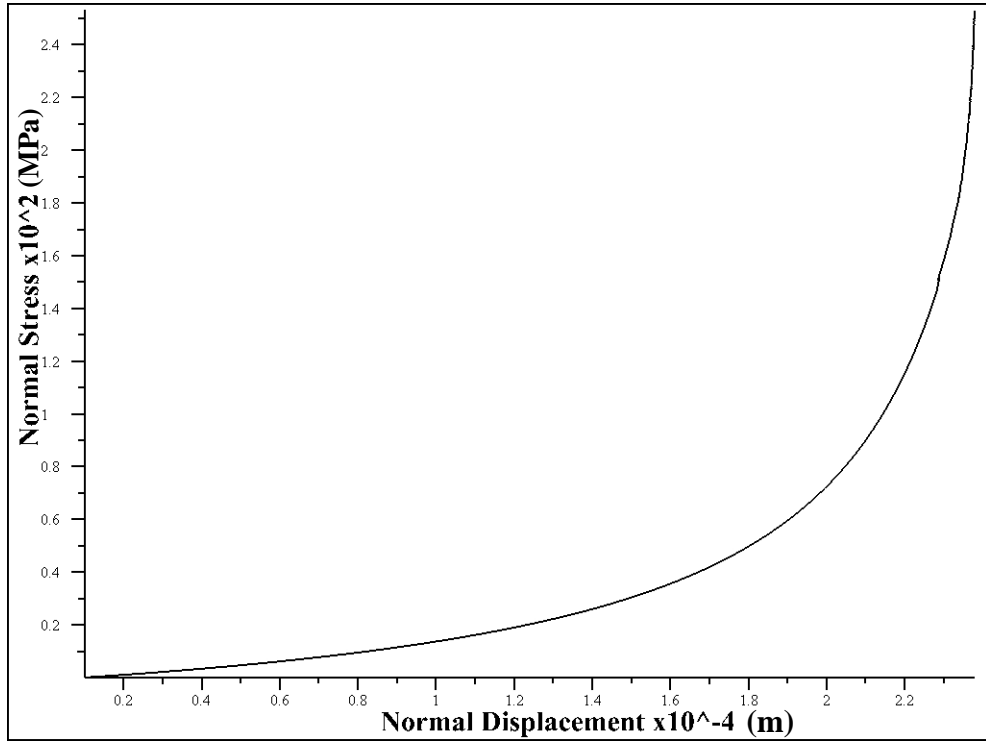


Figure B.23 Normal stress – normal closure plot with $\sigma_c = 70$ MPa

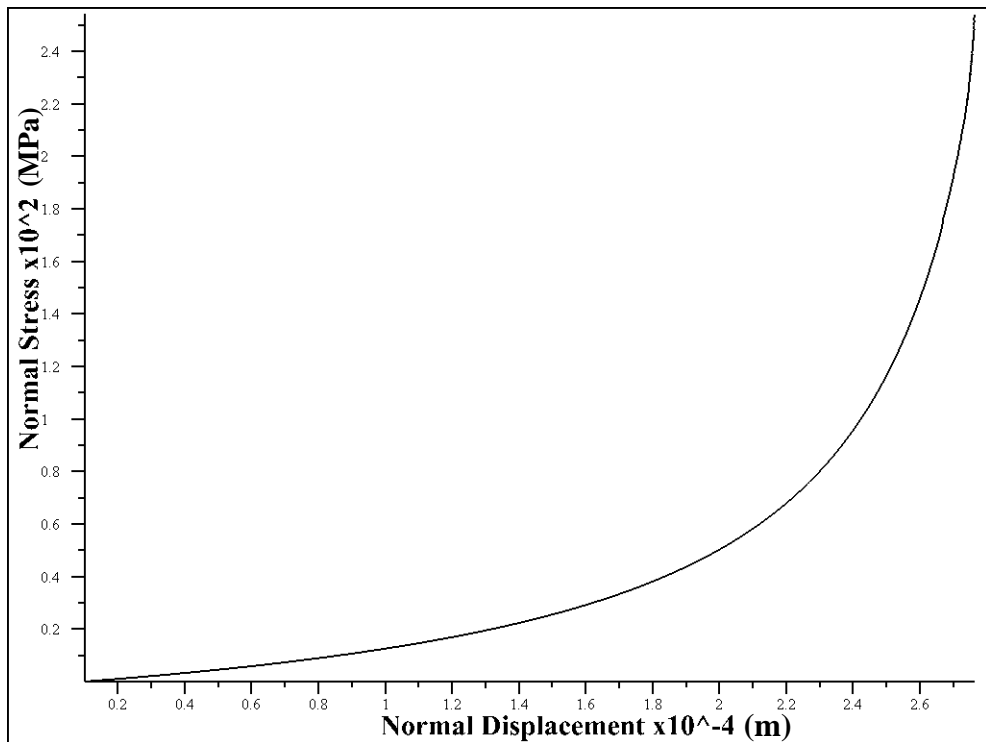


Figure B.24 Normal stress – normal closure plot with $\sigma_c = 80$ MPa

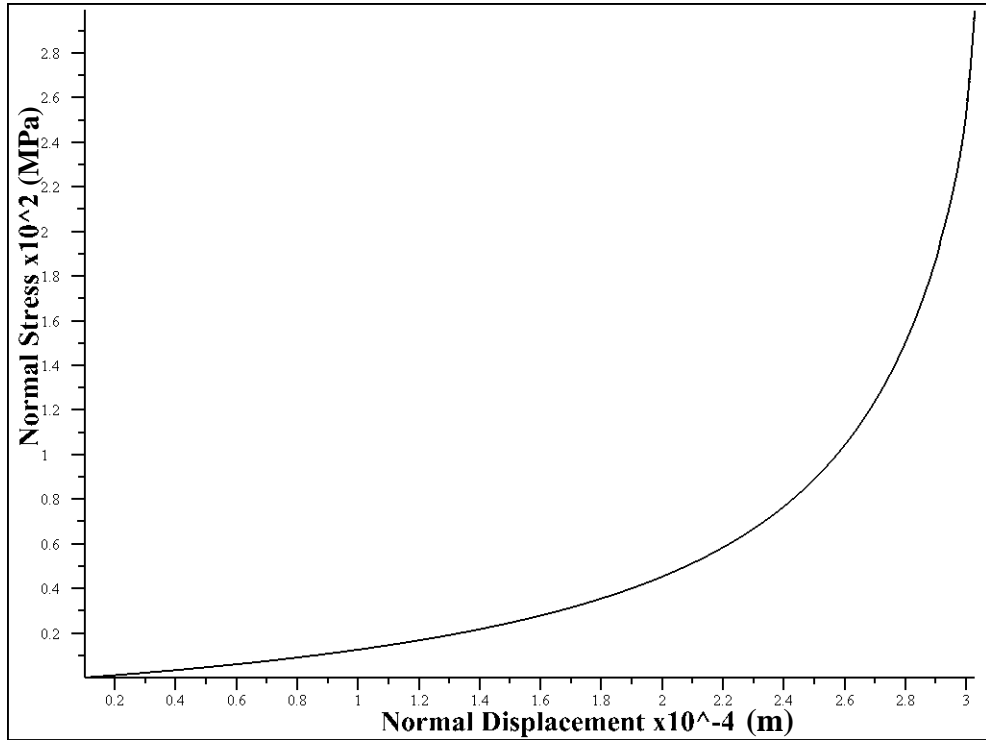


Figure B.25 Normal stress – normal closure plot with $\sigma_c = 90$ MPa

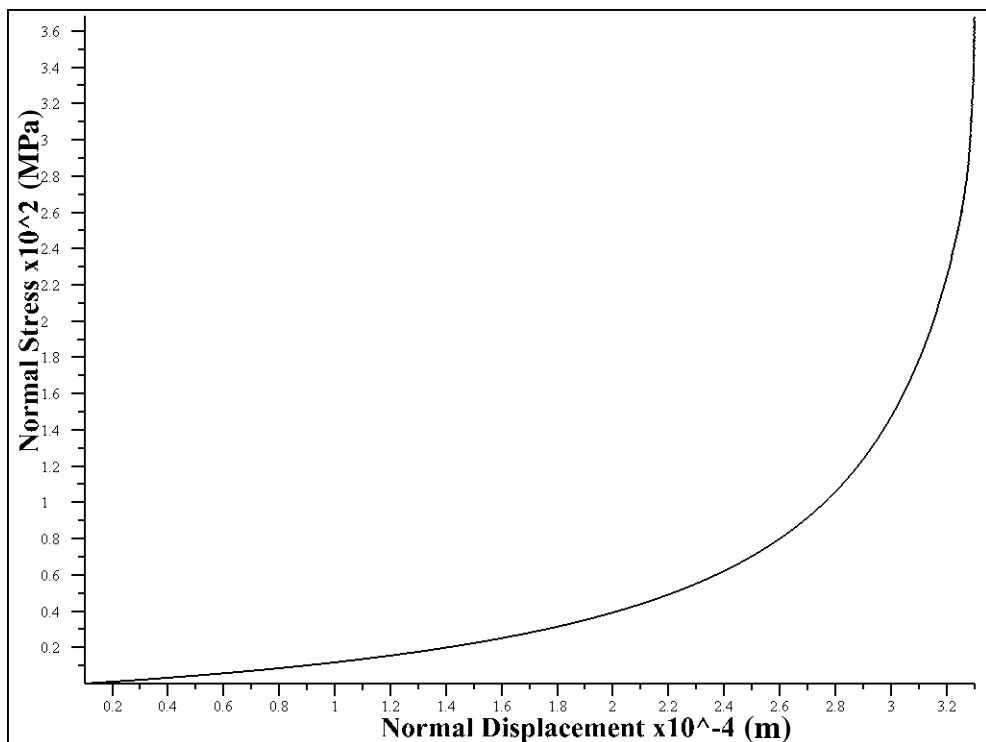


Figure B.26 Normal stress – normal closure plot with $\sigma_c = 100$ MPa

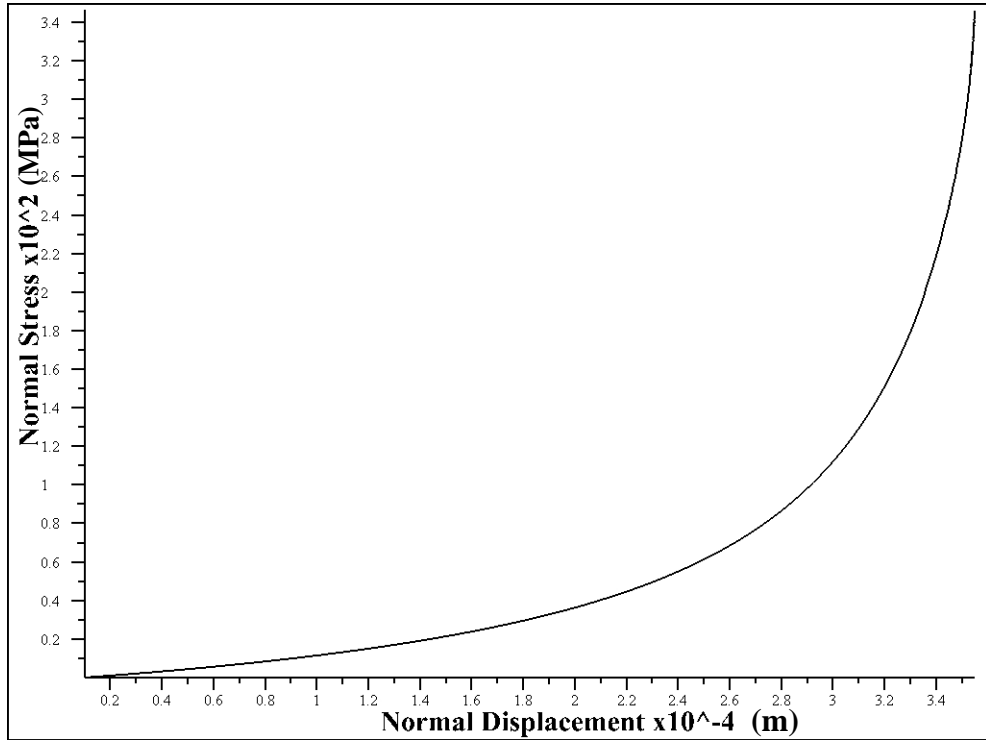


Figure B.27 Normal stress – normal closure plot with $\sigma_c = 110$ MPa

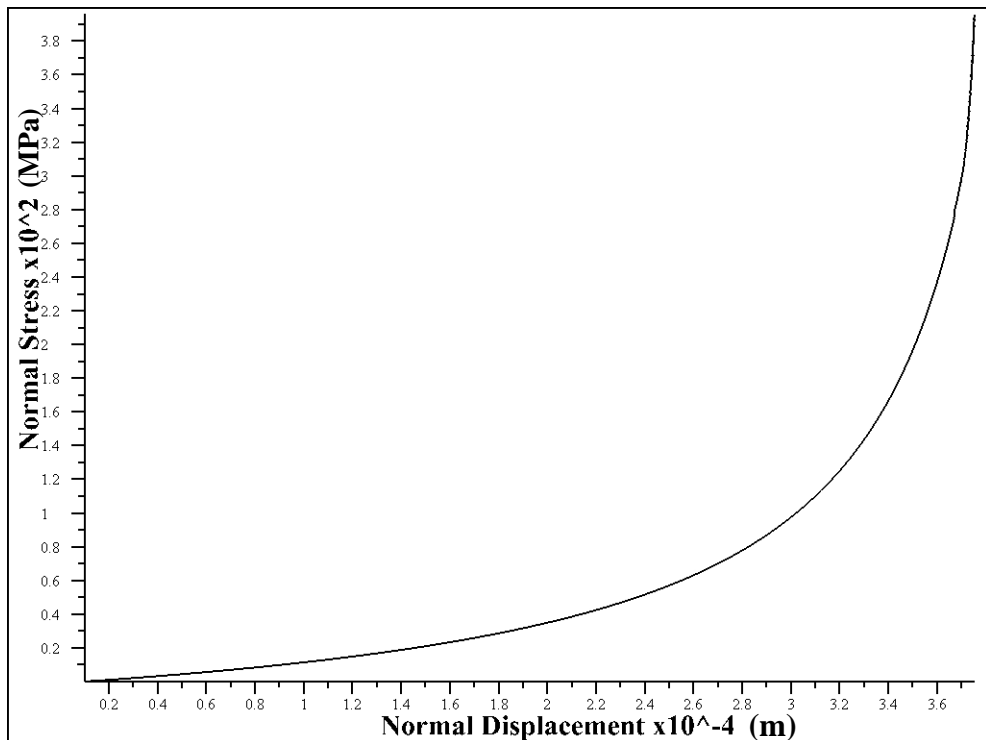


Figure B.28 Normal stress – normal closure plot with $\sigma_c = 120$ MPa

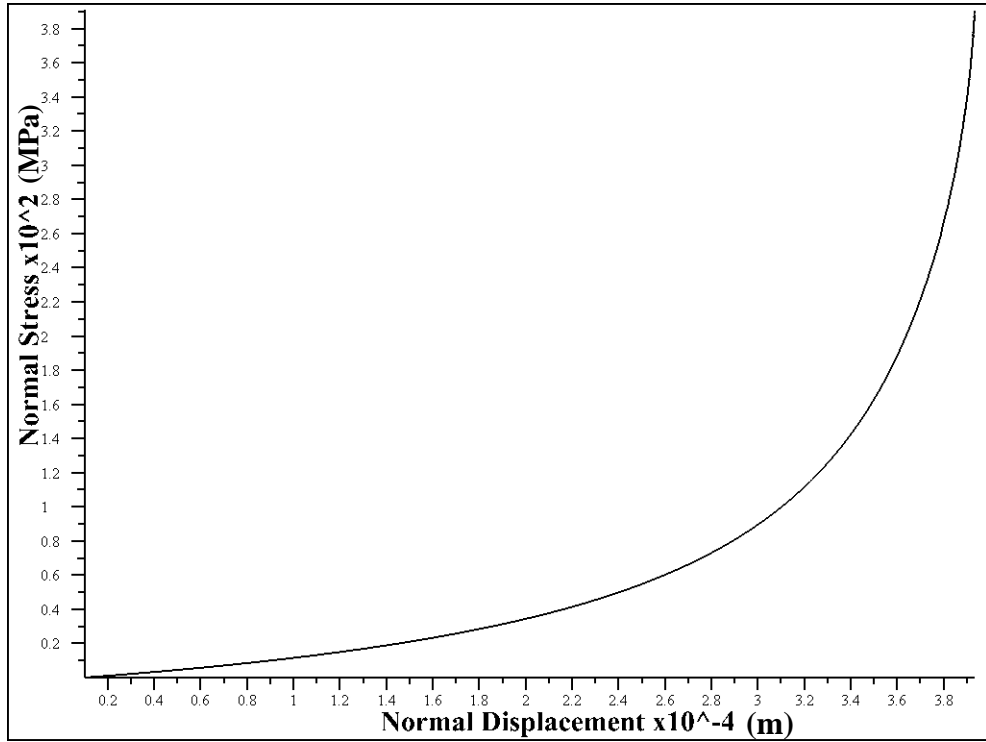


Figure B.29 Normal stress – normal closure plot with $\sigma_c = 130$ MPa

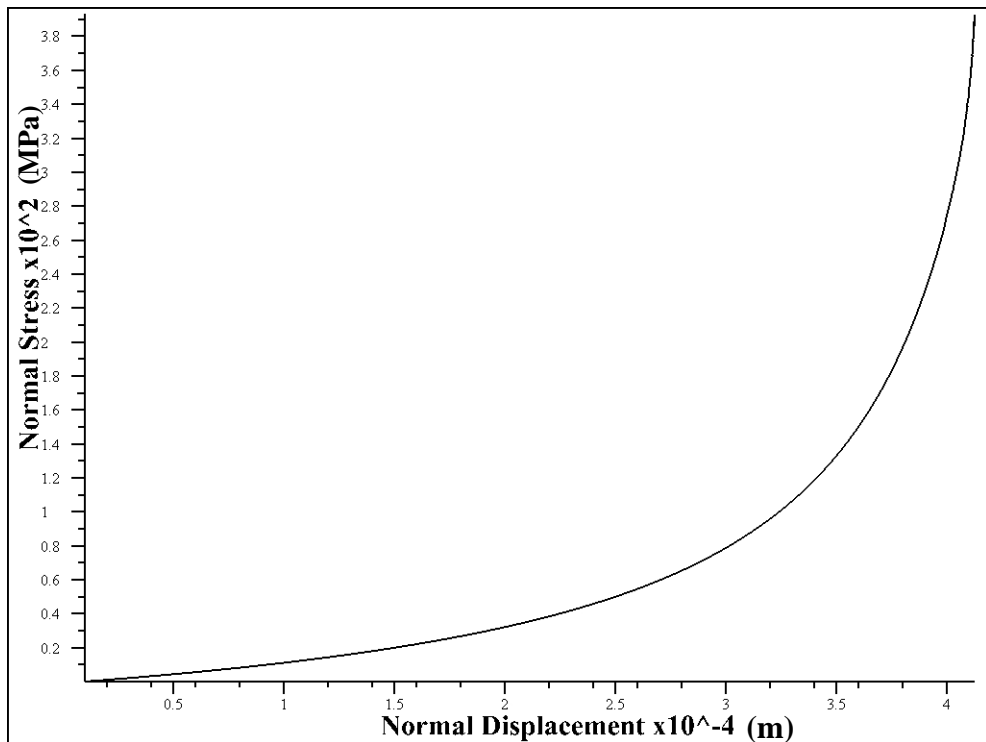


Figure B.30 Normal stress – normal closure plot with $\sigma_c = 140$ MPa

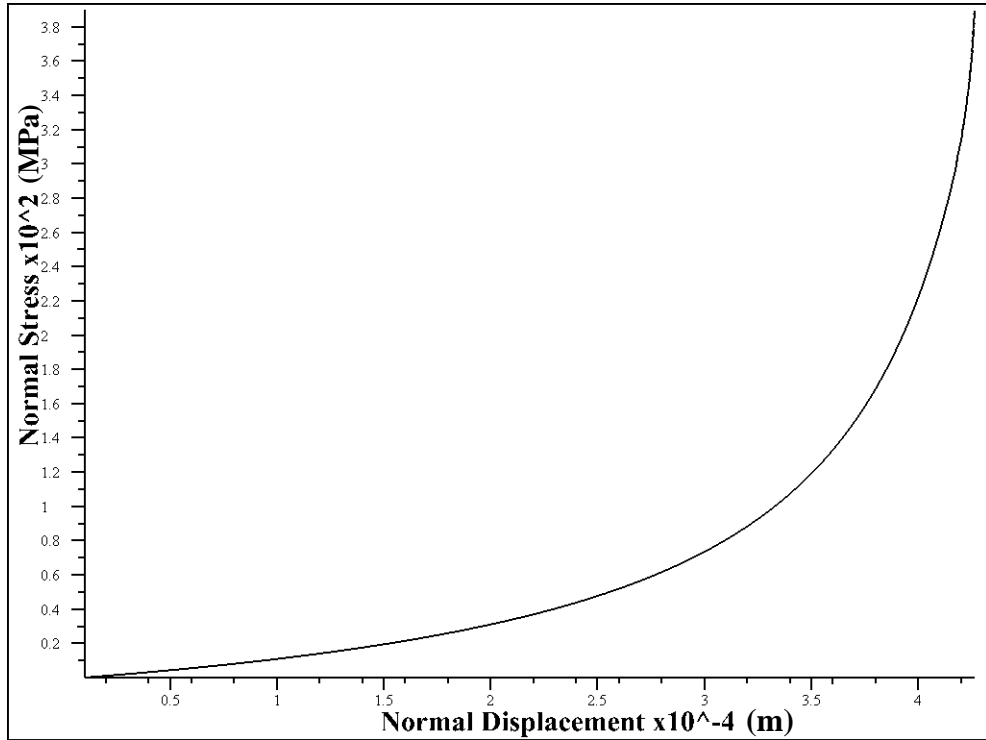


Figure B.31 Normal stress – normal closure plot with $\sigma_c = 150$ MPa

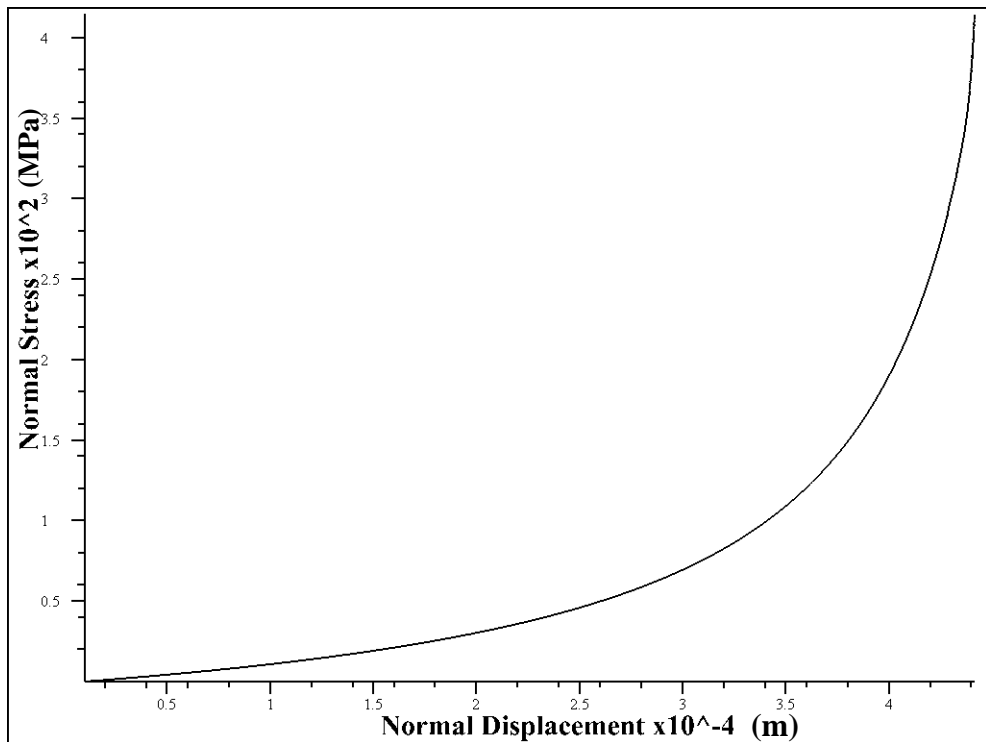


Figure B.32 Normal stress – normal closure plot with $\sigma_c = 160$ MPa

APPENDIX C

SHEAR DEFORMATION BEHAVIOUR

The shear stress vs shear displacement plots with different residual friction angle (ϕ_r), joint roughness coefficients (JRC), joint wall compressive strength (JCS) and normal stress (σ_n) are given in Figure C.1-C.38.

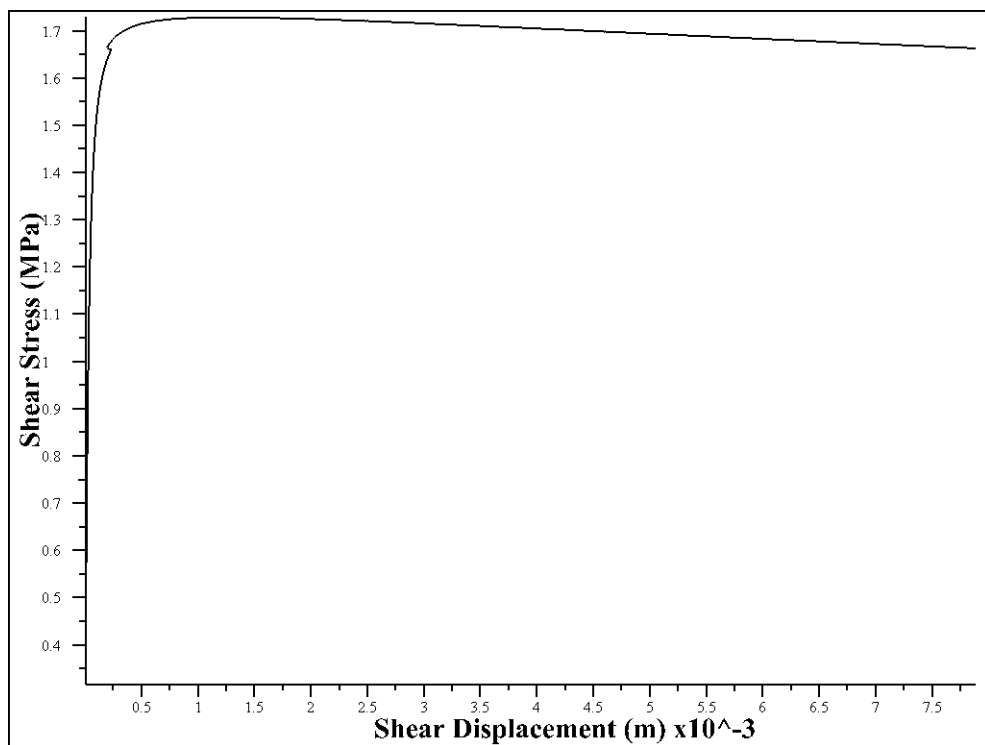


Figure C.1 Shear stress –shear displacement plot with $\phi_r = 10^\circ$

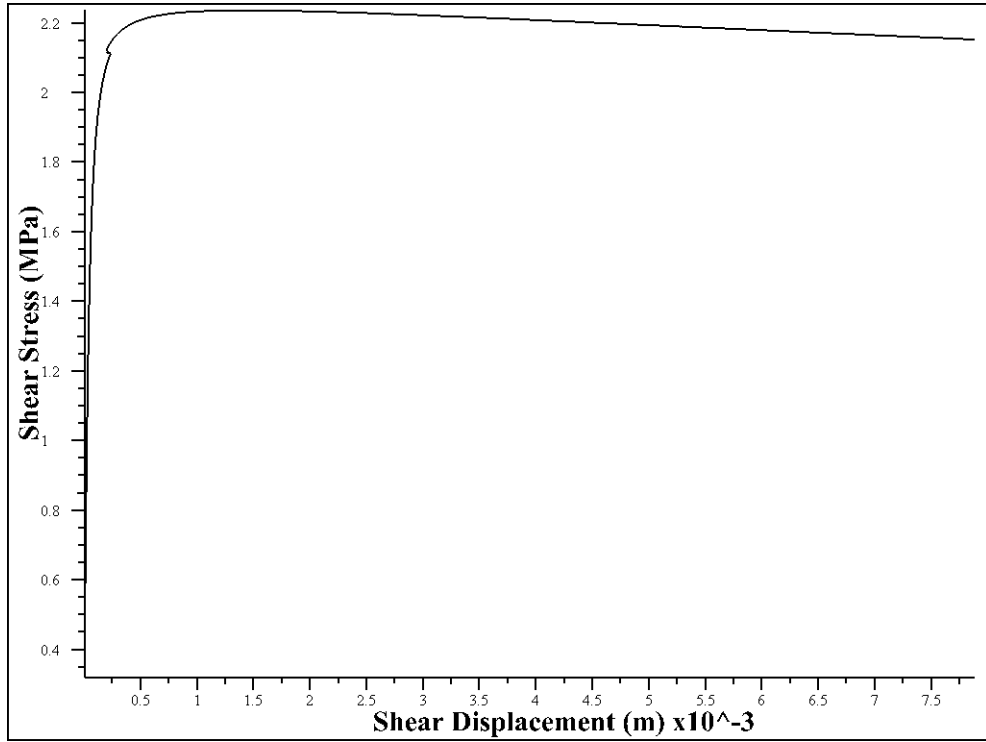


Figure C.2 Shear stress –shear displacement plot with $\varnothing_r = 15^\circ$

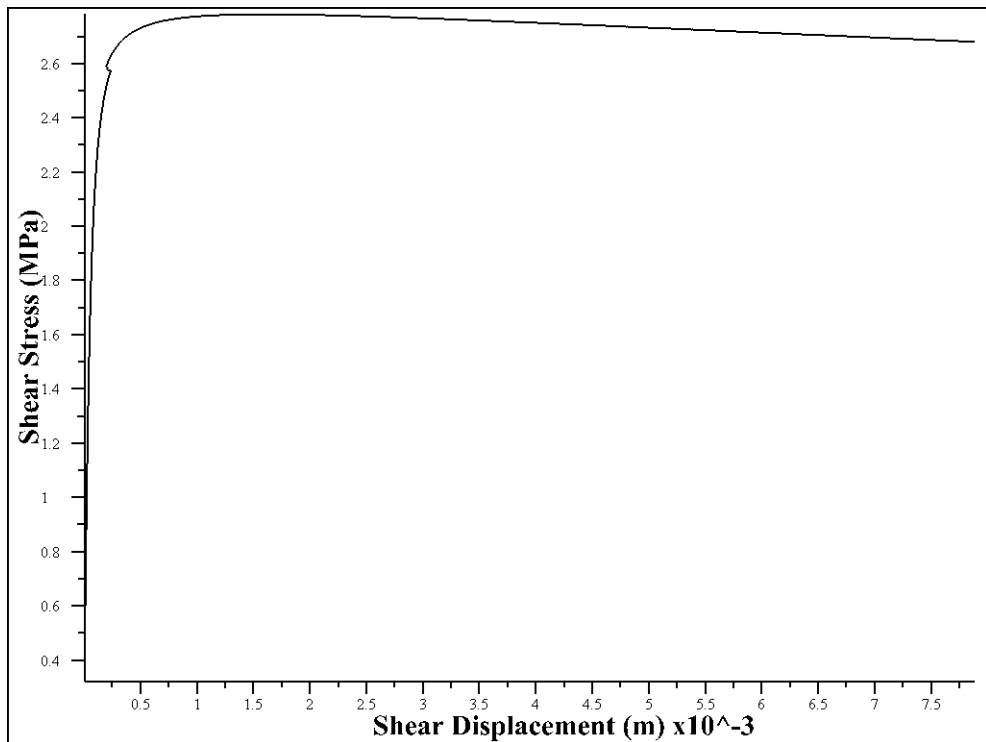


Figure C.3 Shear stress –shear displacement plot with $\varnothing_r = 20^\circ$

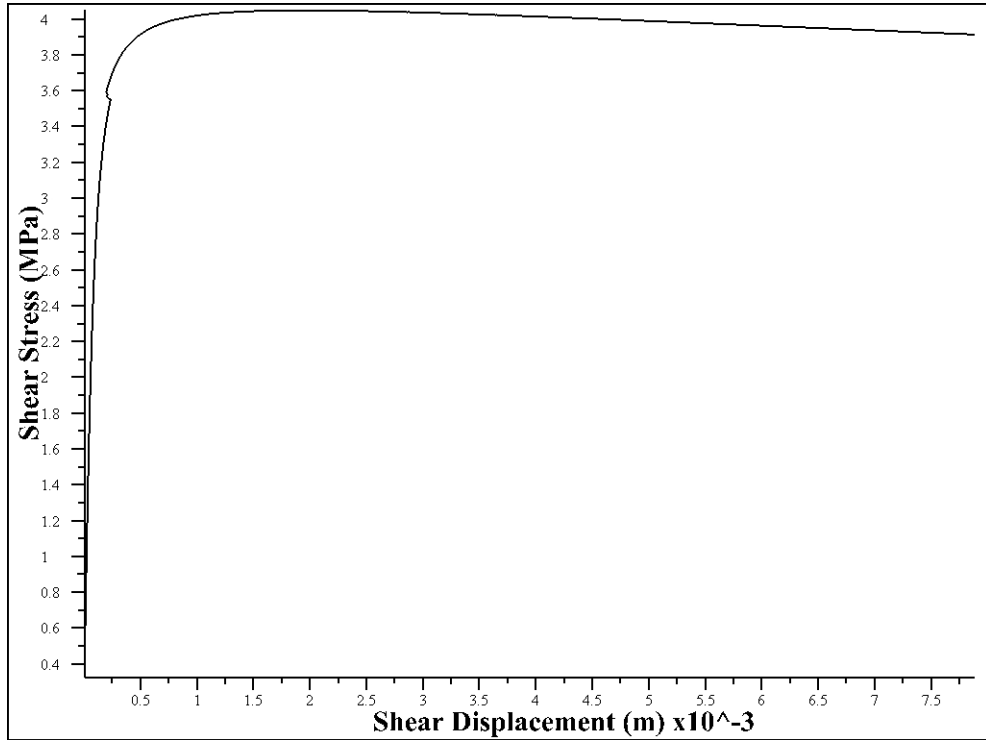


Figure C.4 Shear stress –shear displacement plot with $\phi_r = 30^\circ$

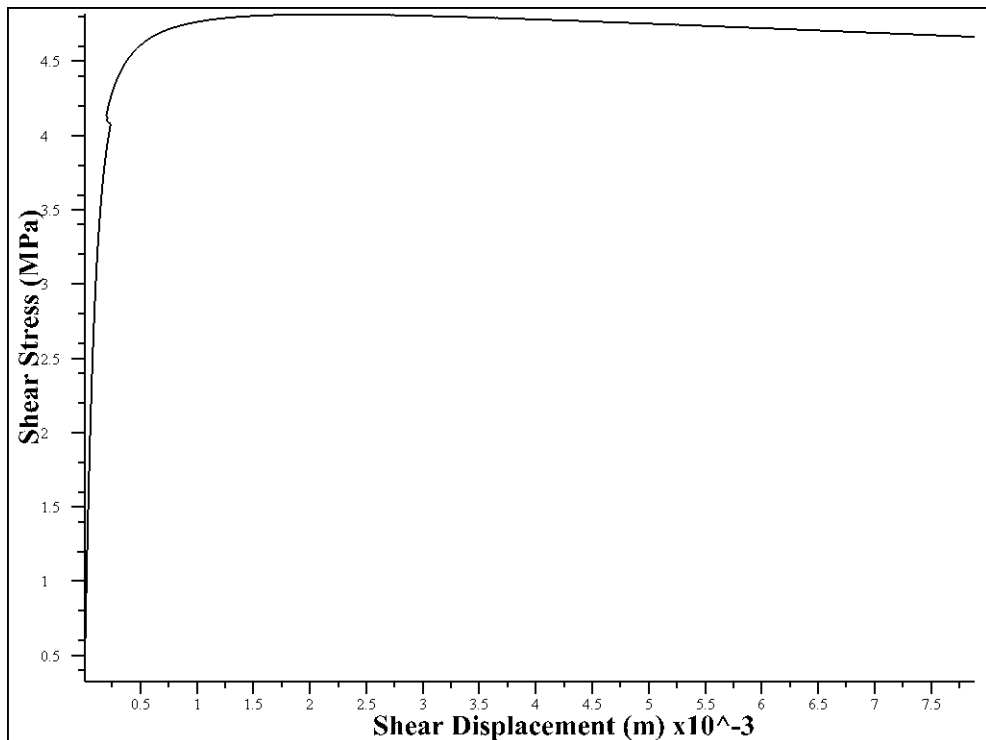


Figure C.5 Shear stress –shear displacement plot with $\phi_r = 35^\circ$

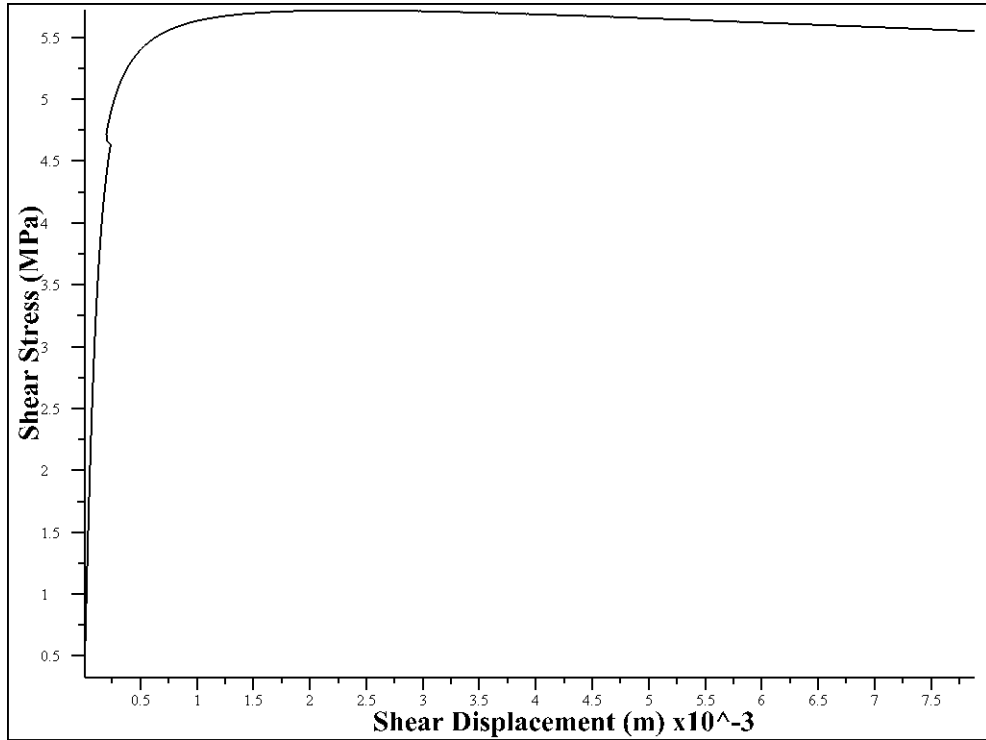


Figure C.6 Shear stress –shear displacement plot with $\varnothing_r = 40^\circ$

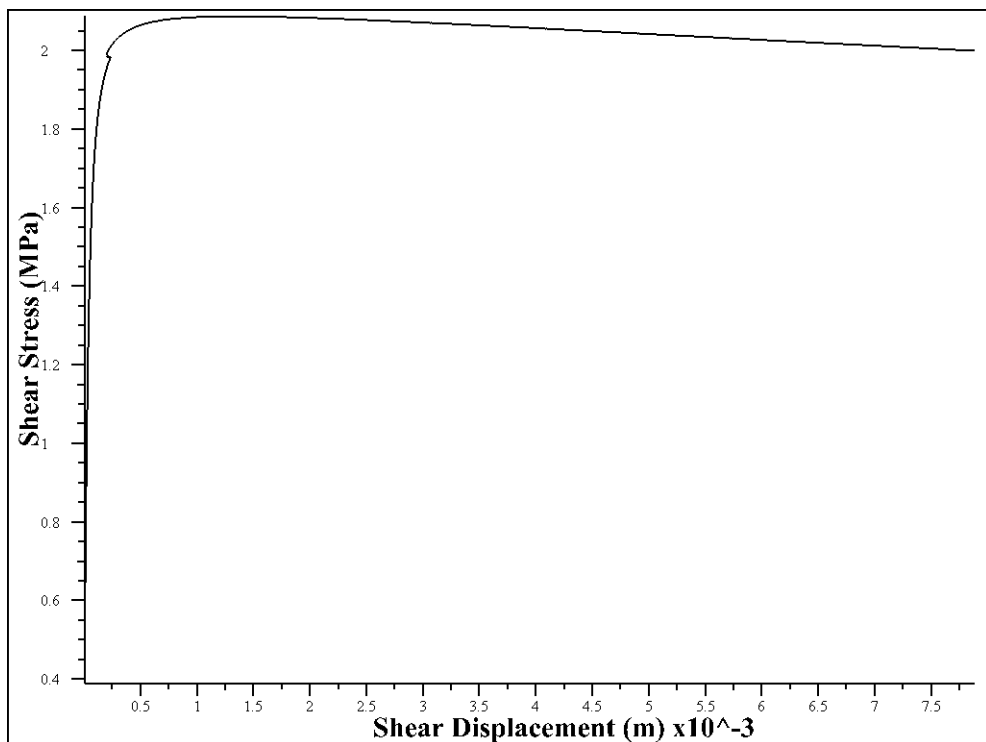


Figure C.7 Shear stress –shear displacement plot with $JRC = 2$

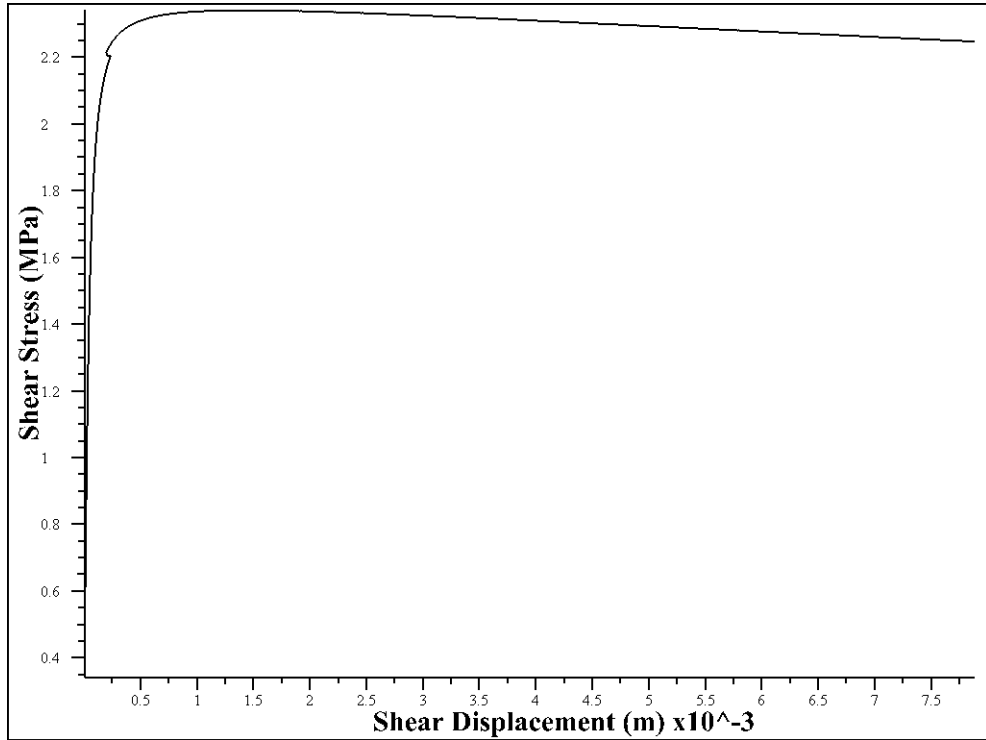


Figure C.8 Shear stress –shear displacement plot with JRC = 4

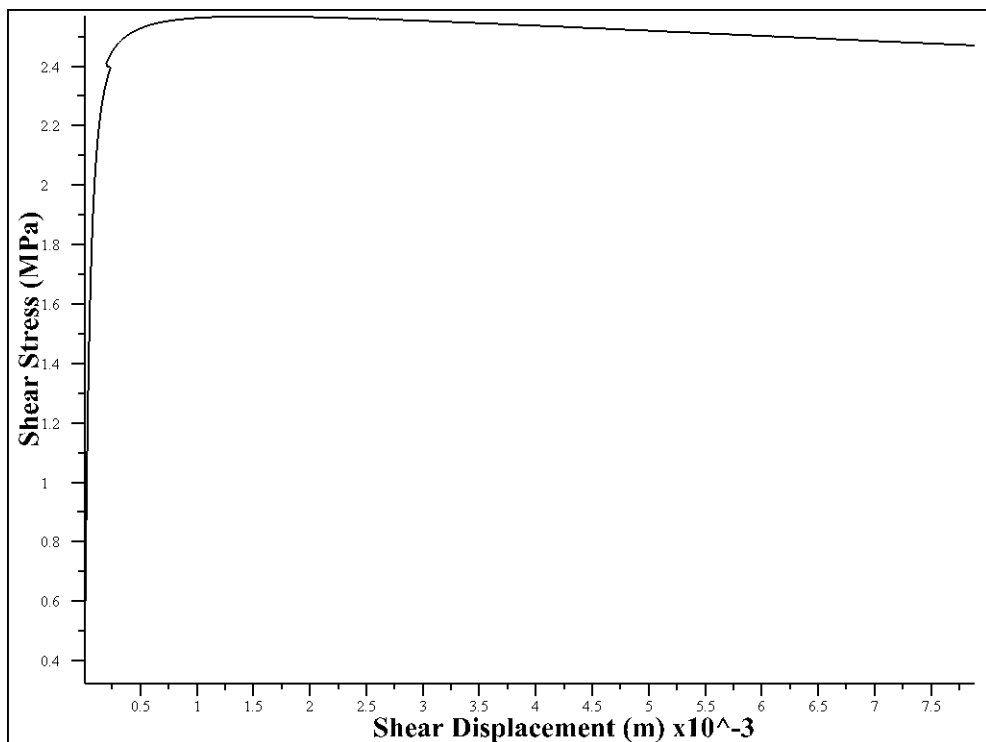


Figure C.9 Shear stress –shear displacement plot with JRC = 6

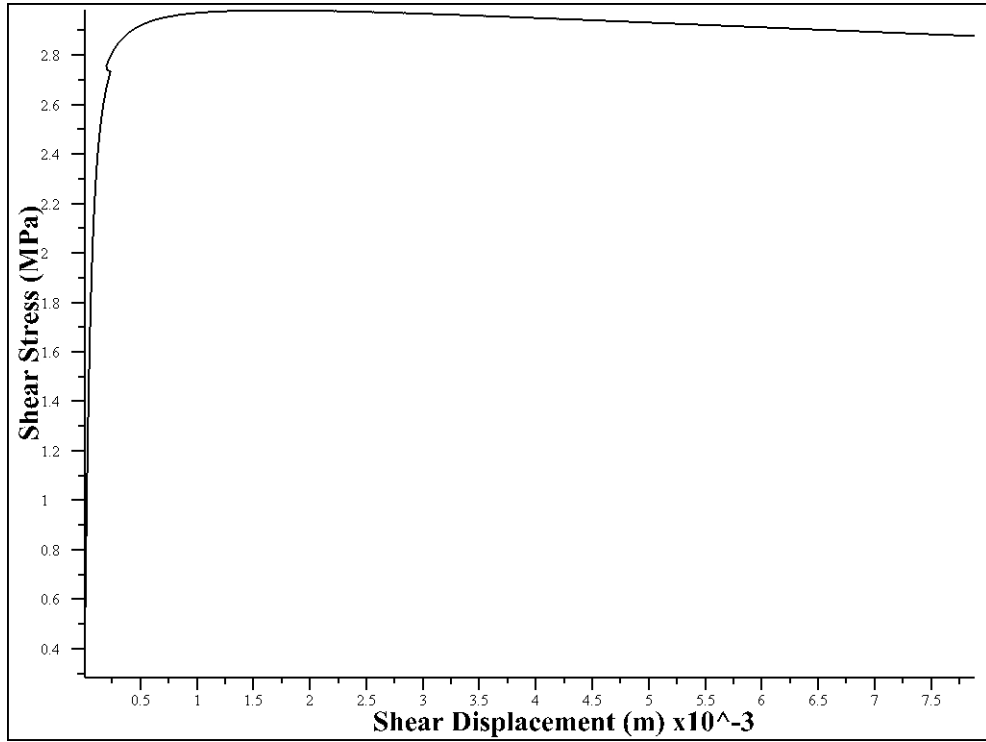


Figure C.10 Shear stress –shear displacement plot with JRC = 10

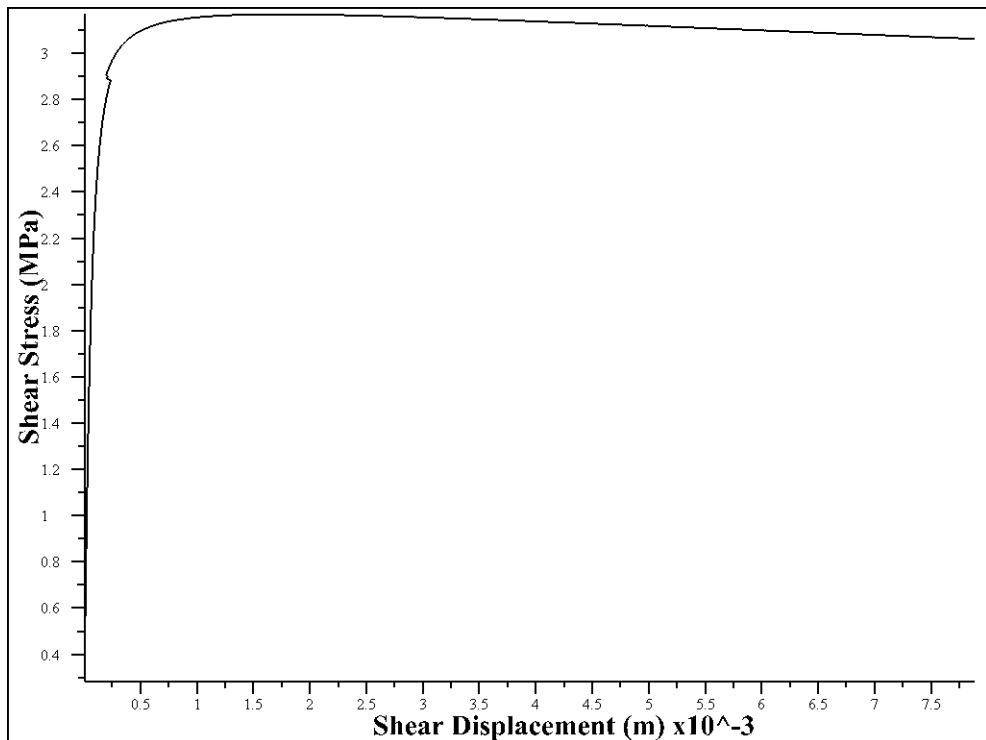


Figure C.11 Shear stress –shear displacement plot with JRC = 12

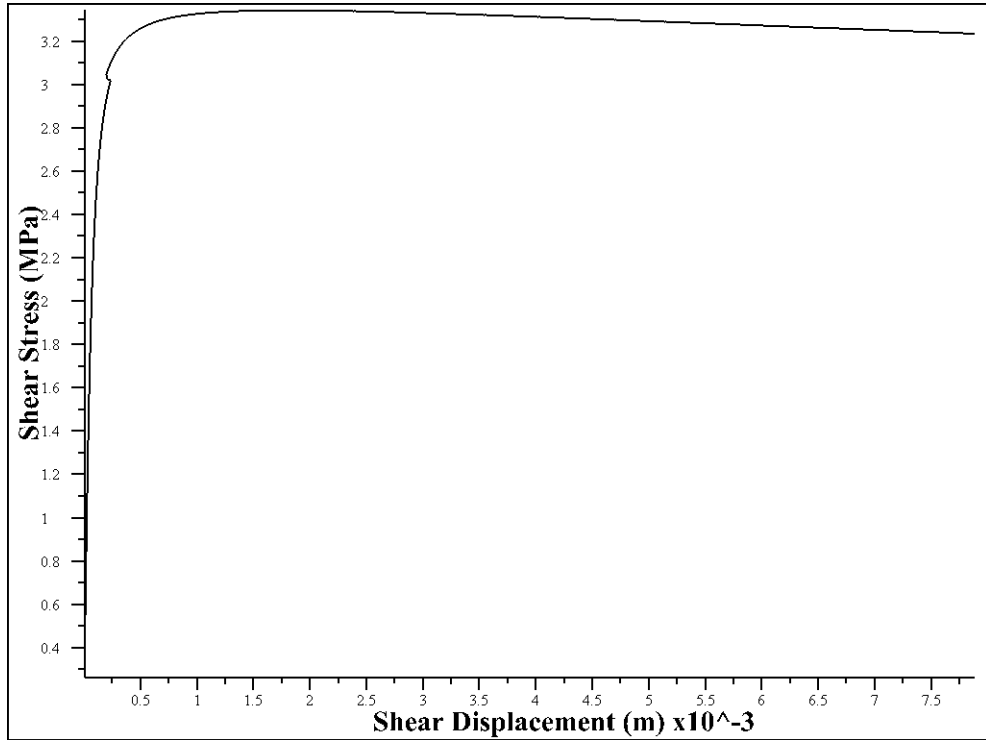


Figure C.12 Shear stress –shear displacement plot with JRC = 14

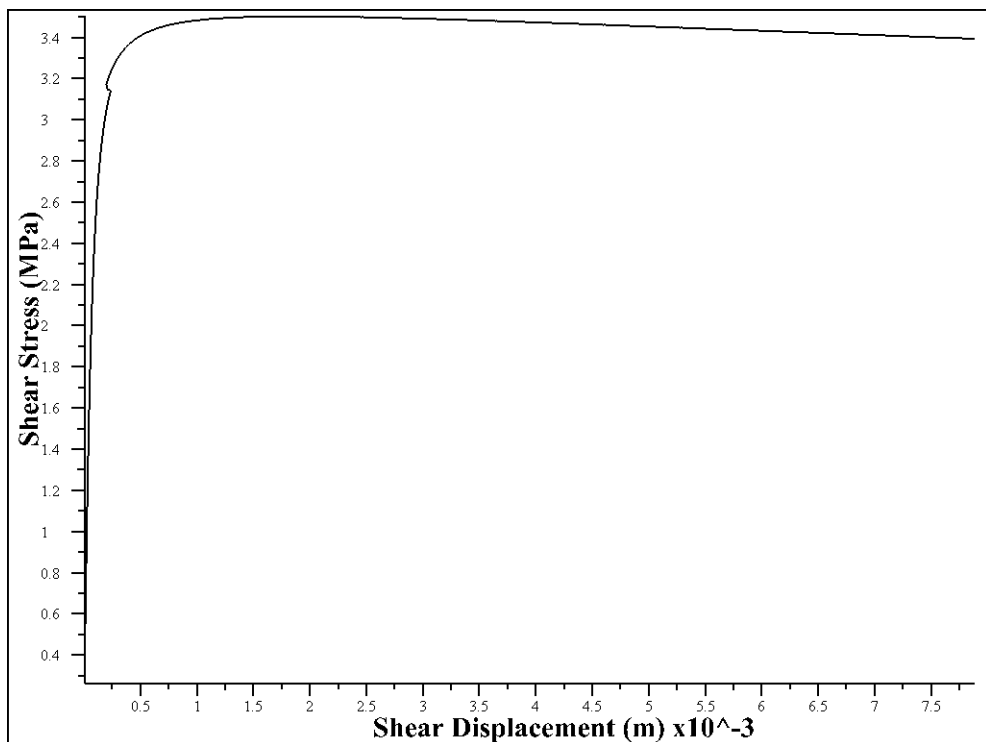


Figure C.13 Shear stress –shear displacement plot with JRC = 16

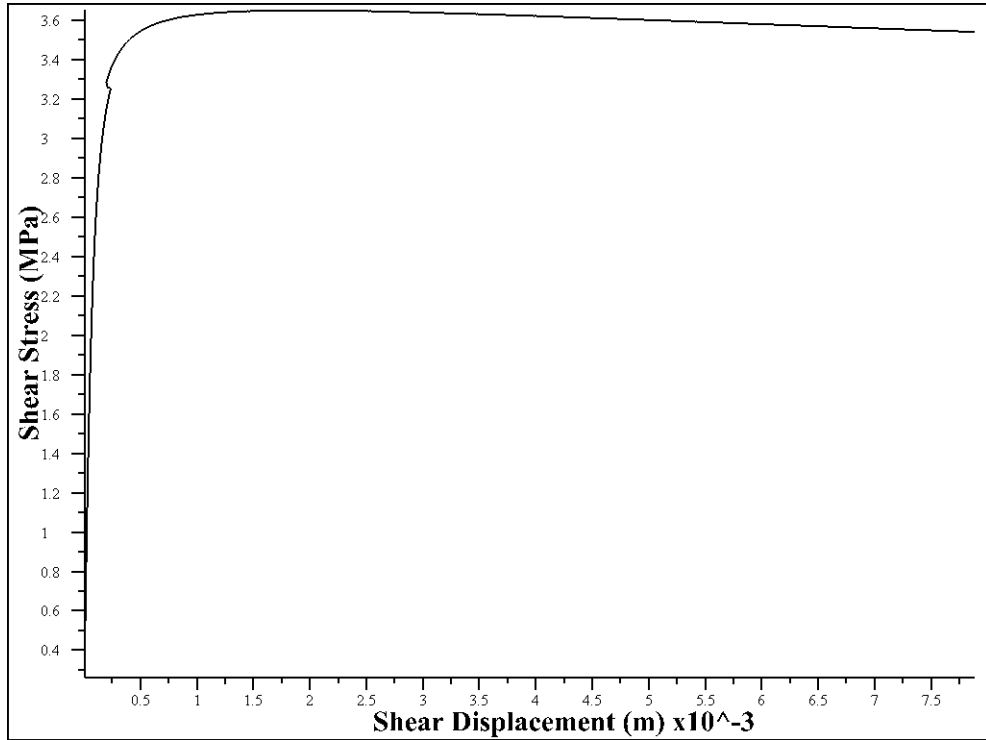


Figure C.14 Shear stress –shear displacement plot with JRC = 18

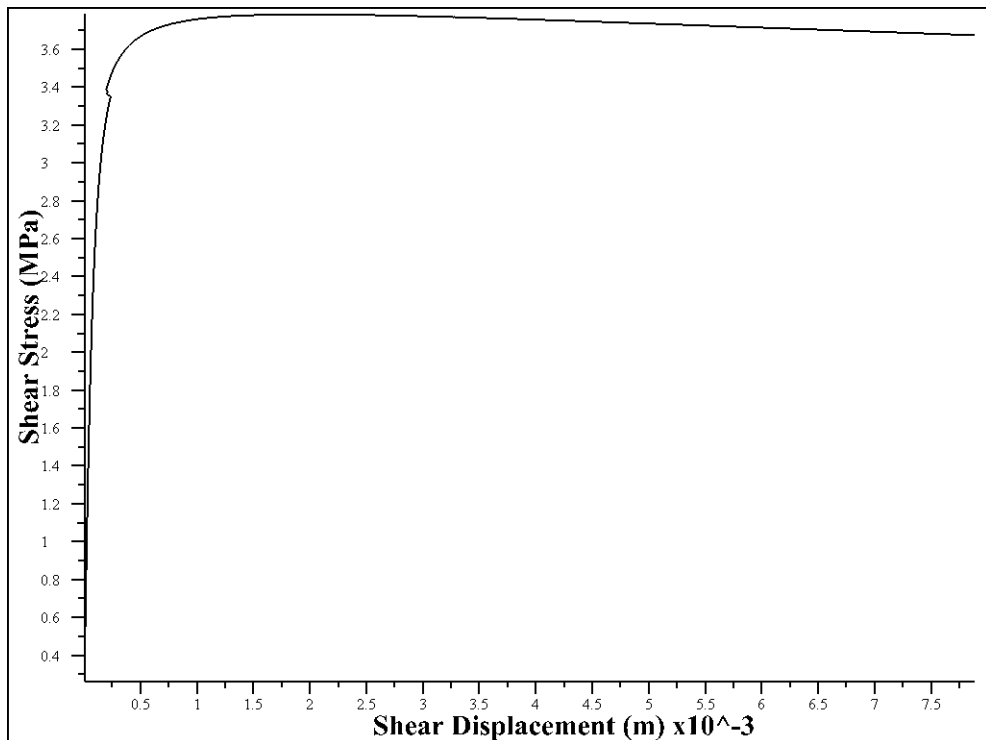


Figure C.15 Shear stress –shear displacement plot with JRC = 20

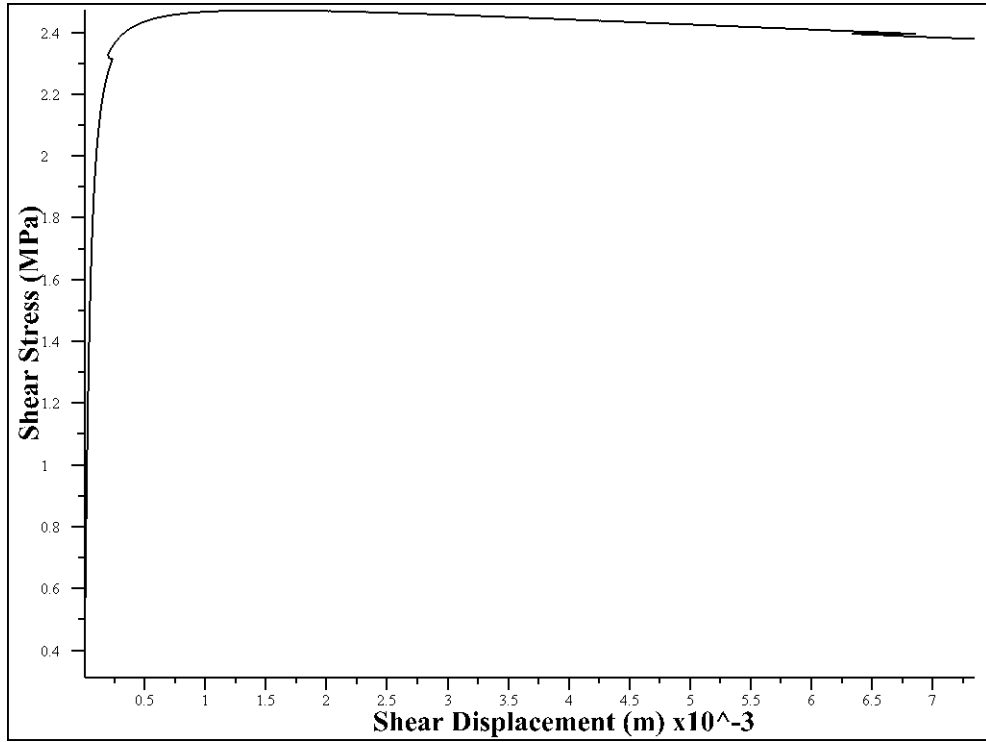


Figure C.16 Shear stress –shear displacement plot with JCS = 40 MPa

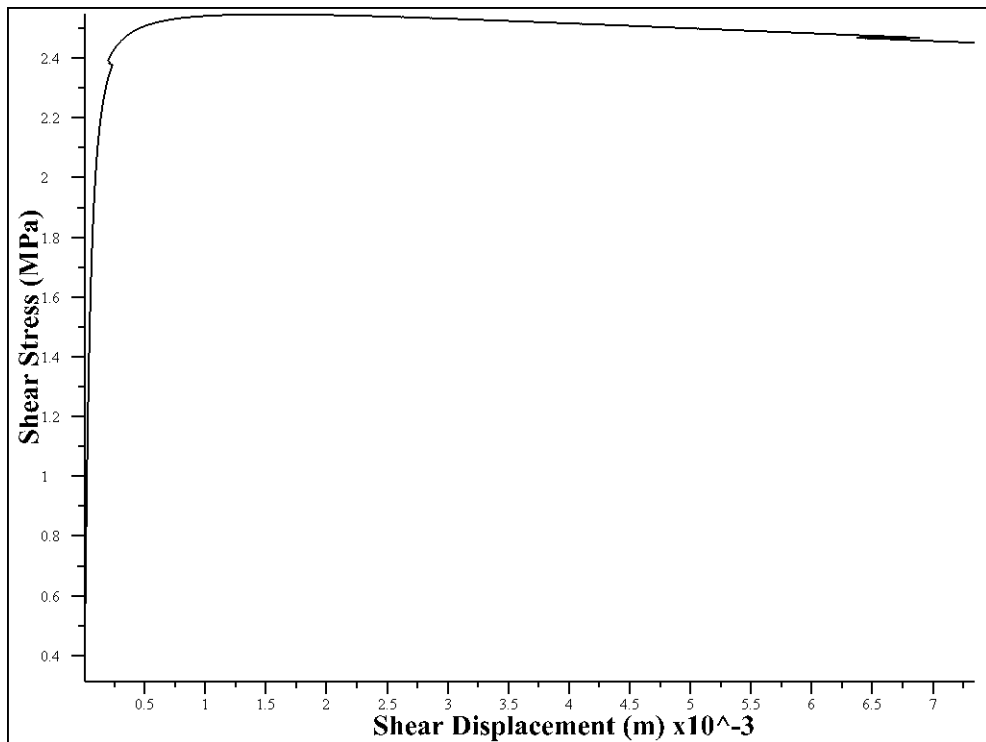


Figure C.17 Shear stress –shear displacement plot with JCS = 50 MPa

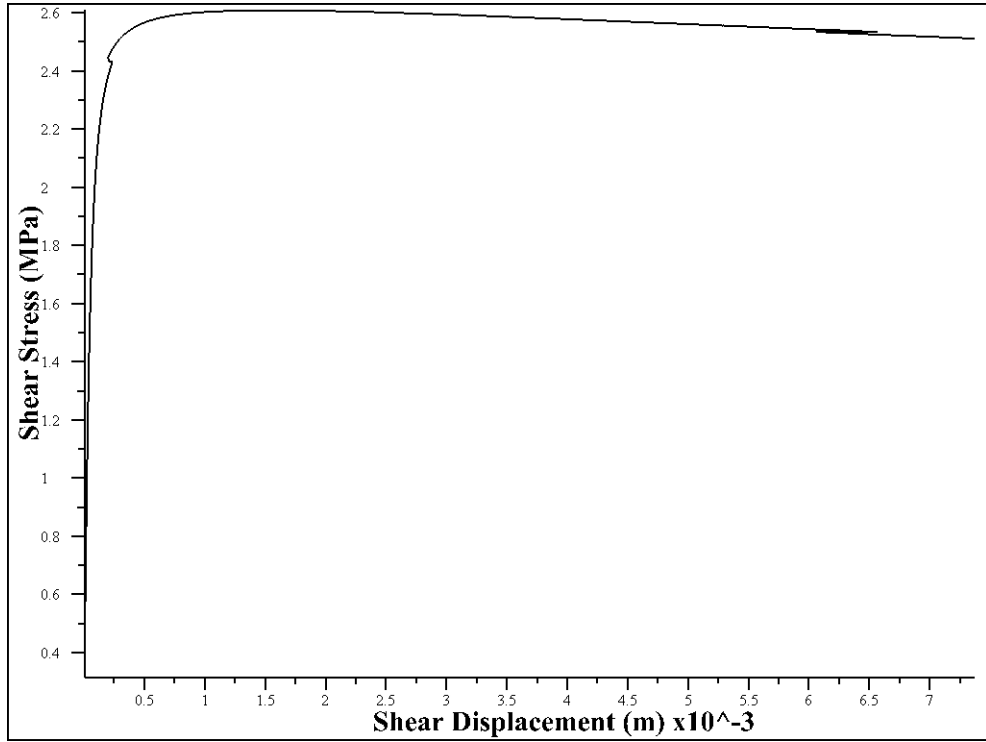


Figure C.18 Shear stress –shear displacement plot with JCS = 60 MPa

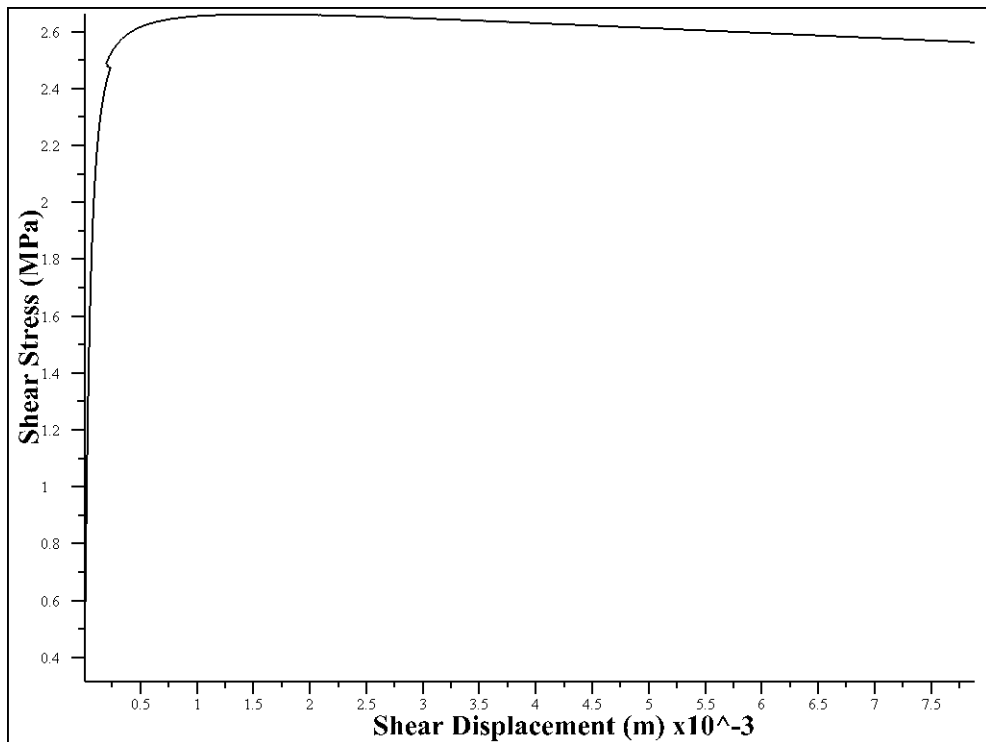


Figure C.19 Shear stress –shear displacement plot with JCS = 70 MPa

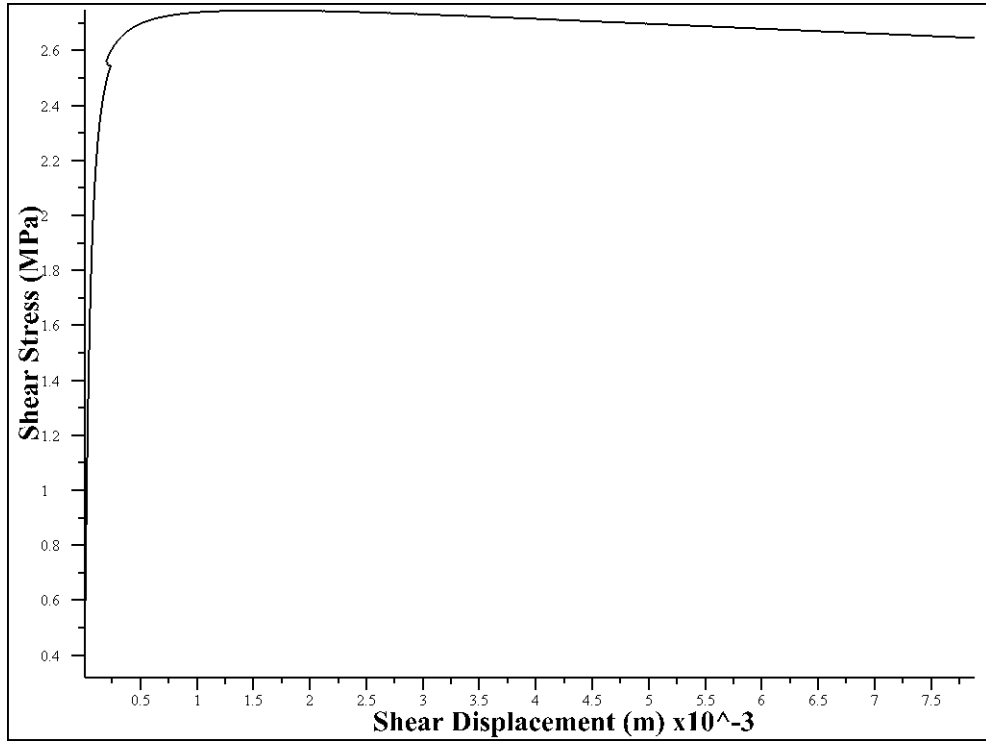


Figure C.20 Shear stress –shear displacement plot with JCS = 90 MPa

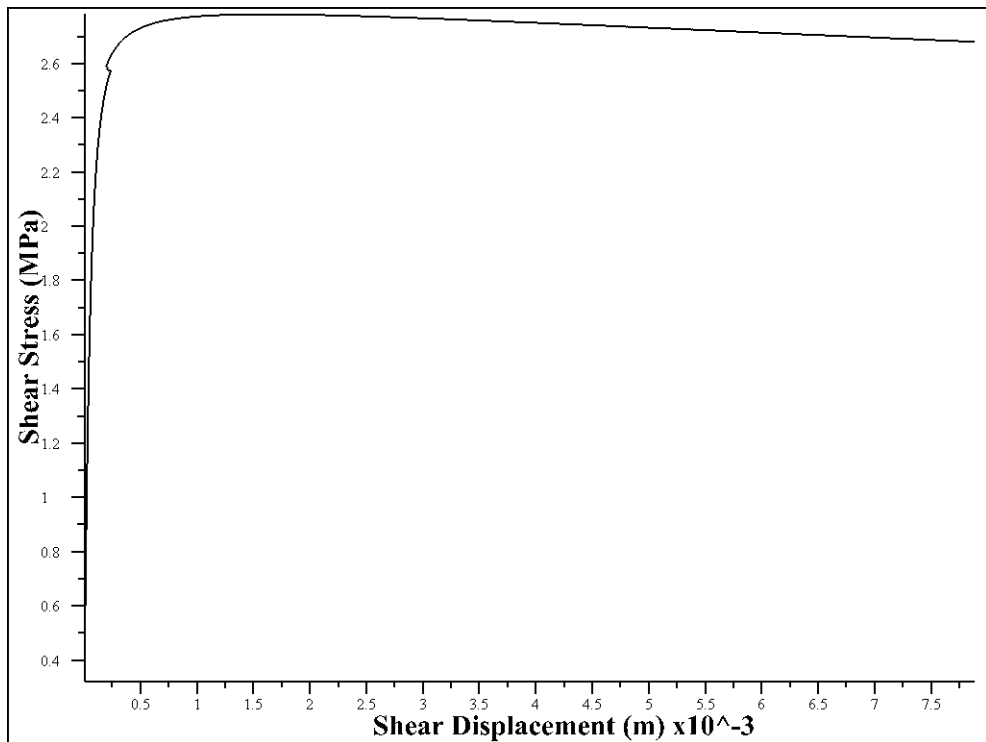


Figure C.21 Shear stress –shear displacement plot with JCS = 100 MPa

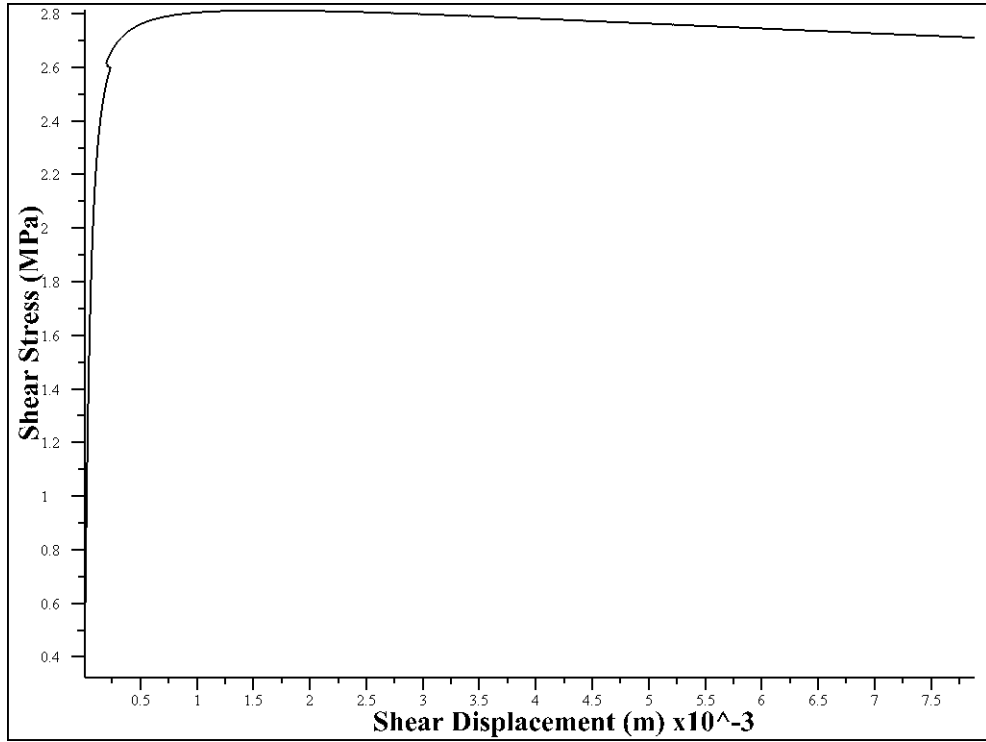


Figure C.22 Shear stress –shear displacement plot with JCS = 110 MPa

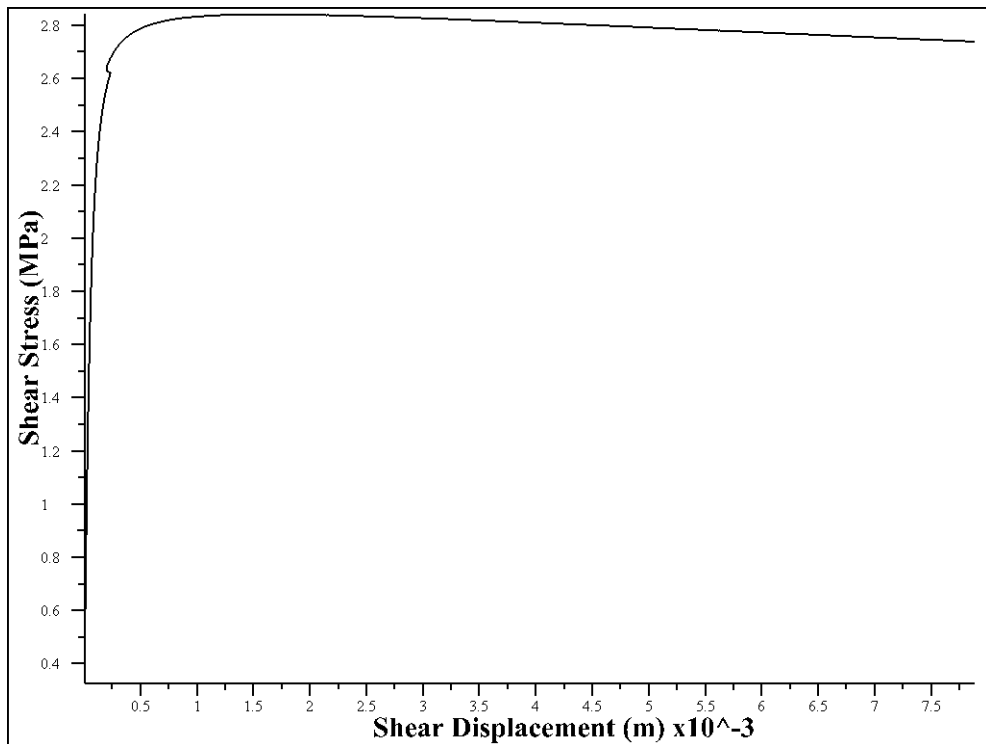


Figure C.23 Shear stress –shear displacement plot with JCS = 120 MPa

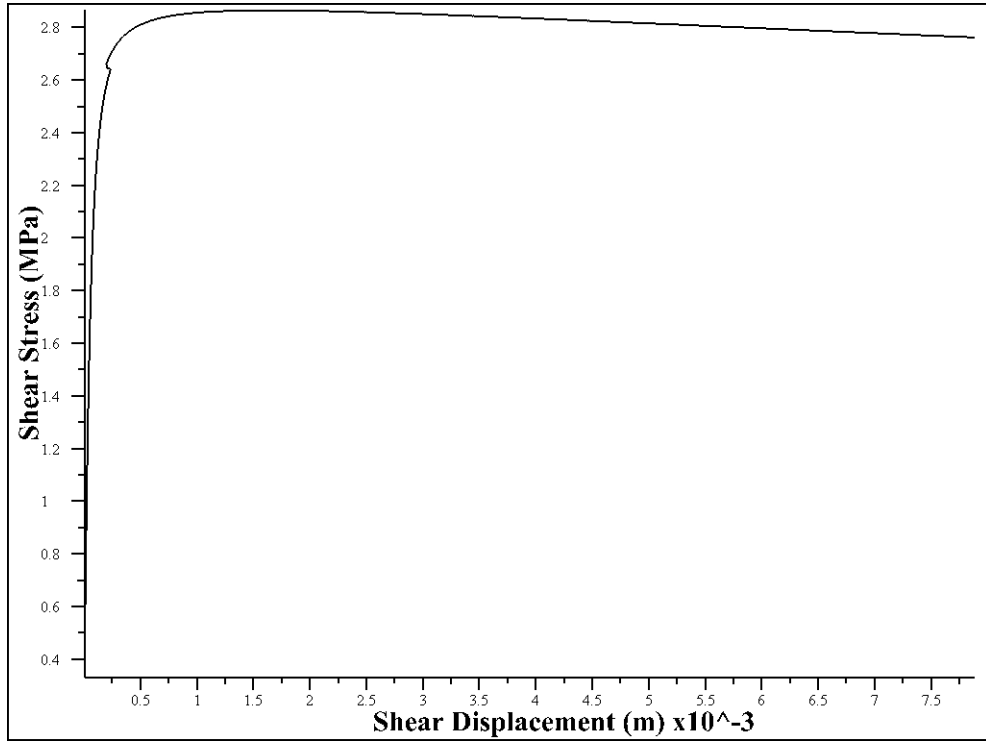


Figure C.24 Shear stress –shear displacement plot with JCS = 130 MPa

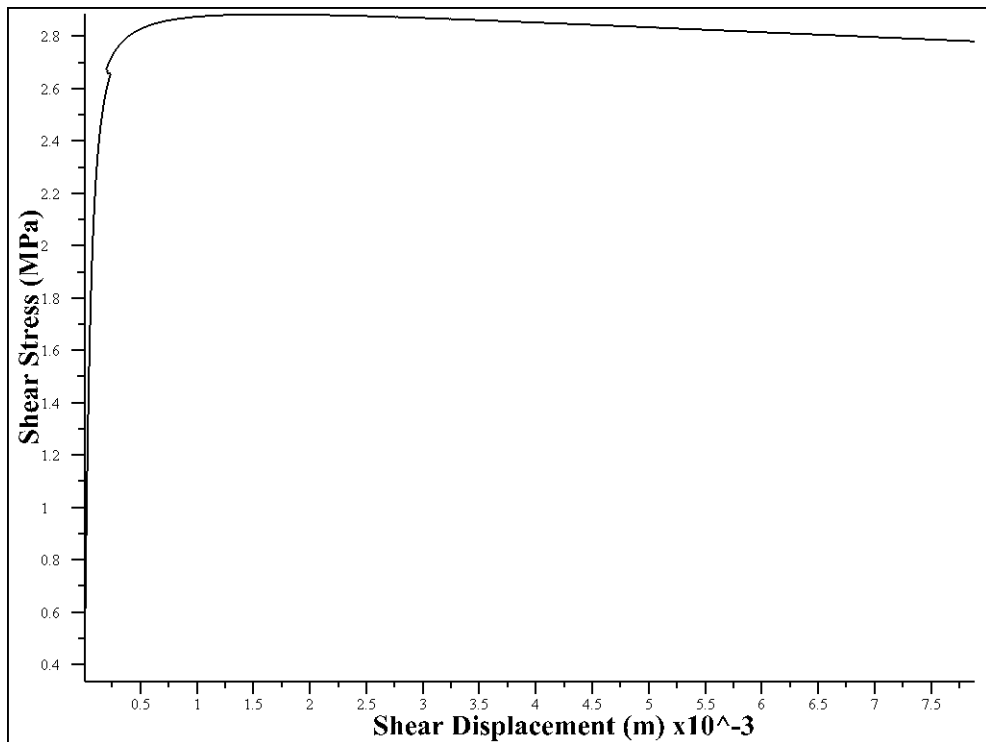


Figure C.25 Shear stress –shear displacement plot with JCS = 140 MPa

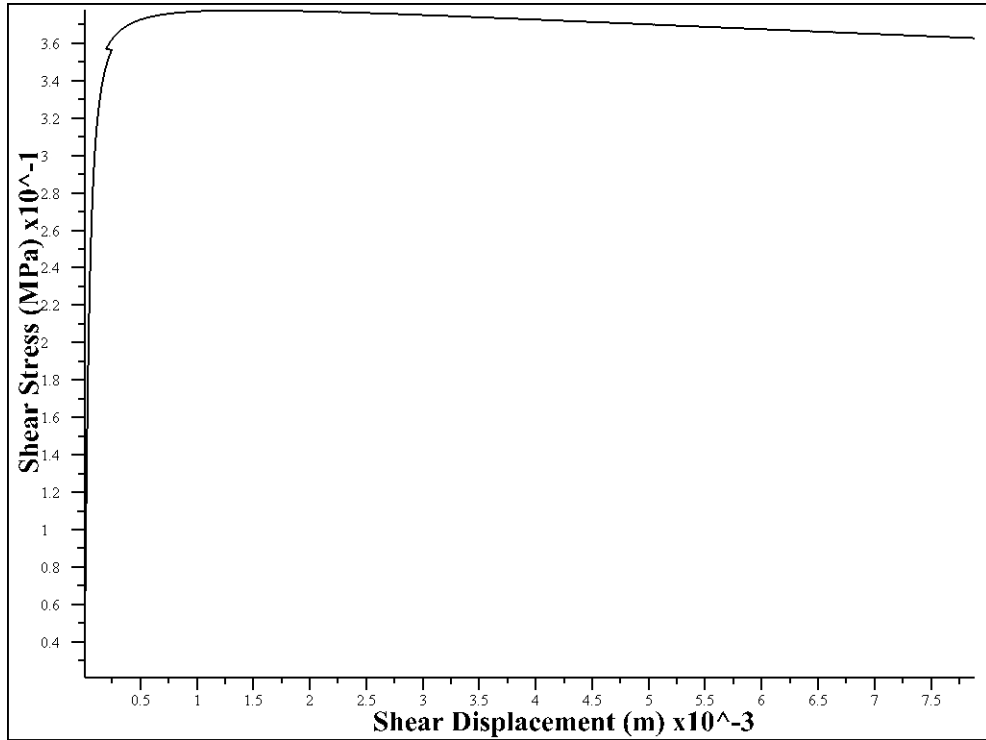


Figure C.26 Shear stress –shear displacement plot with $\sigma_n = 0.5$ MPa

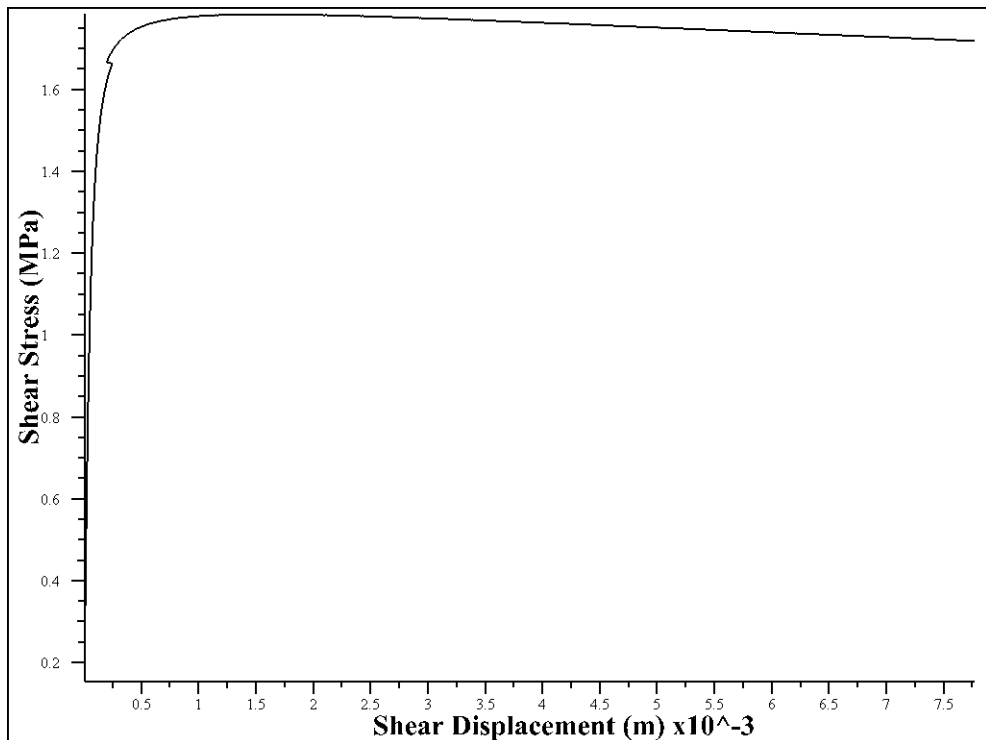


Figure C.27 Shear stress –shear displacement plot with $\sigma_n = 3$ MPa

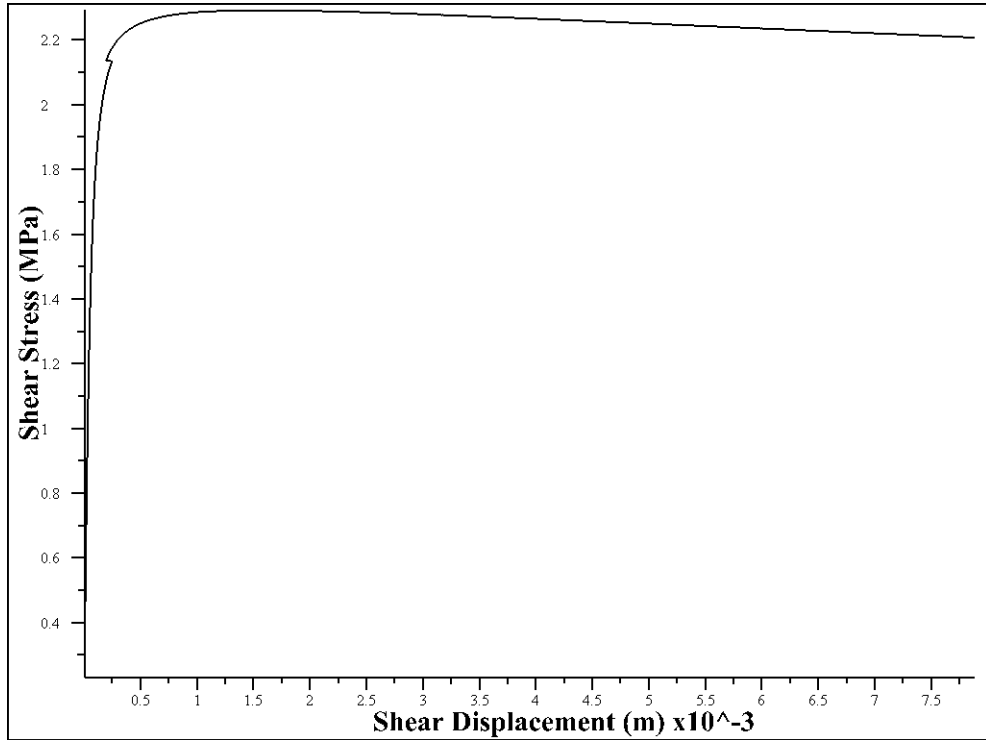


Figure C.28 Shear stress –shear displacement plot with $\sigma_n = 4$ MPa

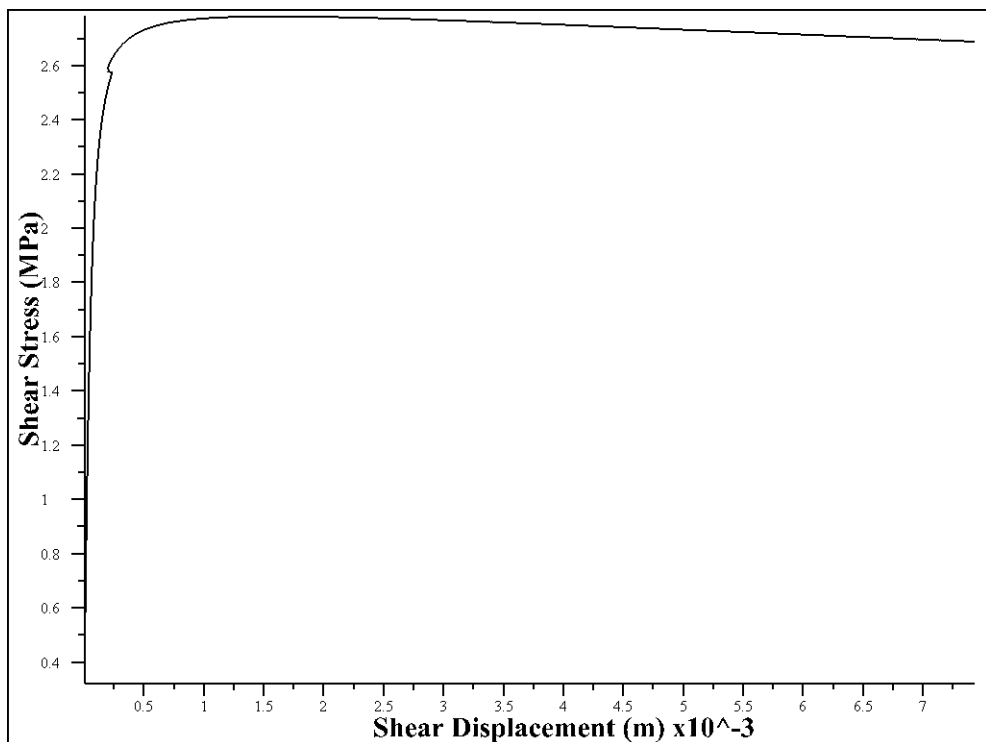


Figure C.29 Shear stress –shear displacement plot with $\sigma_n = 5$ MPa

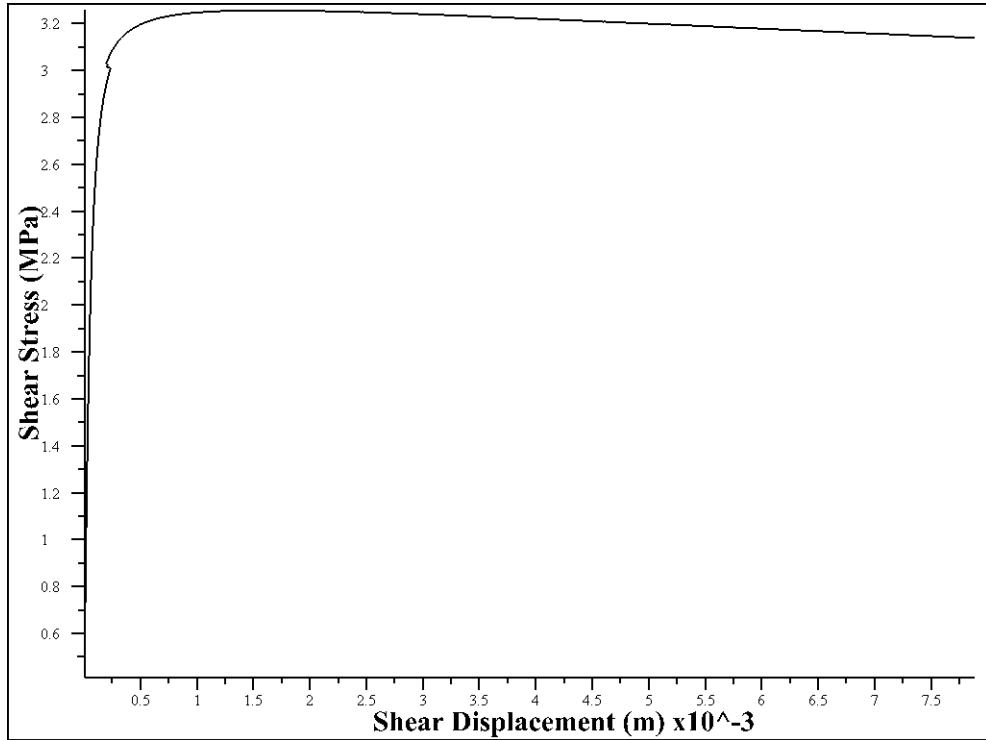


Figure C.30 Shear stress –shear displacement plot with $\sigma_n = 6$ MPa

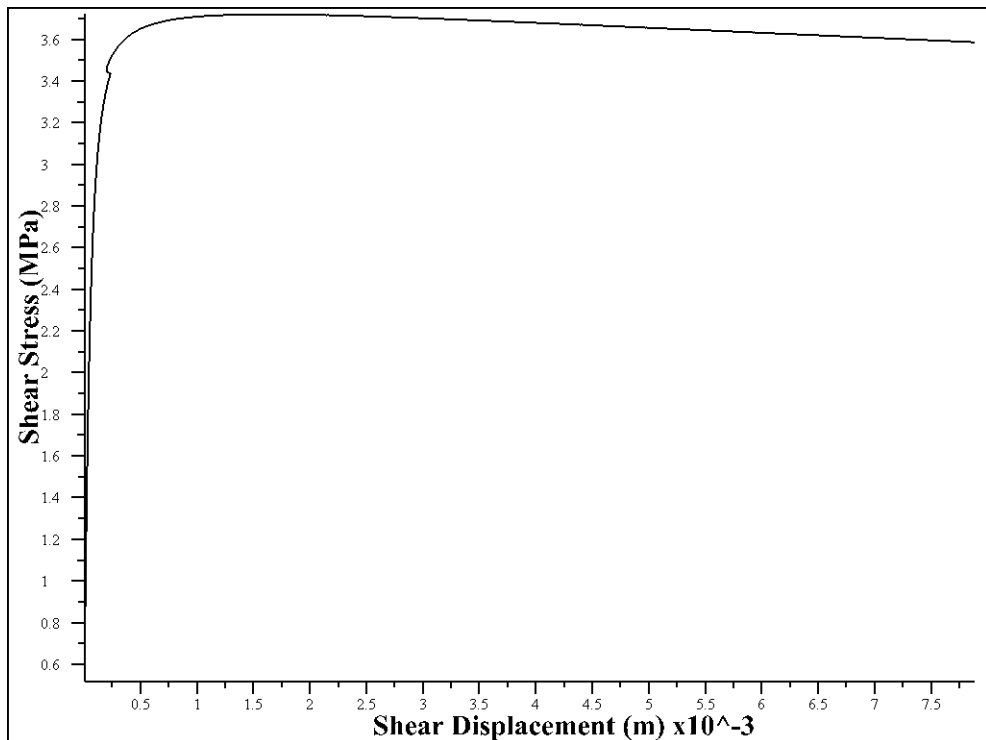


Figure C.31 Shear stress –shear displacement plot with $\sigma_n = 7$ MPa

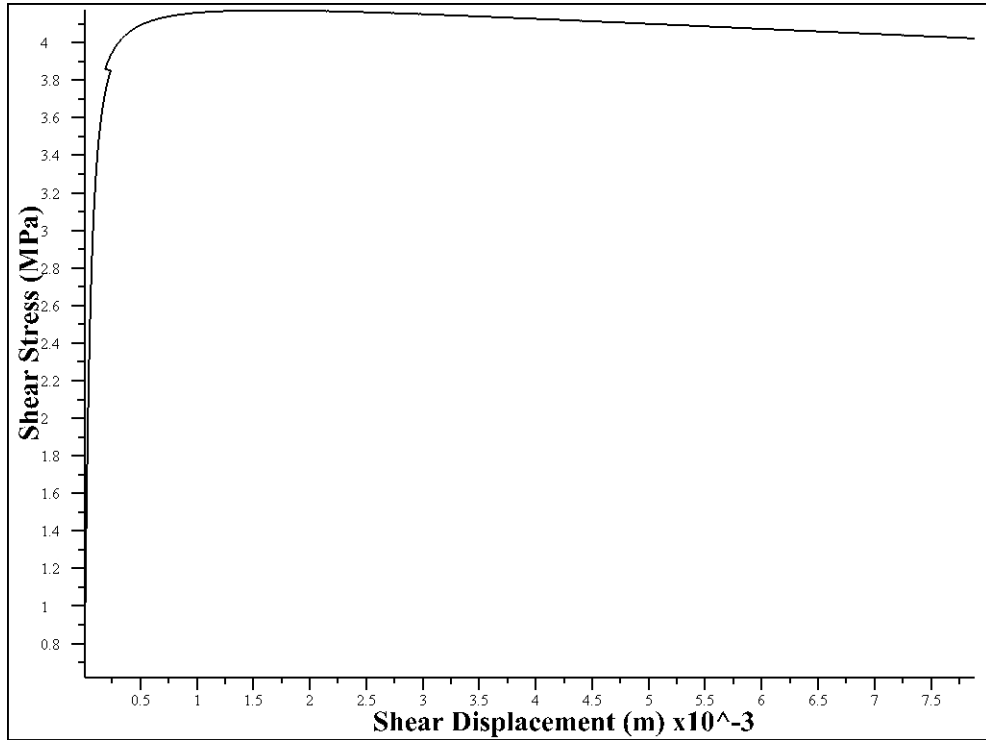


Figure C.32 Shear stress –shear displacement plot with $\sigma_n = 8$ MPa

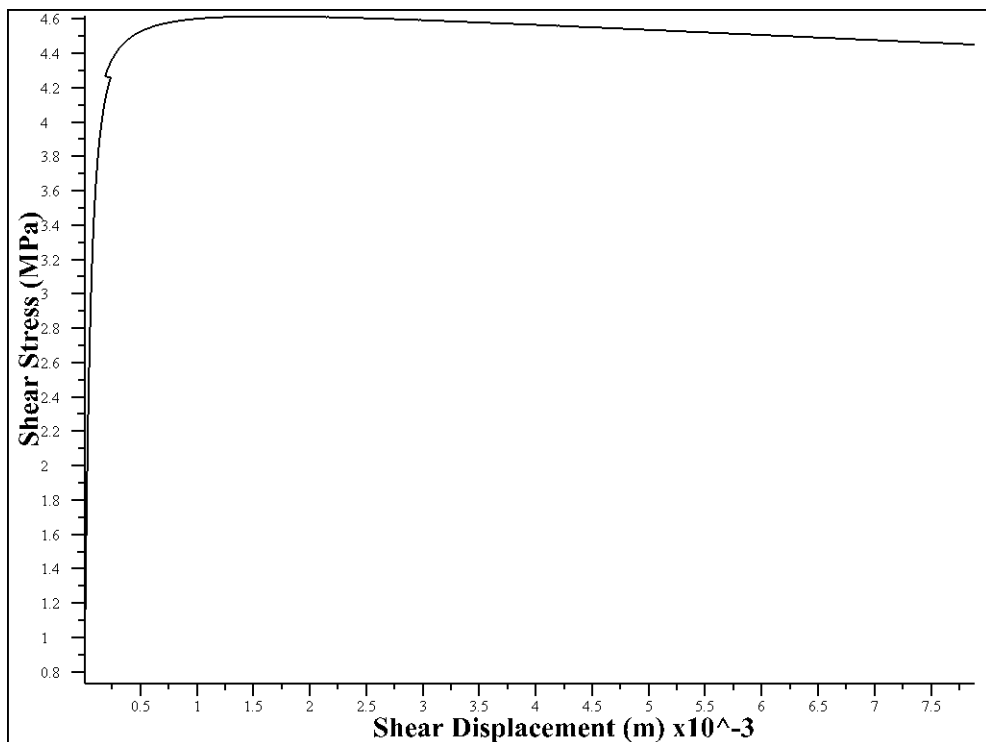


Figure C.33 Shear stress –shear displacement plot with $\sigma_n = 9$ MPa

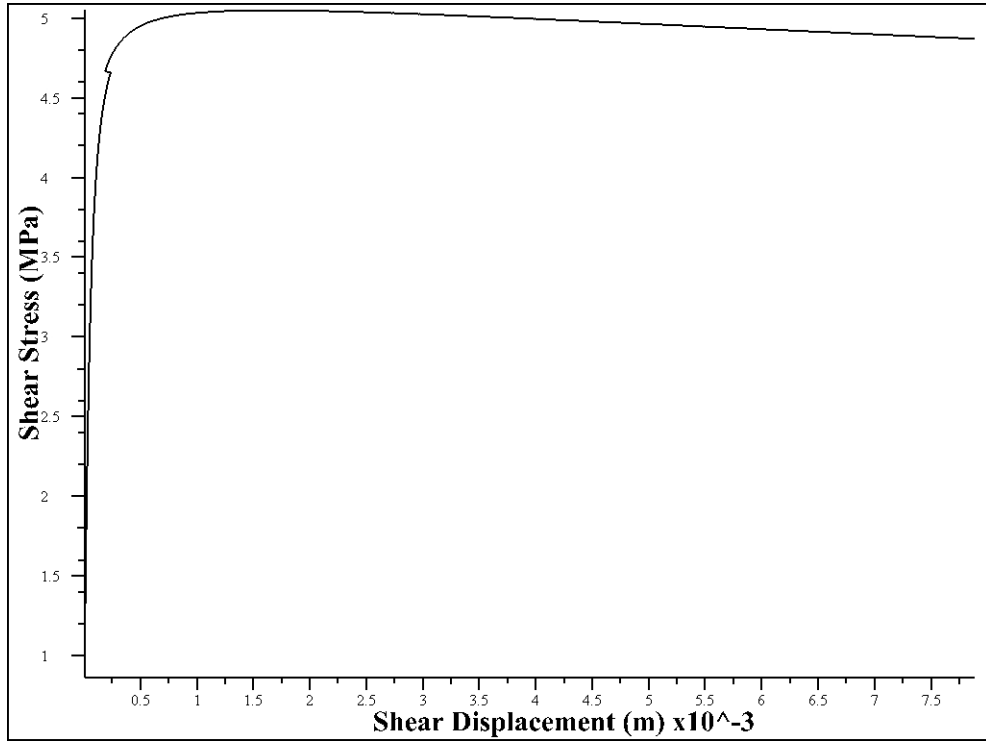


Figure C.34 Shear stress –shear displacement plot with $\sigma_n = 10$ MPa

APPENDIX D

DILATATIONAL BEHAVIOUR

In this part, dilation vs shear displacement and shear stress shear displacement graphs of the sample with residual friction angle of 20° , lab scale joint roughness coefficient of 16, lab scale joint wall compressive strength value of 100 MPa, uniaxial compressive strength of 150 MPa and under a normal stress of 5 MPa is given;

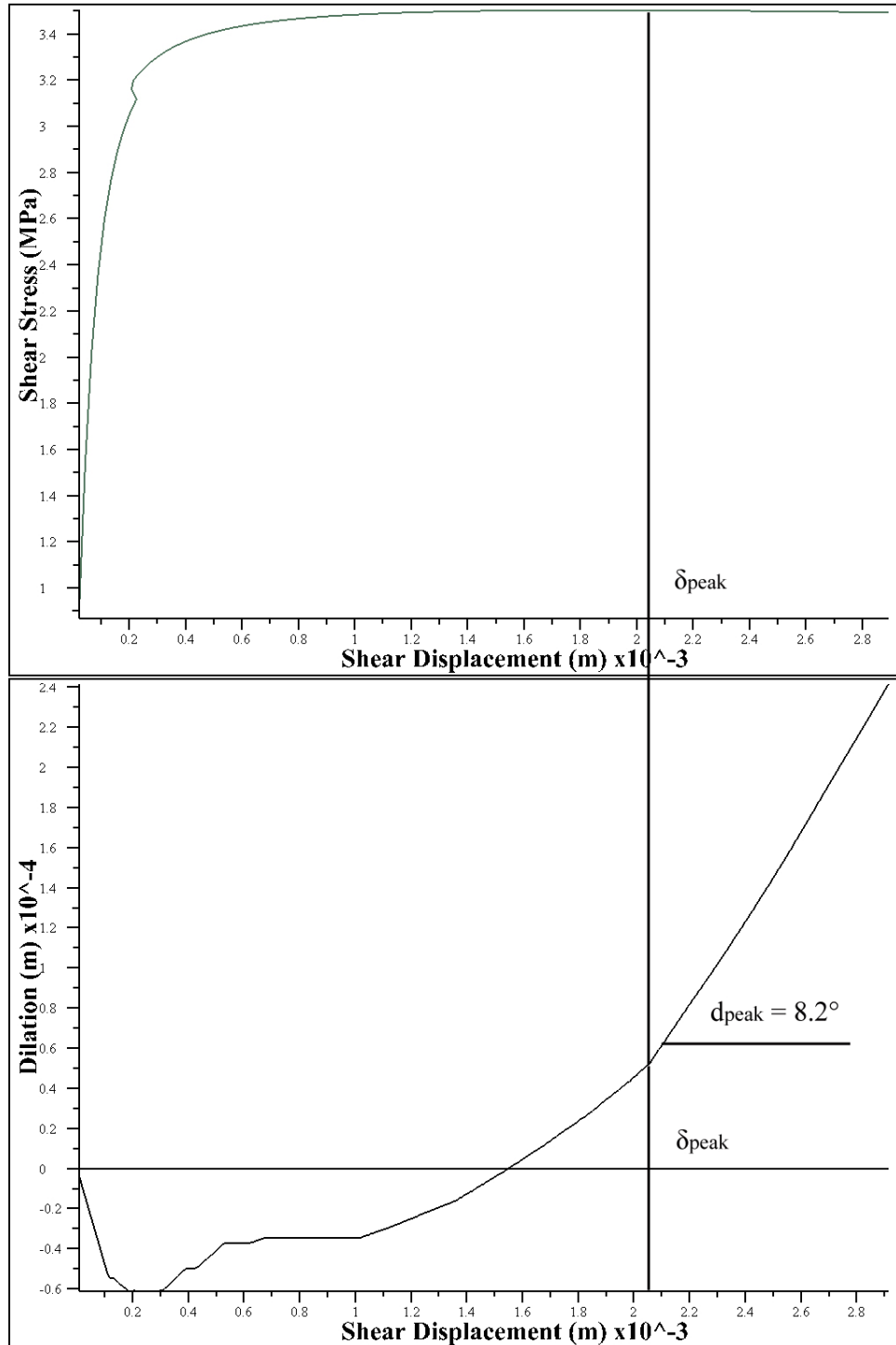


Figure D.1 Graph of Shear displacement vs dilation and shear stress vs shear displacement ($\phi_r = 20^\circ$, $\sigma_c = 150$ MPa, $JRC_0=16$, $JCS_0=100$ MPa and $\sigma_n = 5$ MPa)

CURRICULUM VITAE

PERSONAL INFORMATION

Surname, Name: Koçal, Arman
Nationality: Turkish (TC)
Date and Place of Birth: 5 March 1979, Ankara
Marital Status: Married
Phone: +90 532 367 17 15
e-mail: armarkocal@yahoo.com

EDUCATION

Degree	Institution	Year of Graduation
PhD	METU, Mining Engineering	2008
MSc	METU, Mining Engineering	2004
BSc	METU, Mining Engineering	2001
High School	TED Ankara College	1996

WORK EXPERIENCE

Year	Place	Enrollment
2002-Present	METU, Mining Engineering	Research Assistant
2000 July	Park Teknik A.Ş.	Intern Engineering Student
1999 July	TKİ Yeniköy Linyitleri İşletmesi	Intern Engineering Student

FOREIGN LANGUAGES

Advanced English

PUBLICATIONS

1. Koçal, A., Duzgun, H.S.B. and Karpuz, C., 2004. Discontinuity Mapping with Automatic Lineament Extraction from High Resolution Satellite Imagery, Proceedings of 20 th Congress of International Society for Photogrammetry and Remote Sensing (ISPRS). Vol. 37, pp 1073-1078.
2. Koçal, A., Duzgun, H., S., B., Karpuz, C., 2006. Mapping of discontinuities with automatic lineament extraction from high resolution satellite imagery. Proceedings of Fifteenth International Symposium on Mine Planning & Equipment Selection. pp 1411-1416.

3. L., Tutluođlu, A., Koçal, C., Karpuz, 2006. TKİ ELİ Eynez Bölgesi Karanlıkdere drenaj tüneli kalıcı tahkimat tasarımı. Sekizinci Bölgesel Kaya Mekaniji Sempozyumu, pp 115-120.
4. Koçal, A., Düzgün, H., S., Karpuz, C., 2007. An accuracy assessment methodology for the remotely sensed discontinuities: a case study in Andesite Quarry area, Turkey". International Journal of Remote Sensing, Vol: 28, No: 17, pp 3915-3936.
5. Tutluođlu, L., Karpuz, C., Koçal, A., 2007. Permanent Support Design for an Existing Drainage Tunnel at ELI Mine in Turkey, Proceedings of the Sixteenth International Symposium on Mine Planning and Equipment Selection. pp 1104-1121.
6. Tutluođlu, L., Karpuz, C., Koçal, A., 2008. Design of weak rock slope of BLI open pit coal mine in Turkey, Proceedings of the Seventeenth International Symposium on Mine Planning and Equipment Selection. In Press.

HOBBIES

Football, Movies, Travelling, Aquarium